
WILDFIRE DRONE SWARM FINAL REPORT

Final Report for Design Synthesis Exercise. Course AE3200 of the 3rd year Bachelor Aerospace Engineering 2023/2024, TU Delft. Project group 12 mentored by *Ir. Ronald van Gent*.

Executed and written by:

Ebbe Abbenhuis	<i>Redacted</i>	Björn Kleipool	<i>Redacted</i>
Jack Agterdenbos	<i>Redacted</i>	Vince Lubbers	<i>Redacted</i>
Vittorio Bonanno	<i>Redacted</i>	Aleks Mielczarek	<i>Redacted</i>
Marco Camporeale	<i>Redacted</i>	Takayoshi Nakagawa	<i>Redacted</i>
Kevin Do Cao	<i>Redacted</i>	Andrei Petrache	<i>Redacted</i>

Submitted for assessment to:

Ir. Ronald van Gent, Linh Ngo, Shreyas Anand



TECHNICAL UNIVERSITY DELFT, FACULTY OF AEROSPACE ENGINEERING

KLUYVERWEG 1, 2629 HS DELFT
INFO@TUDELFT.NL, WWW.TUDELFT.NL

Starting date: June 3rd 2024

Completion date: June 19th 2024

This page is left blank intentionally.

TABLE OF CONTENTS

List of Symbols	II		
List of Abbreviations	III		
1 Executive Overview	1		
2 Introduction	5		
3 Project Overview	6		
3.1 Background Information	6		
3.2 Mission Statement	7		
3.3 Mission Concept Description	7		
3.4 Top-level Functional Flow	7		
3.5 Sustainability Strategy	8		
3.6 Top-level Risk Analysis	12		
3.7 Requirement Strategy	16		
4 Mission Logistics & Operations Design	18		
4.1 Operational Modes Definitions	18		
4.2 Location Definition	20		
4.3 Wildfire Models	21		
4.4 Sensors Selection	23		
4.5 Drone Contingent Behaviour	26		
4.6 Swarm Sizing	26		
5 Swarm Design	30		
5.1 Definition of Swarm Framework	30		
5.2 Sector Generation & Path-finding Methods	31		
5.3 Swarm Performance & Comparison	33		
6 Communications Architecture	36		
6.1 Background Information	36		
6.2 System Risks & Requirements	37		
6.3 Assumptions	37		
6.4 Design	38		
6.5 Link Budget Calculation	43		
6.6 Verification and Validation	46		
6.7 Further Recommendations	47		
7 UAV Design	48		
7.1 Design Methodology & Integration	48		
7.2 Weight Estimation	52		
7.3 Flight Performance	53		
7.4 Aerodynamics	57		
7.5 Stability & Control	61		
7.6 Propulsion & Power	73		
7.7 Avionics & Electrical Systems	79		
		7.8 Structures	83
		7.9 Ballistic Recovery System	89
		7.10 Design Results	92
	8	Ground Systems	100
		8.1 Subsystem Risks & Requirements	100
		8.2 Assumptions	100
		8.3 Design	101
	9	Manufacturing and Integration Plan	108
		9.1 Component assembly	108
		9.2 UAV assembly	109
		9.3 GCU assembly	109
		9.4 Logistics	109
	10	Design Assessment	111
		10.1 Requirement Compliance Verification	111
		10.2 RAMS Analysis	113
	11	Financial Valuation	114
		11.1 Cost Analysis	114
		11.2 Market Analysis	119
	12	Conclusion and Recommendations	124
		Bibliography	125
	A	Appendix	132

LIST OF SYMBOLS

Symbol	Definition	Unit	Symbol	Definition	Unit
α	Launch angle, Angle of Attack	[deg]	I	Area moment of inertia	$[m^4]$
β	Deflection angle	[deg]	I	Mass moment of inertia	$[kgm^2]$
β	Sideslip	[deg]	i	Angle of incidence	[rad]
β	Compressibility factor	[-]	J	Advance ratio	[-]
δ	Deflection angle	[deg]	K	Stiffness coefficient	[N/m]
γ	Climb angle	[deg]	K	Buckling coefficient	[-]
γ	Strain	[-]	L	Lift	[kN]
γ	Correction factor	[-]	L	Length	[m]
η	Efficiency, Ratio, Fraction	[-]	L	Thickness location	[-]
λ	Taper ratio	[-]	L	Correction factor	[-]
Λ	Sweep angle	[deg]	L_T, L_P, L_R	Transmitter, Propagation and Receiver Losses	[-]
ν	Poisson ratio	[-]	l	Length	[m]
ω	Angular velocity	[rad/s]	M	Moment	[Nm]
ϕ	Roll angle	[deg]	M	Mass	[kg]
ρ	Density	$[kg/m^3]$	m	mass	[kg]
σ	Axial stress	[MPa]	N	Normal force	[N]
τ	Shear stress	[MPa]	N	Amount	[-]
τ	Aileron effectiveness	[-]	Ni	Noise	[W]
θ	Deflection angle	[deg]	NIR	Near-infrared band of radiation	[Hz]
θ	Pitch	[deg]	n	Revolutions per minute	[RPM]
AR	Aspect ratio	[-]	n	Amount	[-]
X, Y, Z	Force	[N]	n	Load factor	[-]
A	Search area	$[m^2]$	P	Power	[W]
A	Enclosed Area	$[m^2]$	P	Roll rate	[rad/s]
A_m	Section enclosed area	$[m^2]$	P	Load	[N]
a	Speed of sound	[m/s]	P_a	Power available	[W]
B	Effective Noise Bandwidth	[Hz]	P_r	Power required	[W]
BER	Bit Error Rate	[-]	P_T	Transmitter Power	[W]
b	Wing span	[m]	p	Pitch rate	[rad/s]
b	I-beam base	[m]	q	Yaw rate	[rad/s]
b_f	I-beam flange base	[m]	R	Radius, distance	[m]
C	Capacity	[Ah]	R	Hourly cost	[\$]
C	Cost	[\$]	R	Labour hours per person	[hr]
C	Coefficient	[-]	R	Red band of radiation	[Hz]
C_D	Drag coefficient	[-]	RF	Forest risk factor	[-]
C_d	Airfoil drag coefficient	[-]	ROC	Rate of Climb	[m/s]
C_H	Hinge moment coefficient	[-]	r	Radius	[m]
C_L	Lift coefficient	[-]	r	Roll rate	[rad/s]
C_l	Airfoil lift coefficient	[-]	S	Surface area	$[m^2]$
C_m	Moment coefficient	[-]	S	The set of sectors in the search area	[-]
C_X	Opening force coefficient	[-]	S_b	Cross-sectional area	$[m^2]$
C_Y	Chord distribution	[-]	S_{pl}	Planform area	$[m^2]$
C_Y, C_X, C_Z	Force coefficient	[-]	Si	Signal Strength	[W]
C_f	Friction coefficient	[-]	T	Torsion	[Nm]

Table 1 – continued from previous page

Symbol	Definition	Unit	Symbol	Definition	Unit
c	Damping coefficient	[Ns/m]	T	Tension	[N]
c	Chord	[m]	T	Temperature	[K]
\bar{c}	Mean aerodynamic chord	[m]	T	Time	[s]
D	Drag	[kN]	t	Thickness	[m]
D	Diameter	[m]	t	Time	[s]
I	Current	[A]	u, v, w	Velocity	[m/s]
d	Cell width	[m]	V	Shear force	[N]
E	Young's modulus	[Pa]	V	Velocity	[m/s]
e	Oswald efficiency	[-]	V	Volume	[m ³]
f	Factor	[-]	V	Voltage	[V]
G	Shear modulus	[Pa]	V_c	Cruise speed	[m/s]
G	Green band of radiation	[Hz]	V_y	Normal force	[N]
G_T, G_R	Transmitter, Receiver Gain	[-]	W	Weight	[N]
h	I-beam height, Altitude	[m]	x, y, z	Cartesian coordinates	[m]
h_f	I-beam flange height	[m]	X	Force reduction factor	[-]

LIST OF ABBREVIATIONS

Abbreviation	Definition	Abbreviation	Definition
AI	Artificial Intelligence	I2C	Inter-Integrated Circuit
AoA	Angle of Attack	ICAO	International Civil Aviation Organisation
AR	Aspect Ratio	IMU	Inertial Measurements Unit
ATGS	Air tactical group supervisor	IR	Infrared
BRS	Ballistic recovery system	KIAS	Indicated airspeed in knots
BVLOS	Beyond Visual Line of Sight	LG	Landing gear
CAGR	Compound annual growth rate	LiDAR	Light Detection And Ranging
CAWFE	Coupled atmosphere wildland fire environment	MAC	Mean Aerodynamic Chord
CEF	Cost escalation factor	MD	Medium dry soil
CFD	Computational Fluid Dynamics	MODIS	Moderate Resolution Imaging Spectroradiometer
COTS	Commercial off-the-shelf	MTBF	Mean time between failures
CRM	Communication relay mode	MTOM	Maximum take-off Mass
DC	Direct Current	MTOW	Maximum take-off Weight
DoD	Depth of discharge	MTTR	Mean time to repair
DR	Data rate	MW	Medium wet soil
DTR	Daily air temperature range	NACA	National Advisory Committee for Aeronautics
EASA	European Union Aviation Safety Agency	NASA	National Aeronautics and Space Administration
EEA	European Environment Agency	NDVI	Normalised Difference Vegetation Index
EIPA	Environmental Impact Potential Assessment	NF	Noise Figure
EMI	Electromagnetic interference	NIR	Near-Infrared

Table 2 – continued from previous page

Abbreviation	Definition	Abbreviation	Definition
EOM	Empty operational mass	NLR	Nederlands Lucht- en Ruimtevaart-centrum
EPS	Electrical Power System	PDB	Power distribution board
ERM	Emergency recovery mode	PWM	Pulse width modulation
ESC	Electronic speed controller	QC	Quality control
EVI	Enhanced Vegetation Index	RAMS	Reliability, availability, maintainability, and safety
FAA	Federal Aviation Administration	RF	Radio frequency, Risk Factor
FPS	Frames per second	RFI	Radio interference
FOS	Factor of safety	ROC	Rate of climb
FSL	Free Space Loss	RPM	Revolutions per minute
FSS	Fire Suppression System	RTK	Real time kinematics
GCS	Geographic Coordinate System	SD	Secure Digital
GCU	Ground control unit	SF	Safety factor
GDP	Gross Domestic Product	SNR	Signal-to-Noise ratio
GHG	Greenhouse Gases	SWOT	Strengths, weaknesses, opportunities and threats
GIS	Geographic information system	TETRA	Terrestrial trunked radio
GNSS	Global navigation satellite system	UART	Universal asynchronous receiver/transmitter
GPIO	General-purpose input/output	UAS	Unmanned aerial system
GPS	Global Positioning System	UAV	Unmanned aerial vehicle
GS	Ground system	UHF	Ultra-high frequency
HLDs	High lift devices	US	United States
		USDA	United States Department of agriculture
		VSD	Value Sensitive Design
		V&V	Verification & Validation

EXECUTIVE OVERVIEW

In 2022, wildfires in the EU destroyed an area roughly equivalent to the size of Corsica, marking the second worst year in terms of wildfires in Europe since 2006 [1]. The European Commission states: "For the third year in a row, unprecedented wildfire events have caused large environmental and economic damage as well as tragic loss of life" [1]. Furthermore, a 2022 United Nations report predicts an increase of 14% in global extreme wildfires by 2030 and 30% by 2050 [2]. While most of the fires (96%) result from human actions [1], they are aggravated by increasingly volatile conditions driven by climate change [2]. Despite countries becoming more steadfast in wildfire control, the rapid extinguishing of frequent small-scale fires has increased the undergrowth in forests. This has increased large-scale, rapidly expanding wildfires known for their large greenhouse gas emissions. Wildfires not only cause environmental damage, such as ecosystem destruction, drastic changes in vegetation dynamics, atmospheric conditions and biochemistry, but also cause significant human and economic damage [2]: transportation networks and supply chains are disrupted, businesses are closed, employment rates are reduced, and tax revenues fall. For this reason, in the next six years, global demand for wildfire management technology is projected to rise by about 50% with the increasing importance of wildfire management [3]. While new technologies have been developed to predict, detect, monitor and combat wildfires, there are still many gaps in current wildfire management systems that have yet to be tackled. These are mainly limitations in the availability of fuel (vegetation) measurements and accuracy limitations associated with other means of measurement such as satellite imagery [4, 5, 6].

This issue has led the Netherlands Aerospace Centre (NLR) to propose a solution in the form of a UAV swarm that monitors forests in risk areas and collects environmental data. This swarm should be able to both detect ongoing fires and collect data on the environment to improve the understanding of the driving factors in the generation and spread of wildfires. From this data, an ignition and spread prediction model can be created. The resulting model of wildfire risk factors will enhance the wildfire fighting capabilities. With wildfires predicted and detected up to a day before their occurrence, the fire service can more efficiently extinguish and prevent uncontrollable wildfires. This change in the firefighting industry will lead to large savings in the loss of forests and CO₂ emissions, not to mention the economic and social impact of safety and stability for those who live in the affected areas. This vision was enticing enough for TU Delft to commit to further developing the idea by proposing it for a graduation design project for the Bachelor of Sciences in Aerospace Engineering program. This report describes the results of the analysis and design activities that were performed that led to the selected concept entering the detailed design phase. It is motivated that the selected concept will work and meet the requirements.

In previous reports, project planning, baseline, and conceptual design have been presented. The purpose of the conceptual design was to choose a framework for the rest of the project and generate various possible concepts based on which one was chosen. This report aims to present that chosen concept in detail and propose a more refined version of the wildfire drone swarm as a wildfire management system used for forest fire predictions and monitoring.

In the ongoing effort to combat wildfires, every minute is crucial for the safety of firefighting personnel. The wildfire drone swarm presents a revolutionary approach to detection and response, offering significant advantages in safety, speed, and continuous data resolution. One of the key benefits of the drone swarm is its capability to markedly reduce or eliminate human risk, particularly during night-time operations. Traditionally, ground crews and piloted aircraft navigate hazardous and unpredictable conditions to monitor and respond to wildfires. In contrast, drones cover extensive areas without endangering human lives, which is particularly critical under conditions of reduced visibility, such as at night or within wildfire smoke. Furthermore, drones operate continuously through the night, providing real-time data that enhances the efficiency and safety of wildfire response efforts.

An essential feature of the drone swarm is its ability to significantly reduce the time for detection and response, achieving a response time of just 20 minutes. Early detection is vital for effectively managing wildfires, allowing rapid intervention to prevent small fires from escalating into large, uncontrollable blazes. Drones quickly survey vast areas, detect anomalies, and transmit data swiftly to control centres, surpassing traditional monitoring methods. This rapid response capability can distinguish between containing a fire and facing a widespread disaster. Moreover, the drone system provides continuous, high-resolution information, offering a detailed and comprehensive view of the wildfire situation. Continuous monitoring ensures timely detection of any changes in fire behaviour, facilitating informed decision-making and efficient allocation of firefighting resources. High-resolution data enables precise mapping of the fire perimeter, identification of hotspots, and accurate fire spread predictions. Such detailed insights are invaluable for planning and executing firefighting strategies effectively.

Project Overview

The project overview comprehensively summarises the initiative to enhance wildfire monitoring and management through advanced technologies. It begins with a review of existing non-urban wildfire monitoring systems, categorising them into ground-based, satellite-based, and air-based technologies, each with its strengths and limitations. The critical mission needs and objectives are underscored, emphasising the importance of improving wildfire management to reduce emissions, protect nature, and save lives. The proposed solution involves designing a drone swarm system, integrating AI and UAVs for real-time, high-resolution monitoring supported by regulatory advancements.

An integrated overview of system functions is detailed, breaking down the project into pre-operation, operation, and evolution phases, ensuring a structured approach to design and development. The importance of balancing sustainability and cost-efficiency and adopting a value-sensitive design (VSD) approach to address stakeholders' needs and environmental impacts is also discussed. This holistic approach aims to create a low-cost, autonomous drone swarm capable of continuous monitoring and data-driven decision-making, ultimately enhancing wildfire response and proactive disaster management.

Mission Logistics & Operations Design

Mission Logistics & Operations Design outlines the operational modes for UAV swarm operations in firefighting, including Surveying, Monitoring, Deployment, Recovery, Emergency Recovery, Holding, Communication Relay, and Manual Mode. These modes are integrated into existing firefighting procedures to enhance surveillance, communication, and operational flexibility during fire events. It discusses the global significance of wildfires exacerbated by climate change, particularly noting their impact in Europe, the United States, and Australia. Effective wildfire prediction and monitoring systems are crucial to mitigate economic, social, and environmental damage. The drone swarm system, designed for Europe but adaptable globally, is well-suited for monitoring dense forests in regions such as Spain and Italy.

Fire management missions focused on predicting, detecting, and monitoring fire spread are examined. Methodologies such as the CAWFE model, which integrates weather prediction with fire behaviour modules are reviewed. It highlights the integration of drone swarms to provide real-time fire location data critical for these predictive models. The chapter also details criteria for selecting sensors, including infrared, visual, and near-infrared cameras, and LiDAR for terrain mapping. Risk management strategies for drone swarms in high-risk areas are discussed, focusing on autonomous obstacle avoidance, collision prevention with emergency air traffic, and protocols for communication loss scenarios. Finally, the chapter addresses design considerations and constraints for deploying drone swarms, outlining the formula for determining the number of drones required based on area size, speed, and cycle time, emphasising the ongoing data collection needed to optimise operational effectiveness.

Swarm Design

In the Swarm Design chapter, a swarm planning framework is devised for optimal surveillance of a wildfire risk area. The primary goal of the swarm is to optimise the spatial and temporal distribution of UAVs to ensure rapid detection of wildfires, thereby minimising the risk of fires becoming uncontrollable. A framework is adopted where every UAV is allotted a certain subset of the search area called its sector, through which the UAV will trace a pre-defined path. The selected swarm planning framework is validated through simulations, examining the ability of a 20-surveillance UAV swarm to detect wildfires. The results show that the swarm can successfully detect 50% of wildfires in the search area within 16 minutes and 95% of wildfires within 33 minutes. Lastly, the detection performance of the swarm is compared to a single general aviation aircraft with a similar cost profile (Beechcraft King Air 350). This comparison shows that the swarm is more cost-effective, has higher detection performance, and has a higher ground resolution than an aircraft performing the same mission in equivalent conditions.

Communications Architecture

Given the requirements defined by the team, a distributed-decentralised communication system was chosen for the communication section. This led to a relay drone being added to the system to support the high data rates required for the network to operate smoothly. A link budget was estimated to validate the architecture, which yielded a link margin greater than 5 dB for all communications links. From there, the team chose to use a phased array antenna in combination with a blade antenna to increase the gain and coverage of the system. Sizing of the phased array was done via a Matlab simulation. The system fulfilled the design requirements.

UAV Design

The UAV's flight performance depends on critical parameters such as wing loading, power loading, optimal cruise, and climb speeds. These factors determine efficiency, range, and endurance by balancing speed and altitude effectively. Aerodynamic analysis, including airfoil selection and drag estimation, is crucial in sizing the wings and ensuring stability and control through the empennage. The propulsion subsystem, powered by lithium-ion batteries, is designed for efficiency and quick maintenance, supporting sustained flight with minimal downtime. Avionics and electronics, including sensors for data collection and autonomous flight, are integrated into the UAV design to optimise performance and reliability. The structure, made from aluminium 6082, supports all subsystems under varying flight conditions, ensuring robust functionality and operational safety.

Ground Section

A full ground section of the system is designed to ensure continuous swarm operations. The launch rail and arrestor gear are sized to obtain take-off and landing speeds of 23 m/s with a peak acceleration of 5.75 G. The launch rail is designed to be 5 meters long and powered by an electric motor. On the other hand, the arrestor gear is 4 meters tall to ensure that the line has enough distance to bring the UAVs to a halt safely. The physical interaction, storage, and deployment are described and are also shown in Figure 1b. Where the arresting gear and launcher are stored on top of the platform, and the drones are hung below the platform.

Financial Evaluation

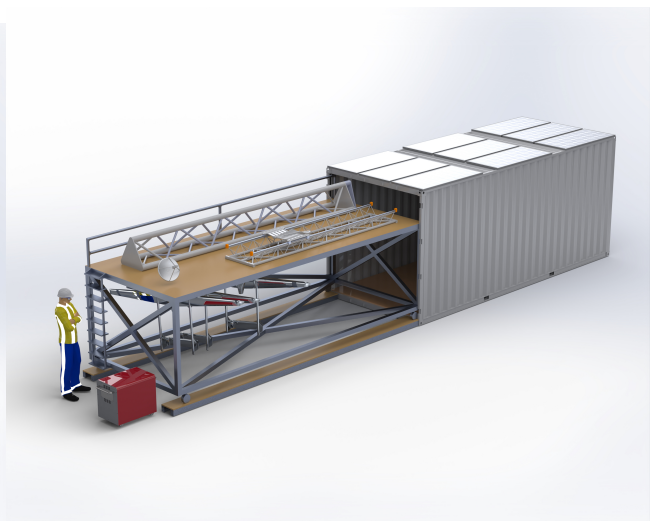
The financial valuation addresses the costs and market potential for developing and deploying a UAV-based wildfire management system. The analysis begins with a breakdown of Research, Development, Test, and Evaluation (RDT&E) costs, encompassing engineering salaries, ground station and software development, and wind tunnel testing. The estimated five-year development timeline and associated costs highlight the complexity and financial investment required for such advanced technology. Additionally, an examination of component and manufacturing costs are analysed, as well as operational costs, which focus on transportation, battery recharging, and maintenance, with a two-week mission estimated to cost approximately US\$28,774,

predominantly driven by operator wages. Finally, the end-of-life costs are estimated. The total swarm cost is found to be between US\$697,000 and US\$826,000.

The market analysis delineates the wildfire management and drone markets, emphasising the collaborative nature of wildfire management and the competitive landscape of the drone market. The various segments within these markets are outlined, such as urban and non-urban firefighting and different types of drones. Market dynamics are explored, identifying growth drivers like increased wildfire incidents, government initiatives, and challenges like certification processes and operating environments. The projected growth of both markets is quantified, with the wildfire management market expected to grow by 40% from 2023 to 2028 and the drone market experiencing even more rapid expansion [3]. The chapter also discusses the stakeholders involved, ranging from government agencies and fire departments to drone manufacturers and investors, highlighting their varying levels of interest and influence. Finally, the proposed system's market positioning, strengths, weaknesses, opportunities, and threats (SWOT) analysis are presented, along with a financial analysis demonstrating the system's return on investment and feasibility within California's wildfire management budget, showing a possible return on investment of 17%.



(a) Rendition of the UAV.



(b) Graphical representation of the system being stored for transportation.

Figure 1: Summary of renders

INTRODUCTION

With the global climate changing at an alarming rate, the threat of wildfires grows immensely. Annually, 3.85% of the global land area is burned by wildfires [7]. These wildfires emit roughly 2 billion megatonnes of CO₂ [8], double that of aviation globally in 2021 [9]. Some wildfire-prone regions, such as California, have forecasted the end-of-century wildfire emissions to increase by a median of 56% [10]. Additionally, wildfires pose a threat to human health and facilities. The US alone has an estimated 50 million houses in the wildlife-urban interface [11]. Tackling wildfires is essential for the health of the planet.

However, managing wildfires presents numerous challenges. Traditional methods often lack real-time data and the ability to adapt swiftly to changing conditions. Effective wildfire management relies heavily on timely and accurate information to make informed decisions. Insufficient data can lead to delayed responses, resulting in greater damage and loss. This is where advancements in technology, such as the deployment of drone swarms for wildfire monitoring, relaying firefighting communications, and wildfire modelling, become invaluable. These systems can significantly enhance the general ability to predict, monitor, and manage wildfires by providing comprehensive, real-time surveillance, data collection, and communication capabilities. This report will explore developing and implementing a wildfire monitoring drone swarm, highlighting its potential to revolutionise wildfire management and mitigate the impacts of these devastating events.

The purpose of this report is to present a method of wildfire prediction and detection utilising a Wildfire Drone Swarm. The project overview is first presented in chapter 3, followed by the mission logistics and operations design in chapter 4. Then, the system is described in more detail from the swarm perspective in chapter 5. After this, the communication architecture is elaborated in chapter 6. The drone design is presented in chapter 7, alongside the ground system in chapter 8. The Manufacturing and integration plan is shown in chapter 9, and the design is assessed in chapter 10. Lastly, the financial valuation is described in chapter 11.

PROJECT OVERVIEW

To define the project well, an overview needs to be created; this is the purpose of this chapter, namely to present the reasoning and the background of the project and walk the reader through the design strategy. First, the project's background information is presented in section 3.1. Then, a mission statement is presented in section 3.2, followed by the mission concept description in section 3.3. With the concepts presented, the Top-level functional flow is presented in section 3.4. Then, a sustainability strategy for the project is presented in section 3.5, followed by the risk analysis in section 3.6. Finally, the requirement strategy is elaborated on in section 3.7

3.1 BACKGROUND INFORMATION

This section examines the existing solutions for non-urban wildfire monitoring by segmenting the technologies into satellite-based, air-based, and ground-based systems. Each segment encompasses various technologies contributing to wildfire detection, assessment, monitoring, and extinguishing. Analysing these technological categories will give a comprehensive understanding of the current capabilities and applications in wildfire management, highlighting potential improvement and innovation areas.

Ground Based Systems Ground-based wildfire monitoring systems play a crucial role in the early detection and management of wildfires. These systems typically include an array of sensors and cameras strategically placed in high-risk areas to monitor environmental conditions and detect fire outbreaks [12]. The sensors can measure variables such as temperature, humidity, wind speed, and smoke levels, providing real-time data that can be used to assess fire risk and behaviour [13, 14]. Advanced ground-based systems often integrate with communication networks, allowing for the rapid dissemination of information to firefighting teams and relevant authorities [15]. This integration facilitates a quicker response to emerging wildfires, potentially mitigating damage and enhancing the effectiveness of suppression efforts. Additionally, these systems can be used to monitor controlled burns and ensure they remain within designated boundaries, contributing to more effective land management practices.

Satellite Based Systems Satellite-based wildfire monitoring systems are integral to large-scale fire detection and assessment. These systems utilise remote sensing technology to capture imagery. Two drawbacks compared to UAVs are that satellites, such as MODIS, have spatial resolutions of no less than 250 meters [16]. Additionally, satellites provide temporal coverage of only multiple times per day [16]. Despite the drawbacks, satellites equipped with thermal imaging sensors can detect temperature anomalies indicative of wildfire activity, even through cloud cover and smoke [16]. This capability allows for the monitoring of vast and remote regions, providing critical information on fire location, spread, and intensity. Furthermore, satellite data can be integrated with Geographic Information Systems (GIS) to create detailed maps that support firefighting strategies and resource allocation [17]. However, the development and operation of satellite systems are highly expensive, which can be a significant barrier to their widespread adoption.

Air Based Systems Air-based wildfire monitoring systems, including manned aircraft, unmanned aerial vehicles (UAVs), and helicopters, are already widely utilised in wildfire management. Manned aircraft and helicopters are often employed for aerial reconnaissance, providing critical information on fire behaviour, location, and spread. One particular example is the ATGS (Air Tactical Group Supervisor) aircraft, which is UAVs, in particular, have seen significant adoption due to their ability to fly at lower altitudes and navigate

challenging terrains, offering high-resolution imagery and real-time data essential for precise fire monitoring and assessment. These UAVs are frequently deployed to map fire perimeters, monitor fire progression, and assess post-fire damage. Their use in hazardous conditions where manned flights would be too risky enhances safety for firefighting personnel. Integrating air-based monitoring systems with ground and satellite-based technologies allows for a more coordinated and effective response to wildfires. However, the certification process for new aerial technologies remains lengthy, and the extreme operating environments pose ongoing challenges. Despite these challenges, the current utilisation of air-based monitoring systems highlights a growing market need for more advanced and efficient wildfire detection and monitoring solutions.

3.2 MISSION STATEMENT

Mission needs and objective statements are required to give a reason for the project's existence and provide general guidelines for the project. The entire design is built with them in mind, and a lack of fulfilling the objective statement of the mission would be considered a total system failure.

A mission is defined by the world's need for the solution it provides, which is summarised in the need statement:

Improve wildfire management to decrease emissions, preserve nature and protect life [18].

To satisfy this need, the following Mission Objective Statement was devised:

Conceptualise, design, and propose a system based on drone swarms to improve wildfire prediction & monitoring by June 28th, 2024 [18].

3.3 MISSION CONCEPT DESCRIPTION

Current wildfire management systems face significant challenges, particularly concerning the accuracy of pre-fire fuel measurements and the capability for real-time monitoring. Traditional methods such as destructive sampling and satellite imagery have limitations in scalability and accuracy across diverse forest ecosystems [4, 19]. Furthermore, existing drone technologies are constrained by low endurance and regulatory restrictions, which impede comprehensive forest coverage and operational efficiency [20].

To overcome these challenges, the proposed solution integrates AI with UAV technology to enable real-time, high-resolution monitoring of wildfire-prone areas. AI algorithms enhance biomass estimation, tree metric determination, and fuel characterisation [21, 22, 23, 24], providing critical data for effective fire risk assessment and management. The development aligns with initiatives such as the FAA-BEYOND Programme, which promotes regulatory advancements for Beyond Visual Line of Sight (BVLOS) operations and swarm management [25].

By deploying a low-cost, autonomous drone swarm, the mission aims to revolutionise wildfire management through continuous monitoring and data-driven decision-making. This approach not only enhances operational efficiency but also reduces risks to field personnel while improving overall wildfire response capabilities. The integration of sub-meter resolution data, including thermal imaging, supports accurate fire behaviour modelling and post-fire recovery assessments [4, 26]. Ultimately, the mission concept seeks to provide comprehensive, real-time wildfire data analytics to support proactive disaster management strategies.

3.4 TOP-LEVEL FUNCTIONAL FLOW

An integrated overview of all system functions has been established to guide future design and operational decisions. This overview covers the entire system life cycle and is detailed in subsequent sections. By

consolidating these elements into a cohesive Top-Level Functional Flow, the system's operational scope and developmental pathway are comprehensively outlined, establishing a robust foundation for subsequent design and implementation phases.

3.4.1 Functional Flow Overview

The functional flow diagram (Figure 84) presented in Appendix A illustrates the logical sequence of actions throughout the system's life cycle stages. This diagram is a comprehensive guide for understanding the functional requirements, categorised into three primary phases: pre-operation, operation, and evolution.

In the pre-operation phase, the system commences with subsystem manufacturing, initiating its functional life cycle. Activities include transporting and assembling subsystems to ensure product quality, followed by validation tests post-assembly to verify functionality and integration.

During the operation phase, activities such as system storage and transportation maintain operational readiness. Functional operations are carried out according to mission requirements, accommodating scenarios with or without inter-system communication capabilities.

The evolution phase focuses on system adaptability and future-proofing. This includes end-of-life processes alongside updates and adjustments to software and mission objectives. Anticipated adaptations to changing operational needs, such as transitioning from data collection to algorithm development, are addressed.

3.4.2 Functional Breakdown Structure

Further categorisation and refinement of the functions outlined in the Functional Flow Diagram are provided in the Functional Breakdown Structure (Figure 85), presented in Appendix A. This breakdown assists in identifying specific requirements crucial for system design and development, facilitating the generation of detailed mission requirements as discussed in section 3.7.

3.5 SUSTAINABILITY STRATEGY

The design process of a new solution to an already preexisting problem often involves several key decisions that significantly impact the environment around the problem itself. In the case of drone swarm application for wildfire detection and observation, the drone design itself needs to be carefully approached. The process should be sustainable and cost-efficient and provide more benefits than the lack thereof. First, the actual impact of the wildfires on the economy, society and the environment is investigated, and then the approach to drone design sustainability is explained in detail.

3.5.1 Impact of Wildfires

Sustainability effects are assessed based on indicators – metrics of sustainable practice. Wildfires have the same sustainability indicator types outlined in the project plan [18]: environmental, social and economic. The impact of wildfires, as shown by these indicators, is expanded upon in the following paragraphs.

The carbon dioxide released during wildfires is in the order of 2000 megatons according to the Copernicus Atmosphere Monitoring Service [27]. This accounts for around 5.7% of the *total* yearly CO₂ emissions of around 36 gigatons [28]. Besides carbon dioxide (88%), these fires release other greenhouse gasses, such as carbon monoxide (6%), nonmethane organic compounds (3.8%) and methane (0.4%) [29]. These all contribute to the trapping of heat within the atmosphere and global warming. Moreover, the fires release fine particulate matter (PM_{2.5}, PM₄, PM₁₀, etc.), which leads to increased health risks and poor performance in terms of social sustainability. It is estimated that between 5000 and 15000 deaths were caused in recent years in the

United States of America (USA) due to $PM_{2.5}$ increase from wildfire smoke [30]. The impact on wildlife is also noteworthy, either directly as damages to specimen health (especially for flora), or indirectly through habitat modifications [31]. The European Commission's Joint Research Centre's Advance Report on Forest Fires in Europe, Middle East and North Africa from 2022 quantifies this habitat destruction, mentioning destruction of protected Natura2000 sites in the order of 365000 hectares [32].

In addition to their impact on the environment, wildfires also have a great economic impact, both due to the cost of suppression and the lasting impacts on the economy. The US National Interagency Fire Center reports an average yearly cost in suppressing fires of around 1.9 billion USD, highly dependent on the severity of the fires in that year [33]. Moreover, studies show that, while suppression techniques are getting more efficient [34], the severity of wildfires – as indicated by burned area – is increasing [30], which would, in turn, cause the suppression costs to rise as well. Finally, research suggests that wildfires can have a more long-lasting impact on the economy, as indicated by the 0.11-0.18% annual GDP decrease figure mentioned by Meier et al. [35].

3.5.2 Value sensitive design

While the environmental, social and economic toll of wildfires cannot be overstated, it is critical that sustainability is considered throughout the design phase to ensure that the developed system is as sustainable and cost-effective as can be within the mission constraints. To achieve this, it has been decided to adopt a Value Sensitive Design (VSD). This methodology and a few different Environmental Impact Potential Assessment (EIPA) techniques will ensure that a holistic approach is used and that all stakeholders and their inherent values are considered [36].

Initially, the preliminary envisioning card method of VSD is applied to the general project analysis. This method consists of four pillars, namely: stakeholders, value, pervasiveness and time. Each of the pillars is further explained and described in the context of the wildfire drone swarm system.

Stakeholders

Stakeholders of the project have already been identified in the baseline review. In value-sensitive design, it is very important to consider all of their needs and concerns during the design process. Meeting the needs of as many stakeholders as possible while simultaneously not disrupting the others is one of the pivotal pillars of the VSD approach and is described through **REQ-SYS-CON-STB-2.1**.

Value

The value pillar describes the meaning and importance associated with concepts by people. With high uncertainty of living conditions for people settled around high-risk wildfire areas, safety and stability are of utmost importance. As presented in the previous section, subsection 3.5.1, thousands of people lose their lives yearly due to wildfire-related reasons. Therefore, the solution to wildfire detection and prediction is strongly sought after. However, using drones to monitor forested areas can raise concerns about the residents' privacy. People value stability but also value calmness and the right to their own space without feeling observed by firefighting drones daily. On the other hand, environmental sustainability is also important to attach value to. As described earlier, the impact of wildfires on the environment is tremendous, but what would be the impact of the drone swarm operations. All of these factors were taken into account and described in **REQ-SYS-CON-STB-3.1**, **REQ-SYS-CON-STB-3.2**, which can be found in Table 50.

Pervasiveness

Pervasiveness focuses on the widespread impact of technology implementation. It moves the focus from the immediate consequences of product implementation to further down-the-line effects of widespread use and its implications. In this instance, extensive forest monitoring with drone swarms could offer complete real-time surveillance of wildfires. No fires would go unattended. However, continuous drone operations can lead to extra strain on wildlife, especially birds, and potentially disastrous effects [37].

Time

Similarly to pervasiveness, the time pillar also focuses on long-term effects, but rather than assume widespread use, it looks into future implications and effects on future generations. With continuous monitoring of forested environments and data analysis of regions affected by wildfires, wildfire prediction models can

be derived, possibly leading to the full eradication of wildfire threats with the assumption of continuous monitoring. However, potential long-term use with fossil fuel propulsion could lead to a rebound effect, wherein the continuous operations of drones worldwide, while preventing wildfires, causes an overall detrimental environmental effect.

Impact on Wildlife

The drone's effect on wildlife is an indicator that is influenced by many factors. First, the drone configuration and flight envelope, namely whether it resembles an aircraft (with a maximum take-off weight, MTOM, larger than 25kg) following **REQ-SYS-CON-STB-1.5a**, a multicopter, or a helicopter (with an MTOM larger than 25kg) following **REQ-SYS-CON-STB-1.5b** changes the analysis that is necessary to assess the vehicle's impact [38]. Second, in both fixed- and rotary-wing cases, a distinction is made between different animal clade's responses [37]. That is, different clades or even species have different responses to the stressing stimuli of the vehicle. As such, each operation's local environment must be individually analysed to discern whether or not a sufficiently sustainable approach has been undertaken. Moreover, it is noted that some species can become habituated to vehicle flight, which decreases the technology's negative impact on the fauna. By the same token, the impact on wildlife can be minimised by avoiding flying in nesting areas during mating season. To provide guidelines for the design, limits are placed on the main stressors produced by the vehicle: the noise and the distance to the vehicle, both measured at the (possible) location of an individual of the relevant species. As such, conditional requirements emerge based on the to-be-determined MTOM and the propulsion system configuration. These can be found in the baseline review. Not every combination of configuration and stressors is considered, but only those that are specified by literature: for fixed- and rotary-wing vehicles, a noise limit of 95dB should be enforced complying with **REQ-SYS-CON-STB-1.6**; for fixed- and rotary-wing vehicles, a minimum distance to specimen limit of 2000m should be enforced, with low-noise flying recommended under 15km; for small, drone-like vehicles, a minimum distance to specimen limit of 600m should be enforced. The distance and noise requirements can be combined, as it is not exactly known which of the two stressors is the actual cause of the animal response. Note that, while noise can be influenced during design, minimum distance to ground and trees is expected to have a greater impact on operations rather than on design.

To summarise, the constraints on the vehicle's operation stem from the specifics of the ecosystem to be surveyed, the system's flight profile and the propulsion subsystem's operation. Investigating local fauna directly or by inquiring relevant authorities before starting an operation in an area is recommended. This information can aid in creating tailored operational constraints for the chosen environment. Additionally, the response of the fauna to the operation should be closely monitored, as some species can have a harder time adapting to the changes in their environment.

3.5.3 Figures of Merit and Design Sustainability

To estimate the maximum environmental impact of the system, a detailed statistical analysis of forest fires must be performed. A forest risk factor (RF) is defined for that purpose, specified below.

$$RF = \frac{\text{Burned area}}{\text{Total forest area}} \quad (1)$$

The risk factor is a metric that measures the burn area over the total forest area in a chosen region. The metric can be used to rank different areas based on fire risk or choose a statistically significant figure that represents a set of regions. Then, assuming that the system being in operation eliminates the wildfire emissions entirely, the maximum emission of the system over a set time can be estimated. For the purpose of this analysis, several countries in Europe and several states from the USA have been selected, with the data from 2016, 2021 and 2022 [39, 40, 32, 41]. The time average RF was defined in all of these regions, and then a threshold was set to filter out all states with an RF below 0.005 that was irrelevant to the analysis. This yielded a rather evenly distributed set shown in Figure 2.

From this set, the mean value was closest to the fires in Spain over the 3 years. Therefore, the value of CO₂ emissions from Spain induced by wildfires has to be higher than a system of drone swarms monitoring all of the forested areas of Spain.

$$n_{swarms} = \frac{\text{Total forest area}}{1000 \text{ [km}^2\text{]}} \quad (2)$$

The number of swarms was estimated from the assumption that the entirety of the forested area of Spain is monitored and that one swarm monitors an area of 1000 squared kilometres. This number was estimated to be 185 swarms. Thus, the maximum allowable emission of each swarm has to be less than:

$$Emission_{swarm} = \frac{CO_{2tot}}{n_{swarms}} \quad (3)$$

Which in turn amounted to 93.8 kilograms of CO₂ per year per swarm transferring into **REQ-SYS-CON-STB-1.3**. Notably, this analysis assumes a uniform distribution of the fires over the year while, in reality, some seasons will have a higher risk of wildfire occurrence. From this number, an emission limit for a single drone will be sourced in the further stages of the development process.

Material sustainability

The production of a sustainable system is a complicated process with its own environmental impact. Various materials will have their own implications, especially regarding the production and the end-of-life (EOL) phase. Therefore, the material selection must be carried out carefully, and all possible factors must be taken into account to achieve a design that not only fulfils all mission needs but is also sustainable. To achieve this purpose through **REQ-SYS-CON-STB-1.2**, several environmentally friendly materials have been considered, such as natural fibre composites like wood [42]. On the other hand, some materials, such as carbon fibre-reinforced polymers (CFRPs), have been ruled out due to the negative environmental effects induced during their manufacturing violating **REQ-SYS-CON-STB-1.1**. Another challenge comes from the stakeholder requirements imposed on the project regarding recyclability: the drone's airframe needs to be at least 90% recyclable according to **REQ-SYS-CON-STB-1.7**. The entire vehicle will not achieve 90% recyclability due to the nature of the battery required for power; however, with this in mind, the rest of the vehicle should be as recyclable as possible.

As per the trade-off performed in the midterm report, the choice of materials is limited to aluminium, wood and plastic (thermoplastics). Following this, a brief discussion of the sustainability of each manufacturing practice will follow. According to the International Aluminium Organisation, Aluminium production costs around 15.1 tons of CO₂ per ton of material. Typical structural mass fractions in aircraft and UAVs range from 25% and 40% [43, 44]. Then, conservatively assuming 80% of the entire MTOM is taken up by structural Aluminium, a drone swarm will not exceed 120kg of Aluminium, which comes up to 1800kg of CO₂. To fulfil the emissions requirement, the swarm should operate for at least 19 years [45]. On the other hand, in terms of recyclability, Aluminium is one of the most recycled materials in the world, even if it does not retain 100% of its initial mechanical properties [46]. Logging produces around 3.83 tons of CO₂ per ton of wood, which, using the same structural mass fraction assumption as above, leads to a maximum of 460kg of CO₂ per swarm [47]. Wood is not as easily recyclable as aluminium, with around 60% of it being recycled. Moreover, semi-finished goods out of recycled wood are profoundly different from ones made out of the original material: for recycled wood, the fibres are cut to various lengths and artificially adhered to each other [48]. Finally, thermoplastics are a vast family of materials whose properties allow them to be heated and reshaped, making them fully recyclable. Their production produces around 2000kg per ton of material, producing a maximum of 240kg of CO₂ per swarm. However, it is important to ensure that the recycling is performed correctly, as plastics

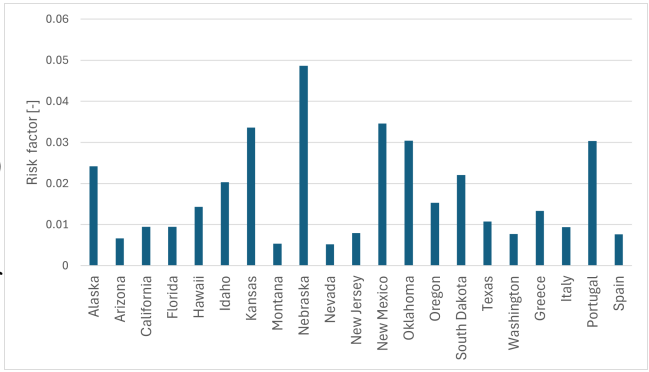


Figure 2: Wildfire risk factor for select European countries and US States, a measure of average yearly burned area per total region area in the years 2016, 2021 and 2022.

greatly threaten the environment due to their poor biodegradability [49].

3.5.4 Shipping costs

The shipping emissions of the swarm also an important factor to consider. Since the system needs to be accessible worldwide, three shipping methods were considered: land, air, and sea. In most cases, transportation by land is preferred, however since the shipping distances can reach very high distances with no roads leading to some locations, air and sea transportation become the only viable option. Transportation by sea is a good solution for long-distance shipments that cannot be achieved by land. However, it is much slower than air transport, and sea shipping has a much lower environmental impact and cost[50]. After analysing a standard shipping container (609.6x234.8 [cm] size) being shipped between two arbitrary points, it was estimated that the well-to-wheel GHG emission of shipping one container from Rotterdam Port to Bilbao Port is 134.27kgCO₂e [51]. After dividing it by the distance between the two ports (1430 [km]), it has been determined that the emission of shipping one container of this size over one kilometre is around 96 grams of CO₂. This number limits the entire system to fit into five containers of this size to satisfy **REQ-SYS-CON-STB-1.4**.

3.6 TOP-LEVEL RISK ANALYSIS

The technical risk analysis has been reviewed and updated in light of the design advancements. Risks initially identified in the baseline and midterm reports [52, 53], that are now deemed mitigated have been removed. The specific risks that were removed and the reasoning for their removal can be found in the draft version of the final report[54]. The remaining risks are assessed again and a new mitigation plan is formulated. Finally, the mitigated risks are reassessed and a contingency plan is generated for those that were not completely removed. The risks that were not mitigated by the midterm report are shown in Table 3.

Table 3: Remaining Risks

ID	Risk	Rationale
R-T-01	Collision with terrain	Driven by the flight computer, swarm strategy, flight conditions, and collision avoidance systems. This will result in the units being damaged having to be repaired/replaced and the collision avoidance system improved.
R-T-04	Collision with birds	Driven by the flight computer, swarm strategy, flight conditions, and collision avoidance systems. This will result in the units being damaged having to be repaired/replaced and the collision avoidance system being improved.
R-T-06	Certification cost exceeds budget	Drivers are the certification procedures, necessary for all possible operation areas and jurisdictions. Results in the system having to be redesigned.
R-T-07	Operational cost exceeds budget	Driven by the design of the system and operations. Will result in redesigning the operation structure becoming necessary.
R-T-08	Manufacturing cost exceeds budget	Driven by the design of the units, such as material cost, and necessary methods for production. Can result in different materials being chosen, or the structure being simplified.
R-T-09	Maintenance cost exceeds budget	Driven by the design, the ease of access to each subsystem, how easy they can be damaged, and the longevity of each component. Can result in having to redesign the structure and modularity of the subsystems, or the choice of components.
R-T-12	Collected data is incomplete	Caused by the telecommunication capabilities and flight conditions. Results in insufficient/skewed data for model training.

Table 3 – continued from previous page

ID	Risk	Rationale
R-T-15	Drone is too damaged to be safely transported	Driven by the damage sustained during flight. Will result in the drone having to be left or repaired before transportation.
R-T-16	System is damaged during transportation	Caused by improper fastening/loading of the system, the condition of the route, and the design of the transport system. Can result in the system having to be repaired before use, and a delay in schedule.
R-T-17	System is damaged during storage	Caused by improper storage, and results in system not performing to standard, or a delay in schedule caused by repairs.
R-T-18	System is too heavy to lift	Driven by the material choice and structural design. Results in the system not being possible/safe to use.
R-T-20	Drone cannot be upgraded/modified	Caused by the design of the fuselage interior design. Results in a new system having to be designed for every application.
R-T-23	Stagnation in Model Improvement	Arises from Model's Oversight of Key Component, Hindering Adaptation and Innovation
R-T-24	System is replaceable	Caused by product redundancy, or a better competitor. Results in the entire product being unnecessary.
R-T-30	Emergency is not recognised	Caused by a faulty flight computer, sensors, or negligent operator. Resulting in the emergency recovery system not engaging and the system unit being lost.
R-T-31	Emergency command is not received	Caused by the units straying outside the capable communications range, issues in communications between units, or the swarm strategy. Results in the emergency recovery not engaging, and the system unit being lost.
R-T-33	Parachute doesn't deploy	Can be caused by the parachute malfunctioning, parachute being improperly prepared/stored/transported. Results in the loss or damage of the unit.
R-T-35	Damaging landing	Caused by improper landing areas, design of self-guided landing system, high landing speed, damaged control surfaces/sensors/subsystems. Results in further damage.
R-T-36	Run out of fuel	Caused by improper fueling, incorrect fuel estimation, faulty sensor, no reserve fuel designed. Results in the unit possibly being lost.
R-T-37	Drone is lost/cannot recover	Caused by a lack of unit tracking (GPS etc), emergency recovery landing in a physically inaccessible location. Results in the unit being lost or recovery being delayed.
R-T-38	Drone provides insufficient power to payload	Driven by the sizing of the power subsystem, improper mission planning, or faulty power plant. Results in the sensors not functioning, and data being incomplete.
R-T-39	Drone provides insufficient stability	Caused by a fault in the control system, damage to the control surfaces, extreme weather conditions, or ineffective obstacle avoidance. Results in low quality/noisy/incomplete data, communication link being lost.
R-T-45	Swarm strategy is not possible	Caused by the training data, and the swarm model. Can result in the units flying on paths that are physically impossible, and colliding.
R-T-46	Drone flies out of mission range	Caused by obstacles, mission/flight path planning, communications loss, or loss of control. Can result in the loss of units, units entering civilian airspace/populated areas or forbidden airspace.
R-T-47	Fuel system catches fire	Can be caused by overheating, improper cooling, improper fuel housing, use of unstable fuel. Can result in damage to the environment, loss or damage to units.
R-T-48	Drone fails to communicate	Driven by communication range, communication structure, swarm planning/strategy. Will result in the loss of units, incomplete data, or collision.

Table 3 – continued from previous page

ID	Risk	Rationale
R-T-49	Communication is not fast enough	Driven by the communications architecture/logic. This results in the payload data not being transmitted or commands not being distributed fast enough.
R-T-51	Parachute deploys prematurely	Caused by the command and data handling subsection of the drone sending the deployment signal to the drones by accident. Results in the UAV losing its flight capabilities and reverting to emergency mode.

These risks are scored with the risk matrix found in Table 47. The risks are scored, their mitigation plans are formulated, and the mitigated risks are rescored. This is found in Table 4. The remaining risks are scored based on the risk matrix seen in the midterm report [53], a mitigation plan is devised for each risk, and the risks are re-scored. The scores and the mitigation plan are consolidated into Table 4. The ID is in continuation with the midterm risk analysis, where the R represents risk, T represents type of risk (either technical or organisational).

Table 4: Mitigation strategies, and implications

ID	Mitigation
R-T-01	Design flight computer to operate on faster terrain/collision avoidance measures with better precision. Verify this through testing once a prototype is manufactured.
R-T-04	Design flight computer to operate on faster terrain/collision avoidance measures with better precision. Verify this through testing once a prototype is manufactured.
R-T-06	Communicate with the FAA and EASA once certification starts to be discussed. Allocate a budget to this once the design is completed, before entering manufacturing and testing.
R-T-07	Allocate budgets to the operations being designed, document and monitor its costs. Design operations to be under its budget, and regularly check for compliance.
R-T-08	Allocate budgets to the manufacturing process being designed, document and monitor its costs. Design the manufacturing process to be under its budget, and regularly check for compliance.
R-T-09	Allocate budgets to the maintenance procedures being designed, document and monitor its costs. Design maintenance procedures to be under its budget, and regularly check for compliance.
R-T-12	Design the flight paths to ensure an overlap in the ground sampling area. Verify this through testing once a prototype is manufactured.
R-T-15	Establish procedures to contact the fire department to ensure safe transportation when necessary. Validate the procedures with the FAA or EASA once the certification process begins.
R-T-16	Design a container that fixes and protects the units from any loads that may be experienced during transportation. Verify this through testing once a prototype is manufactured.
R-T-17	Design a container that fixes and protects the units from any loads that may be experienced during storage. Verify this through inspection once a prototype is manufactured.
R-T-18	Regularly calculate the mass of the UAV being designed, monitor and design the UAV to comply with the weight requirement.
R-T-20	Design the UAV to have an accessible payload section, allowing sensors to be interchanged for newly defined/modified missions.
R-T-23	Evaluate the data collected by the unit and the sensors to place on the unit. Done after a substantial amount of time has passed using the system at a certain forest area.
R-T-24	Design the system to be agile and modular design. Conduct market analysis regularly before each wildfire season.
R-T-30	Design the flight computer to improve its redundancy and ensure the emergency signal is not lost. Protect the wiring and flight computer in a casing to ensure the subsystem is not damaged.
R-T-31	Design redundant telecommunication subsystem to reliably receive signals from the ground station. Add an initial safety margin found from literature research, to the signal strength to ensure the signal loss does not cause the command to be lost. Revisit this and tweak the margin based on testing. Verify through testing of the subsystem, before production of prototype.

Table 4 – continued from previous page

ID	Mitigation
R-T-33	Since the parachute is outsourced, find a more reliable parachute to use. Verify through testing after production of a prototype.
R-T-35	Generate operational guidelines for landing with damaged parts to prevent damage to operators and groundstation. Design arresting gear to ensure the hook does not fail.
R-T-36	Size the fuel to have the required endurance, design the avionics subsystem to reliably monitor the remaining fuel capacity.
R-T-37	Ensure the avionics has a GNSS subsystem to track the drone. Generate operational procedures for the operators in the case of the unit emergency landing in a physically unretrievable place. Verify with testing and inspection with certification authorities FAA and EASA.
R-T-38	Resize the battery. Done after the design, before the prototype manufacturing.
R-T-39	Design the lifting surfaces such as the wing and tail to ensure stability. Test in a simulation environment before production of a prototype.
R-T-45	reevaluate the swarm strategy generating code for edge cases that may be missing. Verify this through testing in a simulation environment.
R-T-46	Design the telecommunications system to have some margin on the communication range so the unit can still be communicated with outside of the monitoring range, and returned to the correct area. Verify through testing in a simulated environment.
R-T-47	Design protective casing of the fuel system to ensure any fire is contained inside the casing.
R-T-48	Design the communications subsystem to ensure a margin on the necessary signal strength. Redesign the subsystem to ensure redundancy by having the unit communicate to the ground station through neighbouring units if the high-flying unit is not reachable. Verify through testing once a prototype is manufactured.
R-T-49	Design the high-flying unit to ensure a communications link with all units at all times. verify through testing in a simulated environment before production.
R-T-51	Design the flight computer to ensure it does not accidentally send the deployment signal to the BRS. Verify through testing before production of a prototype.

Table 5: Initial and Mitigated scores of each risk from the risk matrix (impact/likelihood scores that changed shown in brackets)

ID	P	Impact		Likelihood	Overall	Mitigated
		C	S			
R-T-01	3	3 (2)	4 (3)	2 (1)	6.8	2.8
R-T-04	3	3 (2)	4 (3)	2	6.8	5.6
R-T-06	5	5	5	3 (1)	15	5
R-T-07	1	4	1	2 (1)	3.2	1.6
R-T-08	1	4	1	2 (1)	3.2	1.6
R-T-09	1	4	1	2 (1)	3.2	1.6
R-T-12	5	1	1	2 (1)	5.2	2.6
R-T-15	1	1	5 (2)	3	7.8	4.2
R-T-16	1	3	4	2 (1)	5.2	2.9
R-T-17	1	3	4	2 (1)	5.2	2.9
R-T-18	3	3	5	3 (1)	11.4	4
R-T-20	1	4	4	4	11.2	
R-T-23	4 (3)	1 (2)	1	2	4.4	3.6
R-T-24	1	3	1	4 (2)	5.6	2.8
R-T-30	1	3	3	3 (2)	6.6	4.8
R-T-31	4	4	3	4 (1)	14.4	3.5
R-T-33	1	3	3	3 (1)	6.6	2.4
R-T-35	1	3	3	3 (1)	6.6	2.4
R-T-36	3	3	3	2 (1)	6	3
R-T-37	1	3	3	3 (2)	6.6	4.8
R-T-38	5	3	3	4 (1)	15.2	3.6
R-T-39	5	3	3	3 (1)	11.4	3.6

Table 5 – continued from previous page

ID	Impact			Likelihood	Final	Mitigated
	P	C	S			
R-T-45	4	1	2	4 (1)	10.4	2.4
R-T-46	1	4 (2)	4 (2)	3 (2)	8.4	3.4
R-T-47	1	3	3	2 (1)	4.4	2.4
R-T-48	5	1	3	4 (1)	13.6	3.2
R-T-49	4	2	3	3 (1)	9.6	3.1
R-T-51	4	4 (3)	3	4 (1)	14.4	3.4

The original and mitigated risks are plotted on a risk map as seen in Figure 3.

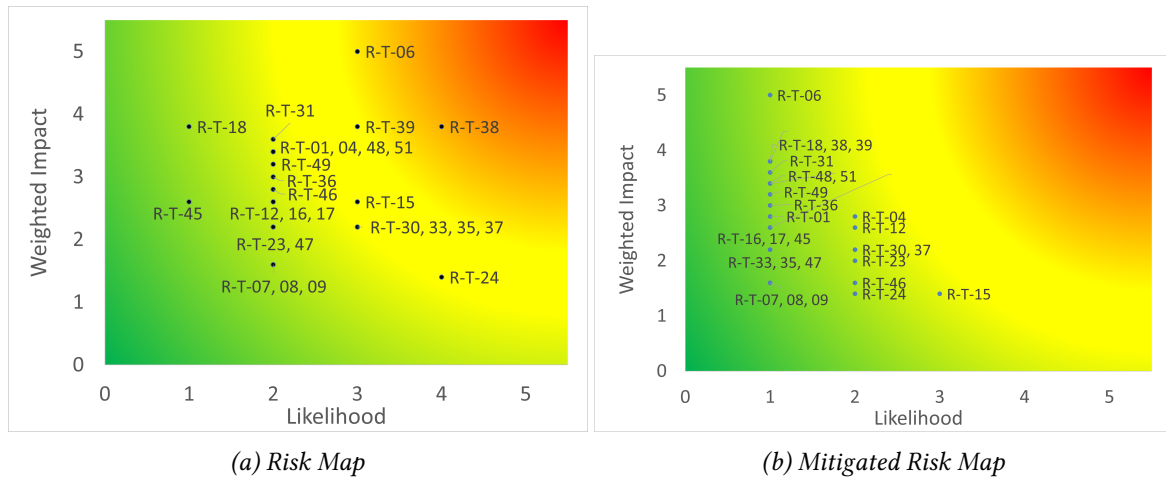


Figure 3: Risk Maps

3.7 REQUIREMENT STRATEGY

One of the key factors to consider when designing any product is the stakeholders that will be impacted by its implementation. A careful analysis of which are the main stakeholders and what are their needs and requirements shapes the direction of the whole project and the choices made. The main stakeholders identified for the proposed mission have been listed in Table 6. Their needs generated a list of stakeholder requirements, which are listed in the Table 7.

Table 6: List of Stakeholders

ID	Stakeholder
FB	Fire Brigade
LG	Local Government
AT	Air Traffic Controllers
AA	Airworthiness Authorities
WE	Wildlife Experts
RI	Research Institutes
LP	Local Population
GP	General Public
IC	Insurance Companies

Table 7: Stakeholder Requirements from the Baseline Report [52]

ID	Stakeholder Requirement
REQ-STK-FB-1	The mission shall produce a live wildfire risk assessment of a predetermined area.
REQ-STK-FB-1.1	The mission shall survey an area of a maximum of 1000 km^2 .
REQ-STK-FB-1.2	The mission shall be able to cycle back to any point in the mission area at least once every 10 minutes.

Table 7 – continued from previous page

ID	Stakeholder Requirement
REQ-STK-FB-1.3	The mission shall be able to refresh the risk assessment model without post-processing.
REQ-STK-FB-2	The mission shall provide assistance to firefighters during firefighting.
REQ-STK-FB-2.1	The mission shall act as a relay system for communication between fire brigade ground units and the command centre.
REQ-STK-FB-2	The mission shall provide assistance to firefighters during firefighting.
REQ-STK-FB-2.2	The mission shall provide a live feed of the wildfire to the fire brigade units.
REQ-STK-FB-2.3	The mission shall assist with evacuation planning for civilians and fire brigade units.
REQ-STK-FB-2.4	The mission shall deploy drones to guide civilians out of endangered areas
REQ-STK-FB-2.5	The mission shall act as a warning system for civilians located in the affected area.
REQ-STK-LG-1	The mission shall increase the safety of the local population by decreasing the risk of wildfires.
REQ-STK-LG-2	The mission shall cost less than a tenth of the prevented cost of the damage due to wildfires prevented by the system.
REQ-STK-AT-1	The mission shall not disrupt the flight of any aircraft in the area.
REQ-STK-AA-1	The mission shall comply with the airworthiness authorities' certification requirements.
REQ-STK-WE-1	The mission shall result in a reduction in the environmental damage due to wildfires.
REQ-STK-WE-2	The mission shall not negatively impact the local environment.
REQ-STK-RI-1	The mission shall provide a comprehensive database of all the key parameters linked with wildfires.
REQ-STK-LP-1.1	The mission shall result in a reduction in the local infrastructure damage due to wildfires.
REQ-STK-LP-1.2	The mission shall result in a reduction in the disruption of local livelihood due to wildfires.
REQ-STK-LP-2	The mission shall not result in a disruption of local livelihood due to the system's operations.
REQ-STK-IC-1	The mission shall result in a reduction in the economic damage to infrastructure due to wildfires.
REQ-STK-GP-1	The mission shall not be cause for additional environmental harm.

With the top-level stakeholder requirements listed, the main boundaries and constraints for the project were set. From here, the top-level system requirements were generated. These were subdivided into technical requirements, operational goals, and mission constraints, and then they were subdivided further.

Technical Requirements	Operational Goals	Mission Constraints
<ul style="list-style-type: none"> • Unit Requirements • Swarm Requirements 	<ul style="list-style-type: none"> • Payload Requirements • Avionics Requirements 	<ul style="list-style-type: none"> • Safety Requirements • Resource Requirements • Legal Requirements • Sustainability Requirements

A comprehensive coverage of requirements was ensured by ensuring that all the generated system requirements fit into those categories. Furthermore, an ID-based system was implemented to keep track of all the requirements based on three-letter identifiers for the specific category the requirement was part of. An example of a system requirement set for the UAV unit's performance would be **REQ-SYS-TEC-UNI-1.1**, with all the other ones following the same structure. The full system requirements list is shown in Table 50, stated in Appendix A. As the project turned towards detailed design in the later design phases, more subsystem requirements were set, again following the same naming and structuring convention used for the top-level system requirements.

MISSION LOGISTICS & OPERATIONS DESIGN

This chapter introduces the mission's logistics and then system's operations. Firstly, the operational modes are defined in section 4.1, then the location of operations is defined in . The wildfire models are presented in along with the sensor selection in section 4.4. Finally, the drone contingent behaviour is discussed in section 4.5 along with the swarm sizing in section 4.6.

4.1 OPERATIONAL MODES DEFINITIONS

Using the mission functions, several operational modes are defined for the operations of the swarm. These are behavioural patterns that the swarm and its UAVs shall adopt under specific sets of circumstances. When considered together, the operational modes shall cover every possible situation and contingency that could be encountered during swarm operations. The purpose of the following section is to discuss the logic behind each of the operational modes. When designing each mode, the intent is to integrate the swarm system as seamlessly as possible with the existing pre-, active- and post-fire operations currently employed by firefighting entities worldwide. The operational modes are introduced in Figure 4.

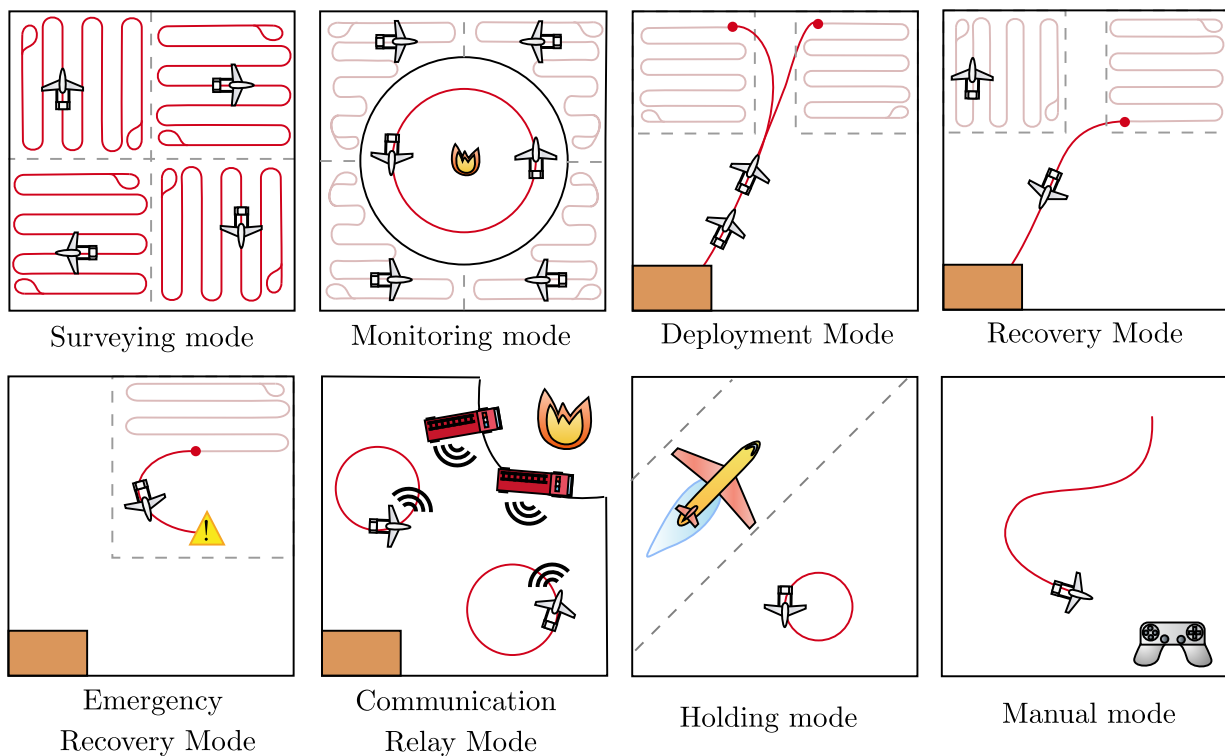


Figure 4: Swarm operational modes.

Surveying Mode Surveying mode is meant to be used in pre- and post-fire surveillance and data-gathering operations. In survey mode, each drone is assigned a sector and flies a predetermined path to cover the entirety of the sector. During flight, the sensors on the drone collect the required data and transmit it to the Relay drones. These drones then relay the communications to GCU (Ground Control Unit). Whenever conditions

are met, the sectors are recalculated by the GCU, and the sector division information is communicated to each drone. Each UAV determines its flight path within its designated sector boundaries to ensure complete coverage of the area. A drone cannot cross over into another drone's sector, and the path generation rules are described in detail in section 5.2. At all times, GCU has access to each drone's last known location, and each drone knows the location of drones assigned to bordering sectors, as well as drones currently known to be in Deployment, Recovery and Emergency Recovery Mode. This is necessary to avoid all reasonable possibilities of a collision, even in the case that a drone temporarily loses communications with the swarm.

Monitoring mode Monitoring mode is the mode the drones enter during the active-fire phase. In monitoring mode, the swarm's search area is restricted to the perimeter of the fire. The drones' objective is to closely monitor the advancing of the fire front and communicate this back to the firefighters. In monitoring mode, all the sensors onboard the drones are still used for their regular purpose of data-gathering, however the flight regime of the drones changes from 850 to 600 [m] to not interfere with the Fire Traffic Area shown in Figure 5. If some drones are in monitoring mode, this does not exclude that the areas outside of the range of the fire can be surveyed by drones in surveying mode.

Deployment Mode Deployment mode is the mode the drones start in when they are first deployed, and ends when the drones reach their predefined sector and enter Surveying or Monitoring Mode. During this time sensor observations are put off. When first inserted into the swarm network, before launch, the drone is assigned its initial sector. GCU computes the required climb path to let the drone reach its cruise altitude and starting position in its path circuit. The drone is launched and follows this path. If the drones are launched in a sequence, more than one drone is allowed to be in Deployment Mode, however only one drone can be in the launch rail simultaneously.

Recovery Mode & Emergency Recovery Mode (ERM) Recovery Mode is activated when a drone has completed its mission or is left with only enough power to recover. While in recovery mode, the drone is given a path to fly back to the arresting gear. The drone exits recovery mode when fully arrested and removed from the arresting gear. Only one drone is allowed to be in Recovery Mode at a certain time, and it is not allowed for a drone to be in Deployment Mode if there is at least one drone in Recovery Mode. This is to minimise collision probability. The possibility that multiple drones run out of battery at the same time can be almost fully mitigated by simply monitoring the battery level of each drone, and timing the Recall commands to each of them.

ERM, on the other hand, is entered whenever a drone has been in holding mode due to communication loss for too long, or if the avionics detects a fatal failure in the drone's subsystems. In ERM the drone simply deploys the BRS and crashes into the ground. If it is able to communicate, the rest of the Swarm updates the risk map to include a higher risk of fire at the crash site. The UAV then awaits manual recovery.

Holding Mode The UAV circles around the last transmitted location for which reception has been confirmed by the GCU. The radius of the circle is 9 km, according to the size of the Fire Traffic Area shown in Figure 5. This mode will be used when other air traffic is expected to pass nearby to prevent collisions, as in **REQ-SYS-TEC-SWM-1**. Examples are firefighting aircraft descending to drop water and other drones in Recovery or Deployment Mode. Holding mode is also entered when a drone loses communication with GCU for longer than 30 [s]. In this last scenario, the drone will circle around and climb at a constant rate. This is intended for the drone to escape any possible smoke formations that could block signals from being received/transmitted.

Figure 5 shows an infographic of the airspace division above the fire zone. Due to aerial firefighting vehicles making dive runs downward, the safest option for the drones is to fly at least 600 [m], which accounts for the minimum 150 [m] of vertical separation [55]. To keep vertical separation from the command and control planes, the drones either have to fly at 600 [m] or above 3000 feet. The nominal altitude of 850 meters is closer to 900 [m], which is the more suitable option. This also allows more margin in the control systems.

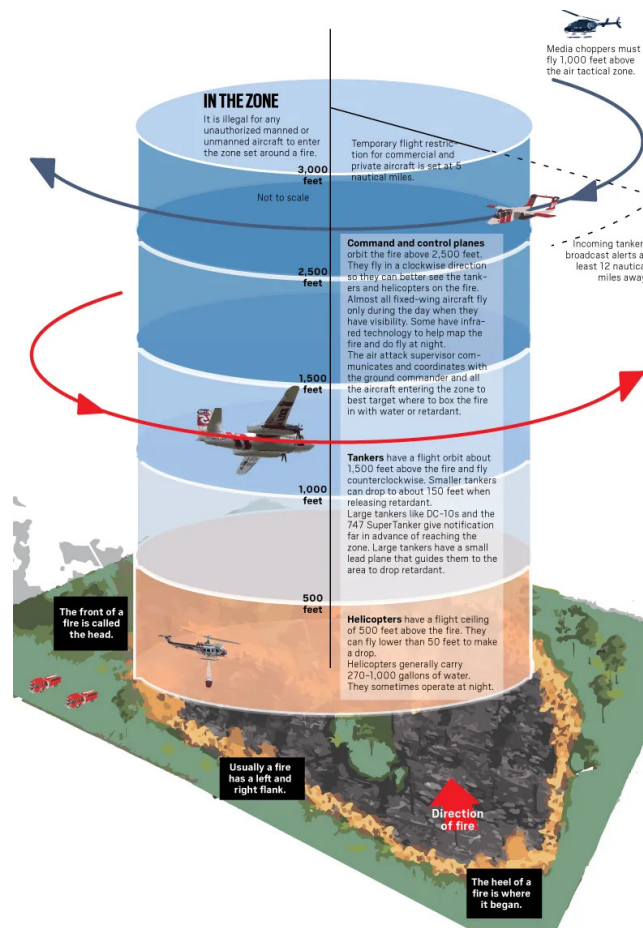


Figure 5: An infographic describing the operations in the fire zone. [55]

Communication Relay (CR) Mode In CR Mode, the flight path looks identical to that of Holding Mode, with the only difference being that in CR Mode, the centre of the circular flight path is communicated by GCR. The drone flies this circle until a new command is issued. During the flight in CR Mode, the drone acts as a communication relay for ground troops. The UAV functionalities required for this mode are further discussed in subsubsection 7.7.3.

Manual Mode Manual Mode is intended for piloted operation. The operator/pilot can always switch to manual control of a single drone. In Manual Mode, a drone can enter any sector and fly any path unconstrained by the swarm logic. During manual mode sensors can still be operated, as this mode is intended to give the operator full control of the operations of one individual UAV.

4.2 LOCATION DEFINITION

Wildfires are a growing global concern, with significant occurrences mainly in Europe, the United States and Australia. This phenomenon is fuelled by climate change, dense human populations and drier conditions [56]. Especially the Mediterranean region in southern Europe has seen a spike in wildfires over the last few years. In 2022 a forest area roughly the size of Corsica has been lost to wildfires just in Europe[1]. In order to minimise the economic, social and environmental losses due to wildfires, an effective wildfire prediction and monitoring system should be implemented in the high-risk areas.

Europe is known for its dense population and complicated terrain with various vegetation shifts and changes. These factors increase the complexity of wildfire management and prediction in these regions, and the

importance of quick response to potential catastrophes as large quantities of communities around risk areas can potentially be exposed to dangers.

The system has been designed with Europe-based operations in mind. However, it is not exclusive and can be implemented worldwide; the drone swarm is a perfect choice for forest monitoring in Spain, Italy or other states of the European Union.

4.3 WILDFIRE MODELS

The mission objectives focus on fire management, specifically predicting, detecting, and monitoring fire spread. However, wildfires are very difficult to model. A lot of effort has already been put into modelling their behaviour. This section studies such existing methods, aiming to determine the data required by the model, which the drone swarm can provide.

The most used fire propagation model is the CAWFE (Coupled Atmosphere-Wildland Fire Environment) model. As described by Coen [57], the CAWFE model combines a numerical weather prediction system with the Rothermel [58] fire behaviour module to simulate wildfires. This simulation considers atmospheric conditions, fire fuel properties, terrain slope, and fire dynamics. It also models essential factors such as fire-induced winds, fire spread, heat release, and smoke production. According to Coen [57], the CAWFE model simulates wildland fires by integrating a numerical weather prediction model with a fire behaviour module.

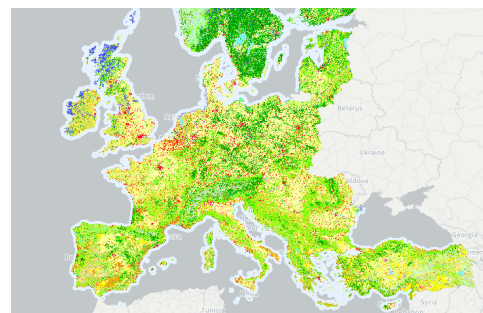
4.3.1 Environmental factors influencing wildfire spread

This subsection outlines the three major factors influencing the spread of wildfires. It will outline the parameters needed to quantify the factors, from which the required sensors on the drone swarm will later be determined.

Fuel Fuel is a term describing everything that can burn. Without fuel there is no fire. There are many types of fuel. It can be segmented into dead and live vegetation. The lack of moisture in dead vegetation makes it more prone to burning. Secondly, the fuel can be separated into three layers: the canopy, consisting of tree trunks and crowns, the surface, which can be plants, grass or litter and the ground layer, consisting of for example duff and decaying plants [59]. Every different type of fuelbed has different properties such as moisture levels and density. Luckily, the USDA provides this data for the United States [60] at a resolution of 20 meters, and the European Environment Agency (EEA) provides similar data for Europe through its Copernicus program [61] at a resolution of 100 meters.



(a) US vegetation map.



(b) EU vegetation map.

Figure 6: Vegetation maps of the United States and Europe.

Topography Topography impacts fire propagation in two ways. Firstly, because heat moves upwards, fire spreads more easily uphill. Therefore, a fire in a valley spreads faster than a fire on a hill. Secondly, the topography influences the local winds, speeding up the flow in mountainous regions. The effect of this is

discussed in the next paragraph. Topography datasets are provided by companies such as NASA and the European Environment Agency, where the most refined global satellite datasets have a resolution of 25 meters.

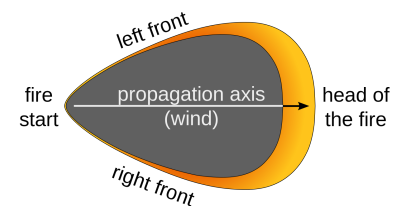
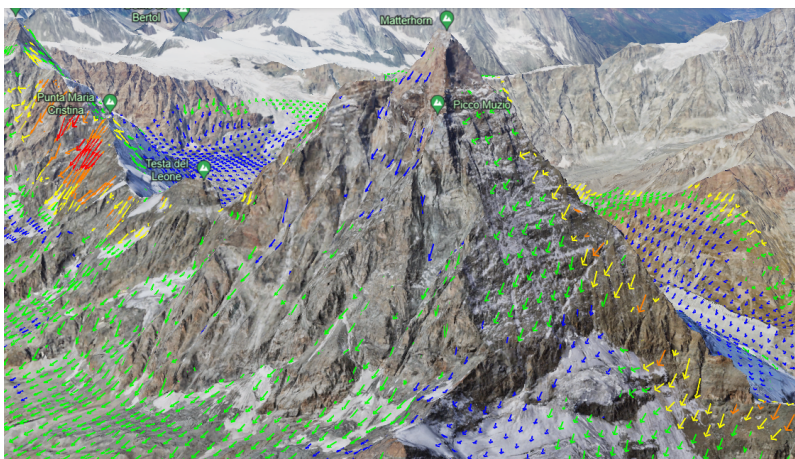
Table 8: Topography datasets available on the internet

Dataset	NASADEM ¹	EU-DEM ²	WORLD GMTED ³	ALOS WORLD ⁴	ASTER GDEM ⁵
Resolution	30 m	25 m	225 m	30 m	30 m
Coverage	Nearly Global	Europe	Global	Global	Nearly Global
Created by	NASA	EAA	USGS & NGA	Japan	NASA & Japan ministry of economy

Weather On a global scale, the weather greatly influences the potential of wildfires. The climate varies hugely around the world. Not only does each climate have its own variety of fuel types, but each has its own burn characteristics. Different biomes also experience different precipitations, humidity and temperatures.

Rain, humidity, wind, and cloudiness locally impact vegetation health and moisture content. Consequently, impacting wildfire behaviour. Heavy rain and storms decrease the likelihood of a fire. However, lightning strikes are often the origin of wildfires. Wind deserves special notice as it dries out the fuel and dictates the fire front propagation, as shown in Figure 7b.

Wind data is known on a macroscopic level. Yet, more local knowledge of wind behaviour is needed to predict wildfire propagation, which is not generally available accurately. Luckily, a model such as WindNinja⁶. This model uses digital elevation maps and global wind profiles to estimate local wind properties, and it can provide more accurate predictions when temperatures and cloud cover are also provided. The resolution of the grid is similar to the resolution of the topographical input data. Figure 7a shows an example of such data.



(a) Wind simulated around the Matterhorn, Switzerland. Using NOMADS-GFS-GLOBAL-0.25-DEG wind data on 12/06/2024 and WORLD GMTED topography data, all were provided by and simulated in WindNinja and visualised on Google Earth.

(b) Wind influence on fire propagation, taken from⁷

Figure 7: Terrain wind simulation and wind influence on wildfire.

¹NASADEM Dataset. URL: <https://www.earthdata.nasa.gov/esds/competitive-programs/measures/nasadem>

²EU-DEM Dataset. URL: <https://www.eea.europa.eu/en/datahub/datahubitem-view/d08852bc-7b5f-4835-a776-08362e2fbf4b>

³WORLD GMTED Dataset. URL: <https://www.usgs.gov/coastal-changes-and-impacts/gmted2010>

⁴ALOS WORLD Dataset. URL: https://www.eorc.jaxa.jp/ALOS/en/dataset/aw3d30/aw3d30_e.htm

⁵ASTER Dataset. URL: <https://asterweb.jpl.nasa.gov/gdem.asp>

⁶WindNinja Software can well estimate the values. URL: <https://weather.firelab.org/windninja/>

4.3.2 Fire Data Input

The CAWFE model requires fire locations as the final input. The model predicts the propagation of the fire given an initial location. This location of the fire is inputted as a 3D location, which is often derived from combining the topological features with 2D camera images [59]. For efficient fire monitoring, the fire input is continuously remeasured and updated, allowing for the predictions to be compared to reality and improved.

4.3.3 Model data conclusion

This section has described the CAWFE model, which is one of the most widely used fire spread models. It has outlined the main environmental factors influencing wildfire spread: fuel, topography, and weather. Each of these factors requires specific data inputs, which are generally well-known. However, the drone swarm can refine the accuracy and resolution of these data inputs if desired.

For fuel, data on vegetation type and moisture levels are available through databases, but the drone swarm can enhance this data with more localised and real-time measurements. High-resolution digital elevation maps are provided for topography. These can be further refined by the drone swarm for more precise modelling in complex terrains. Consequently, this improves the wind modelling.

The only data that is not continuously known at any resolution is the location of active fires. The initial and ongoing detection of fire locations is crucial for the CAWFE model to predict fire propagation accurately. The drone swarm plays a vital role in detecting and updating fire locations in real time, thereby enhancing the model's predictive capabilities and allowing for more effective wildfire management and response. Section 4.4 will translate the required data into sensors, which will be present in the drone swarm

4.4 SENSORS SELECTION

This section outlines the selection criteria for integrating sensors into the drone swarm, which is crucial for providing essential data inputs to the CAWFE model. The chosen sensors must meet specific operational requirements to ensure accurate prediction, detection, and monitoring of wildfire spread:

- **REQ-SYS-OPS-PLD-1.1** - The monitoring units must detect wildfires with a 3-metre resolution.
- **REQ-SYS-OPS-PLD-1.2** - The monitoring units must collect all data required by the CAWFE™ model with a 3-metre resolution.
- **REQ-SYS-OPS-PLD-1.3** - The monitoring units must be capable of receiving radio transmissions from firefighter units on the ground at any frequency within the 380-400 MHz range.
- **REQ-SYS-OPS-PLD-1.4** - The monitoring units must acquire sufficient data measurements to ensure continuous ground track coverage.
- **REQ-SYS-OPS-PLD-1.5** - The monitoring units must be able to store 40 GB of on-board data.

Furthermore, they must be compliant to the mitigation plans of the risk: **R-T-12**, from section 3.6.

The section commences with an analysis of camera selection and the rationale behind their deployment, followed by exploring data processing methodologies to utilise the information captured effectively.

4.4.1 Camera Selection

Infrared Camera The infrared (IR) camera is the most critical sensor for achieving the mission objectives of predicting, detecting, and monitoring wildfire spread while also meeting REQ-SWM-04, which mandates a

3-meter resolution for the required fire location resolution by the CAWFE model. Fires emit energy in the form of infrared radiation due to their high temperatures. Thermal infrared cameras detect this energy within specific infrared frequency bands, producing grayscale images where hot surfaces appear brighter than cooler ones. This makes IR cameras effective for detecting flames and hot spots, even through smoke, ensuring continuous and accurate monitoring [59]. While regular cameras can detect fires by processing the red channel, this approach is less reliable because visible smoke can obscure flames. More complex algorithms, such as those described by Martínez-de Dios [62], can use visible imagery to refine the thermal image threshold, but IR remains superior for detection. The IR camera's ability to provide real-time updates on fire locations is vital for the CAWFE model's predictive capabilities. Continuous fire detection allows the model to simulate fire propagation, improving response strategies and enhancing wildfire management. This makes the IR camera an indispensable tool for the drone swarm, ensuring it effectively meets the primary mission objectives.

Visual Camera The visual camera is another important sensor for the drone swarm, complementing the infrared camera by providing high-resolution imagery for general monitoring and verification purposes. This camera captures detailed images of the fire-affected areas, offering valuable visual context to support data from the IR camera. These images help confirm the presence and extent of fires, validate model predictions, and assess the overall situation on the ground. Additionally, as mentioned before, visual data can be used in conjunction with algorithms to refine the threshold values in thermal images, enhancing detection accuracy [62].

Near Infrared Camera NIR cameras are particularly useful for assessing vegetation health and moisture content [63]. section 4.3 outlined existing datasets which provide general information on vegetation, but the challenge lies in achieving greater specificity in wildfire simulations through higher-resolution datasets, states Oakridge National Laboratory ⁸. The health and moisture can be measured using the EVI index, shown in Equation 4.

$$EVI = G \cdot \frac{NIR - R}{NIR + C_1 \cdot R - C_2 \cdot B + L} \quad (4)$$

In this equation, G represents the blue band of radiation, R is the red band of radiation, and B is the blue band of radiation. Constants C_1 and C_2 are utilised to adjust for atmospheric conditions, while L corrects for the canopy background. The EVI is similar to the Normalised Difference Vegetation Index (NDVI), quantifying vegetation greenness. However, the EVI corrects for certain atmospheric conditions and canopy background noise, exhibiting increased sensitivity in densely vegetated areas [64]. The NDVI, ranging from -1.0 to +1.0, measures the amount and vigour of vegetation. Higher index values indicate healthier vegetation due to their strong NIR reflectance and low red reflectance, resulting from chlorophyll absorption, thus indicating vegetation and soil moisture [65, 66]. The NIR camera can use this to generate more detailed and localised vegetation maps. This refined data allows for a better understanding of fuel properties. By integrating NIR data, the drone swarm can improve the accuracy of the input grid for the CAWFE model. Additionally, in the presence of wildfires, moisture contents change continuously. Therefore, the NIR measurement has to be taken continuously.

LiDAR To improve data on the topography and consequently the wind in the search areas, a LiDAR sensor is used to map the terrain with sub-meter resolution⁹. Since the terrain does not change frequently, these measurements must only be taken once.

⁸Oakridge National Laboratory. URL: <https://www.ornl.gov/news/improving-wildfire-predictions-earth-scale-climate-models>

⁹Riegl Electronics. URL: <http://www.riegl.com/products/unmanned-scanning/new-riegl-vux-18024/>

4.4.2 Mission Sensor Data Flow

section 4.3 has outlined the models used for wildfire detection, and subsection 4.4.1 mentioned the cameras which are present on the drone swarm. In this subsection, the integration of the two is quickly discussed. Figure 8 shows how the camera measurements are utilised and processed to predict the wildfire spread. It can be seen that the topography is either taken from LiDAR measurements or a topography dataset. As explained in subsection 4.4.1, this is because the LiDAR measurements are taken once and can then be saved as the topology does not change.

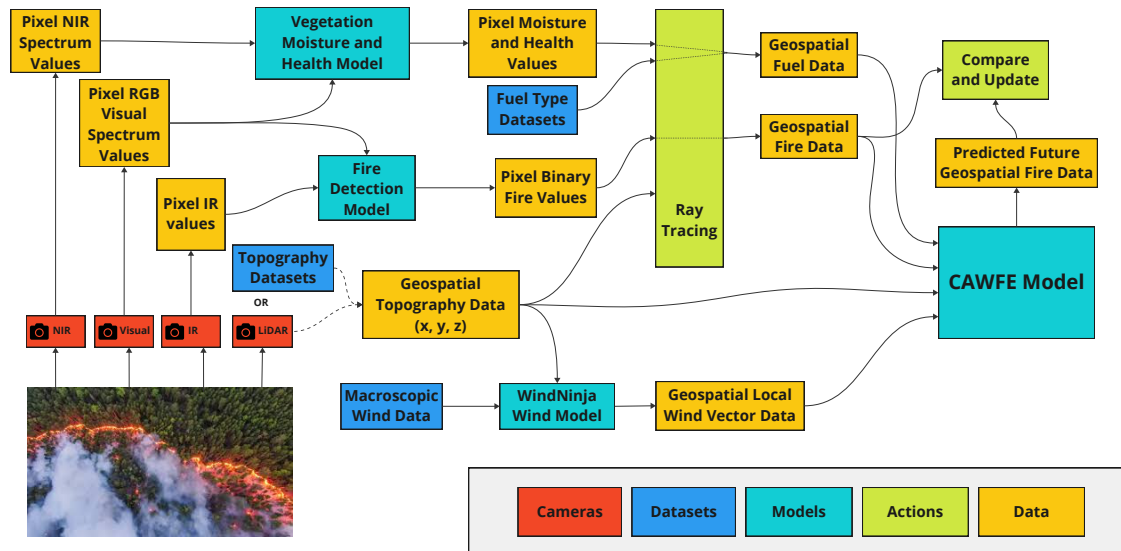


Figure 8: Flow of the Data, from camera and databases to predictions

4.4.3 Avionics Sensors

Various avionics sensors are essential to ensure the drone swarm operates effectively and safely while collecting the necessary mission. These sensors enable accurate navigation and state awareness, which are critical for the mission's success and to fulfil **REQ-SYS-OPS-AVI-1**.

Navigation Accurate navigation is vital for maintaining the correct flight path and efficiently reaching target destinations. Several key sensors work together to provide navigation data:

- **Position:** The GPS sensor determines the exact geographic location of the aircraft, ensuring precise positioning throughout the mission. With additional RTK capabilities, it is possible to increase the spatial accuracy to around a few centimeters¹⁰. Many COTS GPS transceivers are available, out of which the preliminary choice was the Mateksys M10Q-5883¹¹.
- **Velocity:** The combination of Inertial Measurement Unit (IMMU), GPS, and Pitot Tube sensors measures the speed and direction of the aircraft's movement. This data is essential for maintaining the desired flight speed and direction. The preliminary choice of sensors is as follows: for the IMMU, the Adafruit BNO055¹² and for the Pitot tube, the Mateksys ASPD-4525¹³.
- **Acceleration:** The IMMU assesses changes in the aircraft's velocity over time, providing critical information on acceleration and deceleration.

¹⁰<https://globalgpssystem.com/gnss/rtk-gps-understanding-real-time-kinematic-gps-technology/>

¹¹<https://www.mateksys.com/?portfolio=m10q-5883>

¹²<https://eu.robotshop.com/products/bno055-9-dof-absolute-orientation-imu-fusion-breakout-board>

¹³<https://www.mateksys.com/?portfolio=aspd-4525>

- **Orientation:** The IMMU, along with an Angle of Attack (AoA) sensor, tracks the aircraft's attitude, including roll, pitch, yaw angles, and AoA. This information is crucial for maintaining stable flight and executing precise manoeuvres. Unlike the other sensors, a COTS option for the AoA sensor is hard to find for such small vehicle sizes. Instead, a custom, simple AoA vane will be made in-house and attached to an angle position sensor. The preliminary choice for this sensor is the ams-OSRAM AS5048A ¹⁴.

State Awareness Monitoring the aircraft's condition and performance parameters is essential for safe and efficient operation. The following sensors provide critical state awareness data:

- **Air Pressure:** A barometer monitors atmospheric pressure, aiding in altitude determination and weather assessment. This data is crucial for maintaining the desired altitude and understanding environmental conditions. The preliminary sensor used for this measurement is the Bosch BME280¹⁵.
- **Air Temperature:** An external thermometer measures the air temperature, which is important for assessing engine performance and conducting weather analysis. The same Bosch BME280 sensor can also be used for this measurement.

4.5 DRONE CONTINGENT BEHAVIOUR

The drone swarm is expected to encounter a wide range of unforeseen circumstances due to its mission of surveilling high-risk areas. Mitigation of risks in these situations is required for a fast certification process and easy integration with existing firefighting procedures.

The first behaviour considered is obstacles on the UAV surveillance path. The UAVs should be sufficiently able to avoid static obstacles within the search area. This autonomous obstacle avoidance is readily demonstrated in literature [67, 68], so implementing these procedures should sufficiently mitigate this risk. Similarly, UAV collisions with emergency air traffic should be avoided. In this case, when the emergency air traffic (like a firefighting aircraft) communicates the passage through the search area to the GCU, all UAVs in the sectors which cross paths with the aircraft should remain in holding mode for the duration of the aircraft's passage. This way, the aircraft will sufficiently avoid each other, even if UAVs temporarily lose communication with the GCU during their holding pattern.

Secondly, a situation where UAV collisions may arise is when the search areas of the UAVs are redefined. This is mitigated by putting all UAVs in a holding pattern and moving the UAVs to their new sectors one by one. This way, collisions can be avoided even when communications to some UAVs are temporarily lost.

Finally, a consideration of the risk of a UAV losing communication with the GCU for an extended period of time is made. This is mitigated by setting a maximum duration for which a UAV may lose communications with the GCU, which is to be determined based on the frequency of temporary communication loss and the risk associated with a permanent communication loss. An arbitrary time limit of 2 minutes has been set for the purposes of this discussion but will need to be investigated further in further research.

4.6 SWARM SIZING

A drone swarm consists of various drones working together; for further design and analysis, it is important to specify the number of drones the swarm will use. The number of drones per swarm, N , is determined using

¹⁴<https://ams-osram.com/products/sensors/position-sensors/ams-as5048a-high-resolution-position-sensor>

¹⁵<https://www.bosch-sensortec.com/products/environmental-sensors/humidity-sensors-bme280/>

the following formula:

$$N = \frac{A/d}{V_c t_{cycle}} \quad (5)$$

In Equation 5, A is the search area in [m²], d is the cell width in [m], V_c is the drone cruise speed and t_{cycle} is the required **cycle time**, the time an individual drone takes to visit the same cell twice. To restrict the variability in these parameters, a few assumptions can be made:

- The standard search area per swarm will be set at 1000 square kilometres, based on user requirements **REQ-STK-FB-1.1**. In the situation where a customer requires a larger or smaller area to be observed, the swarm size will scale linearly with the area size according to $N = N_{std} \frac{A}{A_s}$.
- The cruise speed is assumed to be 30 [m/s]. From initial sizing, as reported in the midterm report [53], the cruise speed was estimated to be around 34 [m/s]. At this stage, a lower, safer value of 30 [m/s] accounts for future parameter variations.
- The cell area width d can be assumed to be equal to the ground resolution corresponding to the most narrow FOV among the chosen sensors, which in this case is 1.5 [m].

The aforementioned assumptions then constrain the swarm size to the cycle time requirements. Three deciding factors have been identified to determine the minimum required cycle time:

1. **Risk divergence** The cycle time shall be less than the time it takes for any variable involved in the risk analysis function to change by 5%.
2. **Spread prediction divergence** The cycle time shall be less than the time it takes for the fire spread model to divert more than 10% from the actual fire state for any and all model output variables.
3. **Detection Time Optimisation** The cycle time shall be chosen to optimise the average detection time to the number of drones.

Do note that the estimates made in this chapter are based on limited data; the absence of a continuous wildfire monitoring system with frequent measurements has led to many unknowns regarding fire ignition and spread during the initial stages. Therefore, the following section provided an initial swarm sizing. It is recommended that the data gathered over the first years of system operations be used to optimise the sizing further.

First, the most restraining variable is found for **Risk divergence**, and the respective cycle time is calculated. It should be noted that these variable changes are for continuous, dry conditions.

Vegetation & Soil Moisture Fine, flashy fuels have the largest change in vegetation moisture throughout the calendar day and are principally responsible for diurnal changes in fire danger. These dried herbaceous plants or round wood less than 1/4" in diameter have a time lag of one hour, meaning it takes one hour for the vegetation to reach the 63% equilibrium point between its initial moisture state and the environment moisture [69]. Therefore, the vegetation moisture can be assumed to follow the soil moisture rate of change at a reduced speed, making the soil moisture more constraining for cycle time.

The rate of change in soil moisture is a complex problem that affects several factors. The most important of these factors and their relative importance is shown in Figure 9. In the scope of this report, the analysis is limited to soil temperature and humidity, as all other factors' relative importance is less than 10 per cent. However, as described in subsection **humidity**, the change in humidity on a 30-minute interval is extrapolatable and can therefore be considered negligible.

From Figure 10, it can be seen that soil and air temperature change at an almost linear relation. Since the lag between the two can be ignored when calculating the required cycle time, the assumption is that the cycle time needed for soil and air temperatures is equal.

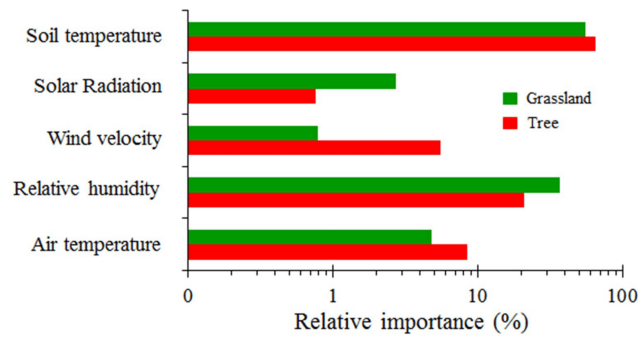


Figure 9: Factors affecting the soil moisture content. [70]

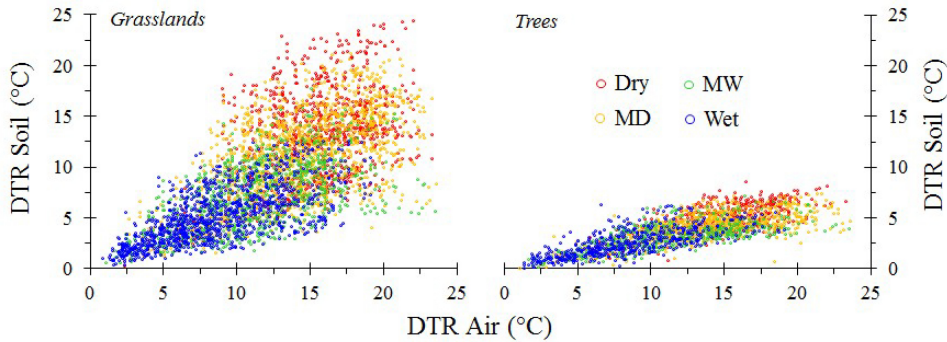


Figure 10: Daily air temperature range (DTR) and its relationship with soil DTR under different vegetation covers and soil moisture states. MD, MW = Medium dry and medium wet soil moisture conditions, respectively. [70]

Humidity The change in humidity on a minute timescale during wildfire climates is a research topic not well documented. However, Table 9 shows the challenges of averaging relative humidity over different time intervals. It highlights that most data points are within 1% of each other for half-hour and hourly intervals, but longer intervals show more significant errors. This suggests that even though the humidity varies significantly, it does not put a stringent requirement on the cycle time of the swarm, as the data can be extrapolated from previous measurements.

Table 9: Comparison of Difference Between Simple Average and Averaging Vapor Pressures [71]

Interval	Minimum	2.5 percentile	25 percentile	Mean	75 percentile	97.5 percentile	Maximum
Half hour	-0.210	-0.015	0.001	0.056	0.052	0.393	5.153
Hour	-0.430	-0.016	0.006	0.126	0.140	0.782	5.663
Three hour	-1.026	-0.032	0.057	0.495	0.651	2.369	7.065
Daily	-0.937	-0.128	2.270	5.164	8.033	11.277	14.829

Air & Soil Temperature The previous subsections have described how air and soil temperature are the most restricting variables as these change the quickest. However, the change rate depends on many factors, including geo-dependent factors. Therefore, for this analysis, inland Spain is chosen as the area of interest as this area is a high-risk area in Europe. Figure 11 shows the locations where the soil and air temperature measurements were taken. The most restricting area is the Parapuños (Spain) region during dry conditions. Here the daily temperature change is roughly 20 degrees Celsius, with a minimum of 25 degrees Celsius. This gives an estimated minimum cycle time of 45 minutes to maintain a maximum 5% temperature deviation between measurements.

Note that ground wind speed is not considered as it does not influence the probability of a fire *igniting* but rather influences the *spread* of fires.

¹⁵https://en.wikipedia.org/wiki/Wildfire_modeling

Spread prediction divergence The CAWFE model for fire spread prediction has not been widely tested, and thus, values for specific 5% deviation times are not available. However, according to the NASA paper publishing the model, "Sequences of 1-2 day CAWFE simulations combined with fire detection data can be applied to predict fire growth from first detection until containment accurately".[72] This suggests that the model is constructed to be accurate on a timescale far larger than 45 minutes. Therefore, it is assumed for now that this is not a constraining factor. However, this might change as the model is tested more. Using Equation 5, a required swarm size of 8 drones is found.

Detection time optimisation Fires spread quickly; thus, the drone swarm must detect new fires quickly. The average detection time is inversely related to the number of drones. However, this relationship approaches an asymptote at 0 detection time. Hence, the benefit of adding a drone decreases with the number of drones. Therefore, this subsection analyses the average fire size upon detection vs the number of drones by running Monte Carlo simulations for different swarm sizes. For the simulations, the following assumptions are made: The drones have an observation width of 1500 meters, fly at a cruise speed of 34.2 meters, fly a simple zig-zag pattern, turn instantaneously, detect all connected fires if one is detected, and spread fires at a rate of 2.5 m/s to all adjacent cells in perfect square sectors where fires ignite randomly.

Figure 12 shows the results of the simulations. The criteria "Fires detected" might give the illusion that a higher score is preferable. However, one must remember that no matter the drone size, all fires will eventually be detected. However, as the average detection time increases, the fire spreads, and thus, more "fires" are created and therefore detected. In summary, a low number of fires detected shows that the drone swarm did not allow fires to spread to large sizes. The simulations suggest an ideal drone size of 20 drones, excluding the communication relay. This is the most limiting amount so far; therefore, this will be the swarm size. The ratio of the relay to observation drones is 1:4. Thus, the required number of drones is 25. The path planning algorithm is refined and optimised in chapter 5. The Dynamic sector division is also introduced. After this optimisation is included, the swarm sizing is performed again.

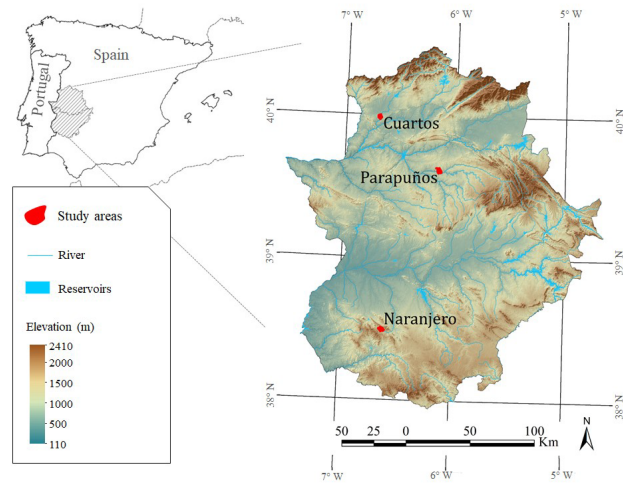


Figure 11: Locations of the measurements taken for air and soil temperature.

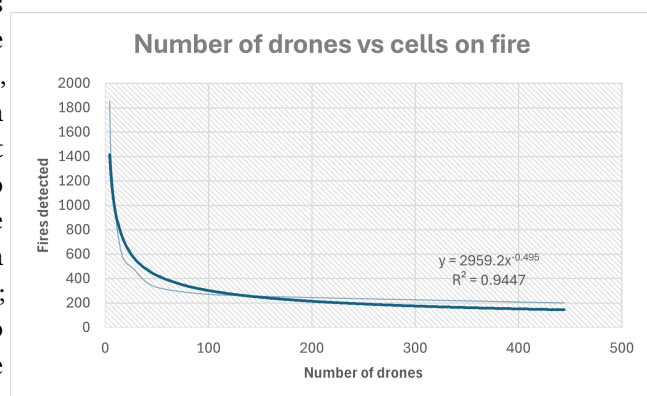


Figure 12: Number of drones vs fires detected.

SWARM DESIGN

This chapter presents the design and operational framework of the UAV swarm that will be used for wildfire detection and monitoring. Firstly, section 5.1 discusses the general operational framework of the swarm and how this flows from the mission requirements. Then, section 5.2 will focus on specifying the methods used to make the swarm perform the mission within the previously defined framework. This includes selecting and analysing sector generation algorithms and UAV path-finding algorithms. Finally, section 5.3 is dedicated to validating the swarm's wildfire detection performance and comparing this performance to alternative wildfire monitoring solutions.

5.1 DEFINITION OF SWARM FRAMEWORK

This section discusses the method by which UAVs search for wildfires in the area of interest. The optimisation of the spatial and temporal distribution of the drones is crucial for the successful operation of the swarm to minimise the risk of a wildfire going undetected and becoming too large to control [73, 74].

For the mission's swarm planning framework, it is crucial that the UAVs do not crash into each other or other air traffic (**REQ-SYS-CON-SFT-1.1**) while also guaranteeing a mean wildfire detection time of at most 15 minutes (**REQ-SYS-TEC-SWM-1.1**). The strict requirement on no possibility of UAV collisions excludes automata-based methods [75, 76], where each UAV operates on an individual set of rules like avoiding other UAVs and moving in the direction of the least surveyed cell. This is unsafe for the application since N^2 continuous communication links must always be operational for a swarm of N UAVs. A single link failure opens up the possibility of a UAV collision, which could cause a wildfire [77]. Likewise, a single UAV losing communication also threatens potential emergency aerial vehicles in the area. These vehicles could be hit at any moment by a UAV flying an unknown trajectory, which poses a high risk for firefighting operations. To summarise, the swarm framework should be made such that the approximate location of the UAV can be pinpointed even when all outside communication with it is lost.

The requirement for the mean fire detection time not exceeding 15 minutes also further restricts the swarm planning framework. For this requirement to be verifiable, there must be a deterministic upper bound on the detection time. On the contrary, many swarm surveillance methods use stochastic paths for route planning, which can only provide statistical upper bounds on detection time [78]. Because the path the UAVs follow is determined by randomness, there is a non-zero chance that some part of the search area stays unexplored for the entire mission. To eliminate this risk, pre-determined paths will be used as waypoints for the UAVs. This ensures that the total coverage of the search area within a given amount of time can be verified.

Taking all this into account, a swarm planning framework can be formulated such that it complies with these constraints. To then comply with **REQ-SYS-TEC-SWM-1.2**, the search area in the chosen swarm framework is divided into square grid cells of dimension $d \times d$ at the start of the mission. The size of the cells is determined by the sensor's footprint, which has the lowest field of view in the cruise. Each cell remains uniquely identifiable throughout the mission to have consistency in measured parameters for different UAVs [78]. At a certain time, each UAV in the swarm is allotted a particular set of grid cells called its sector. All cells in the search area are assigned a sector; each cell may belong to only one sector. The UAV then defines a cyclical path through its sector, which it traces until its battery runs low or until the sectors are redefined. The sectors are redefined when every UAV has completed at least one cycle in their sector, or a UAV returns to the base without a replacement on the way. This sector redefinition happens because the risk information may change in accordance with the newly gathered data by the UAVs, which may demand a different spatial distribution of the UAVs [79]. Note that this redefinition constitutes the only situation with a potential risk of UAV collisions if communication with a UAV is lost while sectors are redefined. This can be prevented by delaying sector

redefinition if some communication links are not responding. To conclude, this swarm planning framework was chosen because it ensures that the UAVs may avoid collisions even when communication is lost and ensures that the entire search area is consistently covered (Figure 13).

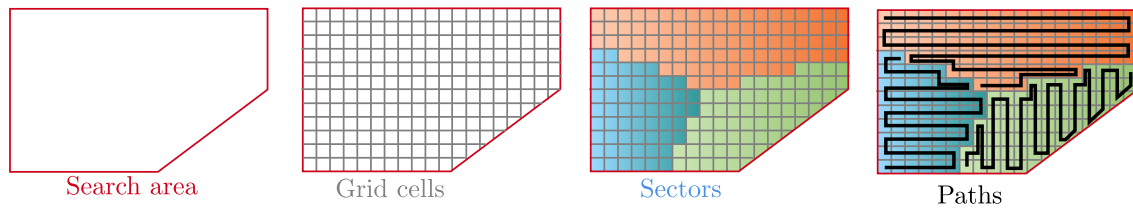


Figure 13: Definition of Search area, grid cells, sectors and paths of the drone swarm.

5.2 SECTOR GENERATION & PATH-FINDING METHODS

The main design decisions concerning the swarm framework are defining the procedure which decides how the sectors are divided, and defining the procedure which generates the paths within the sectors. This section focuses on discussing these procedures. It is designed to comply to the risk: **R-T-45** in section 3.6.

Sector generation method

Two viable methods are considered for dividing the sectors of the search area, which define each UAV's airspace during the surveillance period. The Voronoi and Rectangular sector methods are considered (Figure 14).

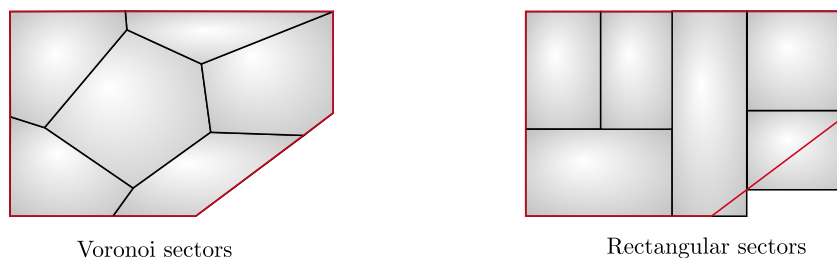


Figure 14: Definition of Voronoi sectors and rectangular sectors.

The Voronoi sectors are defined by a Voronoi tessellation process generated by a set of random points on the search area [80]. The Voronoi tessellation enforces that every cell in the i th sector is closest to the i th generator point. This tessellation method has also seen applications in patrol planning of emergency services and swarm positioning [81, 82]. While in these traditional algorithms, the generator points are uniformly distributed, in the project's application, the empirical risk map can be used as a sampling distribution by using inverse transform sampling [83]. This means that in high-risk regions, the generator points are closer together, resulting in smaller sectors and leading to earlier detection times in those regions. This method has the advantage of rapidly adapting the sectors to new risk information at the cost of using more complex path-generation algorithms within each sector due to the irregular shapes of the resulting sectors.

Alternatively, rectangular sectors are defined by recursively bisecting the search area with horizontal and vertical cuts, such that the aggregated empirical risk on the two halves is equal [84]. The main advantage of this method is that the path generation algorithms are far less complex than Voronoi sectors and that the sectors are deterministic, so they are not based on random sampling like Voronoi sectors. The main disadvantages are that the method is more computationally intensive, less versatile, and much more difficult to implement

than Voronoi sectors. After further analysis, the Rectangular sectoring method was discarded because the algorithm had many rare edge cases, which added excessive complexity and made the results very unreliable. Thus, the Voronoi sector method is selected for this analysis, but the rectangular sector method is still viable for future work.

The objective of the sector generation method is to divide the cells of the search area $C_i \in \Omega$ into K sectors $S_0, S_1, \dots, S_K \in \mathcal{S}$ such that the aggregated risk is the most evenly distributed over the sectors. The objective function is mathematically defined in Equation 6.

$$\begin{aligned}
 S_0, S_1, \dots, S_K &= \operatorname{argmin}_S \left\{ \sum_{s_i \in \mathcal{S}} \left[\sum_{C_j \in s_i} R(C_j) - \frac{1}{K} \sum_{C_l \in \Omega} R(C_l) \right]^2 \right\} \\
 &= \operatorname{argmin}_S \left\{ \sum_{s_i \in \mathcal{S}} (R_{s_i} - \bar{R}_\Omega)^2 \right\} \tag{6}
 \end{aligned}$$

Where $R : \Omega \rightarrow [0, 1]$ is the empirical risk map, R_{s_i} is the cumulative risk of sector s_i and \bar{R}_Ω is the average cumulative risk of the whole search area. For the scope of the project, it is concluded that the objective function is computationally intractable for the generation of sectors since there is no available meta-heuristic available in the literature for this optimisation problem [85]. Instead, the function is used as a performance metric for evaluating the best sector division from a limited number of generated sector divisions. In practice, this will amount to the Voronoi sector algorithm generating multiple tessellations and then selecting the one where the variance of the sector risks is minimised. A post-processing pass of the final tessellation will also be performed to ensure that the sectors are physically traversable. This includes ensuring no cells have zero neighbours of the same sector. Moreover, the post-processing pass also ensures that the sectors can be traversed with minimal backtracking, such that there are no cells with fewer than 2 neighbours of the same sector (in sectors with more than one cell). These post-processing steps are shown in Figure 15.

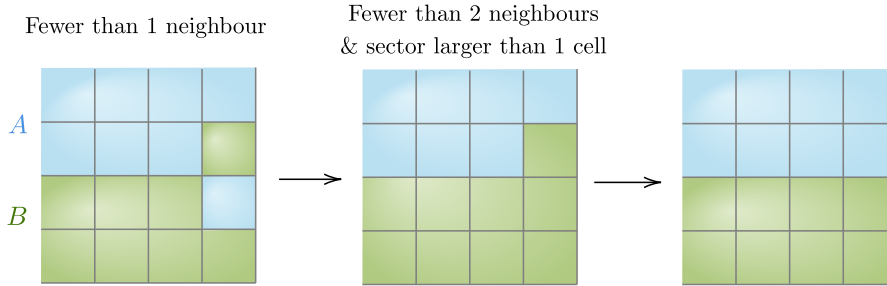


Figure 15: Sector post-processing.

Pathfinding method

Every UAV in the swarm must generate a path through its assigned sector. The path must cover every cell in the sector in a cyclic manner. The pathfinding methods considered are a horizontal zig-zag pattern, a vertical zig-zag pattern and a near-Hamiltonian pattern (Figure 16). The horizontal and vertical zig-zag patterns cover the search area by performing horizontal or vertical sweeps across the length of the sector. This method is widely used in aerial photogrammetry [86, 87]. On the other hand, the near-Hamiltonian algorithm tries to find a cyclic path with the least self-crossings in a given sector using additive Monte Carlo generation of cyclic Brownian paths. This entails that the algorithm starts at a random cell in the sector and then tries to create a closed loop by tracing a path to random adjacent cells (without crossings) until it either returns to the starting cell or runs into a dead end. When a closed loop is formed, it is very likely not to be a total coverage of the sector (a total coverage without crossings is proven not always possible [88]). Therefore, this closed cycle is extended by starting on a random point in the cycle with at least 2 free neighbours and then tracing a path (again without crossings) to a cell adjacent to the starting point. After no points on the cycle with 2 free neighbours are left, the remaining untraversed cells are filled in by moving to that cell and then returning by

backtracking. Although this method is likely to see an increase in pathfinding performance, it was disregarded due to its computational intensity, complexity of implementation and lack of available literature, but it remains a valid approach for future research. The objective of the pathfinding algorithm is to minimise the wildfire

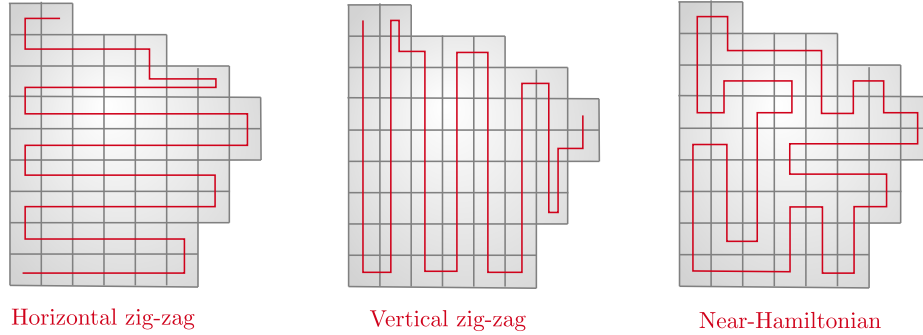


Figure 16: Voronoi sector pathfinding algorithms.

detection risk, which is defined as the risk that a wildfire goes undetected for a certain time. Mathematically, the optimal path p_{opt} , which consists of a sequence of T cells from sector S , is defined as in Equation 7.

$$p_{opt} = \underset{p \in S^T}{\operatorname{argmin}} \left\{ \sum_{C_i \in p} \tau_i R(C_i) \right\} \quad (7)$$

Where τ_i is the maximum time between passes of cell C_i and $R(C_i)$ is the risk of cell C_i . During the validation procedure, it was concluded that the optimal path could be selected sufficiently accurately by minimising the path length (Equation 8).

$$p_{opt} \approx \underset{p \in S^T}{\operatorname{argmin}} \{|p|\} \quad (8)$$

In practice, this will amount to the UAV generating the horizontal zig-zag and the vertical zig-zag path through its sector and then choosing which path to pick based on Equation 8. Furthermore, it is noted from the literature that some surveillance UAVs use gimbaling cameras to increase their lateral range [87], which lends itself well to the zig-zag surveying pattern chosen. This would allow for each UAV to cover a much vaster area in a short amount of time. However, due to current incompatibility with the chosen swarm framework and difficulty of implementation, this method is currently discarded for this design feasibility project but remains a viable technique for further research.

5.3 SWARM PERFORMANCE & COMPARISON

This section will validate the swarm's fire detection performance and compare it to alternative solutions after selecting the sector generation and pathfinding methods in section 5.2.

Simulation Procedure

The validation procedure aims to arrive at a preliminary estimate of the swarm's ability to detect wildfires. This is done by defining a square search area of 22×22 cells of 1.5×1.5 [km²] each, containing a total area of 1089 [km²]. Each cell in this area has a certain risk of wildfire ignition, defined by a risk map. This risk map is generated from a truncated 2D Fourier series with randomised amplitudes to mimic the smoothly varying risk factors like air humidity and soil moisture. The risk map randomly creates a wildfire at a certain cell according to its ignition risk. This fire then spreads to adjacent cells with an average speed of 2.5 [m/s] (as discussed in section 4.6). The swarm uses the risk map to generate the Voronoi sectors for the UAVs. Then, the horizontal and vertical zig-zag paths are generated for every sector, and the shortest path for each is chosen. When the

simulation starts, the UAVs follow the assigned path until one detects a fire. The detection location and time are recorded, and a new simulation starts.

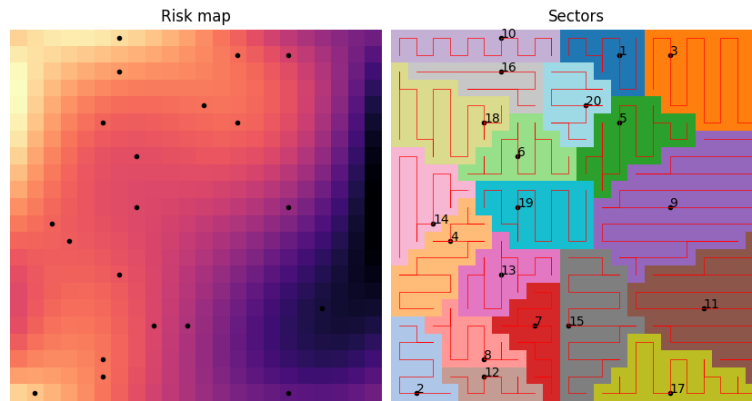


Figure 17: Generated risk map of the search area (left) and produced sectors and paths in the search area (right).

Simulation Results

This simulation procedure can be used to gain insights into the detection behaviour and performance of the swarm (Figure 18). Firstly, a parameter sweep on the number of UAVs in the swarm is run, and their mean detection times are to verify that the swarm size of 20 UAVs (as estimated in section 4.6) complies with **REQ-SYS-TEC-SWM-1.2**. The results of which are shown in Figure 18a, which indeed validates that 20 UAVs can detect wildfires with an average detection time of 15.3 minutes. It is also noteworthy that there are steep diminishing returns in increasing the number of UAVs. Decreasing the detection time from 20 to 15 minutes requires only 5 more UAVs, while decreasing from 15 to 10 minutes requires 10 more UAVs.

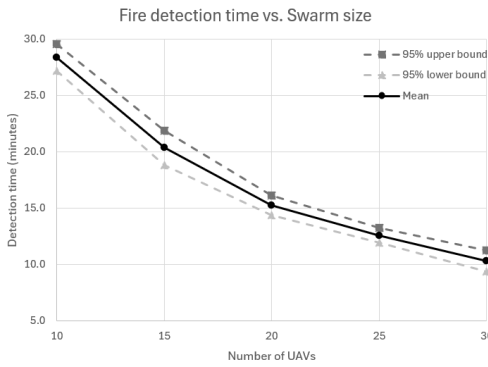
Furthermore, a simulation of a swarm of 20 UAVs with the same risk map was run 30000 times to give the results displayed in Figure 18. From these plots, it can be concluded that the Voronoi sector algorithm, along with the zig-zag paths, is indeed successful in efficiently detecting wildfires because it consistently detects the fires in the highest risk areas the quickest (Figure 18c and Figure 18d). This is corroborated by Figure 18b, which shows that the detection time probabilities are skewed towards lower values, meaning that most fires are detected very quickly. Even in the worst 5% of cases, the fire is still detected within 33 minutes, which is a massive improvement over alternative methods, as will be explained in the next subsection.

Performance Comparison

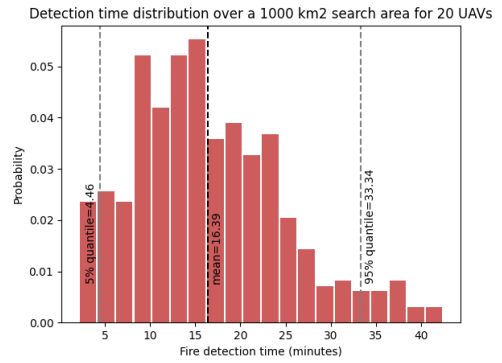
Because the swarm occupies a novel technological niche with its ability to rapidly detect and communicate the location of wildfires locally, it is difficult to compare the swarm's performance to other available technologies directly. Therefore, to demonstrate the superior performance of the swarm over alternative solutions, we compare the swarm's performance with that of a single general aviation aircraft performing the same mission. The mission is assessed on three key metrics: cost, detection time, and ground resolution (Figure 19a).

The alternative aircraft considered to perform the mission is the Beechcraft King Air 350, operating 450 flight hours per year. The average upfront cost of this aircraft is \$ 3.6MM [89, 90]. The annual operating costs are approximately \$ 250k for maintenance and storage, \$ 200k for fuel and \$ 150k for crew and insurance, making a total of \$ 600k, which is a bit higher than the swarm's cost profile (as discussed in Table 11.1.1).

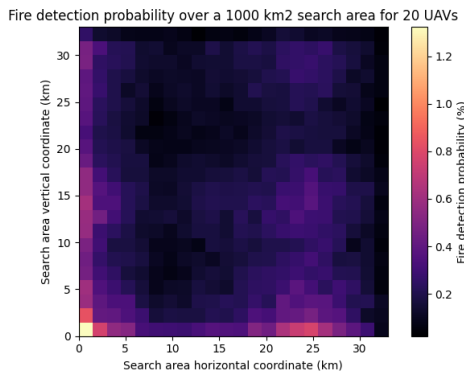
The aircraft is equipped with the Hensoldt ARGOS-II HD infrared camera [91]. To match the swarm's ground resolution of 3 [m], the aircraft is limited to a cruise altitude of 5600 [m], resulting in a ground footprint of 3.2 [km] (a 10×10 grid of cells). At this altitude, the aircraft's speed is limited to 185 KIAS (96 [m/s]), giving a mean detection time of 54.8 minutes, as shown in Figure 19b. This detection performance is worse than that of the swarm, which has a 5% worst detection time of 33 minutes. Conversely, to match the swarm's detection time of 15 minutes, the aircraft needs to fly at its maximum cruise speed of 310 KIAS (159 [m/s]) at an altitude



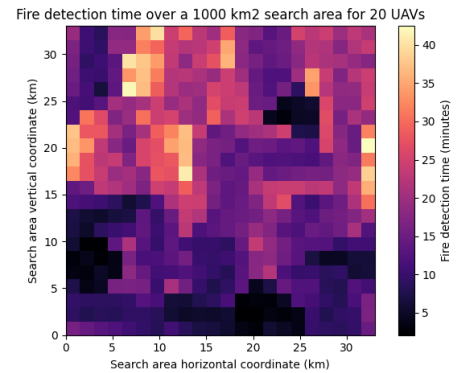
(a) Mean fire detection time for a ranging number of UAVs. 95% uncertainty bounds in the mean detection time are also shown.



(b) Fire detection time distribution, showing a mean detection time of 16.4 minutes, a 5% quantile of 4.5 minutes and a 95% quantile of 33.3 minutes.

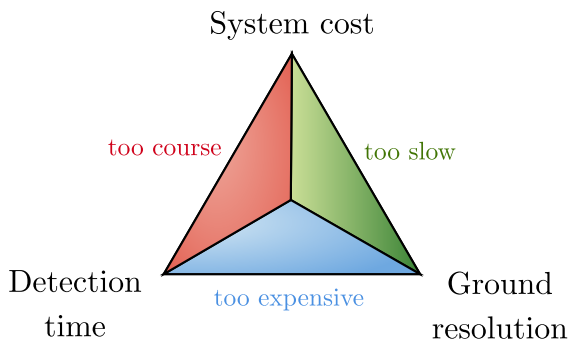


(c) Fire detection probability over the search area. This represents the fraction of all wildfires in the search area that are detected on a particular cell.

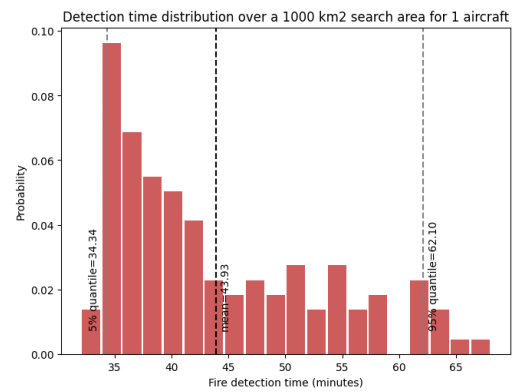


(d) Fire detection time over the search area. This represents the average time that elapses from the ignition of a wildfire until it is detected on a particular cell.

Figure 18: Swarm performance simulation results.



(a) The three key performance aspects of the mission are cost, detection time, and ground resolution.



(b) Fire detection time distribution of a single aircraft, showing mean, 5%, and 95% quantiles.

Figure 19: Comparison of mission performance aspects and fire detection time distribution.

of 8500 [m]. At this altitude, the aircraft will have an average detection time of 14.24 minutes but with a ground resolution is 14.4 [m]. To conclude, if the aircraft is configured to match the ground resolution of the swarm, it will have worse detection performance, and if it matches the detection performance, the ground resolution will be worse.

COMMUNICATIONS ARCHITECTURE

Communication systems for wildfire drone swarms are critical for enhancing the efficiency and effectiveness of wildfire monitoring, management, and mitigation. Efficient and reliable communication architecture is a crucial aspect of drone swarms, especially for those operating in hazardous conditions. Reliability is vital to prevent control loss, reduced effectiveness and environmental damage. The following chapter discusses the design of the communication subsystem and the communication architecture of the swarm and provides a general overview of the approach taken.

6.1 BACKGROUND INFORMATION

From the previous section on mission logistics and operations, it is expected that the drone will partake in pre-, active and post-fire situations and will have to operate with high reliability. Furthermore, it was identified that the drone swarm will operate in remote locations with limited population density. Considering these factors, the challenges faced by the communications subsystem can be reduced to the following points: fire/smoke attenuation and limited infrastructure.

6.1.1 Smoke / Fire attenuation

When designing the system, a major concern that was communicated was whether or not the drone would be capable of maintaining communications during active fires, given the fire and smoke attenuation. Losses concerning these factors have proven to be quite significant. This was notably true for the communication bands between 380 - 400 [MHz], which are commonly used by emergency services globally [92]. Over the distance of 20 meters, signals at this frequency were noted to experience a power loss ranging from 10 to 15 [dB] due to fire attenuation [93]. The influence of smoke is also significant, with power losses ranging from 8 to 11 [dB] over the distance of two meters for the same frequency [94]. These losses are expected to be even more severe for longer propagation distances. That said, the relationship between fire/smoke and signal behaviour is a complex one, and, as of now, research on it has not yet been conclusive. After an extensive literature review, it was determined that quality literature on the topic had proven to be sparse. Multiple experiments have been conducted to measure smoke and fire losses [92][93] [94][95], however, the underlying mechanisms behind these losses have yet to be fully understood and quantified. From the literature analysed, the mechanisms influencing signal attenuation include absorption, scattering, reflection and refraction [95]. From these mechanisms, fire and smoke attenuate signals differently based on a set of local properties, including, but not limited to, temperature, chemical composition, smoke density, signal frequency, signal polarization and more.

The research found that a numerical method that quantifies the combined effect of these losses does not exist yet. Instead, values are obtained experimentally by simulating fire environments on a limited scale. For preliminary analysis, data from experiments which were conducted in a wildfire like conditions were extrapolated to be used for the link budget. Details regarding this methodology will be further elaborated on in subsection 6.5.

6.1.2 Limited Infrastructure

Many wildfires occur in remote locations where communication infrastructure may be limited or unavailable due to the lack of financial incentive to cover the area. Typical Long Term Evolution (LTE) networks used for high data rate telecommunications in urban areas cannot be used for that reason, and satellite communication,

whilst capable of covering regions of high wildfire risk, has uncertainty as to whether it can provide consistent link given the effects of smoke and fire during an active wildfire.

This issue is critical to the mission, as neglecting this could result in the ground control station being unable to receive drone data or transmit instructions to the drones. To make a drone swarm effective in monitoring and managing wildfires, ensuring robust communications through self-sufficiency was deemed the most viable method moving forward.

6.2 SYSTEM RISKS & REQUIREMENTS

Before starting the design phase, the risks and requirements were generated to ensure coherence. The relevant risks are:

- **R-T-31:** Emergency command is not received
- **R-T-48:** Drone fails to communicate
- **R-T-49:** Communication is not fast enough

The relevant requirements are:

- **REQ-SYS-TEC-UNI-4:** The communication system shall always ensure communication between the ground station and active UAV units.
- **REQ-SYS-TEC-UNI-4.1:** The communication system shall relay signals from firefighters during active fire scenarios.
- **REQ-SYS-TEC-UNI-4.2:** The communication system shall require no more than 30 [W] of power.
- **REQ-SYS-TEC-UNI-4.3:** The communication system shall have a mass of no more than 5 [kg].
- **REQ-SYS-TEC-UNI-4.4:** The communication network should be able to relay critical payload data at all times with a margin of 50%.
- **REQ-SYS-TEC-UNI-4.5:** The link margin for the system shall be greater than 5 dB
- **REQ-SYS-CON-SFT-1.3:** The unit shall be able to relay its GCS position following an emergency landing.

The rationale for these requirements are listed in Table 50 (in Appendix A).

6.3 ASSUMPTIONS

ASMP-COMM-01: Atmospheric absorption losses are minimal and can be excluded from the link budget. These losses are mainly dictated by the power absorption of atmospheric gases such as oxygen and water, which causes noticeable attenuation from 10 [GHz] onwards. Figure 25b Given that the operational frequencies are around 440 [MHz] and 2.4 [GHz], atmospheric absorption losses will be lower than 0.01 [dB/km] and can be neglected. This assumption will not significantly impact the accuracy of the results.

ASMP-COMM-02: Smoke attenuation loss can be modelled using an inverse power relation. Alternative functions, such as inverse exponential and inverse logarithmic functions, have also been tried, but the one used by the team was deemed to produce the most reasonable results. Smoke attenuation is a complex topic,

and this assumption can potentially affect the outcome of the link budget greatly. This potentially significantly impacts the results and thus will need to be validated.

ASMP-COMM-03: Pointing losses can be assumed to be low, given the inclusion of an RTK GPS. Given that the distances between drones are not particularly large, the pointing accuracy of the system did not have to be particularly accurate. However, given that smoke attenuation could potentially be quite severe, there were concerns regarding the accuracy of the measured positional location of individual UAVs. The inclusion of the RTK GPS aims to minimise this concern by decreasing the uncertainty of drone position.

ASMP-COMM-04: The system noise temperature of the UAV is at 290 [K]. This value was chosen by referring to the UAV reader. However, during actual operations, this value could differ quite significantly. However, given that measurements were conducted in Kelvin, a difference of +- 30 [deg] would not substantially impact the results, and the noise power would only vary by +- 0.5 [dB] at most.

ASMP-COMM-05: Spreading implementation losses do not need to be included, given that the information sent is not particularly sensitive and security is not a concern. This assumption will not impact the result's accuracy.

6.4 DESIGN

The design phase of the communication subsystems is a critical step that ensures robust, reliable, and efficient data exchange between the UAV and its control station. This phase involves a comprehensive analysis of the data rate requirements, communication architecture, antenna selection and sizing and link budget calculations.

6.4.1 Data Rate Estimation

Before designing the communication system, a rough approximation of the transferred data rate needs to be calculated. Calculations for the data rate determine the approximate scale of information the swarm would handle preceding the architectural decision. Table 10 details sensor image and video resolutions and the employed compression and modulation techniques.

Table 10: Observational Drone Data Rate

Images			
	Visual	NIR	IR
Initial Resolution	1280x720	1280x720	640x480
Pixels (px)	921600	921600	307200
Bit Color Depth (bits)	12	10	14
Compression	Compressed JPG 100% 24bit/pixel		
Comp. File Size (MB)	0.19	0.19	0.06
Comp. File Size (Mb)	1.52	1.5	0.5
Comp. File Size (Mb)	1.9	1.9	0.6

	Lower	Higher
DR_img (Mb/image)	3.5	4.4
Seconds per image	12.5	12.5
FPS (image/sec)	0.08	0.08
FPS margin (-)	30%	30%

DR_img (Mbps)	0.37	0.46
---------------	------	------

Video			
	Visual	NIR	IR
Initial Resolution	640x480	640x480	640x480
FPS	30	30	30
Color Depth (bit)	10	10	10
Compression	H.265 (Good Video Quality)		
Data Rate (Mbps)	0.31	0.31	0.31
Data Rate (Mbps)	0.47	0.47	0.47

	Lower	Higher
DR_video (Mbps)	0.31	0.47

Command and Control (2C)	
Data Rate	0.013

SM (image)	1.25
SM (video)	1.5
2C	1.5

It should be noted that JPEG compression was chosen given its ubiquity and effectiveness in the context of

Table 11: Total Swarm Data Rate

Total Swarm Calculation						
	Prefire		Active Fire		Post Fire	
	Low	Upper	Low	Upper	Low	Upper
Drones sending live image	24		24		24	
Images [Mbps]	9	11	9	11	9	11
Drones sending live video	12		6		12	
Video [Mbps]	4	6	2	3	4	6
Drones receiving controls	24		24		24	
Command and Control [Mbps]	0.31	0.39	0.31	0.39	0.31	0.39
Total DR [Mbps]	13	17	11	14	13	17

image compression. The H.265 video compression was chosen given its improved efficiency over its widely adopted, less computationally demanding predecessor, H.264.

The seconds per image value was decided based on the operational speed and camera coverage. The 12.5 seconds per image requirement was chosen to reduce the overlap between the images taken and ensure effective use of the data transmitted.

The upper bound values provided in the calculations were calculated by applying a scale factor to the lower bound values that were found experimentally. This value was validated by taking an image of similar resolution, adding a 50% noise filter in Photoshop, and compressing it to observe the difference in file size. The difference was less substantial than originally thought and was measured to be < 10%. Nonetheless, a scale factor of 1.25 was used as a safety margin. The same was done for the video, this was one in After Effects instead. The difference was measured to be < 30%, and a scale factor of 1.5 was applied. As for the command and controls (C2), given the importance of receiving controls, a scale factor of 2 was used. The data rate for C2 was obtained by summing the individual data rates in the avionics section.

To minimise the data rate requirements of the system, it was decided that a limit would be imposed on the amount of UAVs sending live video. These values were created because the operator did not have to monitor all drones at all times. Half of the swarm broadcast video was sufficient for the operator to have good situational awareness. This value was further reduced during a wildfire situation to minimise the bandwidth required and alleviate the SNR drop that occurs during an active wildfire scenario. Lower values could be chosen, but these values serve to determine the system's upper limits.

6.4.2 Communications architecture

Based on the aforementioned challenges, an investigation was conducted on the general communication architecture of the swarm. From the previous section on operations, the operational altitude of the drones was defined as 850 meters. At this height, achieving line-of-sight communication will not always be possible as the local environment may get in the way. This problem was solved by implementing a distributed-decentralised communication network (Figure 20), which involves adding a high-altitude relay drone operating at around 4 kilometres. This will be used to establish a communication link between four smaller monitoring UAVs. This architecture satisfies the requirement **REQ-SYS-TEC-UNI-1**.

The combination of a distributed network offers minimal system complexity and high network path redundancy. Network path redundancy is defined by the available alternative routes the information can take to get from the UAV to the GCU and vice versa.

High path redundancy ensures that information will not be lost if a communication path is unavailable due to

⁰Medium. URL: <https://medium.com/delta-exchange/centralized-vs-decentralized-vs-distributed-41d92d463868>

drone malfunction or environmental factors. This feature is unavailable for the centralised communication system, which directly relays information to GCU.

System complexity refers to the complexity level needed to send information across the network. This value was quantified by the number of paths it takes for information to get from one to another. Minimising this value improves system reliability by reducing the number of ways the system could fail. One example of systemic failure is a broadcast storm, where several communication packets are transmitted in a loop due to network misconfiguration, causing congestion, degradation of network performance and sometimes network failure. The less complex the architecture is, the lower the probability of systemic failure.

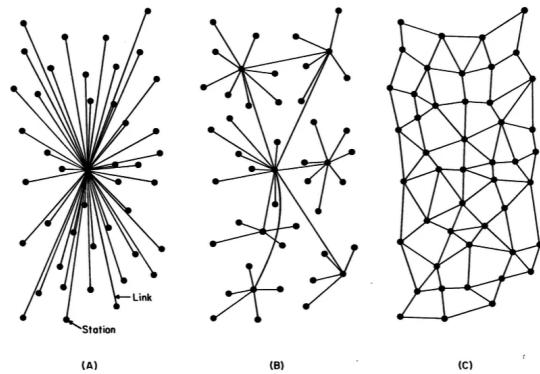


Figure 20: Communication architectures A: Centralised, B: Decentralised, C: Distributed.¹

As for the communication technology and frequency used, it was decided that RF communication technology would be used at a frequency of 2.4 [GHz]. This was deemed the typical frequency used for UAV video broadcasting as the frequency in this band allowed for efficient modulation techniques to be used while minimally impacted by environmental attenuation [96]. This decision satisfies the requirement **REQ-SYS-TEC-UNI-1.1**.

With that, the system functions as follows. Operating at an altitude of 850 [m], the individual UAVs will gather data and firefighter RF communications which are then sent to the relay drone above that operates at an altitude of 4000 [m]. The data collected will then be propagated through the network via the relay drones until it reaches the GCU. As for the RF communications, the information will be sent to the individual UAVs through the relays to broadcast to any firefighters within the range of the UAV swarm.

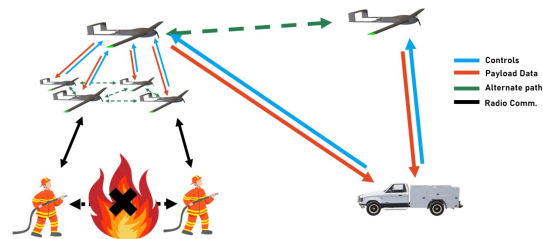


Figure 21: Communication architecture breakdown

The swarm itself requires a complex communication architecture in order to provide reliability and extend range as far as possible. As seen on Figure 21 of the smaller vehicles have a direct link with each other to provide spatial location information and each relay has an established link with other relays around to provide redundancy in the case the direct link to GCU is interrupted. This approach is a mix of distributed and decentralised swarm architecture.

6.4.3 Antenna Selection

Based on the research conducted on smoke attenuation, the conclusion was that high-gain antennas and receivers were both needed. Smoke attenuation proved to be quite severe and generated a loss of -27 [dB]. Combined with the free space losses, this greatly increased the required SNR. The selection of the decentralised-distributed network meant that the antenna selection had to be done for two sets of drones, namely the low-flying surveillance drones and the high-flying relay drones.

Blade Antennas

An omnidirectional blade antenna, specifically the UVW-0430, was chosen to communicate with first responders and neighbouring UAVs. The component can be seen in Figure 22b. The ability to attach the antenna outside of the UAV improves its ability to detect incoming signals and the shape of its profile results in minimal drag being generated.



Figure 22: Blade, Patch and Phased Array

Phased Array Antenna

The phased array antenna comprises an array of smaller antenna elements that can be electronically steered by controlling the phase shift of each antenna such that the combined wavefront forms a directional plane wave. Adjusting the delay in the phase shift changes the orientation of the propagated wave. With careful spacing of the individual elements, the sidelobes of the radiation pattern can also be reduced, which improves the system's energy efficiency.

To communicate with the relay drone, the selected antenna must be directional and provide high gain to communicate through smoke. On a more macro level, factors such as antenna size, weight, operational frequency, power consumption and the mechanical complexity of the pointing mechanism also had to be considered. For that reason, a phased array antenna system was also selected. This system has a minimal profile and weight and can be adapted for the 2.4 [GHz] operational frequency, is power efficient, and can be electronically steered via software. This decision satisfies the requirement **REQ-SYS-TEC-UNI-1.2**.

The selected antenna elements are the Kyocera Ceramic Patch 2.4 [GHz] Antenna. Weighing in at 4.8 grams per unit, the small patch antennas have a moderate peak gain at 3.83 [dB] and have a spatial dimension of 18 x 18 x 4 [mm]. Given its compact form factor, it was decided that a 6 by 6 array of these antenna elements would be used to create the phased array system.

Phased Array Sizing

To the size the phased array, the phased array system toolbox from Matlab was used to simulate the directivity gain of the antenna system. From there, to model the array interaction of patch antennas, a uniform rectangular array (URA) made from N by N elements were generated, each following a cosine radiation pattern. Gaussian and isotropic patterns were also considered but were not selected as they do not represent the radiation pattern of patch antennas as accurately. The spacing between each element was chosen to be at half the wavelength of the signal (6.25 cm) in order to minimise the grating lobes. The following visuals display the antenna array as well as its results. Figure 23b shows the power distribution of the antenna using a normalised power scale, with one being the largest and representing the maximum power. Figure 23c display the same graph but is scaled in decibels.

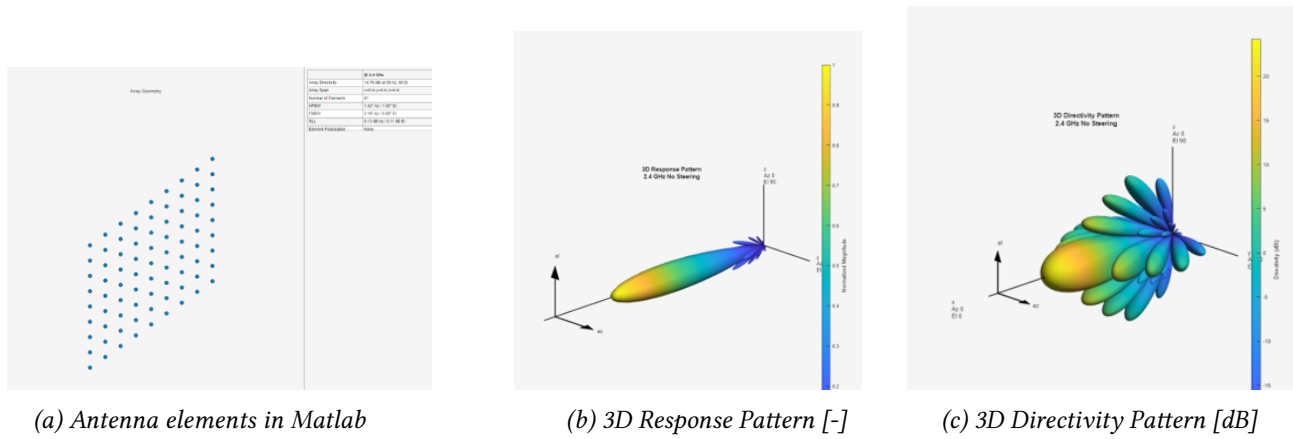


Figure 23: Blade, Patch and Phased Array

During the investigation, it was noted that adjusting the direction of the beam also caused sensor gains to decrease, and after 60 degrees the array directivity noticed a significant drop in power. For a 5 by 5 URA, from 50 to 60 degrees, this drop was 0.4 [dB] but from 60 to 70 degrees, this drop was 1.2 [dB]. It was for this reason, the results the steering angle of the array was limited to 60 degrees in elevation and azimuth. From there, the following results were generated.

Array Size	9x9	8x8	7x7	6x6	5x5	4x4	3x3	2x2
Array Directivity for Az = 0, El = 0 [dBi]	24.23	23.22	22.1	20.78	19.27	17.38	15.1	11.72
Array Directivity for Az = 30, El = 30 [dBi]	23.04	22.01	21.07	19.03	18.13	16.3	14.72	11.04
Array Directivity for Az = 45, El = 45 [dBi]	21.4	20.43	19.32	18.04	16.64	14.7	12.26	8.67
Array Directivity for Az = 60, El = 60 [dBi]	17.85	16.74	15.48	13.99	12.19	9.92	6.95	2.81
HPBW for Az = 0, El = 0 (AZ) [deg]	11.28	12.68	14.5	16.92	20.3	25.4	33.86	50.6
HPBW for Az = 0, El = 0 (EL) [deg]	12	14	16	18	22	26	34	52
Array Directivity for Az = 60, El = 60 [dB]	20	18.89	17.63	16.14	14.34	12.07	9.1	4.96
Element Gain [dB]	5.98							
Total Phased Array Gain [dB]	25.98	24.87	23.61	22.12	20.32	18.05	15.08	10.94
Length / Width [mm]	50.0	43.8	37.5	31.3	25.0	18.8	12.5	6.3
Space Used [mm ²]	2500	1914	1406	977	625	352	156	39

Based on the preliminary size constraints imposed by the structures department (0.7 x 0.25 x 2 mm [L x W x H]) the following phased array sizes were chosen.

Final Array Selection	Array Size	Gain
Observational to Relay	5x5	18.17
Relay to Observational	5x5	18.17
Relay to Relay	9x4	24.05

Final Selection

Based on that, the final configuration of antennas for the observational and relay drone is depicted by the following diagram.

The link budget is then used to verify that antenna selection will provide sufficient gain for the system to operate.

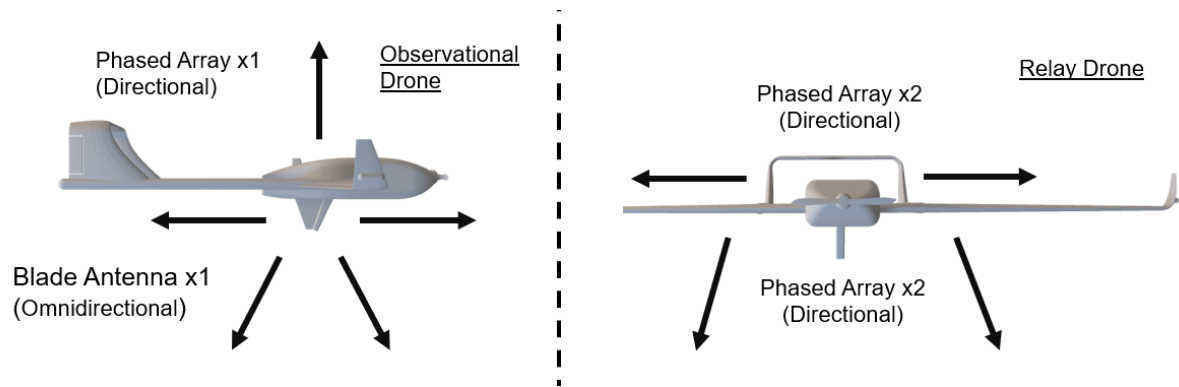


Figure 24: Final Antenna Configuration

6.5 LINK BUDGET CALCULATION

To identify the antennas and power required, a link budget was made to calculate the gains required for a functional communication system. The link budget was completed for different communication scenarios: UAV to UAV, UAV to Relay, Relay to Relay and Relay to the GCU. These can be referred to in Figure 4. During the link budget calculations, the following factors were considered.

Antenna Gain

The main form of gain in a link budget occurs in selecting the antenna used for transmission and receiving. The antenna selection section above refers to the gains used for each link budget.

Free Space Loss

Free space loss (FSL) refers to the reduction in signal strength as an electromagnetic wave propagates through free space. The loss occurs due to the spreading out of the wave as it travels further away from the transmitter. FSL follows the inverse square law where signal power density decreases proportionally to the square of the distance from the source. It also depends on frequency, as higher frequencies have shorter wavelengths, causing the wavefront to spread more rapidly. Thus, this loss can be described by the following equation:

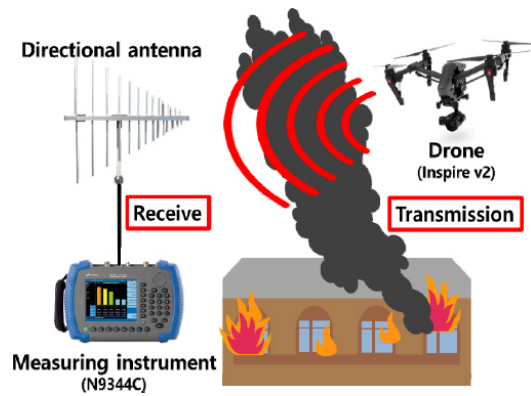
$$FSL = 20\log_{10}(d) + 20\log_{10}(f) + 20\log_{10}\left(\frac{4\pi}{c}\right) \quad (9)$$

where d is distance given by meters, f is the frequency given in Hz and c is the speed of light.

Atmospheric Loss

Atmospheric loss of transmitted signals is mainly driven by water vapour and diatomic oxygen absorption. Water vapour content is mainly driven by relative humidity, whilst the concentration of diatomic oxygen is mainly a function of altitude. A conservative estimate of this value can be obtained by analysing the atmospheric absorption at sea level, where atmospheric absorption per km is the greatest [44].

Given that the drone will operate in areas where wildfires are highly risky, water vapour concentration is expected to be minimal. Furthermore, the system will use frequencies below 10 [GHz] and will have a range of less than 50 [km], making atmospheric losses negligible.



(a) Methodology used to measure smoke attenuation [95]

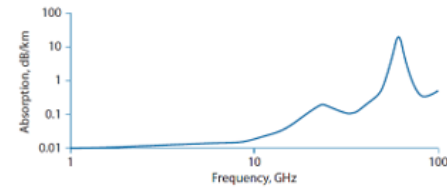


Fig. 12.3 Horizontal atmospheric absorption at sea level.

(b) Atmospheric attenuation at sea level[44]

Smoke Attenuation Losses

To simplify the problem regarding fire-related attenuation losses, only based on a report conducted on signal losses for UAVs being obscured by indoor fires, a 7.7 [dB] loss was measured over a distance of 10 meters [94]. This was then converted into a non-dimension value, which was then extrapolated using the inverse power relation to obtain the losses for the required distances.

Other functions, such as inverse exponential and inverse logarithmic functions, were used to model this relation but yielded loss values that were too large or too small to be considered. At distances of 850 meters and 4000 meters, the losses due to smoke were calculated to be around 22 [dB] and 27.7 [dB], respectively. Face validity was used to confirm the values, and technical experts were consulted to ensure that the used values were reasonable.

Pointing Loss

Pointing losses refer to the decrease in signal strength when a directional antenna is not accurately aligned with the intended target. This value depends on the accuracy of the pointing mechanism and the accuracy of the positional knowledge of the target. Omnidirectional antennas have negligible pointing losses in azimuth, whilst directional, high-gain antennas have higher pointing losses given their smaller beam width. This loss can range from -1 to -3 [dB] for directional antennas, while for omnidirectional antennas, this will be closer to 0 [dB] [44].

Radome Loss

Given the challenging environments the UAV will be operating in, antenna protection against wind, dust and temperature will be needed. Radomes are environmental barriers that are largely electromagnetically transparent and allow signals to be transmitted and received by antennas. However, radomes are not perfectly dielectric, so there are losses. Based on the literature, these losses vary between -0.5 and -1 [dB] depending on the manufacturing approach and system characteristics [44].

Component Line Loss

Component line loss refers to the decrease in signal strength between the transceiver radio and antenna. To reduce this effect, short, low-loss coaxial cables are typically used to connect communication devices, given their effective shielding against electromagnetic interference (EMI) and radio interference (RFI). These losses are dependent on the cable composition, length and operational frequency. Based on the existing market products, for a frequency of 2.4 [GHz], these losses range from -1 to -2 decibels per meter.

Noise

In electronic systems, noise is an unavoidable phenomenon that can significantly impact the performance and sensitivity of devices, particularly in high-precision applications such as those involving Unmanned Aerial Vehicles (UAVs). This section delves into the various aspects of noise, focusing on two critical types: thermal noise power and noise figure.

Thermal Noise Power

Thermal noise power is a measure of noise that is inherent in all electrical circuits due to their temperature and is a fundamental limit to the sensitivity of electronic systems. The following equation was used to quantify this.

$$P_{TN}[\text{dBm}] = 10\log_{10}(k_B \cdot T) + 10\log_{10}B + 30 \quad (10)$$

Given the elevated operational altitudes of the UAV, the internal temperature used for this calculation was estimated to be about 290 [K], which is the value used for preliminary sizing as described by the UAV design reader. The bandwidth was calculated in the previous section about the data rate. This was calculated at -114 [dBm] [44].

Noise Figure

The noise figure is a relative measure indicating how much additional noise a device contributes compared to an ideal, noiseless one. It is usually calculated experimentally by measuring the SNR as a signal passes through a component. Combining the noise figures of all components connected in series gives the system's noise figure as a whole.

Obtaining this value through simulation was out of the question given the lack of detail in the design; thus, to simplify this, the team referred to the UAV design reader [44] and obtained a representative noise figure of -8 [dB] for a system operating in the X-band (8.0–12.0 [GHz]) [44]. This is higher than the operational frequency, given that the noise figure rises with increasing frequency, but this value is a conservative estimate of the actual system noise figure.

6.5.1 Discussion of Results

For all link budgets, the resulting link margin was higher than the 5 [dB] specified by **REQ-SYS-TEC-UNI-4.5**, which is a good indicator that the communication system will be suitable for its operational environment. It should be noted that 10 [W] of power was used for relay to relay communication in order to ensure a sufficient margin. From discussions with Prof. Speretta, using power above 30 [dBm] or 1 [W] will require the system to be certified. This will need to be taken into account in the future.

For the relay to ground downlink, the signal margin was much greater than expected, sitting at 26.4 [dB]. This can mainly be attributed to the large antenna and receiver gains obtained from the phased array antenna as well as the low data rate requirement from controls. Power can be reduced for transmission in that case and used for other systems. The previous reasons would also explain the disparity between the uplink and downlink as the uplink only has a signal margin of 10 [dB].

6.6 VERIFICATION AND VALIDATION

To ensure that the values obtained were correctly calculated and representative of the real world, verification and validation procedures were enforced throughout the design phase to ensure the results were up to standard. The table structure is explained in subsection 7.1.1

6.6.1 Verification

Given its simplicity and versatility, Excel was the main calculation tool. Matlab was also used but was specifically used for phased array simulations.

Table 12: Unit tests

Block Tested	Inputs	Outputs	Tests	Confidence
DR Calculation	Instruments used, Drone Count	DR_{Drone}, DR_{swarm}	Analysis	High
Phased Antenna Calc.	Array Size	Array Gain	Analysis	Medium
Required SNR	Modulation Technique, Bit Error Rate Required	$SNR_{required}$	Analysis	High
Link Budget (Obs. to Obs.)	Gains, Losses, Noise	Link Margin	Analysis	Medium
Link Budget (Obs. to Relay)	Gains, Losses, Noise	Link Margin	Analysis	Medium
Link Budget (Relay to Relay)	Gains, Losses, Noise	Link Margin	Analysis	Medium
Link Budget (Relay to Ground)	Gains, Losses, Noise	Link Margin	Analysis	Low

6.6.2 Validation

Comparison to other models Values for the data rate calculations were compared to other DSE projects to ensure that values used were in the correct order of magnitude. The FLOWS project, which focused on designing a single drone with visual capabilities, also had video and image data rates lower than 1 Mbps.

As for the link budget, the final tables generated by the team were compared to the example used by the UAV design book [44]. The calculated link margins were all within the acceptable ranges as designated by the reader. Some values were lower than what was preferred, but that will be discussed in more detail in the section on further recommendations.

Extreme value testing A wide range of values were tested for the smoke attenuation model to ensure the values were correct. This form of validation allowed the team to identify models and assumptions that were grossly incorrect easily and allowed for the types of functions used to be narrowed down significantly. Linear functions could not be used for modelling losses as they inevitably go negative, whilst exponential functions decrease too rapidly to be considered for modelling smoke attenuation.

Face Validity This was a critical form of validation, as it gave the group more certainty in areas where expertise was limited. During the preliminary estimation of values used in the link budget, Prof. Speretta, a domain specialist in the field of command and data handling systems, was able to provide the team with great insight into the order of magnitude of values as well as the technical advice as to sizing antenna systems. Ronald van Gent, the tutor for this project, also provided valuable information contributing to the smoke attenuation model.

6.7 FURTHER RECOMMENDATIONS

After an extensive review of the research conducted, it was concluded that further work needs to be done to ensure that the communication system will perform up to standards in a real wildfire scenario.

First, more research will need to be conducted on wildfire behaviour to understand the operational boundaries of the drone better. Such behaviours differ for each environment, as factors such as fuel type and composition vary significantly between regions. From there, additional research must be done to quantify fire and smoke attenuation better. As previously stated, quality research on this domain is currently sparse, and there is no definitive relation between signal attenuation and fire and smoke properties.

Given the complexity of the phased array system, further research and simulations will need to be conducted to understand its limitations and capabilities better. Optimally, the system is constructed in real life to be tested to validate the simulation results. Further research is also needed to find a suitable radio interface device capable of supporting the extensive array of elements used for the phased array.

Connecting the antennas to the rest of the electronics system is also an area that needs further investigation. Experimental system testing would also be recommended for the link budget to validate the values being used. This is especially true for the noise figure and thermal noise power, as the team suspects that the values may have been underestimated.

Adaptive modulation techniques should also be investigated to improve the bandwidth usage of the system. By increasing modulation complexity when the signal margin is sufficiently high, higher data rates can be accommodated and high quality pictures and video can be transmitted.

To counter smoke attenuation, adaptive frequencies can also be employed to test which frequencies get the least attenuated to local conditions. This may require an re-evaluation of the existing antennas though, as the current patch antennas do not support a wide range of frequencies.

UAV DESIGN

The following chapter is dedicated to the design of the UAV, its physical systems and subsystems. The design process has been roughly subdivided into departments corresponding to different aspects and subsystems of the UAV. Because each subsystem is interconnected through input and output variables, an integration strategy must be devised. Additionally, an optimisation strategy is also necessary to ensure that the final result is not over-designed.

This chapter is structured as follows. First, in section 7.1, the design methodology is described. This involves a description of the iterative process that has been applied to size each of the UAV subsystems. Then, in section 7.2-subsection 7.9.5 the methods used for sizing each individual subsystem are described and discussed. Finally, in section 7.10 the results of the design process are presented, together with the sensitivity study on the input design parameters and the convergence study on the design parameters involved in the iteration process.

7.1 DESIGN METHODOLOGY & INTEGRATION

The design of a UAV from the ground up involves a wide variety of parameters, linked together by an equally wide variety of estimation functions. Moreover, several functions are interdependent, meaning the inputs/outputs involved are linked to each other in a cyclic manner.

This poses two constraints to the design process:

1. The integration between all of the estimation functions must be ensured, meaning that parameters and quantities must be consistently updated and carried over in between estimations and designs related to different subsystems; this ensures compatibility between the subsystems in the final design [100].
2. The parameters shall be optimised or iterated upon to ensure that the resulting UAV is not overdesigned. This means that no element in the design shall be excessively massive, costly or power-hungry unless this is strictly necessary in order to meet all system and subsystem requirements. In other words, an optimal design is the cheapest, lightest and least power-consuming configuration that can still fully achieve the mission objectives.

To overcome these two challenges, the design work for the UAV was subdivided into 10 different departments divided into two parallel lines of work based on the degree of interdependency between the inputs/outputs of one department and the rest of the design. In the first line of work those departments were included in which the design process can be carried out independently from the rest, meaning the only outputs that are contributing to the rest of the design are the Mass and Power estimations. These departments include Communications, Avionics & Electrical, and Ballistic Recovery System (BRS).

The second line of work includes those departments where the inputs and outputs involved are highly interlinked; these are Weight Estimation, Flight Performance, Aerodynamics, Stability & Control, Propulsion & Power, and Structures. For instance, weight estimation provides loading inputs for wing sizing in aerodynamics. Then, the selected wing geometry dictates the structural sizing, which in turn affects the weight estimation. For the sole reason of their high level of interdependency, these departments will be referred to as "*critical*", while the ones involved in the first line of work will be referred to as "*non-critical*". This division results in the design workflow showcased in Figure 26. Here, the non-critical departments carry out their respective design work independently, then their output is combined with a set of initial guesses to form the input for an *iterative process* that ties together the five critical subsystems.

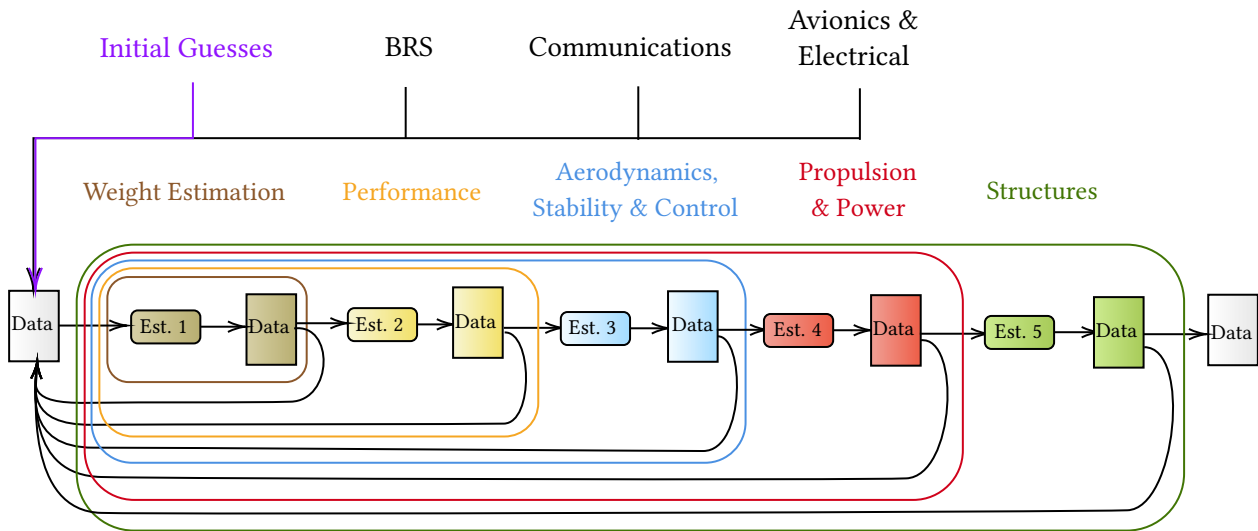


Figure 26: Design methodology. Please note that the Aerodynamics and the Stability & Control departments have been merged together.

More specifically, the iterative process is described as follows. The process starts at the innermost loop, the Weight Estimation. Each loop includes one or more estimation functions that output updated values for some design parameters. The estimation is repeated as long as the difference between the updated parameters and their previously known value (from a previous iteration or the initial values provided to the iterator) is above a threshold of 0.01%. This threshold ensures that the iterator stops when the error falls below a negligible threshold, thereby preventing unnecessary computations that do not significantly affect the outcome. When the error is found to have decreased below this threshold, the estimation moves to the next outer loop in the sequence. If, at any point, an estimation produces a parameter which differs from its predecessor by more than the threshold, the iteration restarts from the innermost loop.

The pseudo-code for the iterator is shown in Algorithm 27. \mathbf{D}_{init} is the dataset made of initial parameters, while \mathbf{D} is the working dataset that is changed at every iteration, and $\hat{\mathbf{D}}$ is the local copy of the updated dataset from the current loop. \mathcal{L} is the loss estimation function, which calculates the loss L according to Equation 11.

$$L = \mathcal{L}(\mathbf{D}, \hat{\mathbf{D}}) = \sum_{(x, \hat{x}) \in (\mathbf{D}, \hat{\mathbf{D}})} \left| \frac{x - \hat{x}}{x} \right| \quad (11)$$

Where L is initialised at infinity, and every loop is broken either if L has decreased below a certain ε threshold, or if the current loop repeats a number n_{max} of times. Lastly, the functions f, g, h, p and q in the algorithm are the modules containing all estimation functions for Weight, Performance, Aerodynamics, Propulsion and Structures, respectively.

Algorithm 1 Design iteration algorithm.

```

D ← Dinit
L ← ∞
while  $i \in [0, n_{max}] \wedge L > \varepsilon$  do:
    while  $j \in [0, n_{max}] \wedge L > \varepsilon$  do:
        while  $k \in [0, n_{max}] \wedge L > \varepsilon$  do:
            while  $u \in [0, n_{max}] \wedge L > \varepsilon$  do:
                while  $v \in [0, n_{max}] \wedge L > \varepsilon$  do:
                     $\hat{\mathbf{D}} \leftarrow f(\mathbf{D})$  #Weight estimation
                     $L \leftarrow \mathcal{L}(\hat{\mathbf{D}}, \mathbf{D})$ 
                     $\mathbf{D} \leftarrow \hat{\mathbf{D}}$ 
                end while
                 $\hat{\mathbf{D}} \leftarrow g(\mathbf{D})$  #Performance
                 $L \leftarrow \mathcal{L}(\hat{\mathbf{D}}, \mathbf{D})$ 
                 $\mathbf{D} \leftarrow \hat{\mathbf{D}}$ 
            end while
             $\hat{\mathbf{D}} \leftarrow h(\mathbf{D})$  #Aerodynamics
             $L \leftarrow \mathcal{L}(\hat{\mathbf{D}}, \mathbf{D})$ 
             $\mathbf{D} \leftarrow \hat{\mathbf{D}}$ 
        end while
         $\hat{\mathbf{D}} \leftarrow p(\mathbf{D})$  #Propulsion
         $L \leftarrow \mathcal{L}(\hat{\mathbf{D}}, \mathbf{D})$ 
         $\mathbf{D} \leftarrow \hat{\mathbf{D}}$ 
    end while
     $\hat{\mathbf{D}} \leftarrow q(\mathbf{D})$  #Structures
     $L \leftarrow \mathcal{L}(\hat{\mathbf{D}}, \mathbf{D})$ 
     $\mathbf{D} \leftarrow \hat{\mathbf{D}}$ 
end while
Dfinal ←  $\hat{\mathbf{D}}$ 
    
```

Figure 27: Pseudo-code for the iterator code.

A more detailed representation of the structure of the iterator (Figure 26) is provided by the N2 chart in Figure 28. This chart fully maps all interdependencies between the values used and shared by the critical departments. Note that the actual working of the methods used in each department is fully discussed in the other sections in this chapter.

Figure 28 features a 5×5 array at its core, with the five critical departments interconnected through their outputs and inputs, distributed respectively along the rows and columns of the array. It should be noted, however, that the chart shown is not a simple N2 chart. The variables visible in the chart are subdivided in *top-level inputs*, *iterables* and *top-level outputs*. Top level means that the variable is not iterated upon by the estimations, but is only given as an input or obtained as an output (not both); iterables, on the other hand, are both inputs and outputs of different departments. Top-level inputs and iterables need to be initialised with a guessed value, while top-level outputs do not. In the chart, the top-left corner contains a preliminary, Class II Weight Estimation that is not included in the loop, but is only used to generate initial guesses for part of the variables involved in the loops. The variables used by the Class II Weight Estimation are listed in the leftmost block. The remaining top level inputs are showcased in the bottom row, where they are subdivided by department according to the five different columns. Similarly, top-level outputs are shown on the rightmost column. Finally, all the variables found in the 5×5 core (Figure 28) are the iterables.

In conclusion, the aim of the iterative process is not only to ensure consistency between the different departments by fully integrating them with each other: by constantly updating mass, power, geometry and performance values, the iterator has the possibility to simulate the so called "snowball effect": a reduction in the mass of one subsystem alleviates the requirements on the other subsystems, which in turn allow the mass to be reduced even more. This means that, conventionally, even small savings can lead to rather large reductions in mass, power and cost of the overall system. Finally, by defining in advance how and through which parameters each department influences every other department, regardless of whether it is critical or not, each critical department can develop their estimations with foresight for the coming integration within the larger iterator code.

7.1.1 Verification & Validation Methods

The Iterator is verified and validated at the end of this chapter, in section 7.10. In addition, the code and calculations used in each department are verified using code tests, described in a Verification Table at the end of each Department section. An example of a Verification Table is included below.

Table 13: Example Verification Table

Block Tested	Inputs	Outputs	Tests	Confidence
Block 1	<block 1 inputs>	<block 1 outputs>	test description	high/low
Block 2				
...				

As can be seen in Table 13, the procedures used in each department are split into Blocks, corresponding to the functions used in the actual code. The code itself is not included for brevity, however it is available on request. Each block is assigned a row in the Verification table, then in the second and third columns the inputs and outputs are listed. The tests used for the verification of the block are described in the fourth column and finally, the fifth column indicates the Confidence Level. The Confidence level is used as a semi-subjective metric, given by the tester, of how much "confidence" the test gives in the assessment of the function/block in question. If a block passes a test that has High confidence, the code within the block is likely to be fully verified and to work as expected. This is the case, for example, for one-line code tests. If a test has Low confidence, more than one test might be required to ensure that the referenced code is verified and works as expected. This can be the case when a block contains calls to other functions or python modules. Please note that these labels are assigned based on the tester's opinion, and are only to be used as a rough indication for the test's reliability.

In the following sections, the methods used for sizing and designing each subsystem, regardless of whether it

is included in the iterator or not, are discussed by each department. The results of the iteration process are then showcased, discussed and verified with a convergence study and a sensitivity analysis, both included in section 7.10.

7.2 WEIGHT ESTIMATION

Before any vehicle analysis can take place, a class II mass estimation based on statistics must take place to provide an initial estimate of the vehicle size and mass that can then be passed through a more detailed system analysis to converge to a final design. Unfortunately due to a relatively young age of UAV technology and a great variety in types and sizes, there are few methods to accurately estimate drone mass. The approach presented below has been proposed by Gundlach [44] and is based on statistical mass estimation methods derived for manned sailplanes, which have been previously shown to be valid for fixed wing electrically propelled drones under the assumption that no wing sweep is present.

The main goal of class II weight estimation method is to estimate the MTOM as accurately as possible, thus including as many components as possible into the analysis.

$$MTOM = OEM + M_{payload} \quad (12)$$

$$OEM = M_{struct} + M_{LG} + M_{EPS} + M_{avionics} + M_{BRS} + M_{comms} \quad (13)$$

The specific commercial off the shelf components' masses used in the vehicle can simply be sourced from the manufacturers, however the structural mass requires statistical relationships presented below:

$$M_{struct} = M_{wing} + M_{fuselage} + M_{emp} \quad (14)$$

$$M_{wing} = 0.0038(n_{max}MTOM)^{1.06} AR^{0.38} S_{wing}^{0.25} (1 + \lambda)^{0.21} (t/c)^{0.14} \quad (15)$$

$$M_{fuselage} = 0.23845(3.28084l_{fuselage})^{0.3796} (2.20462M_{payload}n_{max})^{0.4863} (1.943844V_{cr})^{0.55} \quad (16)$$

$$M_{emp} = M_{tail} + 2M_{booms} \quad (17)$$

$$M_{tail} = 3.12S_{emp}t_{skin}\rho \quad (18)$$

$$M_{booms} = 0.14l_h M_{tail} \quad (19)$$

The electrical power system mass estimation depends mainly on the cruise conditions, with the power required in cruise having a significant impact.

$$M_{EPS} = M_{Gear} + M_{ESC} + M_{motor} + M_{battery} + M_{prop} \quad (20)$$

$$M_{Gear} = 0.00005443104P_{cruise} \quad (21)$$

$$M_{ESC} = 0.00003628736P_{cruise} \quad (22)$$

$$M_{prop} = 0.03N_{props}N_{blades}^{0.391}d_{prop}\frac{P_{cruise}}{(1000N_{props})^{0.782}} \quad (23)$$

Since most of the mass estimation methods have been derived in the imperial unit system, the aforementioned equations have been updated with the conversion factors to the SI system.

The aforementioned equations are used once for Class-II mass estimation, which is an input to the iterative design process. After further analysis, the required parameters flow out as the process outputs and are again inputted into the mass estimation to receive final detailed mass values.

7.2.1 Verification

The verification of the coding and functions used in the Weight Estimation department is done through the code tests showcased in the table below. The table structure is explained in subsection 7.1.1.

Table 14: Block Tests used for Weight Estimation Verification

Block Tested	Inputs	Outputs	Tests	Confidence
MTOM & OEM	$M_{wing}, M_{fuselage}, M_{emp}, M_{LG}, M_{EPS}, M_{avionics}, M_{BRS}, M_{comms}$	MTOM, OEM	Compare Outputs with hand calculations using Equations 12-14	High
Wing Mass Estimation	MTOM, n_{max} , AR, $S_w, \lambda, t_w, c_{root}$	M_{wing}	Compare output with hand calculation using Equation 15	High
Fuselage Mass Estimation	$l_{fuselage}, n_{max}, V_{cr}, M_{payload}$	$M_{fuselage}$	Compare output with hand calculation using Equation 16	High
Empennage Mass Estimation	$S_v, S_h, t_{skin}, \rho, l_h$	$M_{tail}, M_{booms}, M_{emp}$	Compare output with hand calculation using Equations 17-19	High
EPS Mass Estimation	$P_{cr}, N_{props}, N_{blades}, d_{prop}, M_{motor}, M_{battery}$	M_{EPS}	Compare output with hand calculation using Equations 20-23.	High

7.3 FLIGHT PERFORMANCE

Understanding the principles of flight performance is essential in the design and operation of UAVs. It determines the performance point of the UAVs during flight; defining the loads and capabilities they must be designed around. The design done here can largely constrain or free the design of other subsystems. This section analyses the key parameters influencing flight performance, subdivided into four areas: the loading diagram, wing and power loading, optimal cruise and optimal climb conditions. All the equations presented and analysed in this subsection outside of the loading diagram are sourced from or derived using Ruijgrok [101].

7.3.1 Subsystem Risks & Requirements

This subsystem is constrained by the requirements:

- **RSK-SYS-TEC-UNI-1.5:** The unit shall be able to cruise at 850[m] above sea level.
- **RSK-SYS-TEC-UNI-1.6:** The unit shall have a stall speed of 20[m/s] or less.
- **RSK-SYS-CON-SFT-1.2:** The system shall be able to operate in adverse weather conditions.

7.3.2 Assumptions

Certain assumptions have been made to analyse and design the flight performance of the UAV units. These are listed below, along with their identifiers and a short rationale expanding upon their validity and expected impact.

- ASMP-FLPR-01: The optimal cruise conditions of the UAV flight are defined to be steady-state flight conditions, excluding transient effects and dynamic manoeuvres that are not expected in nominal operations [101].
- ASMP-FLPR-02: Altitude and temperature variations adhere to the International Standard Atmosphere (ISA) model, staying consistent with international standards [102].
- ASMP-FLPR-03: The structurally limiting load factor in the manoeuvring envelope is assumed to be 3 in the loading diagram from Gundlach [44].
- ASMP-FLPR-04: The dive speed is assumed to be 1.25 times the cruise speed from Roskam [103].

7.3.3 Design

Wing and Power Loading

Wing loading (W/S) and power loading (W/P) are crucial parameters that represent the surface area required to support the weight of the UAV and the power necessary to propel the UAV. These parameters can be calculated using Equation 24 and Equation 28. For the maximum wing loading case, the limiting case occurs at stall.

$$\left(\frac{W}{S}\right)_{max} = \frac{1}{2}\rho V_{stall}^2 C_{Lmax} \quad (24)$$

Power loading (W/P) is critical for assessing the power-to-weight ratio required for different flight regimes. The equations for maximum power loading in cruise, rate of climb (ROC), and climb gradient are as follows:

$$\left(\frac{W}{P}\right)_{max_{cruise}} = \frac{\eta_{tot} \left(\frac{\rho}{\rho_0}\right)^{\frac{3}{4}}}{\frac{C_{D0}\rho V_{cruise}^3}{2\frac{W}{S}} + \frac{2\frac{W}{S}}{\pi A e \rho V_{cruise}}} \quad (25) \quad \left(\frac{W}{P}\right)_{max_{climb,ROC}} = \frac{\eta_{prop}}{ROC + \frac{\sqrt{2\frac{W}{S}}}{\sqrt{\rho_0} \left(\frac{C_{L,climb}^{3/2}}{C_{D,climb}}\right)}} \quad (26)$$

$$\left(\frac{W}{P}\right)_{max_{climb,gradient}} = \eta_{prop} \left(\frac{1}{\sqrt{\frac{W}{S}}} \left(\tan(\gamma) + \frac{C_{D,climb}}{C_{L,climb}} \right) \sqrt{\frac{2}{\rho_0 C_{L,climb}}} \right) \quad (27)$$

With the equations for wing loading (W/S) and power loading (W/P), a power vs wing loading diagram (Figure 29) can be constructed to illustrate the UAV's flight regime. From Figure 29, Equation 28 can be derived.

$$\left(\frac{W}{P}\right)_{max_{climb}} = \min \left(\frac{W}{P}_{climb,ROC}, \frac{W}{P}_{climb,gradient} \right) \quad (28)$$

The wing loading should ideally fall within the green area as illustrated in Figure 29. Therefore, a design

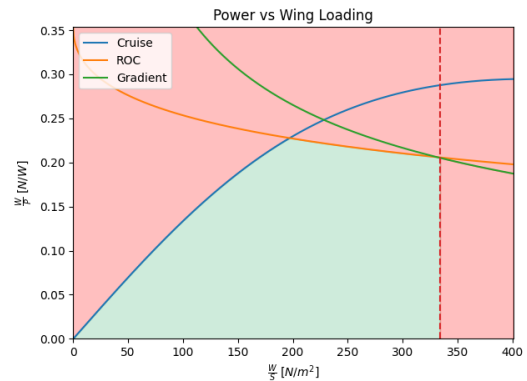


Figure 29: Power Loading vs Wing Loading of the Final Surveillance UAV

Cruise

Flying at optimal cruise conditions is essential for UAVs to maximise energy efficiency and extend their operational range. This approach minimises energy consumption by balancing speed and altitude, allowing UAVs to undertake longer missions and cover greater areas. The decision to optimise for the range was driven by an endurance requirement (**REQ-SYS-REC-UNI-1.2**). The specific cruise velocity and altitude are determined by operational requirements, namely **REQ-SYS-REC-UNI-1.1** and **REQ-SYS-REC-UNI-1.5**, ensuring the UAV operates within design parameters, thus enhancing safety and reliability.

The optimal lift coefficient and cruise velocity can be calculated using the following equations:

$$C_{L_{opt.}} = \sqrt{\pi C_{D_0} A R e} \quad (29) \quad V = \sqrt{\frac{W}{S} \frac{2}{\rho} \frac{1}{C_L}} \quad (30)$$

Due to the known cruise velocity, the optimal aspect ratio can be calculated accordingly. These calculations ensure that the UAV maintains the required minimum endurance (**REQ-SYS-REC-UNI-1.2**). During the cruise phase, the thrust required is equal to the drag.

Climb

During ascent, a UAV needs extra energy primarily to counteract gravitational force. The UAV must increase thrust from its engines or motors as it climbs to overcome gravity, which pulls it downwards. This additional energy is crucial for achieving altitude and maintaining a steady climbing rate, directly impacting the efficiency and endurance of UAV operations.

To reduce the energy needed for climbing, optimal flight speed can be determined using Equation 30 and Equation 31.

$$C_{L_{opt.}} = \sqrt{\pi C_{D_0} A R e} \quad (31)$$

With the optimal climb speed, the optimal rate of climb and climb angle can be obtained using Equation 32 while maintaining a constant equivalent airspeed (V_{EAS}). According to Ruijgrok [101], this method represents the most efficient climb strategy after using energy height. However, since this scenario does not involve a straight climb, it was concluded that the most suitable approach would be to keep V_{EAS} constant. Only straight climbing methods are allowed, as the UAV must be able to climb in any environment.

$$ROC = V \sin(\gamma) = \frac{ROC_s}{1 + \frac{V^2}{g} \frac{d\left(\sqrt{\frac{\rho_0}{\rho}}\right)}{dh}} \quad (32) \quad ROC_s = \frac{P_a - P_r}{W} = \frac{(T - D)V}{W} \quad (33)$$

Equation 34 was derived based on the relationships defined in the International Standard Atmosphere (ISA) [102]. Finally, the climb time can be calculated using Equation 35.

$$\frac{d\left(\sqrt{\frac{\rho_0}{\rho}}\right)}{dh} = 0.00004(1 - 22.558 \cdot 10^{-6} h)^{-3.12795} \quad (34)$$

$$t_{climb} = \int_0^h \frac{dh}{ROC} = \frac{h + \frac{V^2}{g} \left(\sqrt{\frac{\rho_0}{\rho}} - 1\right)}{ROC_s} \quad (35)$$

Loading Diagram

All necessary manoeuvres and gusts are considered when constructing the loading diagram. Following the approach of Gundlach [44], maximum bounds were placed on the manoeuvre load factors based on typical values for UAVs: $n_{\max} = 3$, $n_{\min} = -1$. The curves for the manoeuvres and gusts were then plotted based on the method outlined by Roskam [104].

The gust speeds typically used in aircraft design (see 14 CFR 23 [105] and 25 [106]) are not applicable in most part due to the relatively low flight altitude of 850[m]. Hence, specific data from wildfire operations collected by Kamran et. al. [107] was used, leading to an expected maximum gust loading of 1.5 [g]. The diagram can be constructed with this information, stall, cruise and dive speed information, and lift coefficient and wing loading (W/S) data.

The loading diagram (Figure 30) has been constructed with the values from subsection 7.10.1.

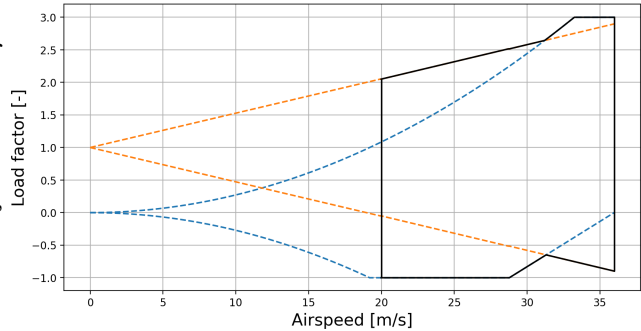


Figure 30: $V - n$ loading diagram

7.3.4 Verification & Validation

Verification of the methods and code used in the Flight Performance department has been performed through the block tests showcased in Table 15. The table structure is explained in subsection 7.1.1.

Table 15: Block Tests used for Performance Verification

Block Tested	Inputs	Outputs	Tests	Confidence
Wing Loading	$h, V_{stall}, C_{L_{max}}$	W/S	Compare output with manual calculation using Equation 24	High
Power Loading	$h, \eta, \eta_{prop}, C_{D_0}, C_{L_{cl}}, C_{D_{cl}}, V_{cl}, V_{cr}, \gamma, W/S, AR, e$	$(W/P)_{cr}, (W/P)_{cl}$	Compare outputs with manual calculation using Equations 25-28	High
Optimal Cruise	$AR, e, C_{D_0}, W/S$	$C_{L_{cr}}, C_{D_{cr}}$	Compare outputs with manual calculation using Equations 29, 30	High
Climb Time	V_{cl}, h, γ	ROC, t_{cl}	Compare outputs with manual calculation using Equation 31	High
Optimal Climb	$AR, e, C_{D_0}, W/S$	$C_{L_{climb}}, C_{D_{cl}}, V_{cl}$	Compare with manual calculation using Equations 32-35	High

7.3.5 Further Recommendations

For further work, a look should be taken at the loading diagram for different manoeuvres. With this a better understanding of the maximum load factor can be obtained.

7.4 AERODYNAMICS

The aerodynamic analysis addresses the fundamental aerodynamic forces and moments that affect UAVs in flight. It comprises an airfoil selection, wing geometry generation, and a lift and drag coefficient calculation. The analysis takes the variables found in Figure 28 as inputs and outputs. Note that there are no requirements and risks associated with this subsystem since the aerodynamic analysis only generates the wing geometry and calculates the aerodynamic coefficients. While no requirements are explicitly stated, the aerodynamic design should satisfy the wing and power loading from the flight performance design.

7.4.1 Assumptions

- ASMP-AERO-01: The units are flying in incompressible flow. Given the flight speed of 30 [m/s] at an altitude of 850 [m] from the midterm report [53], the Mach number is less than 0.3, allowing the assumption to hold since the density of the flow changes less than 5% [108].
- ASMP-AERO-02: The atmospheric parameters are calculated based on the international standard atmosphere; staying consistent with international standards [102].
- ASMP-AERO-03: The lift of the empennage is negligible. This is justified by estimating the lift of the horizontal tailplane at cruise. To do this, the deflection of the horizontal tailplane must be calculated. Given the deflection of the tailplane for moment equilibrium during cruise is expressed as:

$$\delta = \frac{-1}{C_{m\delta e}}(C_{m0} + C_{m\alpha}(\alpha - \alpha_0)) \quad (36)$$

where $C_{m\delta e}$ is the change at the moment coefficient of the UAV with respect to the change in the horizontal tailplane deflection, C_{m0} is the moment coefficient of the UAV at the angle of attack where there is no lift generated. $C_{m\alpha}$ is the change in moment coefficient with respect to the change in angle of attack, α is the angle of attack, and α_0 is the angle of attack where there is no lift generated [109]. Calculating the deflection of the control surface results in a deflection of $\delta = 0.188[deg]$. Examining the lift coefficient of the horizontal tailplane at this angle of attack in Xflr5 returns a lift coefficient of 0.014. Compared to the calculated lift of the entire uav: 0.658, the horizontal tailplane generates an additional lift of 2[%]. This contribution has been assumed to be negligible for the lift and lift-induced drag of the UAV.

- ASMP-AERO-04: The lift and drag generated by the tail booms are negligible. The tail boom has an estimated diameter between four and five centimetres and a length of 0.62 (section 7.8). This results in a drag coefficient of $1.75e - 5$. These contribute to the drag and lift coefficients by less than one percent. Therefore, this contribution has been assumed to be negligible.
- ASMP-AERO-05: The aerodynamic estimation methods by Roskam [110] are applicable to the design of the UAVs. Given the lack of designing guidelines for UAVs, the sizing methods established are assumed to be relevant to the design, following the precedent set in the book: Designing Unmanned Systems by Gundlach [44].
- ASMP-AERO-06: The cruise flight is simulated without sudden sideslip, roll, or pitching moments. For the simplicity of the analysis conditions, the UAV is assumed not to experience any sudden moments caused by turbulence or perturbations.

7.4.2 Design

This can be used in structural analysis to find the size of the wing and loads the UAV must sustain and in propulsion subsystem design to calculate the amount of drag it must counter. The single largest design choice related to this is the airfoil selection. Inspecting the $CL - \alpha$ curves of the airfoil options reveals that the NACA23015 airfoil provides the best solution due to its high maximum lift coefficient as seen in Figure 31. While the E216 generates a similar lift coefficient, the NACA 23015 is favoured due to the higher angle of attack at which stall is encountered, which allows for manoeuvres at higher angles of attack if necessary. Furthermore, The E216, with its lower thickness-to-chord ratio, is undesirable for its capability to sustain structural loads, analysed in section 7.8.

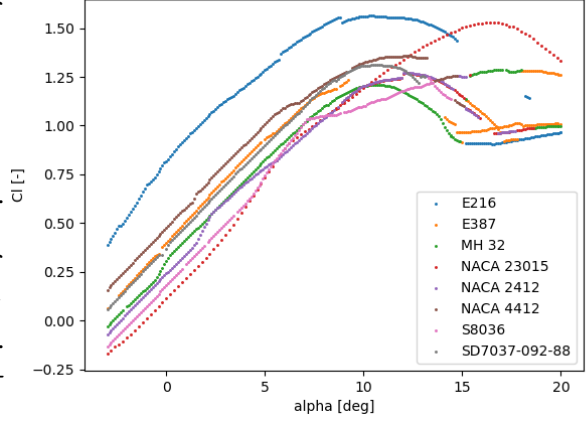


Figure 31: Airfoil Performance

With the airfoil selected, the geometry of the wing can be generated. Given the inputted wing area, aspect ratio from flight performance considerations, and quarter chord wing sweep, Equation 37 finds the span, mean aerodynamic chord, taper ratio, root, tip, and mean geometric chords. The quarter chord wing sweep is decided to be zero, because wing sweep is primarily employed to delay the onset of drag divergence at transonic flight [111].

$$\begin{aligned}
 b &= \sqrt{AR \cdot S}, \quad mac = S/b, \quad \lambda = 0.2(2 + \Lambda_{\frac{c}{4}} \frac{\pi}{180}) \\
 c_{root} &= \frac{2S}{b(1 + \lambda)}, \quad c_{tip} = \lambda c_{root}, \quad mgc = \frac{c_{root} + c_{tip}}{2} \\
 c(y) &= c_{root} - y(\tan(\Lambda_{LE}) + \tan(\Lambda_{TE}))
 \end{aligned} \tag{37}$$

Where λ is the wing taper ratio, $c(y)$ is the chord length at span location y , $\Lambda_{\frac{c}{4}}$ is the wing sweep at the quarter chord point, Λ_{LE} is the wing sweep at the leading edge, Λ_{TE} is the wing sweep at the trailing edge, AR is the aspect ratio, S is the wing surface area, b is the wing span, mac is the mean aerodynamic chord, mgc is the mean geometric chord, c_{root} is the root chord, c_{tip} is the tip chord. With the complete wing geometry, the lift coefficient of the entire UAV can be estimated as the linear equation in Equation 38, calculated with estimation methods defined by Roskam [110].

$$C_L = \alpha C_{L\alpha} + C_{L\alpha=0} \tag{38}$$

Where C_L represents the linear section of the lift curve, $C_{L\alpha}$ is the lift curve slope, and $C_{L\alpha=0}$ is the lift coefficient at zero angle of attack. $C_{L\alpha=0}$ of the UAV can be described as a function of the lift curve of the wing, which in turn is related to the lift curve of the airfoil. The lift curve characteristics of the wing in Equation 40 were found through analysing the wing in Xflr5.

$$C_{l,air\,foil} = C_{l\alpha,air\,foil}\alpha + C_{l0,air\,foil} \tag{39}$$

$$C_{l,wing} = C_{l\alpha,wing}\alpha + C_{l0,wing} \tag{40}$$

Furthermore, the lift curve of the UAV (Equation 38) can be found with Equation 41.

$$\begin{aligned}
 C_{L\alpha} &= K_{wf} C_{l\alpha,wing}, \quad C_{L\alpha=0} = (i_w - a_{L=0}) C_{L\alpha} \\
 C_{L_{max}} &= C_{L_{max,wing}}, \quad \alpha_{max_L} = \alpha_{max_L,wing} - i_w
 \end{aligned} \tag{41}$$

Note, K_{wf} is the wing-fuselage interference factor (see Equation 42), and i_w is the wing incidence angle, the angle of the wing chord line relative to the fuselage. Once the lift coefficient of the UAV has been calculated, the drag coefficient can be found:

$$K_{wf} = 1 + 0.025(df/b) - 0.25(df/b)^2 \quad (42)$$

$$C_D = C_{D0} + C_{DL} \quad (43)$$

where b is the wingspan, C_{D0} is the profile drag, which can be split into three components: the wing, the fuselage, and the empennage, as seen in Equation 44.

$$C_{D0} = C_{D0,wing} + C_{D0,fuselage} + C_{D0,emp} \quad (44)$$

Each component is expressed as seen in Equation 45, Equation 46, and Equation 47, from Roskam's estimation methods [110].

$$C_{D0,wing} = C_{fw}(1 + L_w(t/c) + 100(t/c)^4) \frac{S_{w_{wet}}}{S} \quad (45)$$

$$C_{D0,fuselage} = C_{ffuselage} \left(1 + \frac{60}{(lf/df)^3} + 0.0025(lf/df)\right) \frac{S_{fuselage_{wet}}}{S} + C_{D_{b_{fus}}} \quad (46)$$

$$C_{D0,emp} = C_{femp}(1 + L_{emp}(t/c) + 100(t/c)^4) \frac{S_{emp_{wet}}}{S} \quad (47)$$

Where: C_{fw} , $C_{ffuselage}$, C_{femp} is the turbulent flat plate friction coefficient of the wing, fuselage, and empennage, found from Figure 32. L_w , L_{emp} is the airfoil thickness location parameter of the wing and empennage, found from Figure 33a. $S_{w_{wet}}$ is the wetted surface area of the wing. S is the surface area of the wing. t/c is the thickness-to-chord ratio defined at the mean geometric chord of the wing or empennage. lf/df is the ratio of fuselage length and fuselage diameter. $S_{fuselage_{wet}}$ and $S_{emp_{wet}}$ is the wetted fuselage and empennage area. $C_{D_{b_{fus}}}$ is the fuselage base drag coefficient. The lift induced drag coefficient is calculated similarly by components in Equation 48.

$$C_{DL} = C_{DL,wing} + C_{DL,fuselage} + C_{DL,emp} \quad (48)$$

Where each of the components are calculated as seen in Equation 49, based on Roskam's estimations methods [110].

$$C_{DL,wing} = \frac{C_{L,wing}^2}{\pi A e}, \quad C_{DL,emp} = 0 \quad (49)$$

$$C_{DL,fuselage} = 2a^2 \frac{S_{b,fuselage}}{S} + \eta C_{dc} a^3 \frac{S_{plf,fuselage}}{S}$$

Note $C_{DL,emp}$ is zero due to ASMP-AERO-04 in subsection 7.4.1. A is the wing aspect ratio, e is the Oswald efficiency factor, $S_{b,fuselage}$ is the cross-sectional area of the end of the fuselage, a is the fuselage angle of attack, η is the ratio of the drag of a finite cylinder to the drag of an infinite cylinder (found in Figure 33b), C_{dc} is experimental steady-state cross-flow drag, and $S_{plf,fuselage}$ is the fuselage planform area.

Once finding the drag coefficient, the drag of the UAV can be found with Equation 50.

$$D = \frac{1}{2} \rho V^2 C_D S \quad (50)$$

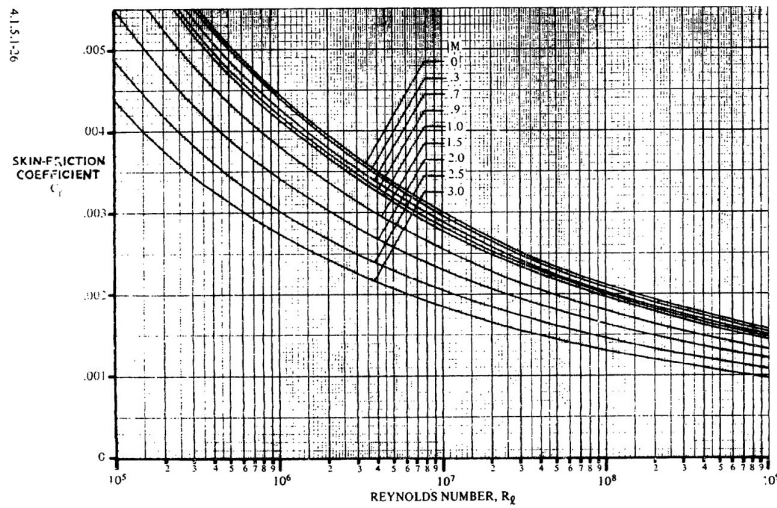


Figure 32: Turbulent flat plate friction coefficient

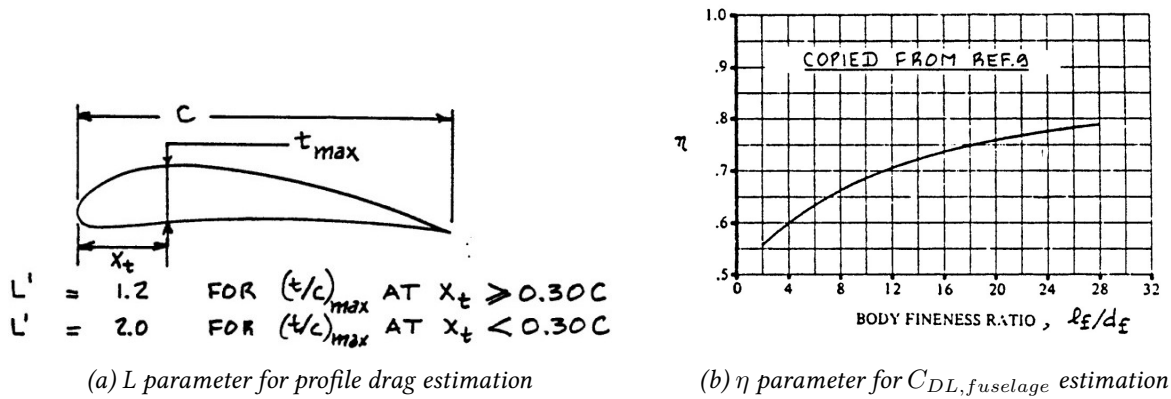


Figure 33: L and η parameters

7.4.3 Verification & Validation

The linearisation of the airfoil lift curve is verified by calculating the R-squared value of the fitted equation. In the analysis, the linearisation is performed for the airfoil and wing lift curve for angles of attack between $-3[deg]$ and $11[deg]$. This results in a satisfactory R-squared value of 0.981 and 0.992 $[-]$. Therefore, the linearised curve expressed in Equation 39 is justified.

Furthermore, the drag estimation of the aerodynamic analysis tool is verified using a preliminary computational fluid dynamic analysis conducted in Xflr5. It is strongly recommended that this verification be redone with a more reputable tool such as Ansys Fluent or Star CCM+. The fidelity of 3D CFD analysis using Xflr5 is dubious because it is not validated with wind tunnel data. This is supported by the documentation of the Xflr5 tool, which states: "All methods (of 3D CFD) tend to underestimate the drag" [112]. This tendency is reflected in the verification conducted. Nevertheless, a verification was attempted. The verification consists of simulating the UAV under cruise and climb conditions and comparing the drag coefficients from the analysis tool and Xflr5.

This results in Table 16, in which Xflr5 underestimates the drag coefficients by approximately 30 [%]. Given the lack of validation of Xflr5, this discrepancy cannot be correctly interpreted for now. This will be solved once a proper analysis is conducted with validated tools.

Table 16: Drag coefficients

	Xflr5	Analysis tool
Climb	0.037	0.055
Cruise	0.028	0.043

Table 17: Unit tests used for Aerodynamics Verification

Block Tested	Inputs	Outputs	Tests	Confidence
Wing Geometry	UAV object, S_{wing} , MTOM, AR, CL_{cr} , CL_{cl}	b_w , c_{root} , MAC, λ , b_h , c_h , S_h , MGC, l_h , $\Delta C_{l_{winglet}}$, $\Delta C_{l_{flaperons}}$	Manual calculation of ge- ometry using Equation 37	High
Wing Lift Calcula- tion	airfoil, wing_geometry, α	$C_{l_{wing}}(\alpha)$, $\alpha_{wing}(C_{L_{wing}})$	Comparison with CFD gen- erated lift curve	High
UAV Lift Calcula- tion	$C_{l_{wing}}(\alpha)$, $d_{fuselage}$, i_w , α	b_w , $CL(\alpha)$, $\alpha(C_L)$	Comparison with CFD gen- erated lift curve	Low
UAV Drag Esti- mation	MTOM, V , wing_geometry, fuselage_geometry,	α , CD_0 , CD_{climb}	CD_{cruise} , Comparison with manual calculation of drag with Equation 47, 46, 45, 49.	Low

7.4.4 Further Recommendations

It is recommended to reconduct the verification for the aerodynamics subsystem. The 30% discrepancy has been accepted as a conservative design for this report, but the source must be identified. This can be done with reliable CFD tools or wind tunnel testing.

7.5 STABILITY & CONTROL

Stability and control are essential for ensuring the safety and efficiency of a UAV. These attributes determine the aircraft's response to pilot inputs and external disturbances, maintaining a balanced and predictable flight path. The design of stability and control systems involves integrating various aerodynamic surfaces and control mechanisms that collectively influence the aircraft's behaviour and handling qualities. This section addresses two critical components integral to stability and control: the flaperons and empennage. Each of these elements will be examined in detail in their respective subsections, focusing on their design. This is then followed by an analysis of the dynamic stability of the unit, which will ensure that the unit returns to its equilibrium state after being disturbed.

7.5.1 Subsystem Risks & Requirements

The necessity to correctly design this subsystem stems directly from the risk **R-T-39** - Drone provides insufficient stability. As mentioned previously in Table 3, this risk, when not addressed can result in insufficient data quality, affecting the effectiveness of the system as a whole. For this reason, the stability and control system of the UAV unit was analysed and the lifting surfaces were sized, with the aim to fulfil the following system and subsystem requirements.

- **REQ-SYS-TEC-UNI-2** - The flight control & stability performance of the unit shall be able to sustain all flight operations.
 - **REQ-SYS-TEC-UNI-2.1**: The unit shall demonstrate longitudinal static stability.
 - **REQ-SYS-TEC-UNI-2.2**: The unit shall demonstrate longitudinal dynamic stability.
 - **REQ-SYS-TEC-UNI-2.3**: The unit shall maintain a longitudinal stability margin of 5%.
 - **REQ-SYS-TEC-UNI-2.4**: The unit shall demonstrate lateral static stability.
 - **REQ-SYS-TEC-UNI-2.5**: The unit shall demonstrate lateral dynamic stability.

7.5.2 Assumptions

To effectively analyse the stability of the UAV and design the control surfaces to meet the aforementioned requirements, assumptions were made. These concern the designing of the flaperons and the sizing of the empennage and are presented below together with their rationale. The following analysis of the dynamic stability of the unit and the assumptions used for the theory and calculations within it are presented further below in subsection 7.5.5.

ASMP-SBCS-01: Integrating flaps and ailerons into flaperons simplifies the overall design and reduces weight, implying benefits in aerodynamic efficiency and controls.

ASMP-SBCS-02: Flaperons provide the same functions as ailerons by mitigating adverse yaw and aileron reversal, thereby enhancing control stability and safety throughout various flight phases.

ASMP-SBCS-03: Flaperons serve the same purposes as flaps by increasing lift, enhancing flight efficiency, and reducing stall speeds.

ASMP-SBCS-04: The streamlined wing design of flaperons reduces weight, comparable to the combined use of flaps and ailerons, thereby significantly enhancing overall aircraft performance.

ASMP-SBCS-05: The aircraft operates under steady flight conditions, assuming stable aerodynamic forces and moments.

ASMP-SBCS-06: Linear relationships between the lift coefficient, moment coefficients, and control surface deflections are assumed, indicating small deviations from steady-state conditions.

ASMP-SBCS-07: The aircraft maintains static stability, ensuring that disturbances induce forces that return the aircraft to its original flight condition without requiring any intervention.

ASMP-SBCS-08: Compressibility effects are disregarded because the flight speeds remain below Mach 0.3, thereby eliminating supersonic airflow over the wing.

ASMP-SBCS-09: There is no downwash effect on the tail from the wing due to the usage of an inverted U-boom-shaped tail. Therefore, tail performance and stability are oversimplified.

ASMP-SBCS-10: The weight of the battery remains constant regardless of its state of charge. This simplifies the calculations related to the aircraft's centre of gravity.

Furthermore, many assumptions were considered in the dynamic stability analysis, to allow for a simplified yet valid analysis of the flight responses of the aircraft. These assumptions are listed further below in Methodology, together with the theory that stems from them.

In the following sections, these assumptions are used to design and size this subsystem with the aim of fulfilling the previously mentioned requirements.

7.5.3 Design

Flaperons

Flaperons combine the roles of flaps and ailerons. They enhance aircraft control and efficiency by mitigating the drawbacks associated with conventional ailerons. Traditional ailerons often induce adverse yaw and aileron reversal, thereby complicating control mechanisms and compromising safety. Flaperons address these issues by reducing adverse yaw and minimising aileron reversal by preventing wing twists. Moreover, flaperons enhance aerodynamic efficiency by consolidating control surfaces, leading to a reduction in weight and the streamlining of wing design [103].

Flaps and ailerons are essential aerodynamic components situated on an aircraft's wings, each fulfilling distinct

yet vital roles. Flaps, also referred to as High Lift Devices (HLDs), primarily serve to augment lift during take-off and landing, thereby enhancing flight efficiency. Extending the flaps increases the wing's curvature, improving its lift characteristics at lower speeds and facilitating aircraft operation at reduced velocities during take-off and landing. Additionally, flaps aid in lowering the stall speed, a critical factor during crucial flight phases. Various flap types are depicted in Figure 34.

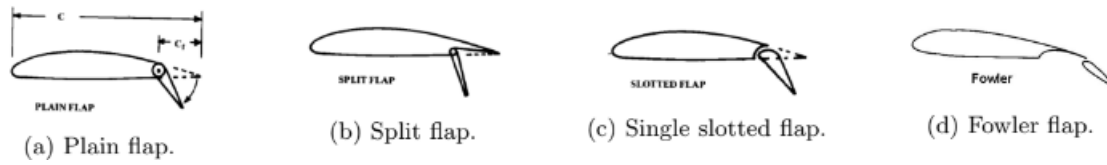


Figure 34: Different Flap Types [103].

In contrast, ailerons are positioned on the wings' trailing edges and are chiefly responsible for governing the aircraft's roll along its longitudinal axis, a fundamental aspect for stability and executing turns. Ailerons modify the lift on each wing through deflection in opposing directions, inducing the aircraft to roll towards the wing with decreased lift. This rolling motion enables efficient banking and directional changes, with precise aileron control being imperative during manoeuvres and landings in crosswinds.

Positioning the flaperon between 10% and 90% of the half-wing span optimises aerodynamic efficiency and enhances control and safety [113]. This strategic placement effectively combines the functionalities of flaps and ailerons, resulting in streamlined wing design, reduced weight, and superior roll control, thereby enhancing overall aircraft performance.

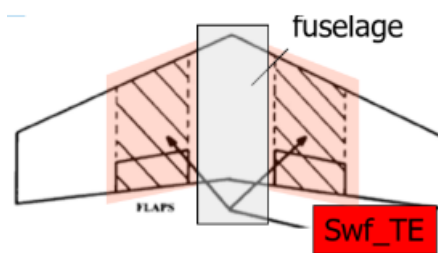
The flap's functionality will be examined first for the flaperon's analysis. Subsequently, the aileron functionality will be assessed. The increase in maximum lift ($\Delta C_{L_{max}}$) can be calculated using Equation 51 [103].

$$\Delta C_{L_{max}} = 0.9 \Delta C_{l_{max}} \frac{S_{wf}}{S} \cos(\Lambda_{hingeline}) \quad (51) \quad \frac{S_{wf}}{S} = (2 - (1 - \lambda)(\eta_1 + \eta_0)) \frac{\eta_1 - \eta_0}{1 + \lambda} \quad (52)$$

Here, $\Delta C_{l_{max}}$ represents the increase in maximum lift for the specific type of flap used, with the value provided in Figure 35a for different HLDs. The definition of the referenced wing flapped surface (S_{wf}) is illustrated in Figure 35b. The parameters η_0 and η_1 in Equation 52 denote the starting and ending positions of the flaps as a percentage of the half wing span.

High lift device	$\Delta C_{l_{max}}$ when fully deployed
TE devices (flaps)	
Plain and split	0.9
Slotted	1.3
Fowler	$1.3 \cdot c'/c$
Double slotted	$1.6 \cdot c'/c$
Triple slotted	$1.9 \cdot c'/c$
LE devices	
Fixed slot	0.2
Leading edge flap	0.3
Kruger flap	0.3
Slat	$0.4 \cdot c'/c$

(a) $\Delta C_{l_{max}}$ For Different HLDs. [103]



(b) Referenced Wing Flapped Surface.

Figure 35: Wing flap surface area and change in maximum lift coefficient.

The choice was made to employ a plain flap due to its simplicity of manufacture and its lightweight nature. Details regarding the geometry definitions can be located in Figure 36. Here, $c_f = \frac{c_f}{c} \cdot c$, where, as per Roskam [103], for a plain flap, the relationship $\frac{c_f}{c} = 0.25$ is applicable. Moreover, the maximum flap deflection (β) is set at 60° .

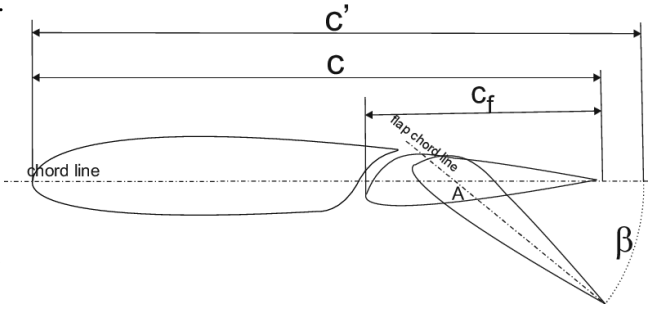


Figure 36: Flap Geometry Definitions

The only additional geometric flap parameters that need to be known are the flap span, and the deployed chord length (c'). These can be determined using Equation 53 and Equation 54

$$b_f = b(\eta_1 - \eta_0) \quad (53) \quad \frac{c'}{c} = 1 - \frac{c_f}{c} (1 - \cos(\beta)) \quad (54)$$

According to Roskam [103], the roll rate due to aileron deflections can be calculated using Equation 55.

$$p = -\frac{C_{L\delta_a}}{C_{L_p}} \delta_a \left(\frac{2V}{b} \right) \quad (55)$$

In the given formula, δ_a denotes the mean aileron deflection, expressed as $\delta_a = \frac{1}{2} (\delta_{a_{up}} + \delta_{a_{down}})$, where, as per Roskam [103], $\delta_{a_{down}} = \frac{3}{4} \delta_{a_{up}}$. Determining the maximum roll rate at a specific velocity involves utilising the equivalence between the maximum flap deflection angle and the maximum aileron deflection angle. Finally, the two aileron control derivatives (aileron effectiveness $C_{L\delta_a}$ and roll damping C_{L_p}) are defined in Equation 56 and Equation 57.

$$C_{L\delta_a} = \frac{2C_{l_\alpha} \tau}{S_{ref} b} \int_{b_0}^{b_1} y \cdot c(y) dy \quad (56) \quad C_{L_p} = -\frac{4(C_{l_\alpha} + C_{d_0})}{S_{ref} b} \int_0^{\frac{b}{2}} y^2 \cdot c(y) dy \quad (57)$$

Here, b_0 and b_1 are defined as $\eta_0 \cdot \frac{b}{2}$ and $\eta_1 \cdot \frac{b}{2}$.

With the aileron chord being equal to the flap chord, the data presented in Figure 37 indicates that for $\frac{c_f}{c} = 0.25$, a value of $\tau \approx 0.46$ can be obtained.

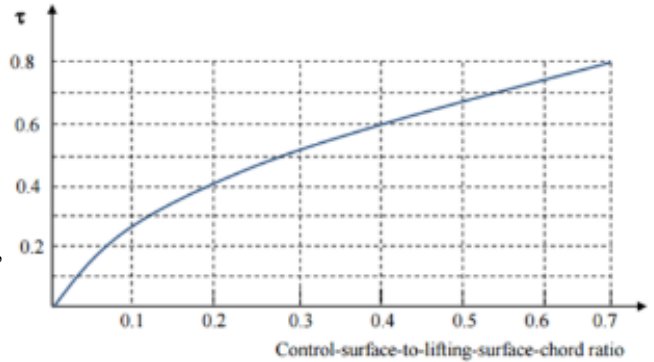


Figure 37: Aileron Effectiveness as a function of aileron chord to wing chord ratio.

Empennage

The empennage is an aircraft component that is pivotal in stability, control, and overall performance. It serves several essential functions vital for safe and efficient flight. Firstly, the empennage provides stability to the aircraft, ensuring it maintains a steady and level flight path. This is achieved through the vertical stabiliser, which prevents side-to-side motion, known as yaw, and the horizontal stabiliser, which counters up-and-down movement, known as pitch. Together, these stabilising surfaces help maintain the aircraft's equilibrium during flight. Additionally, the empennage houses control surfaces such as the rudder and elevator, which are integral

for manoeuvring the aircraft. The rudder controls yaw, allowing the aircraft to turn left or right, while the elevator controls pitch, enabling ascent or descent [114]. It is noteworthy that the chosen airfoil for the empennage is the NACA0015.

Two important parameters for the empennage are the horizontal and vertical tail volume; these are defined in equations 58 and 59, where, according to Kundu [113], a good value for V_v is 0.07. Also crucial are the aspect ratios for both the vertical and horizontal stabilisers, which, as stated by Scholz [115], are approximately 0.95 and 4.0, respectively.

$$V_h = \frac{S_h l_h}{S \bar{c}} \quad (58) \quad V_v = \frac{S_v l_h}{S b} \quad (59)$$

The primary function of the horizontal stabiliser is to maintain the stability of the UAV, ensuring it flies in a straight path. The centre of gravity (CG) and the neutral point (NP) are two critical parameters for achieving this stability. The UAV will exhibit neutral stability if the centre of gravity coincides with the neutral point. For a stable UAV configuration, it is necessary for the centre of gravity to be positioned such that $x_{cg} < x_{np}$. These parameters can be accurately determined using the two equations below. All the equations and figures for the horizontal stabiliser are sourced from Oliviero, et al. [114] and Torenbeek [116]

$$x_{cg} = \frac{\sum x_{cg} m}{\sum m} \quad (60) \quad x_{np} = \frac{\left(\frac{dC_L}{d\alpha}\right)_h}{\left(\frac{dC_L}{d\alpha}\right)} V_h \quad (61)$$

Furthermore, the horizontal stabiliser counteracts any pitching moments caused by aerodynamic forces or changes in thrust, ensuring the UAV maintains its intended flight path. Proper alignment of the centre of gravity and the neutral point is essential not only for stability but also for the overall aerodynamic efficiency of the UAV. Therefore, the horizontal stabiliser's design and positioning are critical to the UAV's overall performance and control. By utilising Equation 62 it is ensured that the horizontal stabiliser is sufficiently sized to maintain stability. Proper implementation of these parameters is essential for achieving optimal performance and safe operation of the UAV.

$$\frac{S_h}{S} = \frac{\frac{\Delta x_{cg}}{\bar{c}} - \frac{x_{np} - x_{cg}}{\bar{c}} - \frac{C_{mac}}{C_{Lmax}}}{\left(\frac{C_{L\alpha}}{C_{L\alpha A-h}} \left(1 - \frac{d\epsilon}{d\alpha}\right) - \frac{C_{Lh}}{C_{Lmax}}\right) \left(\frac{V_h}{V}\right)^2 \frac{l_h}{\bar{c}}} = \frac{-\frac{x_{np} - x_{cg}}{\bar{c}} - \frac{C_{mac}}{C_{Lmax}}}{\left(\frac{C_{L\alpha}}{C_{L\alpha A-h}} - \frac{C_{Lh}}{C_{Lmax}}\right) \frac{l_h}{\bar{c}}} \quad (62)$$

The use of electrical power does not affect the centre of gravity (CG). Thus, the change in the CG position, denoted as Δx_{cg} , is zero. Stability is maintained with an inverted U-shaped boom, ensuring that $\frac{d\epsilon}{d\alpha} \approx 0$. Moreover, the ratio of the horizontal tail volume to the total volume, $\frac{V_h}{V}$, equals one. This configuration is crucial for maintaining aerodynamic stability and efficiency. According to Roskam [103], l_h is defined as $x_{cg} - x_{cg_h} \approx 0.6l_f$. The total moment coefficient of the aircraft around the aerodynamic centre (C_{mac}) is defined as the sum of the moment coefficients around the aerodynamic centres of the wing, flaps, and fuselage, assuming the empennage does not influence this moment. These can be calculated using Equation 63, Equation 64, and Equation 65.

$$C_{mac_w} = C_{m0_{airfoil}} \left(\frac{AR_w \cos^2\left(\Lambda_{\frac{\bar{c}}{2}}\right)}{AR_w + 2 \cos\left(\Lambda_{\frac{\bar{c}}{2}}\right)} \right) = C_{m0_{airfoil}} \left(\frac{AR_w}{AR_w + 2} \right) \quad (63)$$

$$C_{mac_{flaps}} = \Delta C_{m_{\frac{\bar{c}}{4}}} - C_L \left(0.25 - \frac{x_{acw}}{\bar{c}} \right) \quad (64)$$

$$C_{m_{acfus}} = -1.8 \left(1 - \frac{2.5b_f}{l_f} \right) \frac{\pi b_f h_f l_f}{4S\bar{c}} \frac{C_{L_0}}{C_{L_{\alpha A-h}}} \quad (65)$$

The change in the moment around the quarter chord of the wing due to the flaps can be found using the following equation aerodynamic centre's position, a critical parameter in aircraft design, is calculated using Equation 66.

$$\frac{x_{acw}}{c} = \frac{\left(\frac{dC_m}{d\alpha} \right)_{x_0}}{C_D \sin(\alpha) - C_L \cos(\alpha)} + \frac{x_0}{c} \quad (66)$$

Furthermore, to analyse the effect of flap deployment on the wing's aerodynamic characteristics, the change in moment around the wing's quarter chord can be determined using Equation 67. This provides insights into how alterations in flap settings influence the aircraft's stability and control. Such analyses are vital in optimising aircraft performance and ensuring safe and efficient operation.

$$\begin{aligned} \Delta C_{m_{\frac{c}{4}}} &= \mu_2 \left(-\mu_1 \Delta C_{L_{max}} \frac{c'}{c} - \left(C_L + \Delta C_{L_{max}} \left(1 - \frac{S_{wf}}{S} \right) \frac{1}{8} \frac{c'}{c} \left(\frac{c'}{c} - 1 \right) \right) \right) \\ &+ 0.7 \frac{AR_w^2}{AR_w + 2} \mu_3 \Delta C_{L_{max}} \tan(\Lambda_{\frac{c}{4}}) \\ &= \mu_2 \left(-\mu_1 \Delta C_{L_{max}} \frac{c'}{c} - \left(C_L + \Delta C_{L_{max}} \left(1 - \frac{S_{wf}}{S} \right) \frac{1}{8} \frac{c'}{c} \left(\frac{c'}{c} - 1 \right) \right) \right) \end{aligned} \quad (67)$$

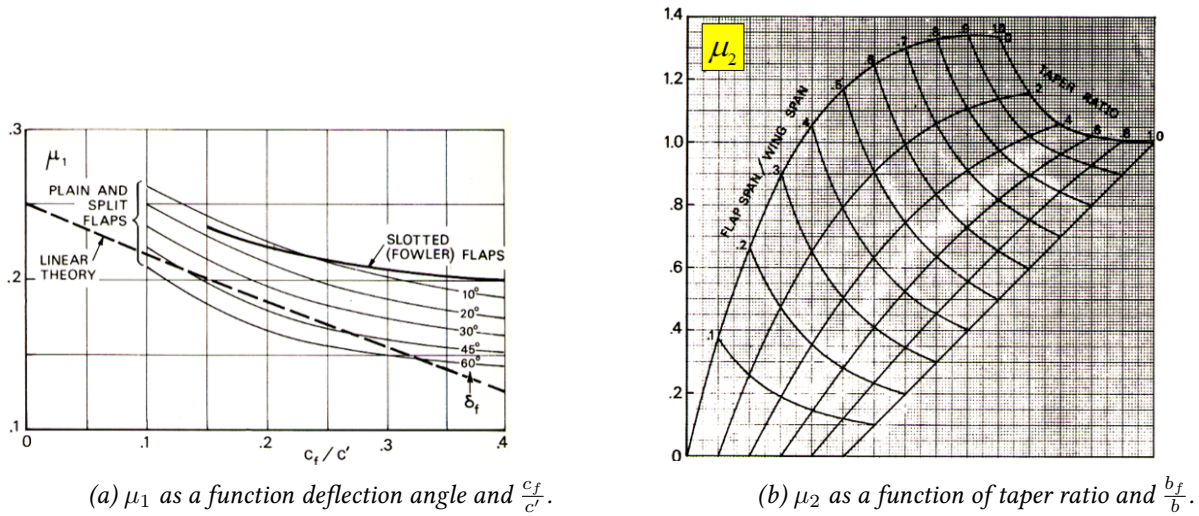


Figure 38: The effect of flap deployment on the wing's aerodynamic characteristics.

As illustrated in Figures 1 and 2, the coefficients μ_1 and μ_2 exhibit dependence on both flap geometry and deflection angle. Consequently, a decision was made to optimise for maximum flap deflection. A linear regression analysis was performed to achieve this, resulting in Equation 68 and Equation 69 for μ_1 and μ_2 respectively.

$$\mu_1 \approx -2.037 \left(\frac{c_f}{c'} \right)^3 + 3.637 \left(\frac{c_f}{c'} \right)^2 - 1.258 \left(\frac{c_f}{c'} \right) + 0.307 \quad (68)$$

$$\mu_2 \approx 0.084 \left(\frac{b_f}{b} \right)^3 - 0.999 \left(\frac{b_f}{b} \right)^2 + 2.293 \left(\frac{b_f}{b} \right) - 0.409 \quad (69)$$

The rate of change of the lift coefficient concerning the angle of attack for both the wind and tail-less aircraft can be determined utilising Equation 70 and Equation 71. Conversely, the lift coefficient of the tail can be computed employing Equation 72.

$$C_{L_{\alpha_{A-H}}} = C_{L_{\alpha_w}} \left(1 + 2.15 \frac{b_f}{b} \right) \frac{S_{net}}{S} + \frac{\pi b_f^2}{2 S} \quad (70)$$

$$C_{L_{\alpha_w}} = \frac{2\pi}{2 + \sqrt{4 + \bar{c} \left(\frac{\beta}{\eta} \right)^2 \left(1 + \tan^2(\Lambda_{\frac{\bar{c}}{2}}) \beta^2 \right)}} = \frac{\pi}{2} \quad (71)$$

Compressibility effects may be disregarded as the maximum flight speed remains below Mach 0.3. Consequently, supersonic airflow over the wing is absent, leading to an approximate value of 0 for β .

$$C_{L_h} = -0.35 AR_h^{\frac{1}{3}} \quad (72)$$

Finally, according to Roskam [103], the chord lengths of the elevator and rudder can be calculated using Equation 73 and Equation 74.

$$c_e = \frac{c_e}{c} c \quad (73) \quad c_r = \frac{c_r}{c} c \quad (74)$$

In this context, Roskam [103] specifies that $\frac{c_e}{c} = 0.4$ and $\frac{c_r}{c} = 0.4$.

7.5.4 Verification

Verification of the methods and code used in the Flight Performance department has been performed through the block tests showcased in Table 18. The table structure is explained in subsection 7.1.1.

Table 18: Block Tests used for Control Verification

Block Tested	Inputs	Outputs	Tests	Confidence
block name	<i>inputs</i>	<i>outputs</i>	Test Method	High/Low
Flaperons	$\Lambda_{hingeline}, \lambda, \eta_1, \eta_2, b, \beta_{max}, C_{l_{\alpha}}, C_{d_0}$	$\Delta C_{L_{max}}, P_{max}, b_f$	Verifies that the returned maximum roll rate and $\Delta C_{L_{max}}$ are correct	High
Empennage	$X_{cg}, X_{np}, \bar{c}, C_{mac}, C_{L_{max}}, C_{L_{\alpha}}, C_{L_{\alpha_{A-h}}}, C_{L_h}, C_{m_0}, AR_w, C_L, b_f, C_{L_0}, h_f, l_f, C_{m_{\alpha}}, C_D, AR_h$	$V_h, V_v, l_h, b_h, b_v, c_h, c_v, c_e, c_r$	Verifies that the values obtained for the empennage are correct	Low
X_{cg}	$X_{cg_{wing-group}}, X_{cg_{fus.-group}}, M_{wing-group}, M_{fus.-group}$	X_{cg}	Verifies that the centre of gravity is calculated correctly	High
X_{ac}	$C_{L_{\alpha_h}}, C_{L_{\alpha}}, V_h$	X_{np}	Verifies that the neutral point is calculated correctly	High

7.5.5 Dynamic Stability Analysis

Finally, once the control surfaces of the unit have been designed, the dynamic stability of the vehicle was analysed, to ensure that **REQ-SYS-TEC-UNI-2.2** and **REQ-SYS-TEC-UNI-2.5** were met.

Dynamic stability is a critical aspect of aircraft design that ensures the aircraft can return to its equilibrium state after being disturbed. This section delves into the dynamic stability analysis of the UAV in cruise. Unlike static stability, which addresses the aircraft's initial tendency to return to equilibrium, dynamic stability examines the time-dependent response, capturing how the aircraft behaves over time following a disturbance.

This section first outlines the mathematical framework and assumptions in Methodology. Then, the acquisition of stability and control derivatives is discussed in Parameter Identification. This has proven to be difficult in absence of windtunnel or CFD data, therefore empirical methods are utilised. After which the dynamic stability of an aircraft is analysed in Results.

Methodology

In conducting the dynamic stability analysis of the UAV, several key assumptions were made to simplify the mathematical modeling and ensure tractability. These assumptions are based on [117]:

- **Body centered axis system is used:** A right handed axis system is used where the x axis is defined pointing forwards through the nose of the UAV, y is pointing towards the right wing, and the z axis points down.
- **Vehicle is a rigid body:** The UAV is assumed to behave as a rigid body.
- **Vehicle's mass is constant:** The mass of the UAV is assumed to remain constant during flight.
- **Earth is non-rotating:** For the purposes of this analysis, the rotation of the Earth is neglected, simplifying the equations of motion.
- **Earth is flat:** The curvature of the Earth is neglected, assuming a flat Earth model which simplifies the calculations of gravitational effects and the aircraft's motion over the Earth's surface.
- **Gravity field is constant:** The gravitational field is assumed to be uniform and constant, providing a consistent downward force throughout the UAV's flight envelope.
- **Aircraft has a plane of symmetry and the body-fixed reference frame is chosen such that I_{xy} and I_{yz} are zero:** The UAV is assumed to have a symmetric design, allowing the simplification that the products of inertia I_{xy} and I_{yz} are zero, thereby simplifying the inertial matrix.
- **Effects of rotating masses are neglected:** The gyroscopic effects of rotating masses, such as engines or propellers, are neglected in this analysis.
- **The resultant thrust vector lies in the symmetry plane and thus only affects the aerodynamic forces X , Z and the aerodynamic moment M :** It is assumed that the thrust vector remains within the plane of symmetry of the UAV, influencing only the longitudinal aerodynamic forces and moments.

These assumptions lead to the following equations of motion shown in Equation 75 to Equation 80:

$$F_x = -W \sin \theta + X = m(\dot{u} + qw - rv) \quad (75)$$

$$F_y = W \cos \theta \sin \varphi + Y = m(\dot{v} + ru - pw) \quad (76)$$

$$F_z = W \cos \theta \cos \varphi + Z = m(\dot{w} + pv - qu) \quad (77)$$

$$\mathcal{M}_x = L = I_{xx}\dot{p} + (I_{zz} - I_{yy})qr - I_{xz}(\dot{r} + pq) \quad (78)$$

$$\mathcal{M}_y = M = I_{yy}\dot{q} + (I_{xx} - I_{zz})rp + I_{xz}(p^2 - r^2) \quad (79)$$

$$\mathcal{M}_z = N = I_{zz}\dot{r} + (I_{yy} - I_{xx})pq - I_{xz}(\dot{p} - rq) \quad (80)$$

In these equations of motion, $W = MTOW * g$ is the UAV weight, which is constant. X, Y & Z are the forces along the axis. $u, v, w, \dot{u}, \dot{v}$ & \dot{w} are the velocities and accelerations in the x, y and z directions. $\phi, \theta, \beta, p, q$ & r are the angles and angular velocities around the axis.

To simplify the analysis, the equations of motion are linearised around the equilibrium flight condition following the methodology presented in [117]. This allows for neglecting the higher-order nonlinear terms and the complicated dynamic coupling effects. The linearisation process involves assuming small perturbations around the equilibrium state, leading to the small angle assumption where $\sin(\theta) \approx \theta$ and $\cos(\theta) \approx 1$. Additionally, the symmetric and asymmetric motions of the aircraft are assumed to be uncoupled. Therefore, the equations are split into both cases. Now, all equations of motion can be linearised to Equation 81 and Equation 82:

Symmetric motion

$$\begin{aligned} -W \cos \theta_0 \theta + X_u u + X_w w + X_q q + X_{\delta_e} \delta_e + X_{\delta_t} \delta_t &= m \dot{u} \\ -W \sin \theta_0 \theta + Z_u u + Z_w w + Z_{\dot{w}} \dot{w} + Z_q q + Z_{\delta_e} \delta_e + Z_{\delta_t} \delta_t &= m(\dot{w} - qV) \\ M_u u + M_w w + M_{\dot{w}} \dot{w} + M_q q + M_{\delta_e} \delta_e + M_{\delta_t} \delta_t &= I_{yy} \dot{q} \end{aligned} \quad (81)$$

Asymmetric motion

$$\begin{aligned} W \cos \theta_0 \varphi + Y_v v + Y_{\dot{v}} \dot{v} + Y_p p + Y_r r + Y_{\delta_a} \delta_a + Y_{\delta_r} \delta_r &= m(\dot{v} + rV) \\ L_v v + L_p p + L_r r + L_{\delta_a} \delta_a + L_{\delta_r} \delta_r &= I_{xx} \dot{p} - I_{xz} \dot{r} \\ N_v v + N_{\dot{v}} \dot{v} + N_p p + N_r r + N_{\delta_a} \delta_a + N_{\delta_r} \delta_r &= I_{zz} \dot{r} - I_{xz} \dot{p} \end{aligned} \quad (82)$$

Lastly, the equations are non-dimensionalised by dividing by $\frac{1}{2} \rho V^2 S$ and the moments are also divided by their characteristic length (chord in symmetric motions, wingspan in asymmetric motions). Full derivations can be found in [117].

Symmetric motion

$$\begin{bmatrix} C_{x_u} - 2\mu_c D_c & C_{x_\alpha} & C_{z_0} & C_{x_q} \\ C_{z_u} & C_{z_\alpha} + (C_{z_{\dot{\alpha}}} - 2\mu_c) D_c & -C_{x_0} & C_{z_q} + 2\mu_c \\ 0 & 0 & -D_c & 1 \\ C_{m_u} & C_{m_\alpha} + C_{m_{\dot{\alpha}}} D_c & 0 & C_{m_q} - 2\mu_c K_{yy}^2 D_c \end{bmatrix} \begin{bmatrix} \hat{u} \\ \alpha \\ \theta \\ \frac{q\bar{c}}{V} \end{bmatrix} = \begin{bmatrix} -C_{x_\delta} \\ -C_{z_\delta} \\ 0 \\ -C_{m_\delta} \end{bmatrix} \delta_e \quad (83)$$

Asymmetric motion

$$\begin{bmatrix} C_Y + (C_Y - 2\mu_b) D_b & C_L & C_Y & C_Y - 4\mu_b \\ 0 & -\frac{1}{2} D_b & 1 & 0 \\ C_\ell & 0 & C_\ell - 4\mu_b K_{xx}^2 D_b & C_\ell + 4\mu_b K_{xz} D_b \\ C_n + C_n D_b & 0 & C_n + 4\mu_b K_{xz} D_b & C_n - 4\mu_b K_{zz}^2 D_b \end{bmatrix} \begin{bmatrix} \beta \\ \varphi \\ \frac{pb}{2V} \\ \frac{rb}{2V} \end{bmatrix} = \begin{bmatrix} -C_y \\ 0 \\ -C_\ell \\ -C_n \end{bmatrix} \delta_a + \begin{bmatrix} -C_\delta \\ 0 \\ -C_\ell \\ -C_n \end{bmatrix} \delta_r \quad (84)$$

Equation 83 and Equation 84 are utilised to analyse system behaviour. Because of the uncertainty in parameters, which will be discussed in Parameter Identification, analysis is performed on randomly initialised datasets, which fall within the bounds provided. This will allow not only for assessing stability of the system, it will also help identify sensitive parameters, thereby providing a sensitivity analysis for stability. The results are discussed in Results.

Parameter Identification

In order to fully define the system, all parameters have to be defined. Dimensional data and weight are known for the UAV as found in chapter 7, however most stability derivatives are yet to be determined. All previously known parameters are shown in Table 19

Table 19: Known parameters after the design of the UAV

Parameter	Value	Parameter	Value	Parameter	Value
h [m]	850	S_h [m ²]	0.12	V_h/V [-]	1
V [m/s]	30	l_h [m]	0.45	α_0 [deg]	-2.09
m [kg]	12.41	mac [m]	0.25	C_{D0} [-]	0.005
e [-]	0.66	b [m]	2.44	$C_{L\alpha}$ [deg ⁻¹]	0.1110
S [m ²]	0.3646	b_h [m]	0.65	$C_{m\alpha}$ [rad ⁻¹]	-0.0032

In determining the other stability derivatives it was found that no method of parameter determination available is reliable for further analysis. XFLR provides some stability derivatives, but these were not found to be representative when compared to statistical data. [118] encountered a similar problem, where they found the semi-empirical data to be too unreliable for further analysis. Therefore they had to physically test their drone. Because computational fluid dynamics simulations or test facilities are unavailable, the approach is taken that stability derivative ranges are constructed based on experimental data of other drones [118, 119] and physical interpretations of the derivatives [117]. All stability derivatives and their ranges are shown in Table 20

Table 20: Stability and Control derivatives

Parameter	Value with upper and lower bound	Parameter	Value with upper and lower bound	Parameter	Value with upper and lower bound
C_{X_u}	-0.1 to -0.05	C_{Z_u}	-0.1 to -0.05	C_{Y_β}	-0.7 to -0.2
C_{X_α}	0.05 to 0.2	C_{Z_α}	-6 to -4.5	C_{Y_p}	-0.1 to 0
C_{X_q}	-0.1 to -0.01	C_{Z_q}	-5 to -2	C_{Y_r}	0.1 to 0.3
$C_{X_{\delta_e}}$	-0.1 to -0.01	$C_{Z_{\delta_e}}$	-0.05 to 0	C_{l_β}	-0.15 to -0.05
C_{m_u}	0	$C_{m_\alpha}^1$	-0.032	C_{l_p}	-0.6 to -0.2
C_{m_q}	-20 to -5	$C_{m_{\delta_e}}$	-2 to -0.5	C_{l_r}	-0.1 to 0.1
$C_{Y_{\delta_a}}$	-0.02 to 0.02	C_{n_β}	0.05 to 0.2	$C_{n_{\delta_r}}$	0.05 to 0.2
$C_{l_{\delta_a}}$	-0.3 to -0.05	C_{n_p}	-0.1 to -0.02	$C_{Y_{\delta_r}}$	0.1 to 0.5
$C_{n_{\delta_a}}$	-0.1 to 0.1	C_{n_r}	-0.5 to -0.05	$C_{l_{\delta_r}}$	-0.1 to 0.1

Results

Because of the uncertainty in the stability and control derivatives (Table 20), a definite system response and characteristic eigenvalues cannot be given. However, the behaviour of the total set of coefficients can be analysed. To achieve this, 2500 sets of randomly generated parameters are initialised in the provided ranges. For each, the eigenmodes and the stability are assessed, using a previously validated dynamic stability model by E. Abbenhuis et al. [120]. An example of converging stability plots for both symmetric and asymmetric perturbations is shown in Figure 39.

It can be seen that for dynamically stable UAVs, all states converge back to the equilibrium condition. The analysis showed that $93.28 \pm 0.41\%$ of the runs converged with confidence. Additionally, all experiments showed stable phugoids, short periods, Dutch rolls and aperiodic rolls. Only the spiral was divergent in the unstable runs. These eigenmodes will be analysed.

¹This value is already determined

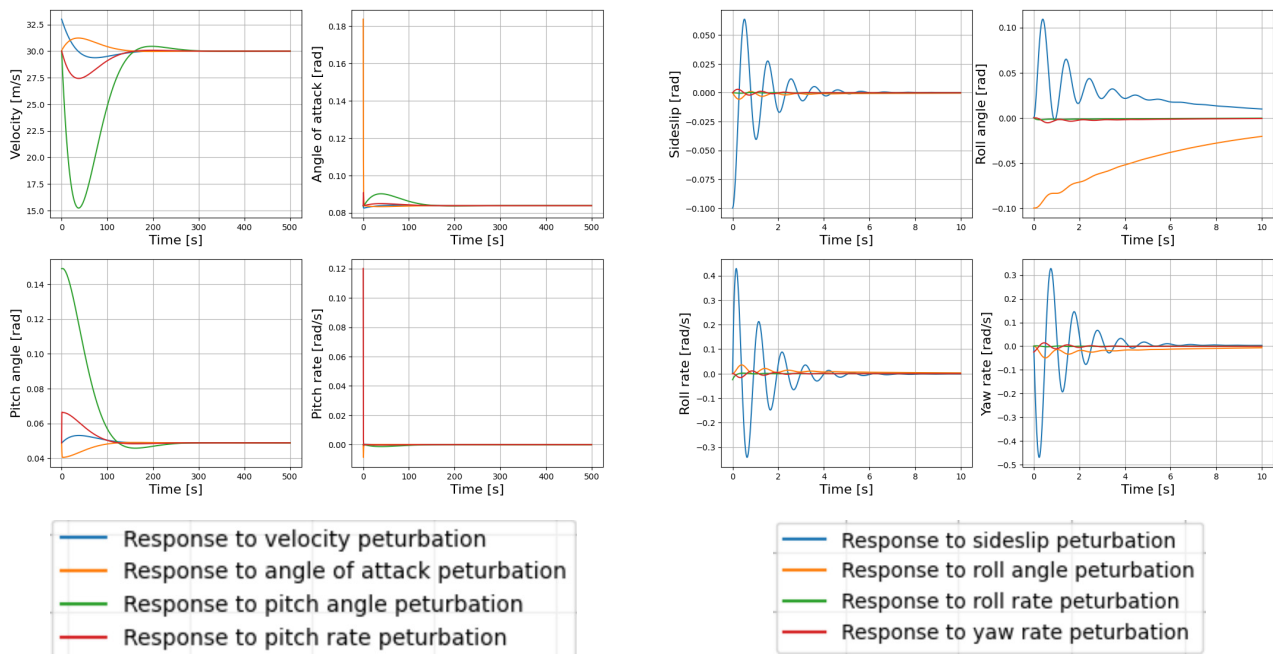


Figure 39: Model Initial Responses. Seed=5

Symmetric Eigenmotions The eigenvalue plot for the phugoid mode, shown on the left, depicts a cluster of eigenvalues distributed around the real part of approximately $-1.5 \cdot 10^{-4}$. The eigenvalues have small imaginary parts, indicating the presence of oscillatory behaviour. The real parts of the eigenvalues are negative, suggesting that the phugoid mode is stable. The clustering around $-1.5 \cdot 10^{-4}$ indicates that the mode is lightly damped, as the negative real part is relatively small. The imaginary parts, around ± 0.0002 , indicate that the phugoid oscillations have a low frequency. This is characteristic of the phugoid mode, which typically involves long-period oscillations. The small damping ratio suggests that these oscillations will decay slowly over time, making the UAV exhibit persistent, albeit diminishing, altitude changes following a disturbance.

The eigenvalue plot for the short period mode, shown on the right, displays a more complex distribution with a wider range of real parts, extending from approximately $-5 \cdot 10^{-2}$ to $-2 \cdot 10^{-1}$. The imaginary parts are also present but relatively small compared to the real ones. The real parts are more negative than those of the phugoid mode, indicating that the short-period mode is more heavily damped. The damping ratios range from 0.85 to 1. The range of real parts suggests a varying degree of damping across different cases. The imaginary parts indicate the presence of oscillations, but the relatively large negative real parts suggest that these oscillations will decay rapidly. The short-period mode primarily involves rapid changes in the angle of attack and pitch rate, reflecting the UAV's quick response to control inputs and disturbances in pitch. The high damping indicates that these oscillations will quickly settle back to equilibrium, providing a stable and responsive pitch behaviour.

Table 21: Ranges of Key Dynamic Stability Parameters for Symmetric Motions

Parameter	Minimum Value	Maximum Value	Median Value
Phugoid Period [s]	100	400	207
Phugoid Damping Ratio [-]	0.2	1.0	0.52
Short Period Half Amplitude Time [s]	0.10	0.35	0.20
Short Period Damping Ratio [-]	0.85	1.0	0.97

Asymmetric Eigenmotions The eigenvalue plot for the Dutch roll mode, shown on the left in Figure 41, depicts a cluster of eigenvalues with both real and imaginary parts. The real parts range from approximately $-2.4 \cdot 10^{-1}$ to $-0.3 \cdot 10^{-1}$, and the imaginary parts span from ± 0.6 . The predominantly negative real parts indicate stability in the Dutch roll mode, with moderate damping suggested by clustering around $-1.0 \cdot 10^{-1}$.

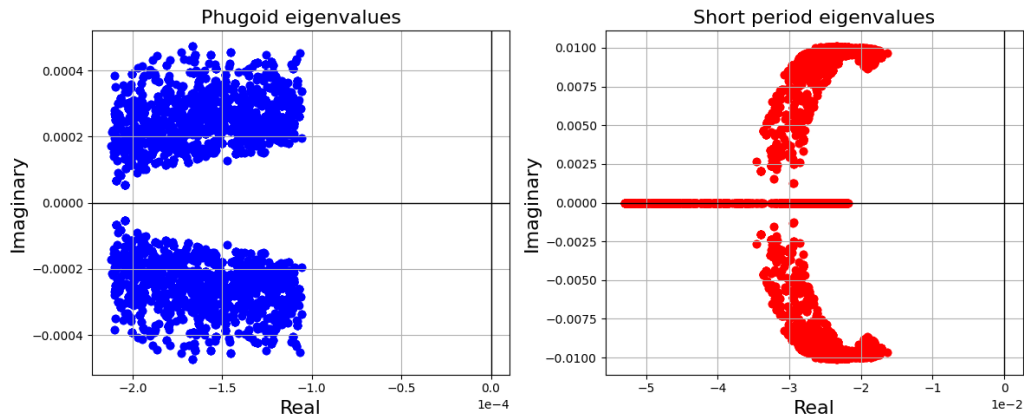


Figure 40: Symmetric eigenvalues of randomly initialised UAVs. $n=2500$

The imaginary parts, ranging from ± 0.2 to 0.6 indicate high-frequency oscillations, characteristic of coupled yaw and roll motions. The period of the Dutch roll is between 0.8 and 2.2 seconds, skewed towards the lower end, indicating a relatively fast oscillatory behaviour.

The spiral mode, shown in the centre, displays eigenvalues that are entirely real, ranging from approximately $-8.0 \cdot 10^{-2}$ to 0 . The predominantly negative real parts, close to zero, indicate that the spiral mode is marginally stable or very slowly divergent. Table 22 shows that the spiral has a wide range of possible half amplitude times. This is because UAVs with negative spiral eigenvalues close to 0 , have a very slowly converging spiral. However, the distribution is skewed towards lower half amplitude times with a median of 4.8 . The zero imaginary parts confirm the non-oscillatory nature of this mode, suggesting that any divergence would be very slow and the UAV would maintain a steady bank angle.

The eigenvalue plot for the aperiodic roll mode, shown on the right, displays real eigenvalues ranging from approximately -1.1 to -0.35 . The negative real parts indicate stable behaviour with strong damping, leading to rapid decay of the roll motion. No imaginary parts confirm the non-oscillatory nature of this mode, indicating quick stabilisation of roll disturbances.

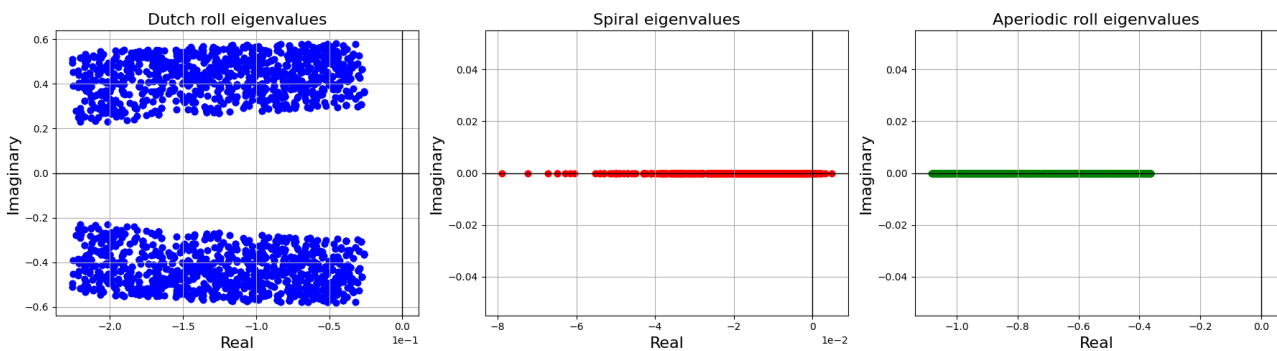


Figure 41: Asymmetric eigenvalues of randomly initialised UAVs. $n=2500$

Table 22: Ranges of Key Dynamic Stability Parameters for Asymmetric Motions

Parameter	Minimum Value	Maximum Value	Median Value
Dutch Roll Period [s]	0.88	2.23	1.13
Dutch Roll Damping Ratio [-]	0.06	0.69	0.26
Spiral Half Amplitude Time [s]	0.71	1768	4.80
Aperiodic Roll Half Amplitude Time [s]	0.05	0.16	0.08

Coefficient Importance To investigate the factors contributing to asymmetric instability in various UAV configurations, a random forest classifier was trained using a dataset of stability derivatives, labelled whether the

configuration converges. The classifier achieved an accuracy of 96%, indicating its effectiveness in distinguishing between stable and unstable configurations. By analysing the feature importance scores generated by the classifier, the most critical stability derivatives influencing UAV stability were identified.

The random forest classifier's feature importance analysis revealed that certain coefficients significantly impact the UAV's asymmetric stability. These include derivatives related to lateral and directional stability such as C_{n_r} (yawing moment derivative with respect to yaw rate), C_{l_p} (rolling moment derivative with respect to roll rate), and C_{n_β} (yawing moment derivative with respect to sideslip angle). High feature importance scores for these coefficients suggest that they contribute the most to the lateral instability of the UAV. Understanding the influence of these key stability derivatives allows for targeted modifications and optimisations in the UAV design to enhance stability. Further research and design of this problem is covered in the future recommendations.

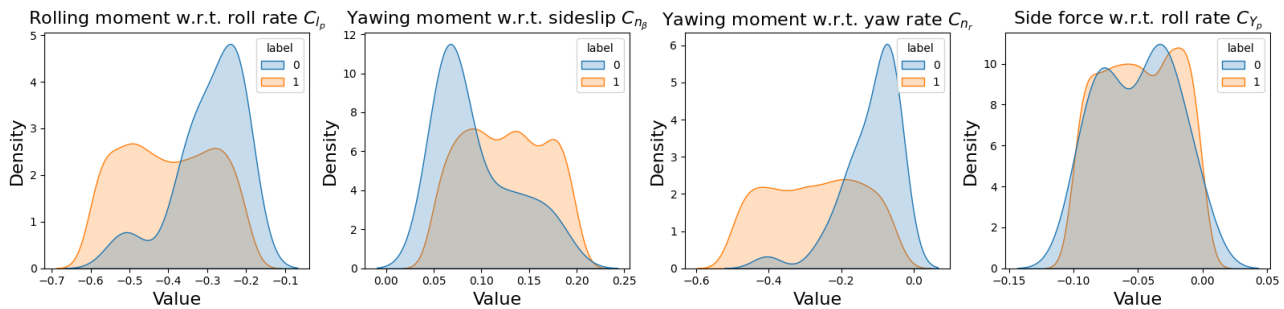


Figure 42: Distributions of Stability Derivatives for Stable and Unstable UAV Configurations

Verification & Validation

As the performance of the dynamic stability models have been previously verified and validated [120], this section will not repeat these procedures, but rather discuss the applicability of the model to this analysis. The conclusion of E. Abbenhuis et al. [120] was that the model can predict the dynamic responses of aircraft accurately, but that one must be aware of the limitations of the model. The main limitations stem from the amount of assumptions made in the model. These assumptions are identical to those made in Methodology. Additionally, the model was designed for the Cessna Citation 520 and not for UAVs. However, none of the assumptions made restrict the applicability to UAVs, and all stability and control coefficients are measurable too, justifying the use of the dynamic model.

Further Recommendations

In the future, the dynamic analysis should be refined. As stated in Parameter Identification, the absence of wind tunnel data and CFD simulations limit the accuracy of the control derivatives. It is suggested that these parameters are refined by first simulating the model in CFD and, after a scale model has been built, test it in a wind tunnel. Secondly, regarding the possible instability in the spiral eigenmode of the drones, two approaches can be considered to address the identified instability issues. Firstly, it may be acceptable to acknowledge that the UAV might exhibit instability in the spiral mode, which can be mitigated using a flight computer to actively manage and correct the flight path. Alternatively, future improvements to the UAV design could be implemented to push the stability derivative values into a more stable range. These improvements might include adjustments to the aerodynamic surfaces, alterations to the mass distribution, or enhancements in control surface effectiveness.

7.6 PROPULSION & POWER

The primary function of the Power & Propulsion subsystem is to ensure that the UAV has a constant and sufficient power supply to ensure the continuous functioning of the payload and the propulsion source. This follows from the system requirement **REQ-SYS-TEC-UNI-1**, which sets some of the performance requirements

for the propulsion subsystem. Four key components were sized to achieve the performance needed: the propeller, the electric motor, the Electronic Speed Controller and the battery. With the wide availability on the market of many different models and types for each, the main factors that were prioritised and optimised were the efficiency and weight of all the components so that the total unit weight could be minimised and the required performance achieved.

7.6.1 Subsystem Risks & Requirements

From the risk analysis, there were three main risks surrounding the propulsion subsystem that were identified, plus another risk that while not directly related to the subsystem, is still heavily reliant on it. The first ones being **R-T-36** - Run out of fuel, **R-T-38** - Drone provides insufficient power to payload and **R-T-47** - Fuel system catches fire. All of these risks posed a high level of threat, in particular the first and third, as they both would cause the possible loss of the unit, with the last posing a threat to the surrounding environment as well. Furthermore, **R-T-18** - System is too heavy to lift, which is a risk indirectly affected by the propulsion subsystem. While this risk concerns the UAV unit as a whole, it is particularly relevant for the propulsion subsystem, as the battery represents the single most massive element within the drone. Sizing it correctly will thus be essential to ensure the risk is avoided. To ensure that these risks are thus mitigated properly while still achieving the required performance, the following were the subsystem requirements that this subsystem aimed to comply with.

The following technical requirements were set to ensure that the UAV units perform as required.

- **REQ-SYS-TEC-UNI-1.1:** The propulsion system of the units shall be able to achieve a ground speed of no less than 30 m/s.
- **REQ-SYS-TEC-UNI-1.2:** The propulsion system of the unit shall achieve an endurance of no less than 6 hrs.
- **REQ-SYS-TEC-UNI-1.3:** The propulsion system of the units shall be able to operate nominally at temperatures between 0 and 45 °C.
- **REQ-SYS-TEC-UNI-1.4:** The battery shall provide a maximum power of 1 kW.

However, the following requirements were also followed when designing the propulsion subsystem to ensure that the units can perform their operations within the mission constraints the stakeholders gave.

- **REQ-SYS-CON-SFT-2.2:** The system units shall be lighter than 25 kg.
- **REQ-SYS-CON-SFT-3.1:** All flammable substances within the units shall be encased in protective casings.
- **REQ-SYS-CON-SFT-3.2:** The protective casings of flammable substances shall withstand loads during all landing cases.
- **REQ-SYS-CON-SFT-3.3:** The protective casings of flammable substances shall contain the substance in case of ignition.
- **REQ-SYS-CON-SFT-3.4:** All toxic substances within the units shall be encased in protective casings.
- **REQ-SYS-CON-SFT-3.5:** The protective casing of damaging substances shall withstand loads during all operational cases.
- **REQ-SYS-CON-STB-1.3:** The system operations shall not produce more than 93.8 kg of CO₂ per year per system.

The first of these requirements is set to ensure that a single operator can safely lift and move the UAV on its own, reducing the number of operators required to run the whole swarm, which stems from **R-T-18** mentioned

earlier. The following five safety requirements are set to ensure no leak or exposure to flammable and toxic substances at any point, especially in an emergency landing. These requirements stem directly from **R-T-47** and are important. Finally, the last requirement is one of the main findings of the sustainability strategy generated in the Midterm Report [53], and it critically impacts the choice of propulsion type.

7.6.2 Assumptions

To properly calculate the required performance of the propulsion subsystem and find the most suitable components from the current market, a few assumptions had to be made.

ASMP-PROP-01: The battery was based on the Amprius lithium-ion cell. This cell was used as it provides 450Wh/kg [121] of energy density while still being an independently validated product[122] and has already been used in known projects, including the Airbus HAPS project Zephyr[123]. To safely size the battery pack, only 80% of the energy is discharged at each cycle, as recommended by Amprius, and a packing ratio of 0.84 was used. This value was taken as it represents the state-of-the-art of battery packing in recent years. Despite some packing ratios reaching values of up to 90% recently, a more conservative value of 84% was taken as a reference, which was based on the one found in the Samsung 60Ah prismatic lithium-ion cell produced in 2013 [124]. Once both the depth of discharge constraint and the packing ratio factor are taken into account, the effective energy efficiency of the full battery is reduced to 302.4 Wh/kg. This value is much lower than the starting energy density, but it represents a much more realistic value for the current technology that is available on the market, ensuring that **REQ-SYS-CON-RSC-2.3** is still being complied with.

ASMP-PROP-02: The motor efficiency was taken from a database that tested the motor on a static stand. The use of a static test has no effect on the values used, as the only data taken from it were the mechanical power (torque x rot. speed) and the electrical value (voltage x current). Both of these measurements are not affected by the correction from static to dynamic testing, as that one only affects the effective thrust.[125]

ASMP-PROP-03: For the climb drag, the air density was maintained the same as for the cruise drag. This was done to simplify the calculations for the thrust requirements, as integrating the air density with altitude would only have a marginal effect on the result, given that the air density at cruise height is only 92% of the air density at sea level. Furthermore, this only affects the climb condition of the flight, which was calculated to be only between 3 and 5% of the total energy requirement of the flight.

ASMP-PROP-04: For the propulsion type, only electric batteries and motors are considered. No combustion engines, including those with SAF fuels, have been considered. This decision was taken to comply with **REQ-SYS-CON-STB-1.3**, as it was calculated that a full 25-unit swarm would emit an estimated 502.75 [kg] of CO₂ per year [53]. This overshoots the maximum emissions set by the sustainability strategy by a large margin and thus fully eliminates the possibility of using this energy source.

Propeller Selection

The first component to size was the propeller. The central aspect that was considered is the output thrust that it is expected to produce in both cruise and climbing flights. Like all other propulsion design choices, the propeller selection is part of the design iterative loop, so all input variables used were initially kept in variable form.

Preliminary analysis of the propeller types that would be considered indicated that for the expected cruise speed of 0.10 Mach, a two-blade propeller was the most suitable [126]. Furthermore, given the small variation in operating speeds and altitudes, the team opted for a simpler, lighter fixed-pitch propeller. Finally, following Equation 85, the maximum value for the product of D and n, the blade diameter and rotational velocity of the propeller, can be calculated. By adhering to this equation, the propeller tips do not reach speeds above 0.72 Mach, which is deemed to be the point where compressibility effects cause a drastic increase in noise and efficiency loss.

$$D \cdot n = \frac{\sqrt{(0.72 \cdot a)^2 - V^2}}{\pi} \quad (85)$$

For a cruise altitude of 850 [m] above sea level and a cruise velocity of 30 [m/s], then $D \cdot n > 76.64$. Thus, the lower bound for the advance ratio, J , can be calculated and then used for the preliminary propeller search.

$$J = \frac{V}{D \cdot n} = 0.3914 \quad (86)$$

With the minimum advance ratio known, a suitable set of propellers was sought. The main criteria considered were the advance ratio, the thrust produced and at which airspeed, to ensure that the propeller could achieve the thrust required at both cruise and climb conditions. The propeller database provided by *APC Propellers*² included many different propellers, with different diameters and pitches, with many options that fit with the preliminary J , thrust and velocity values. Once reformatted and included within the design iterative loop, given the two different flight conditions, all the propellers that could achieve both conditions were considered, and the one with the highest efficiency at cruise was selected. This was chosen due to the cruise accounting for the majority of the energy spent throughout one sortie, as previously mentioned in ASMP-PROP-03. Once the design was iterated, the final propeller model that was selected for the 8.8 N of thrust required for a cruise was the APC Propeller 13.5x13.5. With a propeller efficiency of 81% at 5817 RPM, it generated the required force to propel the UAV with the highest efficiency out of the propellers in the considered database.

Motor & ESC Selection

The following components to size were the electric motor and its ESC. Similarly to the method used to find a suitable propeller, a database with performance parameters for different motors was found and analysed³. This time the main criteria that were used to select the most suitable motor were the electric efficiency of the motor and ESC combination for the specific mechanical power required to spin the previously selected propeller at the required RPM. Given the substantial weight of some of the motors in the database, this criteria was also minimised. Once again, both the climb and the cruise phases were considered, so to ensure that the motor could indeed perform adequately in both flight conditions. The cruise phase was then used again as the optimisation point, for the same reason as in the propeller selection. After the design iteration was performed, the required electrical power required for the cruise phase was calculated to be 382.59 W, while the one for the climb phase was 898.67 W. All the motors from the database that fit these requirements were then plotted in Figure 44, showcasing the electrical efficiency at cruise and the motor mass of each option.

From Figure 44, the best motor and ESC choice for optimal efficiency at cruise is shown as a red cross, that being the 5015 IPE V3.0 motor with the AMPX 60A 5-14S ESC by Mad Components⁴ shown in Figure 43. This motor and ESC combination gave the highest electric efficiency for the required mechanical power. When producing the cruise power of 253.64 W, the motor runs with an efficiency of 81.8%, which in combination with the 13.5x13.5 propeller, gives a total cruise propulsion efficiency of 66.3%. With a total propulsion mass of 361 grams, the combination of propeller, motor and ESC was deemed to be the most suitable for the expected cruise parameters for the UAV unit. On top of this, the 5015 IPE V3.0 motor is rated to work nominally in temperatures of up to 103[°C] [127], adhering with **REQ-SYS-TEC-UNI-1.3**.

²Performance Data - APC Propellers. URL: <https://www.apcprop.com/technical-information/performance-data/>

³Tyto Robotics Database. URL: <https://database.tytorobotics.com/tests>

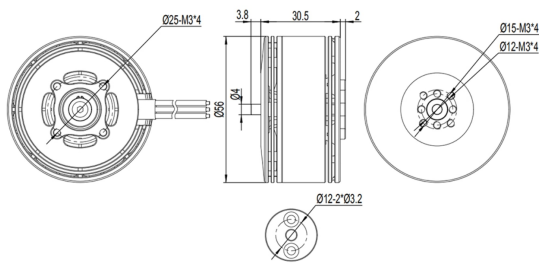


Figure 43: Technical Drawing of the 5015 IPE V3.0 motor [127]

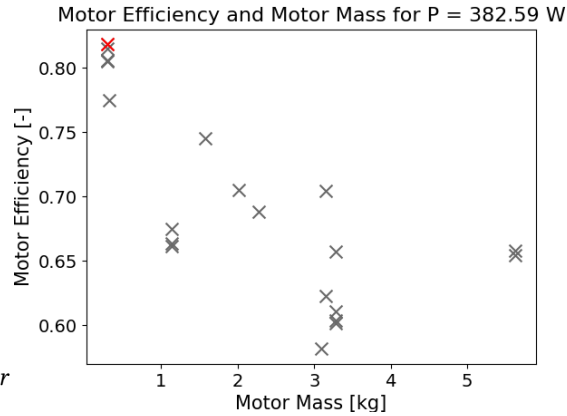


Figure 44: Motor electrical efficiency and mass for the cruise power of 382.59 W

Battery Selection & Sizing

When selecting and sizing the battery for a UAV, ensuring ample power supply for its various components is crucial. The engine, payload, avionics, and ballistic recovery system (BRS) all contribute significantly to determining the appropriate battery configuration.

The engine's specific voltage and current requirements necessitate a battery capable of delivering adequate power for seamless operation. Similarly, the combined power demands of the payload, avionics, and BRS must also be considered in selecting the battery. All components of the UAV are interconnected in parallel, requiring the battery to supply sufficient voltage and current collectively.

Calculating the minimum battery capacity (C_{bat}) is crucial, determined by Equation 87. Furthermore, the number of cells wired in series (N_{series}) and parallel ($N_{parallel}$) can be computed using Equation 88 and Equation 89.

$$C_{bat} = I_{bat}t \quad (87) \quad N_{series} = \frac{V_{bat}}{V_{cel}} \quad (88) \quad N_{parallel} = \frac{C_{bat}}{C_{cel}DoD} \quad (89)$$

Here, Depth of Discharge (DoD) indicates how much the battery is discharged in each cycle. Finally, the total battery mass and power can be determined using Equation 90 and Equation 91.

$$m_{bat} = N_{series}N_{parallel}m_{cell} = N_{tot}m_{cell} \quad (90) \quad P_{bat} = I_{Bat}V_{bat} \quad (91)$$

While designing the full battery architecture was deemed beyond the scope of this project, an initial sizing can already be estimated. By taking the industry-proven SIMAXX^TM 450Wh/kg battery from Amprius, which gives an effective energy density of the battery pack of 302.4 [Wh/kg], as expanded upon in ASMP-PROP-01, the battery mass was calculated. However, given these constraints to the battery, the required battery mass to support an endurance of 6 hours, as required in **REQ-SYS-TEC-UNI-1.2**, would have been too large and would have pushed the total mass of the units to an unacceptable level. Instead, a new endurance of 5 hours was selected. This was acceptable from an operational point of view, as the units' downtime has been significantly reduced by including redundant batteries. For this new endurance, the calculated required battery capacity was found to be 2.151 kWh, and as a result, the total battery mass was estimated to be 7.11 kg. This battery was split into 4 separate batteries fitted within the fuselage of the unit and were allocated to allow for the quick swapping upon recovery, to allow for minimum downtime. For this reason, two sets of batteries for each unit will be included in the swarm components so that every unit may be launched again immediately instead of

⁴MAD COMPONENTS - 5015 IPE V3.0. URL: <https://www.mad-motor.com/products/mad-components-5015-ipe-v3.html?VariantsId=10470>

having to wait for the battery to be recharged. Finally, to ensure that **REQ-SYS-TEC-UNI-1.4** is met, the team recommends that in future research, if the battery architecture is developed, the composition of cells in series and in parallel should be made so that a maximum of 1 kW can be outputted, as this is the expected power requirement for the climb phase. This is expected to be a reasonable requirement to achieve, as the achievable voltage and current give a larger possible power output.

To uphold the requirements **REQ-SYS-CON-SFT-3.1** up until **REQ-SYS-CON-SFT-3.5**, it is necessary to include a protection and containment system for the battery to avoid the packs from being pierced or damaged and in preparation for the outbreak of a battery fire. This can be caused during emergency landings, by the battery overheating or being damaged in other ways during the operation. A battery fire can reach more than 1000 [°C] and is volatile to conventional firefighting methods such as water. Therefore, it is necessary to use fire suppression material designed especially for battery fire suppression. A preliminary mass, size, and cost analysis is conducted based on available market options. The material chosen is a mix of Kevlar and carbon fibre, treated to be corrosion resistant; used in the Heavy Duty Lithium-Ion Battery Fire Containment Blanket offered by Brimstone Fire Protection [128]. The product properties in Table 23 are found based on their 5x6 square feet product.

Table 23: Product Properties

Category	Value	Unit
Size	147 x 180	[cm × cm]
Cost	855	[\$]
Mass	5.44	[kg]

From this, the specific mass and cost of the material is estimated to be 2.05 [kg/m²] and 321.5 [\$/m²]. With the sized battery, the cost and mass of the fire suppression lining can be estimated with Equation 92.

$$\begin{aligned}
 C_{liner} &= 321.5S \\
 m_{liner} &= 2.05S
 \end{aligned}
 \tag{92}$$

Where C_{liner} is the cost of the liner, m_{liner} is the mass of the liner, and S is the necessary surface area of the liner. It is

recommended to revisit this analysis and deepen the understanding of the liner since it was not explored fully at this point in the design.

7.6.3 Verification

Verification of the methods and code used in the Propulsion & Power department has been performed through the block tests showcased in Table 24. The table structure is explained in subsection 7.1.1.

Table 24: Block Tests used for Propulsion & Power Verification

Block Tested	Inputs	Outputs	Tests	Confidence
Thrust Calculator	MTOM, C_{Dcl} , C_{Dcr} , V_{cl} , V_{cr} , h , S_w , γ	T_{cr} , T_{cl}		
Propeller Selection	V_{cl} , T_{cl} , V_{cr} , T_{cr}	prop_model, d_{prop} , M_{prop} , RPM_{cr} , RPM_{cl} , $\eta_{prop_{cr}}$, $\eta_{prop_{cl}}$	Check that selected propeller meets the Thrust requirements	Low
Motor Selection	V_{cl} , T_{cl} , V_{cr} , T_{cr} , $\eta_{prop_{cr}}$, $\eta_{prop_{cl}}$	motor_model, ESC_model, η_{cr} , η_{cl} , P_{cr} , P_{cl} , $P_{el_{cr}}$, $P_{el_{cl}}$, $M_{motor+ESC}$	Check that selected propeller meets the Thrust requirements	Low
Battery Mass	$E_{density}$, P_{comms} , $P_{avionics}$, $P_{payload}$, t_{climb} , t_{cruise} , $P_{el_{cr}}$, $P_{el_{cl}}$	E_{req} , $M_{battery}$	Compare outputs with manual calculation using Equations 87-91	High

7.7 AVIONICS & ELECTRICAL SYSTEMS

The electronics and avionics subsystems are crucial components of a UAV, serving as the backbone for its navigation, communication, control, and data acquisition functions. This section of the report provides a detailed overview of the electronic and avionics architecture designed for the UAV, outlining the integration and selection criteria of all relevant components identified at this stage of the design. Please note that verification has not been performed in this section because no calculations have been performed that require verification. Validation of the results obtained is deferred for future developments.

7.7.1 Subsystem Risks & Requirements

From the risk analysis in section 3.6, the avionics subsystem has the risk: **R-T-01**: Collision with terrain, **R-T-04**: Collision with birds, and **R-T-36**: Avionics fail to detect fuel depletion.

From the requirement generation in section 3.7, the Avionics subsystem must satisfy: **REQ-SYS-OPS-AVI-1**: Each unit shall be able to measure all the state data required to allow for automatic flight.

7.7.2 Assumptions

The subsystem is designed with the following assumptions:

- ASMP-AVIO-01: The flight control software is assumed to be an adaptation of the linearised state-space model detailed by Mulder et. al. in their Flight Dynamics lecture notes [109]. This is a reasonable assumption as per the indication of the authors, so long as the representative flight conditions are taken into account during the linearisation of the equations of motion.
- ASMP-AVIO-02: The design of electronics systems typically has a large portion related to appropriate component selection. Since this is too detailed for the present report, it is assumed that the functionality required from this system is achievable by COTS components. This is validated through a preliminary survey of available market options as shown in section 7.7; however, a detailed investigation in the future must precede a final verdict on the matter.
- ASMP-AVIO-03: The chosen sensors capabilities are assumed to be sufficient for ensuring all successful flight operations. The data rates mentioned in section 7.7 correspond to measurement frequencies in excess of 20Hz, which, compared to a study by Horssen et. al., are at least twice as high as what is required by a manned operation of the Cessna Citation II [129].

7.7.3 Design

The general outline of the hardware is shown in Figure 45 for the drones, with all top-level interconnections between the hardware and the software shown in Figure 46.

First, the electrical system is described in Electrical system, followed by the communication and data handling architecture shown in Communication and Command Data Handling.

Electrical system

A general overview of the electrical system of the UAV can be summarised by the following block diagram. It includes all the generic components used by both the observational and relay drone, but excludes additional payload elements such as the lidar camera.

To minimise noise and chance for error, control and command instructions are sent as a digital signal and decoded at the receiving end. For motors, the digital signals are decoded as PWM signals are then used to

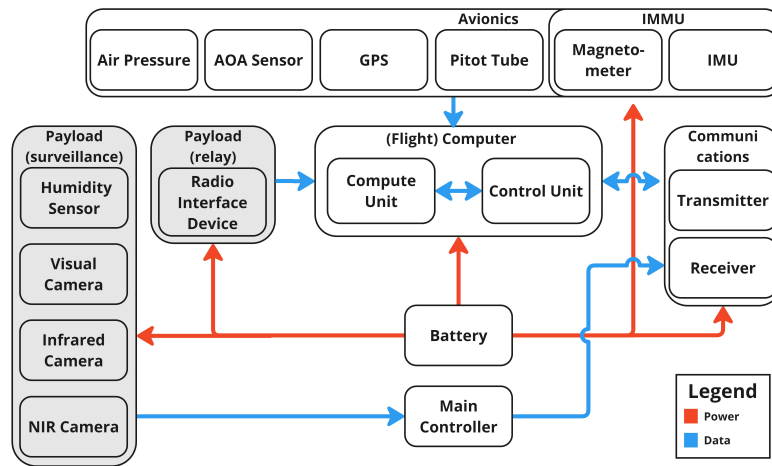


Figure 45: Hardware Diagram of the Drones. The blocks in gray indicate that the payload consists of either the sensors or a radio interface device, depending on whether the drone in question is a survey or relay one, respectively.

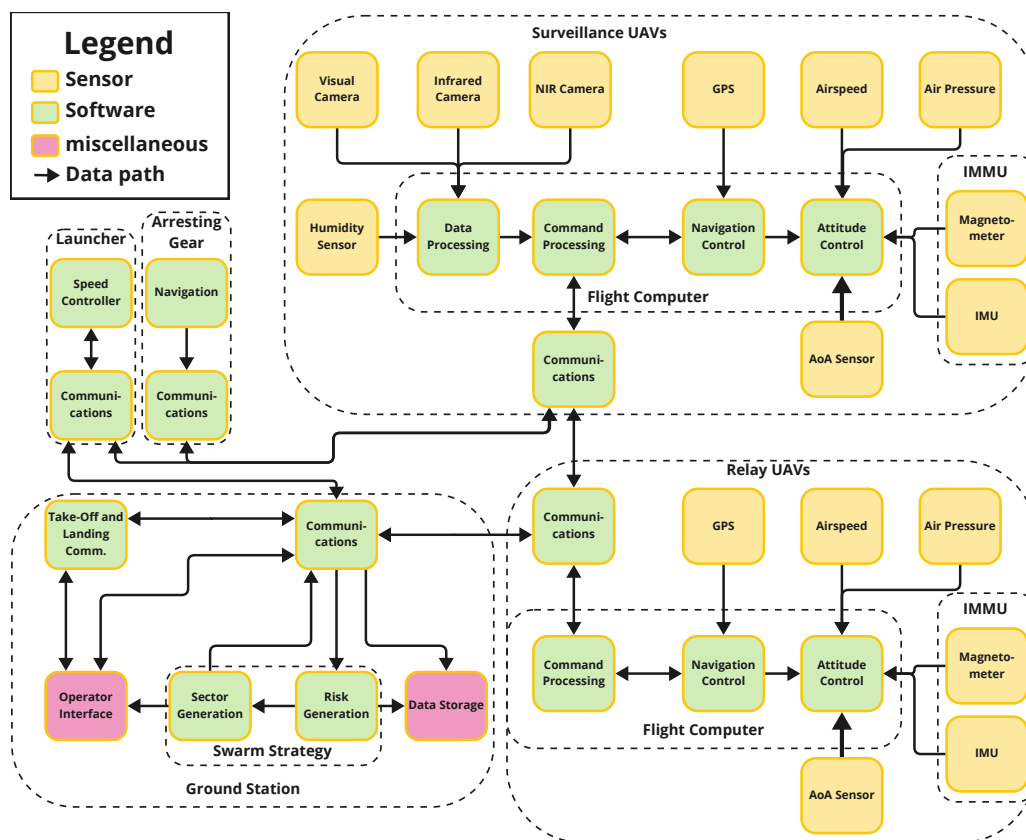


Figure 46: Software Diagram.

control the relevant motors. For instruments, UART was chosen as the preferred method of communication given its simplicity and reliability for straightforward communication. As for servo control, I2C was chosen given its capability of managing multiple devices on a single bus. It is also often used when managing more complex servo tasks.

For the actuators, RC servo motors are used, as they should provide sufficient torque to combat typical control surface hinge moments. In a similar manner to the stability and control derivatives discussed in subsection 7.5.5, the hinge moment coefficients necessary for computing the control surface hinge moments are hard to obtain without experimental data [109]. While semi-empirical methods based on airliner data can be employed, such as the ones developed by Roskam [110], it would be difficult to evaluate their applicability to the system at hand and are therefore not considered at this stage.

Communication and Command Data Handling

The communication system design and infrastructure is presented in chapter 6. Here, the communication is coupled with data handling and the intersection between the two is shown.

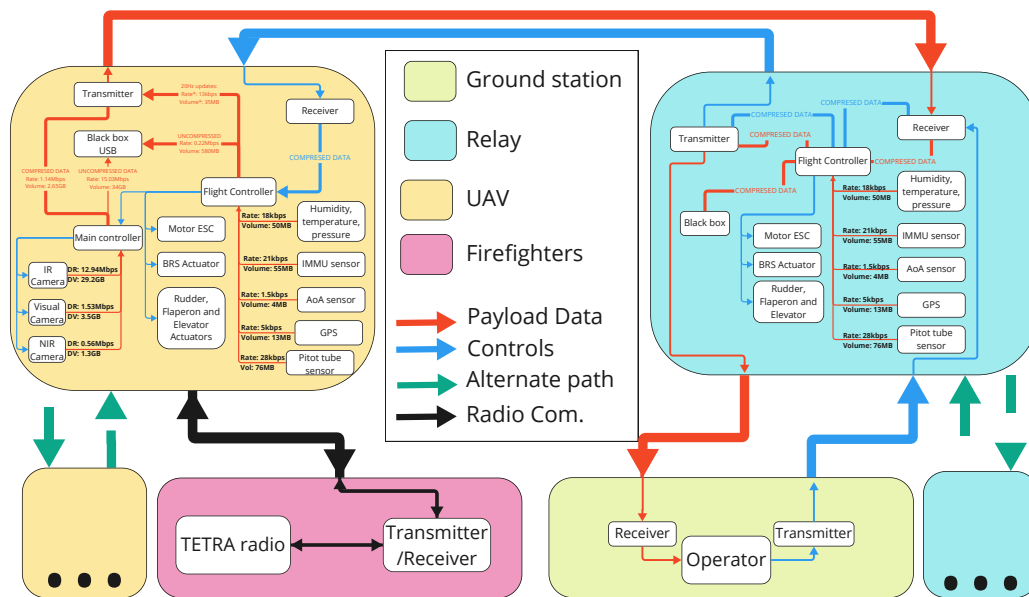


Figure 48: Communication and Data Handling Diagram.

As seen from Figure 48, the flow of information can follow a payload link, control link or radio communications link with the last one being used exclusively as a relay link between firefighting groups on ground. Since the swarm has the ability to relay information through other UAVs the diagram presents alternative paths to other vehicles with identical architecture indicated by the three dots and a green path.

As for the data handling, two separate controllers were used for the avionics and actuation on one hand, and for the payload camera management on the other. The flight controller is the processor responsible for collecting the sensor data, processing it and feeding it to an autonomous flying program embedded in the processor. The flight control program is a linearised model as outlined by Mulder et. al. [109]. The model would be linearised around two distinct points, climb and cruise, and outputs the necessary control surface deflections for stable flying. After the data is processed, it is sent to the UAV “black box”, which stores it for post-flight investigations. This black box is an SD card with a minimum capacity of 40 [GB], as it must accommodate the large amounts of image sensor data in addition to the avionics data. Moreover, it must accommodate a maximum write speed of 15 [Mb/s] coming from the system. Such SD cards are widely available on the market today¹¹ and are easily integrable with the system.

7.7.4 Further Recommendations

Currently, the avionics and electric subsystems are only briefly outlined based on their requirements. In the future, a detail design leading up to flight and main controller schematics would be desirable. This would require a more thorough research into components and their datasheets, ensuring proper compatibility and functionality. Besides the hardware part, the processor software required to control all components on a board will need to be written and debugged. This code would contain both flight control logic (flight controller), as well as actuation, read and write capabilities for the sensors (main controller).

¹¹SanDisk Extreme PRO SDXC UHS-II Card: <https://www.westerndigital.com/products/memory-cards/sandisk-extreme-pro-sd-uhs-ii-v60?sku=SDSDXEP-064G-GN4IN>

7.8 STRUCTURES

The UAV's structure is a subsystem enabling the proper functioning of all other subsystems: it houses all necessary components and maintains the desired shape throughout all design flight conditions. In order to account for possible changes and lack of inclusion of fasteners and other components, the safety factor of two has been included in the following analysis. Aviation factors of safety have historically been in the range of 1.5 [133], with lower values being introduced as more advanced materials came into use. However, following the recommended practices of ESA, the safety factor is increased to 2 in order to account for the immaturity of the project and the early stage of design [134].

This preliminary UAV structural design focuses on the following: (1) flight conditions and load determination, (2) wing box analysis, (3) fuselage skin analysis and (4) arresting gear hook analysis. Each section will include all relevant assumptions made during the analysis with their expected impacts on the final result.

7.8.1 Subsystem Risks & Requirements

The relevant requirements from Table 50 are:

- **REQ-SYS-TEC-UNI-5.1:** The structure of the unit shall provide an interface infrastructure for all other unit subsystems.
- **REQ-SYS-TEC-UNI-5.2:** The structure shall provide the main load-carrying capability of the unit.
- **REQ-SYS-TEC-UNI-5.3:** The structure shall withstand a maximum static load factor of 3.
- **REQ-SYS-TEC-UNI-5.4:** The structure shall be able to withstand thermal loads due to temperatures between 0 and 45 °C.
- **REQ-SYS-TEC-UNI-5.5:** The structure shall withstand shock loads of 6.5 G.
- **REQ-SYS-CON-STB-1.2:** The structure of the system shall not include any components composed of toxic materials.

7.8.2 Assumptions

- **ASMP-STRC-01:** Lift is assumed to be elliptically distributed along the span. This is a conservative assumption since the actual lift is expected to be lower than the ideal elliptical case. Indeed, a simple comparison with the results of XFLR5 for an accurately modelled wing shows that the elliptical lift is slightly greater than the true wing distribution. The discrepancy between the two lift values is depicted in Figure 49.
- **ASMP-STRC-02:** The fuselage is modelled as a thin-walled structure. Typically, a thin-walled structure has a thickness in the order of 100 times smaller than any other relevant dimension. This is indeed the expectation when taking values from the midterm report [53].
- **ASMP-STRC-03:** The fuselage is modelled as a cylinder of constant diameter, which is the maximum diameter expected of the structure for housing all the necessary components. This is conservative due to the increase in both normal and shear stresses with distance from the neutral lines, which are aligned with the cylinder's axes for a symmetric loading case. Therefore, a larger cylinder would accumulate larger stresses within its walls.
- **ASMP-STRC-03:** The fuselage weight is assumed to be a constant distributed force distributed along its length. In reality, the fuselage would have an uneven distribution according to the chosen aerodynamic shape.

- ASMP-STRC-04: The wingbox is assumed to have the same diameter at the root as at the tip. This is conservative, as the stress magnitude increases with the distance from the neutral line(s) to the skin, which is higher for a larger diameter beam.
- ASMP-STRC-05: No flutter analysis is performed for any of the structures. This is a fair assumption, as aircraft with low aspect ratio wings flying at low speeds typically do not encounter this issue, as per NACA TN4197 [135]. This can be quickly checked by using a simplified formula for the critical flutter velocity, V_f , found in Equation 94.

$$V_f = a \sqrt{\frac{\left(\frac{G}{1.337AR^3P(\lambda+1)}\right)}{2(AR+2)\frac{t^3}{c}}} \quad (94)$$

While this is checked again with the final design values, using preliminary estimates from the midterm report [53] lead to a flutter velocity of around 700 [m/s], which is much higher than anything in the realm of what is expected of a UAV of this size.

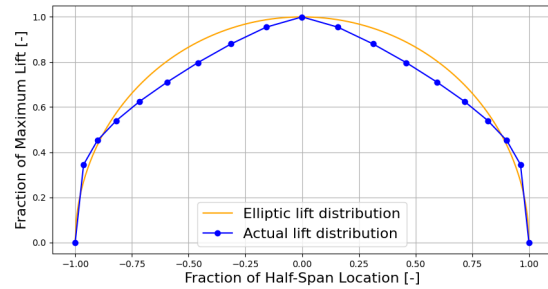


Figure 49: True lift distribution (blue) and simplified elliptic distribution (orange) as fractions of maximum lift plotted against the location along the span as fractions of the half-span.

7.8.3 Design

Load determination

In order to satisfy **REQ-SYS-TEC-UNI-5.2**, the loads on the structure must first be defined. The loads on the aircraft are the lift, drag, weight and thrust. To identify the most straining loading condition, the maximum load factor of 3 must be used as per the load diagram (preliminary one in Figure 30), which was the generated **REQ-SYS-TEC-UNI-5.3**. The loads are modelled as follows:

- Lift has an elliptic distribution acting on the line of airfoil centres of pressure, perpendicular to the chord.
- Drag is proportional to lift following the lift-to-drag ratio, so it is also elliptically acting at the centres of pressure perpendicular to the lift.
- Wing weight is a distributed force varying span-wise proportional to the length of the chord, while fuselage weight is a constant distributed load.
- For the fuselage analysis, the wing's lift is considered a point load acting at the wing mean aerodynamic chord's aerodynamic centre. In order to maintain static equilibrium, the tail also produces a little lift to prevent the pitching motion of the UAV. Moreover, due to the shock load requirement **REQ-SYS-TEC-UNI-5.5**, an appropriate normal concentrated load was applied at the location of the BRS attachment.

The loads on the fuselage and wing are shown in Figure 51, Figure 50 respectively. With the loads identified, static stability analysis has been performed. From the known weights of each component and their locations along the length of the vehicle, the required wing and tail lift have been calculated for the equilibrium situation.

The vehicle has been split into three structure groups: the fuselage, boom and empennage. Each one of these groups has been analysed for internal shear and bending forces based on the static analysis conducted earlier.

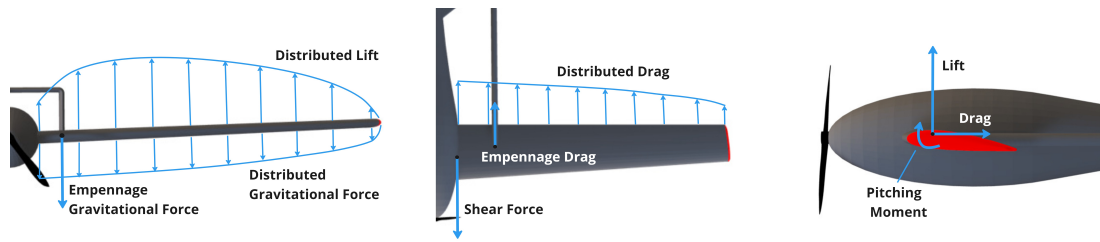


Figure 50: Forces acting on the wing of the preliminary UAV concept

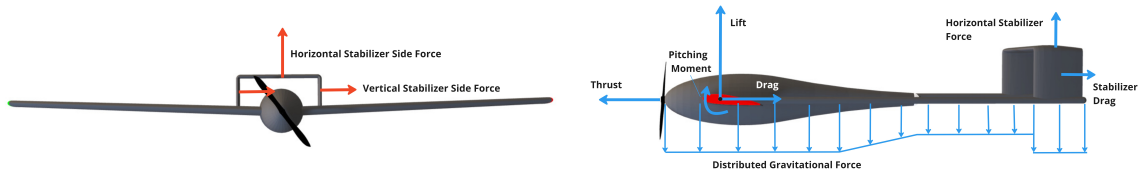


Figure 51: Forces acting on the fuselage of the preliminary design.

The internal loading diagram for the fuselage is presented in Figure 52. As seen from the diagrams, the component's weights have a much higher impact on the internal forces than the structural weight itself, with the maximum force peaking at 430 [N]. Similarly, for the moment loading, the biggest influence is induced by the weights and spacing of the internal components, with the most drastic change at the wing location. The moment values peak at 82 [Nm].

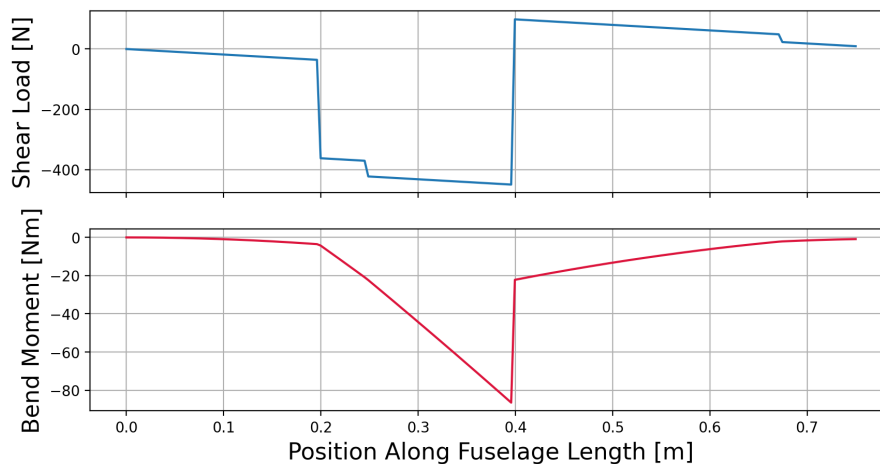


Figure 52: Internal shear and moment diagrams for the fuselage

Similarly to the fuselage loading, the boom internal loading diagrams are visible in Figure 53. Clearly, the loading of the booms is more straightforward than the fuselage itself. Compromising just the weight of the booms, empenage and the tail lift, the plot is linear, peaking at around 62 [N]. Similarly, the internal bending diagram peaks at 45 [Nm] and follows a quadratic function that reaches zero at the end of the boom.

To obtain the internal loads of the wing, first, the external loads have to be calculated. The contributions to the wing loading are the drag and lift force, which results in moments along all three axes. The aerodynamic forces are spread and differ along the length's span and chord. For this analysis, the assumption is made that the resultant force acts at the centre of the pressure of the chosen airfoil at cruise speed, although this point moves slightly throughout the flight regime. Furthermore, the spanwise lift distribution for a tapered wing can be estimated as a parabolic curve, where the wingtip has 0 [N] lift and drag.

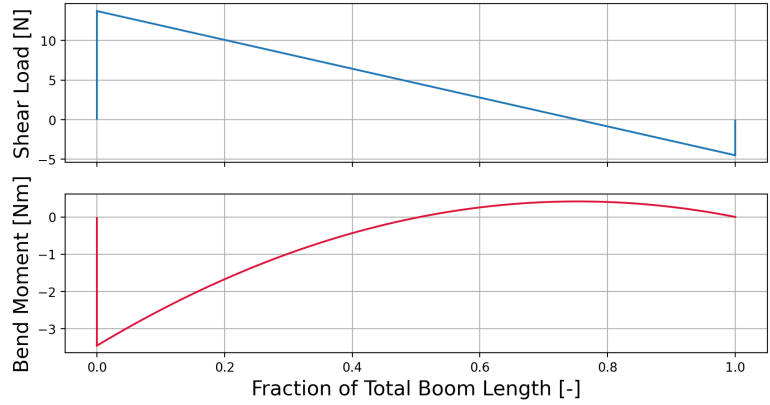


Figure 53: Internal shear and moment diagrams for the booms of the UAV.

As can be seen in Figure 54a, the main contribution to drag at low speeds is the lift-induced drag. Thus, to simplify the analysis, the drag is assumed to be the same shape as the lift but scaled down by the inverse of the lift-to-drag ratio. Note that the total drag force does consider the parasitic drag; it is merely the distribution that is affected by this simplification. Furthermore, the contribution of the horizontal force to the lateral moment is neglected due to the small moment arm.

To find the lift distribution, first, the peak load per unit span at the root is calculated using Equation 95, which is then used in Equation 96 to find the lift distribution, following the definition of elliptical lift distribution provided by Anderson [136].

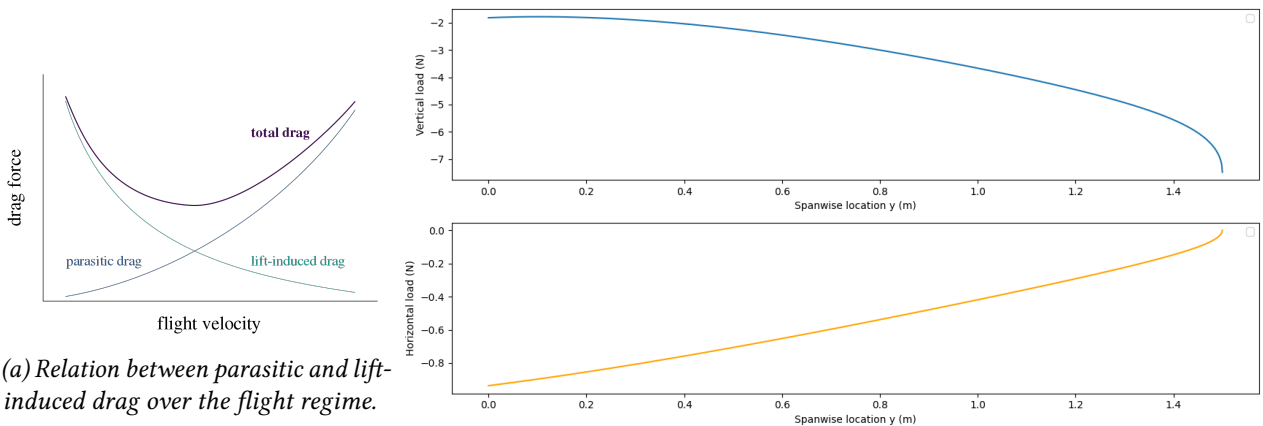
To find the lift distribution, first, the peak load per unit span at the root is calculated using Equation 95, which is then used in Equation 96 to find the lift distribution, following the definition of elliptical lift distribution provided by Anderson [136]. Where C_Y is the chord distribution given by Equation 97. Furthermore, the weight of the wing is assumed to be proportional to the chord length, calculated using Equation 98. The results are shown in Figure 54b.

$$L_0 = \frac{4L_{total}}{\pi b \cos(\Lambda)} \quad (95)$$

$$L_Y = L_0 C_Y \sqrt{1 - \frac{2y^2}{b}} * \cos(\Lambda) \quad (96)$$

$$C_Y = C_{root} (1 - (1 - \Lambda) (\frac{2|y|}{b})) \quad (97)$$

$$W_Y = \frac{M_{wing} \cdot g \cdot C_Y}{\int_0^b C_Y dy} \quad (98)$$



(a) Relation between parasitic and lift-induced drag over the flight regime.

(b) Vertical and horizontal loads along the half span.

Figure 54: Comparison of parasitic drag and wing loads.

Using the results in Figure 54b, the moments acting along the wing are found using the `scipy.integrate.cumtrapz`

library in Python. The results are shown in Figure 55

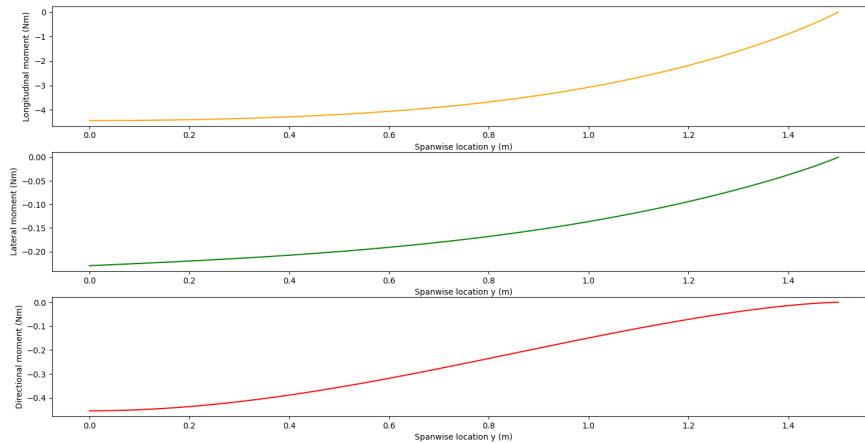


Figure 55: Longitudinal, lateral, and directional moment along the half span.

Material properties

The chosen material for the UAV design is 6082 aluminium alloy. It is one of the strongest commonly used aluminium alloys in the aerospace industry, offering high strength and ductility. While not as performant as the 7000 series alloys, it is around 80% cheaper¹², which is a very important consideration for a new product. The detailed material properties of aluminium 6082 are presented in Table 25. These properties have been used throughout the design process for vehicle sizing.

Table 25: Material properties of Aluminium 6082. [137]

Property	Value	Unit
Density	2.7	g/cm ³
Yield Strength	250	MPa
Ultimate Strength	290	MPa
E-modulus	70	GPa
Shear Strength	210	MPa
Shear Modulus	26	GPa

Wing Analysis

The wing analysis was approached using a circular thin, walled beam resembling the wing box as a stiffening load-bearing element of the wing structure. This approach enables structural analysis of a wing as a cantilever beam subjected to predetermined loads. Moreover, the circular cross-section allows freedom in airfoil choice shape as a more complex wing box would depend on greater detail on specific airfoil geometry.

The wingbox analysis began with bending stress analysis using the equation presented below [138].

$$\sigma_z = \frac{(M_x I_{yy} - M_y I_{xy})y + (M_y I_{xx} - M_x I_{xy})x}{I_{xx} I_{yy} - I_{xy}^2} = \frac{M_x}{I_{xx}} y + \frac{M_y}{I_{yy}} x \quad (99)$$

Due to the symmetry of the circular cross-section, the bending stress equation can be simplified. The above-mentioned equations were used to calculate the axial stresses experienced by the wing box under bending loading determined in subsection 7.8.3.

The presence of bending also implies significant shear stress in the structure. The shear stress has been split into the stress resulting directly from torsion applied to the wings and the stress resulting from forces acting in the plane aligned with the cross-section of the stiffening element.

¹²6082 sample price: <https://www.gemmel-metalle.de/aluminium/bleche/6082/1.html>, 7075 sample price: <https://www.gemmel-metalle.de/aluminium/bleche/7075/1.html>

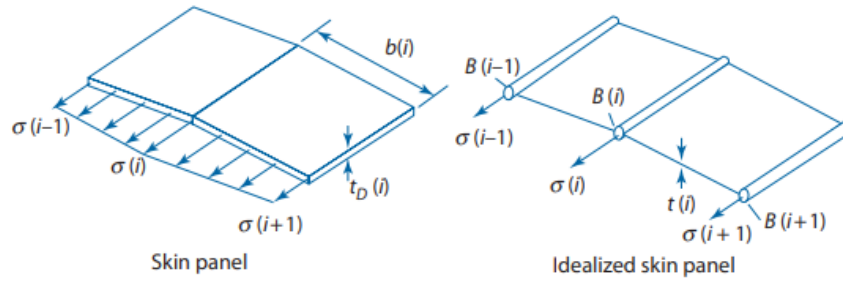


Figure 56: Visualisation of structure idealisation used in fuselage analysis [44]

The stress due to torsion was calculated using the following equation [138]:

$$\tau_T = \frac{T}{2tA_m} \Rightarrow A_m = \pi(d/2 - t/2)^2 \quad (100)$$

For the purpose of calculating the shear stresses resulting directly from the shear forces, the moments of area and inertia has been calculated as shown below [138]:

$$I = \frac{\pi t d^3}{8} \quad (101) \quad Q = \frac{\pi t d^2}{4} \quad (102)$$

With that estimation, the shear stress was estimated using the following equation:

$$\tau_S = \frac{V_y Q}{I t} \quad (103)$$

Having collected the axial and shear stresses, the von Mises failure criterion shown in Equation 104 can be used to check whether the structure is failing [139].

$$\sigma_{vm} = \sqrt{\sigma_z^2 + 3(\tau_T + \tau_S)^2} < \sigma_y \cdot \text{FOS} \quad (104)$$

Other than the yield criterion, the thin-walled structure of the wing box is expected to be susceptible to buckling. The buckling analysis of the wing structure has two aspects: bending and torsion/shear. For bending, the critical axial stress at which the skin buckles is given by Equation 105 as per NASA's Astronautics Structures Manual [140].

$$\sigma_{cr} = \frac{\gamma t_{\text{wing}} E}{r_{\text{wing}} \sqrt{3(1 - \nu^2)}} \quad (105)$$

where γ is an empirical correction factor that depends on the thickness-to-radius ratio. On the other hand, the shear stress at which the skin buckles in pure shear/torsional loading is given by Equation 106.

$$\tau_{cr} = k_s \frac{\pi^2 \frac{E t_{\text{wing}}^3}{12(1 - \nu^2)}}{L_{\text{wing}}^2 t_{\text{wing}}} \quad (106)$$

Here, k_s is the non-dimensional buckling coefficient, dependent on the so-called curvature parameter $Z = L_{\text{wing}}^2 / (r t) \sqrt{1 - \nu^2}$ according to graphs shown in the NASA Astronautic Structures Manual [140].

Fuselage analysis

The fuselage analysis was carried out following the Boom-Web method explained by Gundlach [44]. The method models the load-bearing skin as stiffening elements (booms) that carry only axial loads and the skin element that only carries shear. An example of the idealisation is presented in Figure 56.

With the idealisation performed, the simplified structure was analysed for resistance to bending and shear

using the data determined earlier and presented in Figure 52.

Tail boom analysis

The tail booms geometry was chosen using the same von Mises criterion approach. The booms were modelled as thin-walled circular beams loaded as presented in Figure 53. The results of the analysis are presented in Figure 57. For the rest of the iterative process, the tail boom is modelled as a part of the empennage.

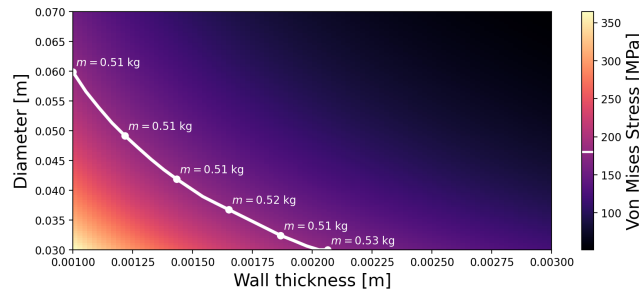


Figure 57: Tail boom maximum von Mises stress as a function of cross-section diameter and skin thickness. Highlighted in white is the yield strength threshold, including a safety factor of 2. For some points along this threshold, an indicative mass of one of the booms is shown, including the empennage, assuming a density of $2700 \text{ [kg/m}^3\text{]}$.

7.8.4 Verification & Validation

Verification of the methods and code used in the Structures department has been performed through the block tests showcased in Table 26. The table structure is explained in subsection 7.1.1.

7.8.5 Further Recommendations

The structural analysis can be improved by refining parts of the model, as well as by performing more detailed verification activities. In general, the structural design shown in this report is strength-based, while stiffness-related considerations are neglected – these could be explored in future works. The wing model can be improved by representing the wing geometry more accurately, instead of a cylindrical wingbox with constant diameter. Additionally, other options for the wingbox geometry can be considered, which have the potential to reduce weight (e.g. leading edge with one spar forming an enclosed “wingbox”). For the fuselage, an analysis of an orthogonally stiffened structure could be beneficial, as this would be more representative of typical real-world structures (even the inclusion of mounting plates would influence the directional properties of the structure). As for the booms, the most important recommendation regarding future investigations relates to its analysis as a 3D frame rather than a 2D cantilever beam. This would incorporate asymmetric effects, such as the torsion caused by the tail lift during a turn.

7.9 BALLISTIC RECOVERY SYSTEM

The ballistic recovery system (BRS) is an element meant to ensure the proper operability of the vehicle in adverse conditions. More specifically, the BRS is responsible for ensuring a safe landing in case of loss of control or of malfunctioning of various components, such as the battery, motor, control surface actuating servo motors, etc.

7.9.1 Subsystem Risks & Requirements

The relevant risks from section 3.6 are:

Table 26: Unit tests used for Structures Verification

Block Tested	Inputs	Outputs	Tests	Confidence
Boom Geometry	$n_b, d_{fuselage}, \zeta$	$(x, y)_{nodes}$	Compares with hand calculated boom locations	High
Fuselage Stress	$(x, y)_{nodes}, M_x, M_y, M_x, F_x, F_y, B, \sigma_{max}, \tau_{max}, L, \rho, SF$	$\sigma_{vm}^f, \sigma_{diff}^f$	Compares with hand calculated stress as per Equation 104	Low
Wing Stresses	$M_x, M_y, T, V_y, t_{wing}, t_{wb}, \sigma_{max}, \tau_{max}, SF$	$\sigma_{vm}^w, \sigma_{diff}^w$	Compares with hand calculated stress as per Equation 104	Low
Wing Chord Distribution	c_{root}, λ, b_w	$c(y)$	Compares with hand calculated chord lengths for a low no. of spanwise locations	High
Wing Lift Distribution	$c(y), L_0, b_w, \Lambda$	$L(y)$	Compares with hand calculated lift values as per Equation 95 through 97 for a low no. of spanwise locations	High
Wing Drag Distribution	$c(y), D_0, b_w, \Lambda$	$D(y)$	Compares with hand calculated drag values for a low no. of spanwise locations	High
Wing Weight Distribution	$c(y), M_{wing}, b_w, \Lambda$	$W(y)$	Compares with hand calculated weight values as per Equation 97 through 98 for a low no. of spanwise locations	High
Fuselage Load Distributions	$L_{fuselage}, MTOM, n_{max}$	$x_{LE}, V_y(x), M_x(x)$	Compares with hand calculated values as per methods outlined in [141] following the loads in Figure 51.	High
Wing Sizing	$\sigma_{diff}, d_{wb}, b_w, \rho$	t_w, M_{wing}	Checks if, given the thickness of the wing and the loading, the difference between allowable and maximum stress is minimal but positive.	Low
Fuselage Sizing	$\sigma_{diff}, L_{fuselage}, d_{fuselage}, \rho$	$t_{skin}, M_{fuselage}$	Checks if, given the thickness of the wing and the loading, the difference between allowable and maximum stress is minimal but positive.	Low

- **R-T-33:** Parachute doesn't deploy when necessary.
- **R-T-35:** The UAV is damaged during landing.
- **R-T-51:** Parachute deploys prematurely.

The relevant requirements from Table 50 are:

- **REQ-SYS-TEC-UNI-3.1:** The BRS deployment shall minimise damage to the unit.
- **REQ-SYS-TEC-UNI-3.2:** The BRS landing shall minimise damage to the environment surrounding the unit.
- **REQ-SYS-TEC-UNI-3.3:** The BRS shall ensure a landing velocity of 5 m/s.
- **REQ-SYS-TEC-UNI-3.4:** The BRS shall withstand shock loads of 6.5 G upon deployment.
- **REQ-SYS-TEC-UNI-3.5:** The BRS shall be fireproof.

7.9.2 Assumptions

The BRS system is designed under the assumptions:

- ASMP-BRFS-01: The BRS system is assumed to be deployed in conditions of maximum mass and airspeed. This is an appropriate assumption for an emergency system, as one desires it to be operable in any condition.
- ASMP-BRFS-02: It is assumed that the maximum allowable impact velocity is 5[m/s], as indicated by data from companies dealing in UAV decelerators¹³. As shown in subsection 7.9.5, an even lower impact velocity of around 3.7[m/s] is acceptable based on the parachute opening loads. Such a low impact velocity would have potential effects on the size and mass of the decelerator, which could have an undesirable positive mass snowballing effect.

7.9.3 Design

The BRS consists of a decelerator with its gores and riser, a deployment system and a Command and Data Handling (C&DH) unit responsible for the automatic activation of the deployment. The most fundamental aspect of the decelerator is the drag it produces, which must be at least equal to the MTOW of the UAV in order to ensure its recoverability in any situation. A key parameter of interest is the so-called *drag area*, $C_D S$, which characterises a decelerator and is given by Equation 107:

$$C_D S = \frac{2 \cdot \text{MTOM}}{\rho V_{\text{land}}^2}. \quad (107)$$

It is immediately clear from the equation that the landing velocity is an important parameter in determining the drag area. Further information about the geometry and the drag coefficient can then yield a value for the required diameter. After satisfying the drag requirement, another important consideration is the deployment load. For a first estimate, Knacke [142] uses Equation 108:

$$F_{\text{open}} = C_D S \frac{1}{2} \rho V_{\text{open}} C_x X_1, \quad (108)$$

where C_x is the opening force coefficient and X_1 is the force reduction factor. A range of empirical values for these two can be found in Knacke's [142] work. By combining Equation 107 and 108, one can obtain a relationship between the opening load and the two characteristic velocities: deployment airspeed and impact velocity. This relationship is shown in Figure 58.

Since the deceleration can be quite powerful, it was limited to the maximum acceleration generated during take-off, namely 6.5 [G] [53]. This would allow the same supporting structure to carry both the loads of the BRS deployment as well as, of the take-off and the landing. Figure 58 also confirms that a 5 [m/s] impact velocity with deployment at maximum airspeed as per **REQ-SYS-TEC-UNI-3.6** is comfortably achievable while limiting the deceleration.

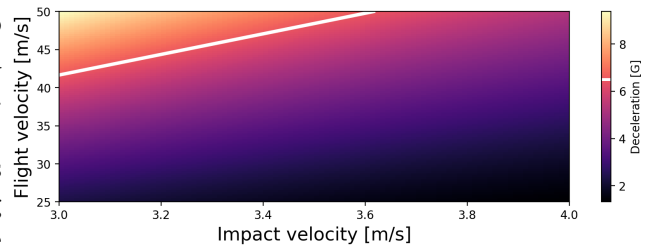


Figure 58: Parachute opening force as a function of opening airspeed and impact velocity. The white line highlights the maximum allowable 6.5[G] deceleration.

¹³<https://www.skycat.pro/>, <https://fruitychutes.com/>

7.9.4 Verification & Validation

Verification of the methods and code used in the BRS sizing has been performed through the block tests showcased in Table 27. The table structure is explained in subsection 7.1.1.

Table 27: Unit tests

Block Tested	Inputs	Outputs	Tests	Confidence
Drag Area	MTOM, ρ_{atm} , V_{land}	C_{DS}	Checked with hand calculation as per Equation 107	High
Deployment Load	C_{DS} , ρ , V_{open} , C_x , F_{open} X_1		Checked with hand calculation as per Equation 108	High

7.9.5 Further Recommendations

Currently, the BRS is deemed to have too high a design complexity for its priority in the overall system and is therefore outsourced. The greatest improvement in this subsystem is then to perform a complete sizing and set up procedures for in-house manufacturing. This would allow the production of the system to be independent of decelerator companies, as well as tailor the subsystem to the specific requirements of the UAV. As previously mentioned both in this section and in Knacke's work [142], in order to perform such a detailed sizing, experimental data is paramount. Hence, an experimental investigation of prototypes and continuous iteration would be necessary.

7.10 DESIGN RESULTS

After having described the working of all the subsystem estimation methods, this section focuses on achieving the final design values by iterating on these estimation methods. First, the final design values are presented, and the UAV architecture is visualised. Then, the convergence behaviour of the iterator is discussed, and a sensitivity study is conducted to analyse how stable the design point is with respect to several key parameters. After the convergence study, the iterator code is verified and validated against an existing UAV design. Finally, a mass and power budget is generated. This mass budget is used to verify the compliance to the risk mitigation of risk: **R-T-18** (section 3.6).

7.10.1 Final Design Parameters

The values obtained from the iterative process are computed and presented in Table 28. This table provides a comprehensive overview of the final design parameters for the surveillance drone.

Table 28: Final Design Parameters Surveillance Drone

Parameter	Value	Parameter	Value
MTOM	14.59 [kg]	Mass propeller	0.07 [kg]
OEM	14.09 [kg]	Motor model	5015 IPE V3.0 ¹⁴
Fuselage Mass	0.91 [kg]	Battery Energy	2151.43 [J]
Wing Mass	1.95 [kg]	Climb power	527.46 [W]
Empennage Mass	0.56 [kg]	Cruise power	253.64 [W]
Payload Mass	0.5 [kg]	Cruise Prop. Eff.	0.66 [-]
Misc. Mass	3.3 [kg]	Climb Propulsive Efficiency	0.59 [-]
Fuselage Diameter	0.25 [m]	Propeller Diameter	0.34 [m]

¹⁴5015 IPE V3.0: <https://www.mad-motor.com/products/mad-components-5015-ipe-v3.HTML?VariantsId=10470>

Table 28 – continued from previous page

Parameter	Value	Parameter	Value
Fuselage Length	0.75 [m]	Propeller Model	PER3 13.5x13.5 ¹⁵
Climb IAS	24.71 [m/s]	Wing area	0.43 [m ²]
Cruise Thrust	8.81 [N]	Wing Aspect Ratio	13.13 [-]
Climb Thrust	21.35 [N]	Leading edge mac loc.	0.42 [m]
Climb time	394.85 [s]	Wing mac	0.18 [m]
Climb RPM	6987 [-]	Wing span	2.37 [m]
Cruise RPM	5817 [-]	Average wing thickness	3.87e-02 [m]
Mass battery	7.11 [kg]	Wing taper ratio	0.4 [-]
Mass motor	0.29 [kg]	Centre of gravity loc.	0.49 [m]
Span horizontal tail	0.57 [m]	Tail length	0.75 [m]
Thickness horizontal tail	2.16e-02 [m]	Vertical tail area	0.08 [m ²]
Cruise AoA	5.54 [deg]	Horizontal tail area	0.09 [m ²]
CL max	1.48 [-]	Horizontal tail chord	0.14 [m]
CL cruise	0.71 [-]	Vertical tail chord	0.30 [m]
CL climb	0.89 [-]	Vertical tail span	0.30 [m]
CD climb	5.54e-02 [-]	Vertical tail thickness	4.74e-02 [m]
CD cruise	4.39e-02 [-]	Climb AoA	7.68 [deg]
CL alpha	8.36e-02 [-]	CL/CD cruise	16.24 [-]
Oswald factor	0.67 [-]	CL/CD climb	12.89 [-]
Elevator chord	0.05 [m]	Rudder chord	0.13 [m]
Total iterations		499067	

Figure 59a shows a render of the drone designed according to the final parameters. The engine is put in the front of the fuselage for compatibility with the launch rail. Furthermore, the BRS is pointed backwards horizontally. Since the attachment point is behind the centre of gravity, the drone will tend to land its nose down. Therefore, to avoid the parachute line and horizontal tail colliding, the parachute deploys underneath the horizontal tail. The BRS is connected directly to the wing box so that no moment is created. Furthermore, a large stress peak will occur during parachute deployment, so it is beneficial to connect these loads directly to the strongest point of the drone. The same goes for the hook that will connect to the arrestor wire. This hook is also directly connected to the wing box and points downwards at an angle. The hook extends from its base to allow for a larger flight altitude margin during the landing approach. In the renders, the hook is shown in its extended state. Directly behind the hook base is the fin antenna to minimise aerodynamic drag.

Figure 59b shows a render of the drone with a transparent hull such that the internal structure is visible. For clarity, the main elements are outlined and named. The technical drawing of the final UAV design is then shown in Figure 60

7.10.2 Convergence Study & Conclusions on Code Robustness

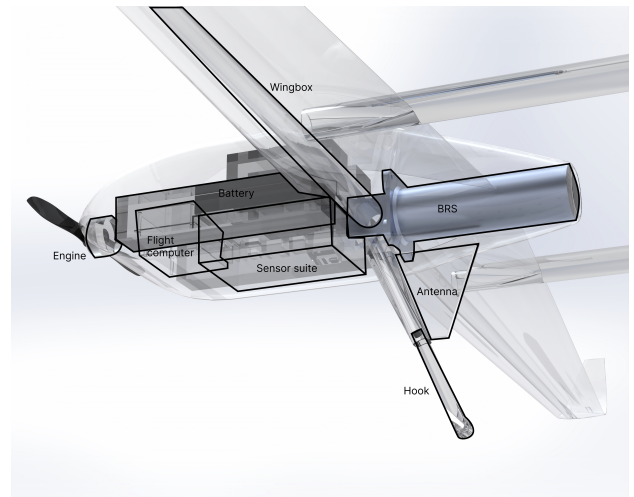
The convergence behaviour of the iterator can give insight into the sensitivity of key parameters and whether the system is over/under-designed. In Figure 61, the evolution of the key mass parameters of the UAV are plotted against the number of iterations. From this plot, it can be concluded that the mass first "snowballs up" at the start, then makes small adjustments down, until a large drop in motor mass eventually makes the MTOM settle at a mass of 14.6 [kg].

In addition to running the iterator normally, a few, relatively straightforward tests can be performed as verification of the code robustness. These are showcased in Table 29. The results obtained from these tests allow to draw the conclusion that the iterator code is robust, given that a sufficient n_{max} is selected. This

¹⁵PER3 13.5x13.5: <https://www.apcprop.com/product/13-5x13-5/>



(a) Isometric view of the UAV.



(b) Rendition of the UAV with a transparent hull, large internal structures are outlined and named.

Figure 59: Rendition of the UAV based on the final design values.

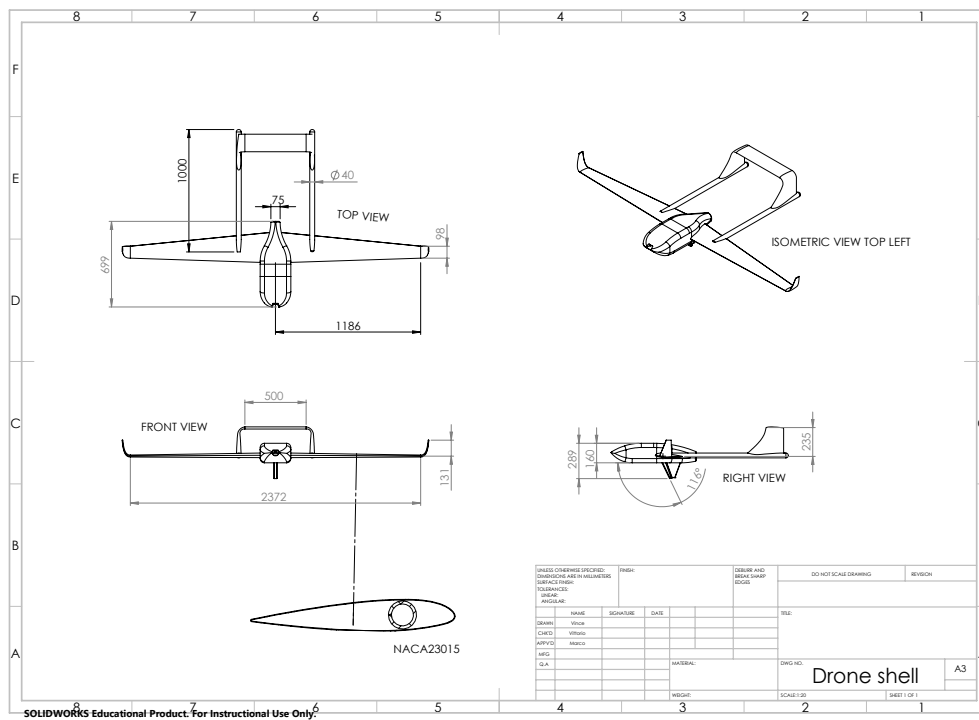


Figure 60: Technical drawing of the final UAV design.

number was not found, although it was found that it is smaller than the used value of $n_{max} = 100$. This means that for the current results, the code is deemed as robust. As a recommendation for future work, the team suggests to integrate the iterator in a larger loop that tests it at more different values of n_{max} to further analyze the robustness of the process.

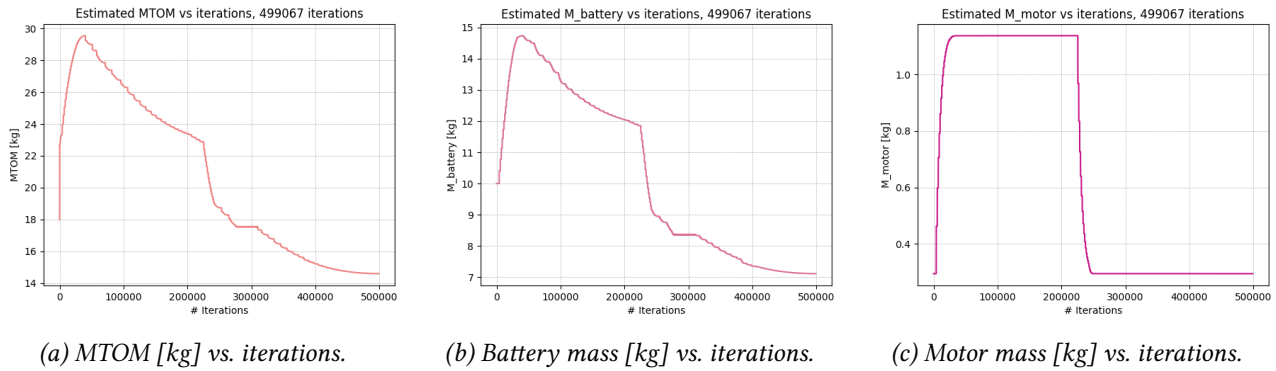


Figure 61: Convergence of key mass parameters of the UAV.

Table 29: Iterator Tests

Test Performed	Expected Result	Actual Result	Rationale
Use the iterator results listed in section 7.10 as initial guesses for a new iterator run.	Iterator outputs should be equal, or almost equal, to inputs.	Refer to Figure 62a. Test is passed, however the initial spike in mass parameters indicated that the Class-II weight estimation used in the first loop drastically overestimates the mass of the UAV components.	As it is made to simulate the snowball effect and only stop whenever there is no more room for extra increases/decreases in mass, the iterator should converge quickly once it is given, as inputs, values that it has already converged to in another run.
Compare the iterator results with $n_{max} = 10, 20, 100$ and 200	At low n_{max} , the iterator should give inconsistent results that change with changing n_{max} . This should not occur at higher values of n_{max} . The total amount of iterations ran should increase more slowly as n_{max} is raised.	Obtained plots are shown in Figures 61a, 62b, and 62c. $n_{max} = 10$ gives 26000 iterations, $n_{max} = 100$ gives about 500000, and $n_{max} = 200$ gives about 550000. The latter two cases output nearly the same MTOM.	At low n_{max} , each inner loop in the iterator code is stopped before convergence, and its results are passed on to the next outer loop. If this happens repeatedly, the overall results will suffer considerably from error propagation. Above a certain n , however, (almost) all loops achieve convergence before cutting off, hence results do not differ much the total number of iterations ran does not increase significantly when n_{max} is increased from 100 to 200.

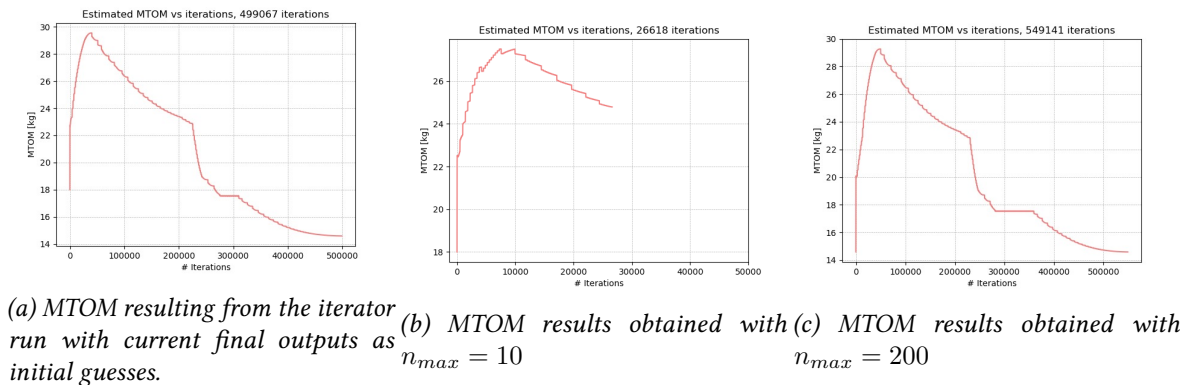


Figure 62: MTOM results with varying maximum iterations

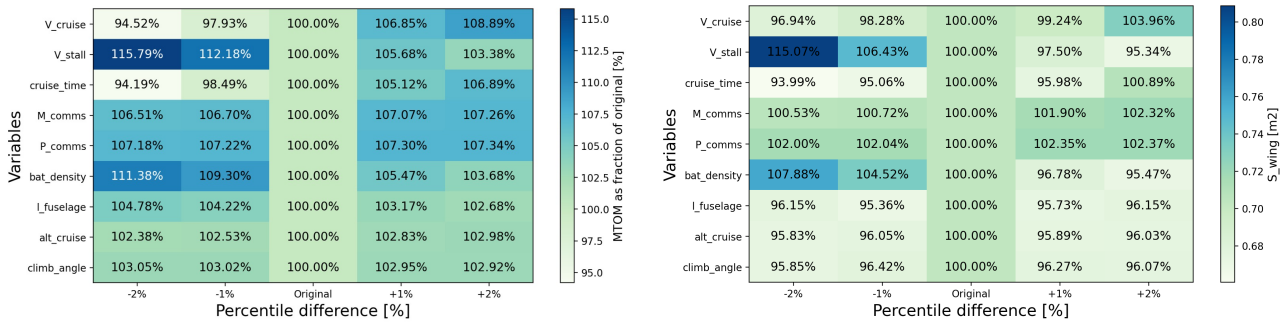
7.10.3 Sensitivity Study & Conclusions on Design Robustness

In addition to studying the convergence behaviour of the iterator, it is also important to gain insight into how sensitive the final design parameters are to the initial inputs.

To analyse this, a Jacobian matrix with the partial derivatives of all the outputs y_0, y_1, \dots, y_m concerning all the inputs x_0, x_1, \dots, x_m as entries, evaluated on the final design point \mathbf{x}_0 (Equation 109) can be constructed.

$$\mathbf{J}|_{\mathbf{x}=\mathbf{x}_0} = \begin{bmatrix} \left. \frac{\partial x_1}{\partial y_1} \right|_{\mathbf{x}_0} & \left. \frac{\partial x_1}{\partial y_1} \right|_{\mathbf{x}_0} & \cdots & \left. \frac{\partial x_n}{\partial y_1} \right|_{\mathbf{x}_0} \\ \left. \frac{\partial x_1}{\partial y_2} \right|_{\mathbf{x}_0} & \left. \frac{\partial x_2}{\partial y_2} \right|_{\mathbf{x}_0} & \cdots & \left. \frac{\partial x_n}{\partial y_2} \right|_{\mathbf{x}_0} \\ \vdots & \vdots & \ddots & \vdots \\ \left. \frac{\partial x_1}{\partial y_m} \right|_{\mathbf{x}_0} & \left. \frac{\partial x_2}{\partial y_m} \right|_{\mathbf{x}_0} & \cdots & \left. \frac{\partial x_n}{\partial y_m} \right|_{\mathbf{x}_0} \end{bmatrix} \quad (109)$$

Due to the high complexity and slight numerical instability of the iterator, arriving at consistent estimates for the partial derivatives proves challenging and computationally intensive. Therefore, the key input parameters $V_{cruise}, V_{stall}, t_{cruise}, M_{comms}, P_{comms}, \rho_{battery}, l_{fuselage}, h_{cruise}$ and γ_{climb} and the key output parameters $MTOM$ and S_{wing} are chosen for the analysis. For every input, the percentage change in the output is plotted against a $\pm 2\%$ change in every input parameter. This way, a qualitative intuition can be gathered on the sensitivity of a positive and negative change of the inputs. The sensitivity of the $MTOM$ is shown in Figure 63a and the sensitivity of S_{wing} is shown in Figure 63b.



(a) Sensitivity of the maximum take-off mass to design variables.

(b) Sensitivity of the wing area to design variables.

Figure 63: Sensitivity analysis of design variables.

As can be seen in Figure 63, the most noteworthy top-level inputs are the stall and cruise speeds, the endurance and the battery density. This is logical, as these inputs are linked with wing area and battery mass, the two greatest contributors to the weight. Another observation is that the figures suggest that the $MTOM$ is nearly in a local minimum concerning the selected input parameters, while the S_{wing} is nearly in a local maximum. The results suggest that some top-level inputs are of especially high importance, namely the stall speed, cruise speed, cruise time and battery density.

In order to assess the robustness of the design w.r.t. the inputs, two questions must be asked: (1) are the input intervals considered representative of real, possible input values, and (2) can the design always fulfil the mission given the variability in inputs? For the former, the small nudging performed in the sensitivity analysis means that the effects on the design are assessed at comparable design configurations. For the latter, even with a maximum increase in $MTOM$ of 15% for a 2% lower V_{stall} , the design remains within the 25 [kg] bound specified by **REC-SYS-CON-SFT-2.2**. More generally, the design is expected to stay within the requirement for any decrease less than 20% in the stall speed – the most restrictive input.

7.10.4 Mass and Power Budget

This subsection explores the creation of a detailed mass budget alongside two distinct power budgets: one designated for cruise and another for climb. This aims to clarify the distribution of the mass and power along its components. The mass budget is presented first, followed by the power budgets for the climb and cruise phases.

Mass Budget

The preliminary mass allocation of the developed UAV is a pivotal phase in the design process, outlining mass distribution among its diverse components. These components comprise Avionics, Battery, BRS, Communications, Empennage, Fuselage, Miscellaneous, Motor Payload, Propeller, and Wing. The Miscellaneous category incorporates wiring, arresting gear hooks, and actuators. For a detailed breakdown of these masses, see Table 30. Meanwhile, the mass distribution of sensors, payload, and avionics collectively is specified in Table 31.

Table 30: Miscellaneous Mass Breakdown

Component	Mass [g]	Relative Mass [%]
Wiring	50	10.6%
Arresting Gear Hook	335	71.3%
Actuators	85	18.1%
Total	470	100%

Table 31: Sensors Mass Breakdown

Component	Mass [kg]	Relative Mass [%]
IR. Camera	7.5	7.5%
VIS. Camera	10	10%
NIR Camera	30	30%
GPS	3	3%
IMMU	3	3%
AoA	10	10%
Barometer	12	10%
Pitot Tube	24.5	24.5%
Total	100	100%

The comprehensive mass distribution is detailed in Table 32. Additionally, a pie chart illustrating this breakdown is presented in Figure 64. From subsection 7.10.3, an uncertainty in the total mass of 95% to 115% is derived for an input uncertainty of $\pm 2\%$. When normalised, this results in a total mass uncertainty of 97.5% to 107.5%. Consequently, the uncertainty in the mass of each component can be determined and is highlighted in Table 32 within braces. Furthermore, from this table it is confirmed that the mass of the UAV is indeed maintained below the 25 [kg] mark, thus complying with **REQ-SYS-CON-SFT-2.2** and also making **REQ-SYS-CON-STB-1.5b** no longer relevant for the design. Instead, **REQ-SYS-CON-STB-1.5a** is followed, and also complied with, given that the UAVs are going to be cruising at a higher altitude than 600 [m]. This cruise altitude also results in **REQ-SYS-CON-STB-3.1** being met.

Table 32: UAV Mass Breakdown

Component	Mass [kg]	Relative Mass [%]
Avionics	0.5 (0.49 - 0.54)	3.4%
Battery	7.11 (6.91 - 7.64)	48.7%
BRS	0.73 (0.71 - 0.78)	5.0%
Comms.	1.5 (1.46 - 1.61)	10.3%
Empennage	0.56 (0.54 - 0.6)	3.8%
Fuselage	0.91 (0.88 - 0.98)	6.2%
Misc.	0.47 (0.46 - 0.51)	3.2%
Motor	0.29 (0.28 - 0.31)	2.0%
Payload	0.5 (0.49 - 0.54)	3.4%
Propeller	0.07 (0.07 - 0.08)	0.5%
Wing	1.95 (1.9 - 2.1)	13.4%
Total	14.59 (14.18 - 15.68)	100%

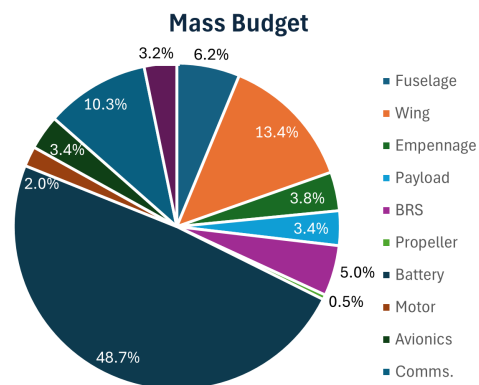


Figure 64: Pie Chart of the Mass Budget

Power Budgets

The power budgets for cruise and climb stages are pivotal in the UAV design process, delineating the allocation of power among critical components to ensure efficient operation during different flight phases. These components include Avionics, Communications, Motor and Payload. For a detailed breakdown of payload power, see Table 30. Meanwhile, the power distribution of avionics is specified in Table 31.

Table 33: Payload Power Budget

Component	Power [W]	Relative Power [%]
IR. Camera	0.5	9.1%
VIS. Camera	2.5	45.5%
NIR Camera	2.5	45.5%
Total	5.5	100%

Table 34: Avionics Power Budget

Component	Power [W]	Relative Power [%]
IMMU	0.04	28.9%
AoA	0.08	48.9%
Barometer	0.01	6.0%
Pitot Tube	0.03	16.3%
Total	0.15	100%

During climb, it's noteworthy that the Payload component is not utilised, thus requiring no power allocation. Detailed breakdowns for both cruise and climb power budgets are presented in Table 35 and Table 36 respectively. Moreover, to visualise the distribution comprehensively, pie charts illustrating these breakdowns can be found in Figure 65 and Figure 66.

Table 35: UAV Power Breakdown for Cruise

Component	Power [W]	Relative Power [%]
Avionics	4	1.4%
Comms.	18	6.4%
Motor	253.6	90.2%
Payload	5.5	2.0%
Total	281.1	100%

Power Budget for Cruise

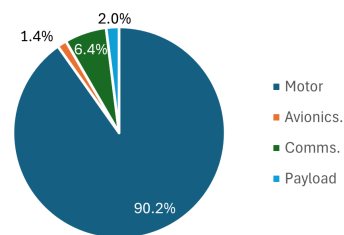


Figure 65: Cruise Power Budget

Table 36: UAV Power Breakdown for Climb

Component	Power [W]	Relative Power [%]
Avionics	4	0.2%
Comms.	18	0.8%
Motor	2151.4	99.0%
Payload	5.5	0.0%
Total	2173.4	100%

Power Budget for Climb

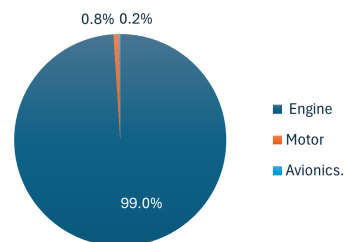


Figure 66: Climb Power Budget

7.10.5 Additional Designs

There have been several variations on the UAV architecture proposed in previous parts of the report. These variations include a LiDAR drone which maps the search area with a LiDAR sensor at the start of the mission, as mentioned in section 4.4, along with a relay drone which is primarily used for relaying the transmissions of the surveilling UAVs, as mentioned in subsection 6.4.2. The architecture of these designs will now briefly be discussed.

LiDAR Drone The LiDAR drone differs from the surveillance drone in the payload mass, which is a 2.7 [kg] LiDAR camera instead of a 0.5 [kg] sensor package. Since the LiDAR drone flies only once per mission, it is favorable to reuse the surveillance drone design in the interest of budget. Therefore, the increase in payload mass can be compensated for with a decrease in battery mass. The battery mass can be changed from 7.11 [kg] to 4.91 [kg], which reduces the endurance from 5 hours to 3.5 hours. Since covering the entire 1000 [km²] search area takes 5.5 hours, 2 LiDAR drones are required to map the entire search area in 2.8 hours. These drones can then be repurposed as surveillance drones during the mission.

Relay Drone The relay drone differs from the surveillance drone in its flight regime, cruising at a 4000 [m] altitude instead of 850 [m] altitude. This regime change requires a modified architecture. The design iteration method presented in section 7.1 has been used to size this UAV as well. Preliminary results showed that this UAV will have a MTOM of 17.4 [kg], a battery mass of 8.67 [kg], a wing area of 0.71 [m²] and a wingspan of 3.0 [m]. Though these parameters are preliminary estimations, these architectures will have to be studied in detail in further research.

GROUND SYSTEMS

The swarm requires several support systems on the ground that are vital to succeed in the mission objectives. This section describes these systems and shows the ground system's transport and deployed state.

8.1 SUBSYSTEM RISKS & REQUIREMENTS

The relevant risks from section 3.6 are: **R-T-15**: Drone is too damaged to be safely transported, and **R-T-16**: system is damaged during transportation.

The relevant requirements from Table 50 are:

- **REQ-SYS-TEC-GRD-1.1**: The system shall ensure that 25 units are airborne at all times during operations.
- **REQ-SYS-TEC-GRD-1.2**: The launcher system shall be able to accelerate the UAV units up to 20 m/s.
- **REQ-SYS-TEC-GRD-1.3**: The launcher and recovery system shall not exact load of more than 6.5 G to the units during launch and recovery.
- **REQ-SYS-TEC-GRD-1.4**: The recovery system shall guarantee that the unit is brought to a full stop in the recovery area.
- **REQ-SYS-TEC-GRD-1.5**: The recovery system shall guarantee that the unit is recovered with minimal/no damage.
- **REQ-SYS-TEC-GRD-1.6**: The entire ground system shall be transportable by semi-truck.
- **REQ-SYS-TEC-GRD-1.7**: The units shall be stored such that they are not damaged.

8.2 ASSUMPTIONS

Once again, the assumptions that were made within the designing of this subsystem are listed below.

ASMP-TOAL-01: At the low speeds associated with UAV takeoff, drag can be neglected. This simplifies the equations of motion by eliminating the quadratic velocity term, potentially underestimating the required launch rail length. This leads to an easier derived analytical solution.

ASMP-TOAL-02: Based on existing launcher designs, similar UAVs can withstand accelerations of up to 8.5g. This assumption ensures that the UAV structure can withstand accelerations between 5g and 6g for a conservative preliminary sizing.

ASMP-TOAL-03: The operational normal stresses on the wire do not exceed the yield strength of the wire material. This prevents the wire from yielding or failing under operational conditions, ensuring the reliability and safety of the launch and arresting systems.

ASMP-TOAL-04: The operational normal stresses on the poles do not exceed the yield strength of the wire material. This prevents the poles from yielding or failing under operational conditions, ensuring the reliability and safety of the launch system.

ASMP-TOAL-05: Normal stress calculations ensure the wire and poles can withstand operational forces. This prevents the wire and poles from yielding or failing under operational conditions, ensuring the reliability and safety of the arresting system.

ASMP-TOAL-06: The deflection angle of the poles will not exceed 1 degree. This ensures the structural integrity and reliability of the arresting gear during operation, maintaining safe performance standards.

8.3 DESIGN

There are several functions from the Functional Breakdown Diagram that the ground systems needs to fulfil:

- **O-F2 Transport System.** Before the beginning of flight operations, the swarm must be transported to the location of interest. Requirements related to this functionality are **REQ-SYS-TEC-GRD-1.6**.
- **O-F3 Launch System.** To enter flight, the system must be launched. For this, a Launcher rail has been designed according to **REQ-SYS-TEC-GRD-1.2, 1.3**. Additionally, to ensure portability according to **REQ-SYS-TEC-GRD-1.6**, the Launcher can be packed inside the transport system infrastructure.
- **O-F4.4 Process Data.** The data that is collected by the operational swarm must be received and processed by the ground station to update the risk map and the swarm strategy, according to **REQ-SYS-OPS-PLD-1**.
- **O-F4.5 Distribute Commands.** Once the data is processed, the ground station shall be able to transmit data and commands to the drone swarm. For this, an antenna and radio interface must be designed or selected. This is currently outside the scope of the report.
- **O-F5 Recover System.** To recover from flight, the drones must be brought to a full stop according to **REQ-SYS-TEC-GRD-1.4**. This is done by using an Arrestor Gear, of which the design is discussed at the end of the section.
- **O-F6 Transport System.** After end of operations, the entire system must be transported back to the storage facility.

Firstly, the aerodrome is designed in subsection 8.3, and the interaction between different components, together with the transport logistics, is described in subsection 8.3.

Aerodrome

The aerodrome intended to fulfil functions O-F3 and O-F5 are designed. The aerodrome comprises the Launcher Rail for Take-off and an Arrestor Gear for landing and recovery. These components must be sized to ensure that the takeoff and landing loads are sustainable for the UAV's structure. Additionally, the design ensures the system's manufacturability and portability. Figure 67 includes detailed diagrams to illustrate the final design of these features.

UAV Electric Launcher

As seen in Figure 67a, the drones are launched through an electrically actuated system. The system goal is to accelerate the drone above its stall speed to a velocity of V_{TO} , in the smallest possible distance and without subjecting it to unsustainable acceleration loads. An electric motor applies a force $F = \frac{T}{r}$ to the pulley cable, where T is the applied torque and r is the moment arm. The cable transmits the motion to the cart that supports the drone on the rail. The radius at which the cable is attached to the rotating shaft of the motor is constrained by the maximum speed that has to be achieved in the cart, which is also the speed at which the cable is pulled.

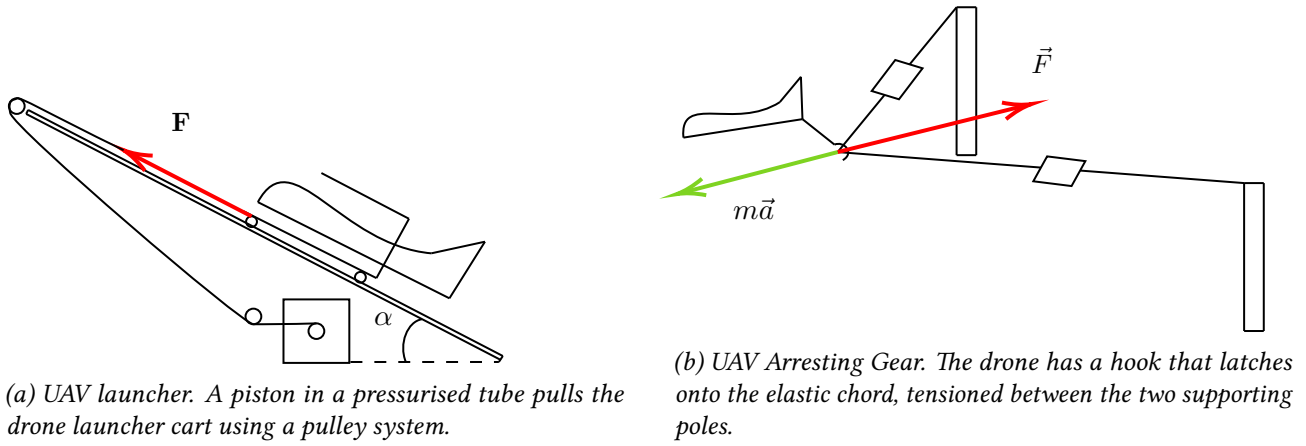


Figure 67: UAV launch and recovery systems.

This means that $r = V/\omega$, where ω is the RPM (Revolutions Per Minute) of the motor. In turn, this means that $F = T\omega/V$. The drone is pulled through the length of the launch rail, l_{TO} , and it accelerates to the take-off speed V_{TO} in time t_{TO} . The objective of the sizing is to calculate l_{TO} as a function of all other parameters. The Free Body Diagram (FBD) in Figure 68 represents the situation more in detail.

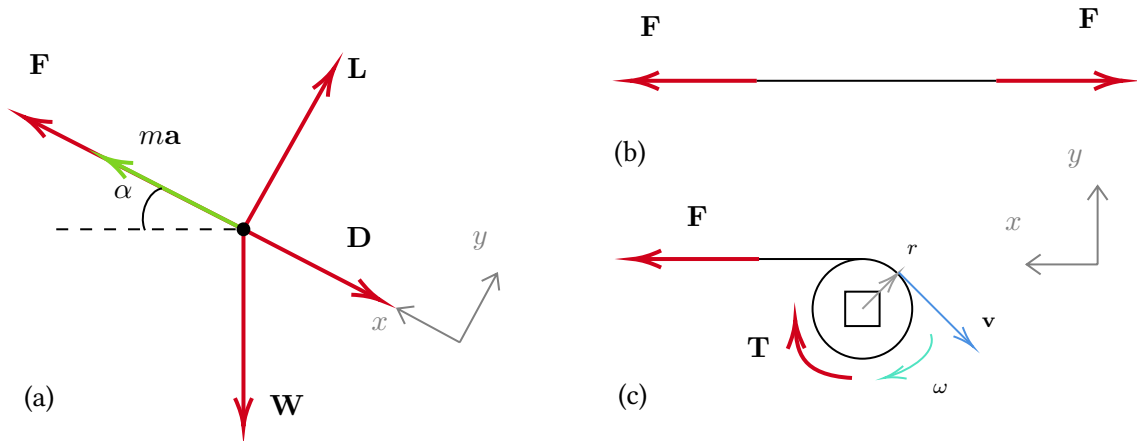


Figure 68: FBD of the pneumatic system. (a) FBD of the UAV while in the launch rail. (b) FBD of the cable transmitting the motion and (c) FBD of the piston.

From Figure 68, the equation for force along the UAV x-axis is derived in Equation 110.

$$\sum F_x : F - D - W \sin \alpha = ma \tag{110}$$

To simplify the analysis, the assumptions stated below have been made.

1. Drag is negligible at the low speeds associated with the takeoff and landing of the UAV. This is essentially a linearization of the equations of motion, as neglecting drag means eliminating the quadratic velocity term. This important assumption leads to a possible underestimation of the required launch rail length, which must be verified and possibly discarded.
2. The UAV can withstand a maximum acceleration along its x-axis between 5 and 6 g. This is inferred from pre-existing pneumatic launcher designs, such as the UKRSpec GLS-1A [143], which launches at 8.3g, and the ElevationX Scorpion, which launches similarly-sized drones at 8.5g [144].
3. The UAV has a stall speed V_{stall} of 20 [m/s]. This is not an assumption, as this is required by **REQ-SYS-TEC-UNI-1.6**. However, to rule out the possibility that due to imperfections or mechanical losses the

drone reaches the end of the Launcher rail before achieving an airspeed larger than the stall speed, a safety factor of 1.15 has been used, raising the take-off speed V_{TO} to 23 [m/s]

Applying the assumptions above to Equation 110, a linear differential equation is obtained and stated in Equation 111.

$$\frac{dV}{dt} = \frac{T\omega}{mV_{TO}} - g \sin(\alpha) \quad (111)$$

Motor Selection Using Equation 111 with $m=15\text{kg}$ (taken from section 7.10), a launch angle α of 25 degrees, and a maximum acceleration of 5.75g following from assumption 3, the following plot (Figure 69) is obtained for required motor torque as a function of required motor RPM. As can be seen in Figure 69, the inflexion point of the Torque-RPM curve is close to the origin. To avoid restraining the motor selection, keeping the RPM requirements in a range of 1800 - 3600 RPM is best. The research found that most motor catalogues have the largest availability regarding different motor models and specifications in this range¹. In light of this, a choice was made to take an RPM value of 3000, meaning the required torque T is 66.50 [Nm]. Many commercially available motors can meet these specifications.

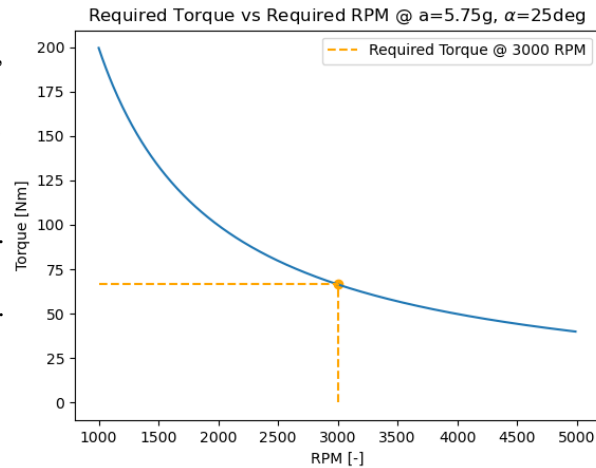


Figure 69: Required motor Torque as a function of required motor RPM. The point represents the chosen RPM and the corresponding required Torque.

Although a trade-off could be performed in this situation, because the Launcher motor selection is not particularly influential on the rest of the design as long as the selected motor is up to specification, the **Rockwell Automation 480 V ac Servo Motor**² was picked. This motor can spin at 3000 RPM and provide a maximum torque of 87 Nm.

Launch Rail Sizing To determine the minimum required length of the launch rail, l_{TO} , the analytical solution of Equation 111 and its derivative are necessary. These are stated in Equation 112 and Equation 113.

$$V(t) = \left(\frac{T\omega}{mV_{TO}} - g \sin(\alpha) \right) t + C_1 \quad (112)$$

$$l(t) = \frac{1}{2} \left(\frac{T\omega}{mV_{TO}} - g \sin(\alpha) \right) t^2 + C_1 t + C_2 \quad (113)$$

The boundary conditions are: $V(0) = 0$ [m/s] and $l(0) = 0$ [m], hence $C_1 = C_2 = 0$. Using the newly found $\omega = 3000$ [RPM], $T = 66.5$ [Nm], and again $m = 15$ [kg], $\alpha = 25$ [deg], and $V_{TO} = 23$ [m/s], a minimum required launch rail length l_{TO} of 4.75 [m] was found. For extra safety, this length can be rounded up to 5 [m] without significant concerns, as the only other requirement on launch rail length is **REQ-SYS-TEC-GRD-1.6**, constraining it such that the rail fits within the container used for transport. The launch system consists of several components. These components include the wire, pneumatic piston, truss structure, and rail. Each element has specific design requirements to meet the overall system performance criteria.

¹Source: Baldor Motor Catalogue, <https://www.baldor.com/catalog>

²<https://nl.rs-online.com/web/p/servo-motors/2561952>

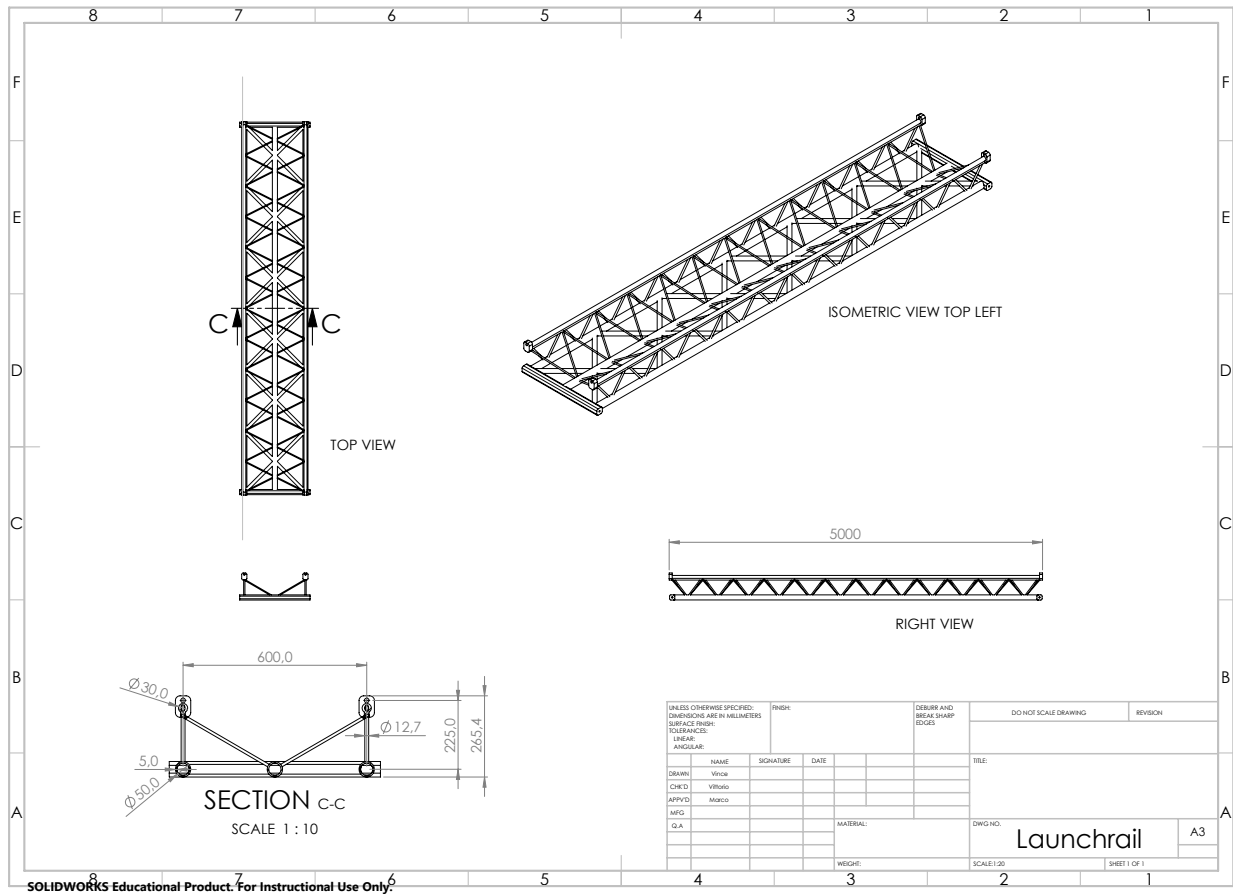


Figure 70: A CAD model of the launcher system.

Wire The wire of the launch system must be capable of withstanding forces without yielding or failing. To ensure this, it is crucial to consider the stress imposed on the wire and keep it within safe limits, as defined by the material’s yield strength. The normal stress, σ_n , in the wire can be calculated by dividing the force by the cross-sectional area of the wire. To ensure the wire does not fail, the following condition must be satisfied: $\sigma_{yield} > |\sigma_n|$. Where σ_{yield} is the yield strength of the wire material. This ensures that the wire can handle the operational forces without experiencing permanent deformation or failure.

Truss Structure The truss structure of the launch system is constructed from aluminium due to its advantageous properties. Aluminium is lightweight, relatively inexpensive, and durable. Its durability is essential for withstanding environmental elements, thus ensuring the truss maintains its integrity over time. However, according to Ashby et al., [145], aluminium corrodes when in contact with peat (acidic soil). A protective coating must be applied to prevent direct contact between the aluminium and peat.

Additionally, a CAD model of the truss and rail was developed and used to estimate the total mass of the Launcher system. The final value is 75 [kg], with a 95% confidence interval of 50-100 [kg]. The technical drawing is shown in Figure 70.

UAV Arresting System

A similar analysis to the one conducted in the previous subsection can be used to size the Arrestor gear. The Arrestor gear essentially functions as a reverse slingshot: two beams placed at a distance l from each other hold a slightly tensioned, elastic wire of unstretched length roughly equal to l at a certain height h . The landing drone flies into the wire, hanging onto it with its arrestor hook. The wire deforms, therefore slowing the UAV down due to the elastic force. Dampeners can be included at the base of the wire and tuned in order to achieve critical damping and bring the drone to a stop in a faster manner. Figure 67b shows the two forces mainly acting on the drone + arresting gear system. A more accurate depiction of the geometry and forces is presented in Figure 71. The distance between the two beams, the elastic and damping coefficients, as well as the height of the beams need to be chosen/sized in this subsection.

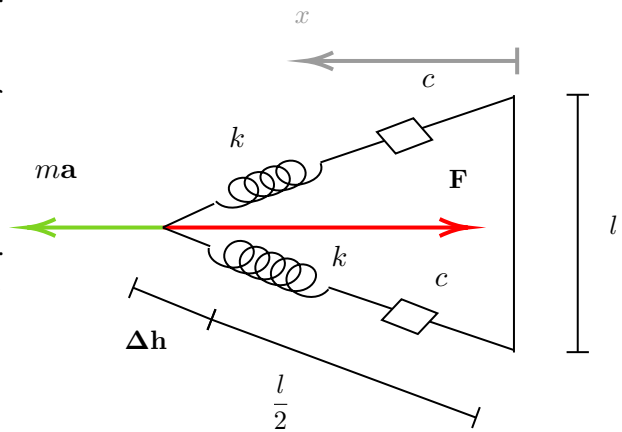


Figure 71: FBS of the arresting gear

From the geometry shown in Figure 71, the following expression for the elastic cord elongation Δx is derived in Equation 114.

$$\Delta x = 2\sqrt{\left(\frac{l}{2}\right)^2 + \Delta h^2} - l \quad (114)$$

Slingshot Sizing The goal is to obtain an estimate for the maximum extension of the wire, as well as a minimum required beam distance and height.

The equation of motion along the x-axis is given in Equation 115.

$$m \frac{d^2 x}{dt^2} + 2c \frac{dx}{dt} + 2k \sqrt{\left(\frac{l}{2}\right)^2 + x^2} - kl = 0 \quad (115)$$

Equation 115 represents a second-order, non-linear, non-homogeneous differential equation in x , which is solved numerically using the `scipy.integrate` module in Python. The boundary conditions are $V_0 = V_l$ [m/s] and $x_0 = 0$ [m], indicating the velocity and position with respect to the arresting gear at $t = 0$ [s].

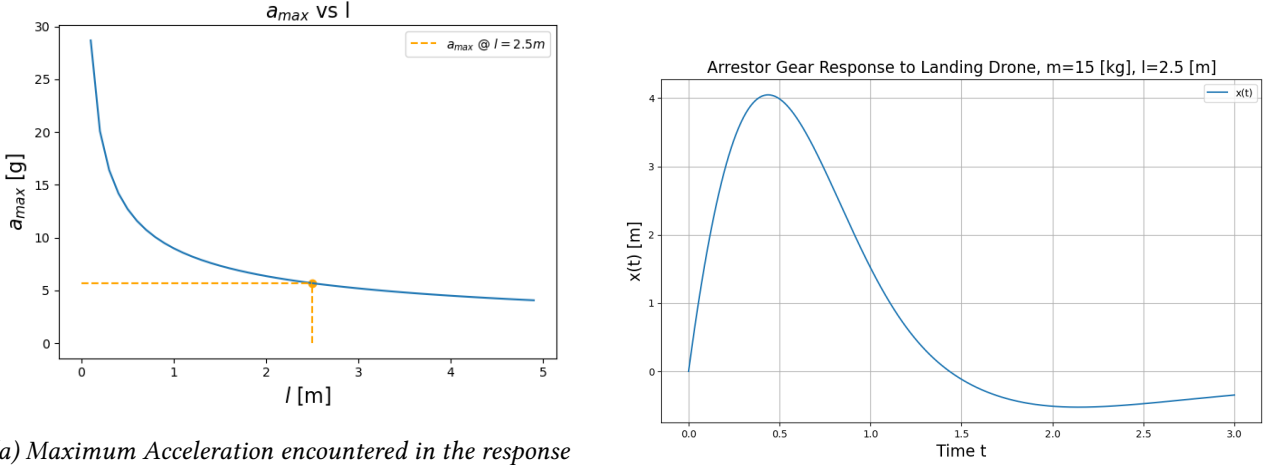
To obtain numerical values for the maximum deflection, a material for the wire must be selected. To keep it simple, Styrene Butadiene Rubber is directly chosen for the wire, with a Young's Modulus of 10 [MPa]^3 . This is a relatively stiff rubber that was found to perform relatively well as a wire material, as will be shown in the results of this subsection. Given E , the elastic coefficient k of the wire is given by

$$k = \frac{\pi r^2 E}{l} \quad (116)$$

Where r is the wire cross-sectional radius, assumed to be 2.5 [mm] , the damping coefficient c is 0.6 (found by simulation) and l is the wire length, e.g. the distance between the two I-beams. This parameter can be varied to obtain a plot of the maximum acceleration a_{max} obtained from the response function to Equation 115, with respect to the beam distance l . From the resulting plot (Figure 72a), it appears that at around $l = 2.5 \text{ [m]}$, lowering the boom distance more cause increasingly larger values of a_{max} . To keep the Arrestor gear within reasonable dimensions while still abiding by the maximum g-force TOL requirement (**REQ-SYS-TEC-GRD-1.3**), $l = 2.5 \text{ [m]}$ has been chosen. The response of the Arrestor gear to a UAV of mass 15 [kg] attaching to it

³<https://www.azom.com/properties.aspx?ArticleID=1844>

with a horizontal velocity of 20 [m/s] (equal to the stall speed, e.g. the speed the UAV has when landing) is shown in Figure 72b.



(a) Maximum Acceleration encountered in the response vs distance between booms. With $l = 2.5$ [m], $a_{max} = 5.67$ [m/s²]

(b) Position and Acceleration as a function of time, $l = 2.5$ [m].

Figure 72: Arresting gear maximum acceleration and response function.

Figure 72b shows that the maximum elongation of the arresting gear, during landing of a regular UAV, is about 4 [m]. This is horizontal elongation, however because the UAV slows down rapidly, in reality this displacement will be pointed at an angle towards the ground. This means that, in the worst case scenario, it is sensible to constrain the booms height h to be at least 4 [m] too.

Finally, both the wire and poles (I-beams) must withstand the operational forces without failure. This is achieved by calculating the normal stress on both components and comparing it to the yield strength of the employed materials. These normal stresses can be obtained with Equation 117 and Equation 118 [138]. At the same time, the spring constant of the wire can be computed with Equation 116 [138].

$$\sigma_{n_{wire}} = \frac{N}{A} = \frac{T}{4\pi r^2} \quad (117) \quad \sigma_{n_{pole}} = \frac{My}{I} = \frac{6LhT}{(bh^3 - b_f h_f^3)} \quad (118)$$

$$T = \frac{F}{2} \sqrt{1 - \left(\frac{l^2}{l^2 + 4\Delta x^2} \right)} \quad (119)$$

Here, T represents the tension in the wire resulting from the force F . For the arresting system to be safe and reliable, it is crucial that both the wire and poles satisfy the condition $\sigma_{yield} > |\sigma_n|$. This requirement ensures that they can withstand the applied forces without permanent deformation or failure. By meeting this criterion, the arresting system operates within the material's elastic limit, ensuring durable and dependable performance. Additionally, the bending angle of the poles can be determined using Equation 120; typically, this deflection angle should not be greater than 1 degree [138].

$$\theta = \frac{12L^2T}{E(bh^3 - b_f h_f^3)} \quad (120)$$

The result of the abovementioned structural estimations is as follows: where according to Hibbeler [138], the normal stresses in the wire and poles are less than the yield stress of the used materials.

$$\sigma_{n_{wire}} = 4.15[\text{MPa}] \quad \sigma_{n_{pole}} = 4.25[\text{MPa}] \quad T = 326[\text{N}] \quad \theta = 0.05[\text{deg}]$$

Component interaction and transport

This section shows how the different ground systems interact with each other in a physical sense, as well as how they are stored during transportation and set up for use. An artistic visualisation of the system is shown in Figure 73. A full system containing 25 drones will be transported in two containers; only one is shown for clarity. An operator is included for scale.



Figure 73: Artistic visualisation of the ground system with the rail and backup generator already dismantled

The container is a standard 20-foot shipping container. These are cheap, available, and made to be easily transported. Shipping containers are also somewhat waterproof and can be securely locked, making them convenient and secure storage options. After the operator opens the container, two planks can be removed and placed in front of the container. These planks are at the same height as the container floor and serve as an even surface for the internal roll-out structure. Furthermore, the planks distribute the pressure of the wheels and prevent them from getting stuck in the ground.

Next, the inner structure can be rolled out. This wheeled structure matches the container in width and length but is slightly shorter by approximately 0.5 meters. One side of the internal structure does not have cross-beams, which allows the operator to access the underside of the structure. Here, up to 14 drones are hanging nose-up in a row. The drones hang nose-up to place the centre of gravity as far up as possible to minimise swinging during transport. The drones can be easily taken off their respective hook and carried out by a single operator.

On the short side of the structure, a ladder is present that provides access to the top platform. Here, other ground system components are stored. The launch system and one side of the arrestor structure are included in the container shown, next to the communications parabolic dish and a generator. The second container would, in this case, carry the rest of the arrestor mechanism. The satellite dish is permanently placed on top.

Whereas the operator would lower the other parts to ground level, where they can be assembled and put somewhere else near the container but at a safe distance. On top of the container are 6 solar panels of 400 W, each providing power to the ground system and power for recharging the drones. One backup generator per container, so two in total, is also included in case of solar obstruction or solar panel malfunction. This generator, which would also be stored on the top platform, is shown in red in the render. An overall overview of the hardware of the ground station and the aerodrome can be seen in Figure 74.

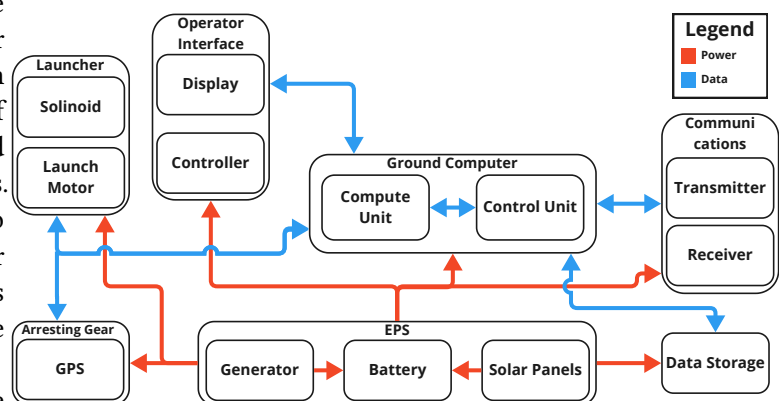


Figure 74: Hardware Diagram of the Ground Station

MANUFACTURING AND INTEGRATION PLAN

In order to streamline the production process and provide a general overview of the system integration order, a manufacturing flowchart has been presented in Figure 75. As seen from the chart, the system assembly has been split into three sections, each one of which is elaborated on below. After each section has been completed, the system is finalised and ready for quality control. With the quality control passed, the system is ready to begin operation.

In order to minimise costs and risks of human errors, the entire production line is planned to ultimately be fully automated and robotised, with the exception of the vehicle painting. This can change when the production grows beyond the initial estimates, the manufacturing plan will need to be adjusted to the new situation in case of rapid business growth.

9.0.1 Risks & Requirements

The relevant risks for the manufacturing from Table 50 are:

- **REQ-SYS-CON-STB-1.1:** The manufacturing process of the system shall not include any toxic materials.
- **REQ-SYS-CON-STB-1.4:** The delivery of the system to its operational location shall not produce more than 0.5 kg of CO₂ per km.
- **REQ-SYS-CON-STB-1.6:** The end of life disposal procedure shall be able to recycle at least 90% of the materials.
- **REQ-SYS-CON-STB-3.2:** The adoption of the system shall be announced to the local public before being operated.

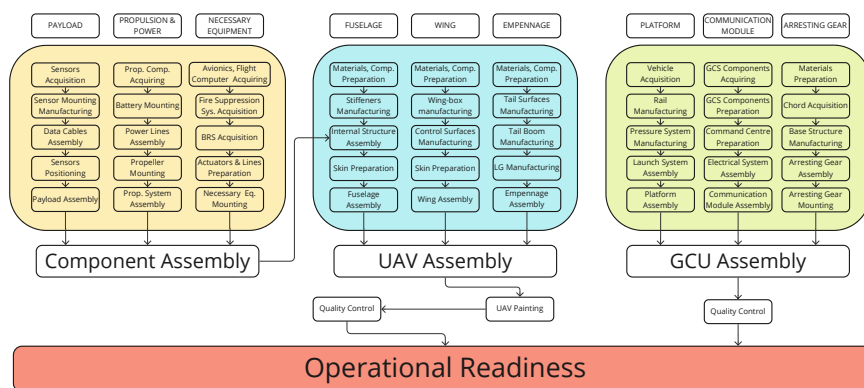


Figure 75: UAV manufacturing flow plan

9.1 COMPONENT ASSEMBLY

Components of the vehicle are the core of the system and, as such, need to be realised in the first stage of the production process. The UAV assembly can not proceed without the internal components mounted inside of the fuselage; that is why all of the components need to be ready for assembly. The components itself consist of three groups. The payload is the most important part of the vehicle mission-wise. All of the payload needs

to be carefully sourced and prepared for the mission. Power and propulsion components are vital to the operations of the vehicle. This system assembly consists mainly of mounting the battery and power lines. The entire propulsion system needs to be carefully placed and prepared to ensure safe operations. The necessary equipment of the vehicle consists of everything needed for safe and reliable operations, including the Ballistic Recovery System (BRS), Fire Suppression System (FSS), power lines and actuators used for control of the aircraft, but also avionics and flight computer, which are absolutely necessary for any aerial vehicle.

9.2 UAV ASSEMBLY

The vehicle structure itself consists of three main groups: the fuselage, wing and empennage. All groups are planned to be realised simultaneously to increase efficiency and minimise waiting time. All groups start with material preparation, proceed with manufacturing structural elements, and finish assembling all components into a full vehicle. The fuselage production will first focus on creating the aircraft's internal skeleton and assembling it with the components already in place. Once the vehicle skeleton is ready, the skin is laid in panels on the structure and fastened together on site. The wing follows a similar path to the fuselage production, first the wing-box, the main stiffening load bearing element of the wing, is manufactured. The control surfaces are then produced and connected with the commercially sourced mechanisms and actuators attached through the wing box. Lastly, the skin is laid on the entire structure, closing the wing. The empennage has the most extraordinary elements of the vehicle. Due to the lack of structural stiffeners inside the tail, the tail surfaces are first manufactured and assembled with internal control mechanisms. Then, the boom tails are manufactured to bridge the empennage and the rest of the vehicle. Lastly, the landing gear (LG), which is a long hook, is manufactured and connected to the rest of the structure. With all groups completed, the vehicle is assembled together, painted and subjected to quality control (QC). If passed, the vehicle achieves operational readiness.

9.3 GCU ASSEMBLY

Similarly to the previous sections, the Ground Control Unit (GCU) production also consists of three separate groups. The platform is the base of the entire ground station; the communication module is the command centre and the base of operations of the swarm, and the arresting gear is used for landing. The platform itself is based on the back of a motor vehicle to ensure the mobility of the system. Therefore, the process starts with the vehicle acquisition. Then, the take-off system manufacturing starts with the rail and the pressure system production. The launch system is assembled on top of the vehicle and that concludes the platform assembly. The communication module starts with purchasing the pre-selected commercial components, connecting them to a command centre and assembling the entire electrical system. Then, the entire module is assembled and stored. The arresting gear of the system consists of the base structure and an elastic chord used for UAV landing. The entire structure is manufactured and assembled on-site. Then, the system is mounted together and stored. With the GCU components finished, the entire station can be assembled together, after which the system undergoes QC. If passed, the GCU achieves operational readiness.

9.4 LOGISTICS

With the general outline of the system manufacturing presented, the logistics and operations of the production process need to be addressed. The following section presents the quantities, timelines and logistical approach to production. The system production and assembly will occur in the same country to ensure a smooth and efficient production course, without high costs or delays. Due to the fact that the system has been developed with Europe-based operations in mind, coupled with the necessity for low production costs, it has been deemed necessary to choose a country within the EU with relatively low production costs and sufficient infrastructure for production. This will flow from future financial analysis on the swarm production. The facilities will consist

of a structural manufacturing plant and an assembly line plant combining all components. A preliminary

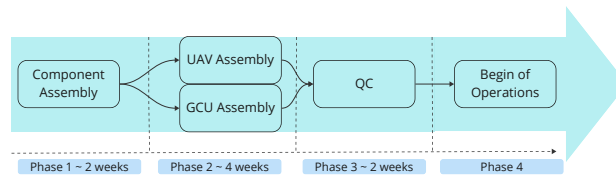


Figure 76: Production flow and preliminary timeline

manufacturing timeline is shown in Figure 76. Excluding delivery times and transportation, each drone is estimated to take around 8 weeks to produce from zero until operational readiness. Multiple vehicles undergo various stages of production at the same time, optimising the timeline with the principles of lean manufacturing. It is expected that around 90 drones can be produced within one year, which translates to three complete swarms.

DESIGN ASSESSMENT

This chapter treats the topic of design assessment. To begin with, a presentation of the requirements compliance verification in section 10.1, followed by the RAMS analysis in section 10.2.

10.1 REQUIREMENT COMPLIANCE VERIFICATION

In this final section of the design assessment, the final design is verified by checking the compliance status of the previously generated requirements presented in Table 50 in Appendix A. This is done in the form of a compliance matrix for all the system requirements. This was not expanded to include all the subsystem requirements, as the top-level system requirements are only met when all the subsystem requirements that stem from them are also met. Along with the compliance status of each requirement, the verification method has been listed in the form of a testing ID. Here the letters mean **A - Analysis**, **D - Demonstration**, **I - Inspection** and **T - Testing**.

Table 37: Compliance Matrix

ID [REQ- SYS-...]	Requirement	Compliance Status	Rational	Verifi- cation
Subsystem Requirements				
Technical Requirements				
Unit Performance				
TEC- UNI-1	The flight performance of the unit shall be able to sustain all flight operations.	✗	REQ-SYS-TEC-UNI-1.3 was not met. The unit was sized for 5 hours of endurance as explained in section 7.6	A, D, T
TEC- UNI-2	The flight control stability of the unit shall be able to sustain all flight operations.	✓	All subsystem requirements are met, as described in section 7.5	A, D
TEC- UNI-3	The unit emergency recovery system shall be able to recover the unit during any phase of mission.	✓	All subsystem requirements are met, as described in subsection 7.9.5	A, D, T
TEC- UNI-4	The communication system shall ensure communication between the ground station and active units, at all times.	✓	All subsystem requirements are met, as described in chapter 6	A, D, I, T
TEC- UNI-5	The structure of the unit shall ensure structural integrity in all operating conditions.	✓	All subsystem requirements are met, as described in section 7.8	A, I, T
Swarm Performance				
TEC- SWM-1	The swarm system shall be able to coordinate the movement of every airborne unit.	✓	All subsystem requirements are met, as described in section 5.1	A, D, T
Ground System Performance				
TEC- GRD-1	The ground system shall be able to support the continuous operation of the swarm.	✓	All subsystem requirements are met, as described in chapter 8	A, D, T

Table 37 – continued from previous page

ID [REQ- SYS-...]	Requirement	Compliance Status	Rationale	Verifi- cation
Operational Goals				
Payload				
OPS- PLD-1	The monitoring units shall be able to collect sufficient data for the mission success.	✓	All subsystem requirements are met, as described in section 4.4	A, D, T
Avionics				
OPS- AVI-1	Each unit shall be able to measure all the state-data required to allow for automatic flight.	✓	All subsystem requirements are met, as described in section 7.7	T
Mission Constraints				
Safety				
CON- SFT-1	The individual system units shall perform the mission safely.	✓	All subsystem requirements are met, as described in section 5.1	D, T
CON- SFT-2	The system shall ensure the safety of its operators.	-	REQ-SYS-CON-SFT-2.1 has not been yet complied to, as it is dependent on the correct training of the operators and is outside the conceptual scope of this project.	D, I
CON- SFT-3	The system shall not harm the environment.	✓	All subsystem requirements are met, as described in section 7.6	I, T
Resources				
CON- RSC-1	The project shall stay within the allocated budget.	✓	All subsystem requirements are met, as described in Table 11.2.4	I
CON- RSC-2	The project shall be completed within the set time.	✓	All subsystem requirements are met, as described in chapter 9	D, I, T
Legality				
CON- LGL-1	The system shall comply to all certification requirements.	-	This requirement cannot be met yet, as it requires the application for special FAA regulations. This would happen at a later stage within the system development.	I
CON- LGL-2	The production of the system shall comply with local and international legislation.	-	This requirement cannot be met yet, as it is dependent on the particular area of operations for the system and it is assessed on a case by case basis.	I
CON- LGL-3	The system's operations shall adhere to the local and international legislations.	-	This requirement cannot be met yet, as it is dependent on the particular area of operations for the system and it is assessed on a case by case basis.	I
Sustainability				
CON- STB-1	The system shall meet the predetermined environmental sustainability requirements.	✗	REQ-SYS-STB-1.6 was not met. While the entirety of the structure of the UAV's structure is recyclable, the batteries cannot be recycled as of today. This is explained further in section 3.5.	I, T
CON- STB-2	The system shall be designed for economic sustainability.	✓	All subsystem requirements are met, as described in section 3.5	D

Table 37 – continued from previous page

ID [REQ- SYS-...]	Requirement	Compliance Status	Rationale	Verifi- cation
CON- STB-3	The system shall meet the predetermined societal sustainability requirements.	✓	All subsystem requirements are met, as described in section 3.5	D, T

While two subsystem requirements have not been complied with and some have a status that is still pending, the majority of the key requirements have been met. Furthermore, for those that have not been met, the team made sure that they would not cause a failure of the system's mission, as they didn't impact the outcome fatally.

10.2 RAMS ANALYSIS

The RAMS analysis for the wildfire prediction and detection drone swarm underscores the importance of reliability, availability, maintainability, and safety in enhancing operational effectiveness and resilience during firefighting operations. By adhering to these principles, stakeholders can ensure the drone swarm operates optimally in detecting wildfires, facilitating real-time communication between firefighters and ground stations, and ultimately supporting swift and coordinated responses to wildfire emergencies.

10.2.1 Reliability

Reliability is fundamental for the drone swarm, predicting and detecting wildfires and ensuring consistent and accurate operation in identifying and forecasting wildfires. The drones should achieve a high Mean Time Between Failures (MTBF), targeting 5 hours of operational flight time. Redundant sensors and communication systems are essential to mitigate single points of failure. The ground station, acting as the central control hub, must be equipped with redundant power sources and communication links to ensure continuous operation, thereby enhancing overall system reliability. The launcher system should also be reliable and robust, facilitating rapid deployment of drones in response to wildfire alerts.

10.2.2 Availability

Availability focuses on ensuring the drone swarm is deployable at all times, particularly during peak wildfire seasons. The target availability during wildfire seasons should exceed 95% [146]. This requires efficient maintenance schedules and readily available spare drones to minimise downtime. The ground station's redundancy in power sources and communication links plays a crucial role in maintaining the high availability of the drone swarm system. Additionally, the robustness of the launcher system ensures that drones can be deployed swiftly and reliably, contributing to overall system availability.

10.2.3 Maintainability

Ensuring prompt repair and maintenance of drones and communication systems is essential to minimise operational disruptions. Designing drones for easy maintenance is crucial, with a target Mean Time to Repair (MTTR) of less than 5 hours for minor issues. It is assumed that the maximum MTTR should be around 5% of the typical 100-hour A check for commercial aircraft [147]. Standardised components and modular designs enable quick field repairs. Redundant systems and communication links at the ground station improve reliability and simplify maintenance, reducing the risk of extended downtime from infrastructure issues. A reliable launcher system enhances maintainability by swiftly redeploying drones after maintenance or repairs.

10.2.4 Safety

Safety is paramount in the operation of the drone swarm, particularly in shared airspace with firefighting aircraft and secure data transmission. Drones must prevent incidents with firefighting aircraft. The launcher system's reliability and the ground station's redundant infrastructure enhance safety by ensuring that drones can be launched and controlled safely in diverse environmental conditions. Using an arresting system for drone landings further enhances safety, enabling controlled landings even in challenging terrain or adverse weather conditions, thereby minimising risks to both the drones and surrounding personnel.

FINANCIAL VALUATION

Understanding the financial implications of the project is critical to ensuring its success and sustainability. This chapter examines the economic aspects of the drone swarm. Firstly, Table 11.1.1 provides a detailed breakdown of the costs associated with the design, development, and deployment phases, including expenses for hardware, software, and operations. In Table 11.2.4, the comprehensive landscape of UAV-based wildfire management is analysed, covering both the wildfire management and drone markets and addressing stakeholders and potential buyers. The entire analysis has been performed in US dollars because most components and services are listed in the currency, as well as that 80% of wildfire startups are located in the United States [3].

11.1 COST ANALYSIS

This section analyses the costs of the system, over the entire lifetime. First, the R&D costs are found, then the manufacturing costs and finally, the operational costs are estimated. At the end of the section, a complete overview of the total costs is given.

11.1.1 Risks & Requirements

The relevant risks from section 3.6 are:

- **R-T-06:** certification cost exceed budget
- **R-T-07:** Operational cost exceed budget
- **R-T-08:** Production cost exceed budget
- **R-T-09:** Maintenance cost exceed budget

The relevant requirements from Table 50 are:

- **REQ-SYS-CON-RSC-1.1:** The marginal cost of one system shall not cost more than \$ 1.8 million.
- **REQ-SYS-CON-RSC-1.2:** The total operating cost of one system shall not cost more than \$ 650 per hour.
- **REQ-SYS-CON-RSC-1.3:** The units shall promote ease of development with a modular design.
- **REQ-SYS-CON-RSC-2.1:** The manufacturing of one system shall not take longer than 8 weeks.
- **REQ-SYS-CON-RSC-2.2:** The operational lifetime of one system shall be of at least 12 years.
- **REQ-SYS-CON-RSC-2.3:** The system shall be designed with existing technology.

Research, Development, Test, and Evaluation Cost Research, Development, Test, and Evaluation (RDT&E) costs encompass all expenses associated with designing, developing, integrating, and testing a new system or technology to ensure it meets required specifications and is ready for production. These costs include labour, ground station & software development, testing facilities, and other necessary resources for validating and refining the system.

The salary of an engineer is approximately US\$63 per hour¹. When considering that the cost of an employee is 30% higher than their salary², the total hourly cost of an engineer is US\$81.90 per hour. The DSE has 3760 hours of work. However, to fully design, manufacture and test a product, more time is required. New technologies can sometimes take years to enter the market, therefore a development time of 5 years is estimated³.

The ground station development cost encompasses the development of the launcher, recovery system, ground communication systems and ground station software. The development costs for the ground station can be estimated as per Equation 121

$$Cost_{GS} \approx US\$55,000 * EOM * CEF(2004) \quad (121)$$

Here, EOM is the empty mass of the UAV in [kg] and CEF is the cost escalation factor since 2004 to account for inflation [44]. As of 2024, the $CEF(2004)$ is 1.70. The estimation of the ground station cost is based on the Global Hawk and DarkStar CGS development, likely underestimating the cost for small UAVs [44]. However, it does provide an initial estimate.

To estimate the software cost, which excludes the ground station software, two factors are taken into account. Firstly, the cost of an autopilot for student projects range from US\$0.5k - 5k . However, small UAS autopilot developments can cost up to US\$300k [44]. Another estimation method is

$$Cost_{software} \approx US\$8600 * EOM * CEF(2004) \quad (122)$$

Using Equation 122 would result in a software cost of approximately US\$ 150k, which is in the middle of the first estimate. This estimate will be used.

Lastly, the cost for testing the drone is considered. For this the assumption is made that 40 hours of wind-on time is needed to fully characterise the drone [44]. Wind tunnel cost can be estimated with Equation 123.

$$Cost_{WT} = T_{WT} \cdot (R_{WT} + N_{pers} \cdot R_{pers}) + C_{travel} + C_{model} \quad (123)$$

Here, T_{WT} is the time spent in the wind tunnel and R_{WT} is the hourly cost of the wind tunnel, which is assumed to be \$1200 per hour [44]. N_{pers} & R_{pers} are the number and cost of engineers. Wind tunnel testing will be performed by 3 members of the design team. C_{travel} is assumed to be negligible, and C_{model} is also assumed to be negligible compared to the wind tunnel cost, as the model will be made out of foam and plastic.

Component Costs The component costs of the drone comprise all the payload and avionic sensors, flight computers, batteries, motors, propellers, communication infrastructure, actuators, and materials for the structure. Some components are specific to the relay or surveying drones. To keep development costs as low as possible for the system, commercial off-the-shelf components are used where possible. The total component costs for the UAV, the payload and the ground station are found in Table 39, Table 40 and Table 41. When specific cost data is not available, estimations with provided ranges are used to ensure accurate budgeting and cost management.

One component that requires analysis is the battery. Because Amprius⁴ does not disclose the price of the batteries chosen in subsection 7.6.2, an estimated price is extrapolated from the market. Figure 77 illustrates the forecasted battery density and price through 2030. As of 2024, battery prices are \$100 per kWh. The system's development is expected to be completed post-2024, leading to further reductions in battery costs.

¹Engineer salary. URL: <https://www.bls.gov/ooh/architecture-and-engineering/aerospace-engineers.htm>

²Wage vs cost. URL: <https://business.gov.nl/running-your-business/staff/payment-and-wages/overview-of-personnel-costs/>

³Development time, estimated in discussion with Linh

⁴Amprius Technologies, Url: <https://amprius.com/products/>

Consequently, the 2024 price is considered an upper-bound estimate, with the 2030 forecast providing a lower bound.

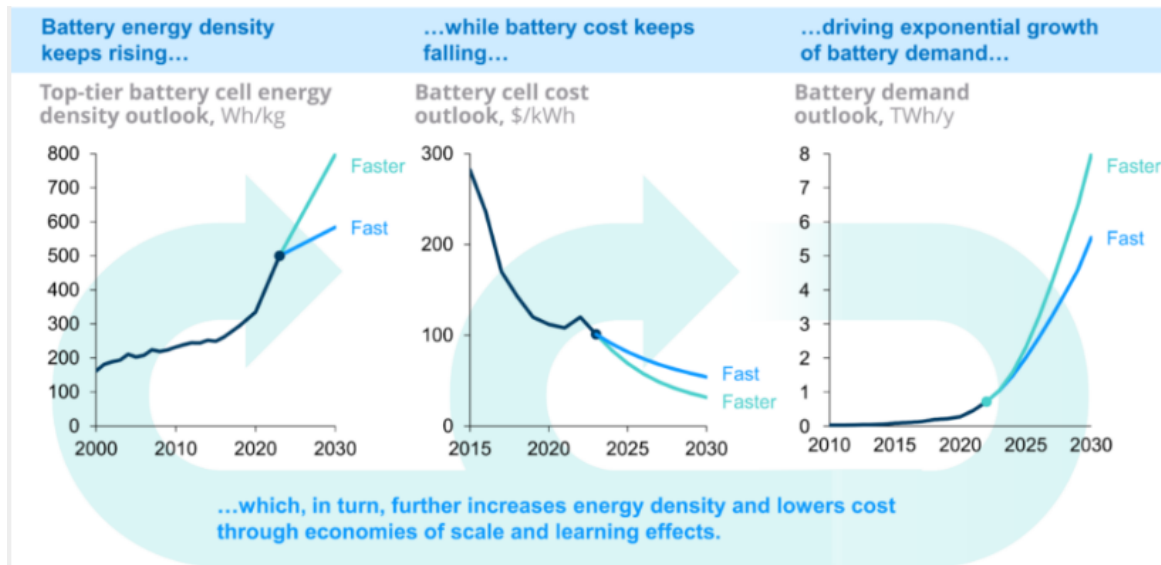


Figure 77: A reinforcing feedback loop between battery quality, cost and market size [‡]. Source: Ziegler and Trancik (2021) before 2018 (end of data), BNEF Long-Term Electric Vehicle Outlook (2023) since 2018, BNEF Lithium-Ion Battery Price Survey (2023) for 2015-2023, RMI analysis.

Manufacturing costs The manufacturing costs for the drone system are primarily determined by the labour hours required for production, and the costs of equipment. These costs are estimated using a parametric formula that accounts for the empty weight of the aircraft and the material factor. The formula is given by [44]:

$$Hr_{\text{Manf, RDTE}} = 10.4 \cdot W_E^{0.605} \cdot f_{\text{Matl}} + T_{\text{manf}} * R_{\text{pers}} \quad (124)$$

where $Hr_{\text{Manf, RDTE}}$ represents the manufacturing labour hours, W_E is the empty weight of the drone, and f_{Matl} is a material factor that varies depending on the construction materials used (e.g., metal, composites, wood). For the drone f_{Matl} is equal to 1. Note that these are cost estimations for small-scale production. Here, each drone is expected to take 3 days to manufacture. To comply with **REQ-SYS-CON-RSC-2.2**, 3 manufacturers are needed. If the system is deployed at a larger scale, these costs could be significantly reduced due to economies of scale and more efficient manufacturing processes. Table 11.2.4 outlines potential drone manufacturers who might be interested in manufacturing the system at a more commercially viable scale.

Operational Costs The operational costs are all the costs for the customer (e.g. a fire department) when using the system. All these costs occur only after the drone swarm has been purchased. The succes of the system is dependent on whether **REQ-SYS-CON-RSC-1.2** is met, which implies that the operational costs should be beneficial to the costs of alternative monitoring methods.

The first cost in operations is the transport of the drones to the search area. The fuel costs depend on the distance travelled and the fuel price. The maximum drive time is based on European Regulation (EC) No 561, which limits the daily driving hours to 9 ⁵. During operations, the operators are paid an hourly rate, which are assumed to cost \$81.90 an hour, as estimated in the RDT&E cost estimation. Additional costs are recharging costs for the batteries, which are governed by local electricity costs. additionally, the batteries need to be replaced every 300 cycles, therefore the difference between buying and selling value of the batteries

⁴energypost newsletters, url: <https://energypost.eu/batteries-are-still-getting-exponentially-cheaper-more-efficient-re>

⁵Regulation (EC) No 561. URL: <https://transport.ec.europa.eu/transport-modes/road/social-provisions/driving-time-and-rest-periods>

is considered in the operational costs. Lastly, two hours of inspection is scheduled after a mission. These inspection costs are as a contingency to cover any potential damages or maintenance that is not quantifiable at this stage in the design. For a primary estimate it is based on the salary of an engineer. Additionally, four hours are expected for single drone maintenance after BRS landings, which are expected to occur 0.1% of the time. With 20 drones, BRS maintenance is expected once every 50 missions. A final overview of operational costs is given in Table 42. The total operational cost for a 2 week mission is US\$28,774 at most, of which 92% are operator wages. This is approximately US\$ 200 per flight hour (excluding insurance), which is beneficial to the section 5.3 mentioned Beachcraft King Air 350, which has an operating cost of US\$1300 per flight hour. Therefore it also meets **REQ-SYS-CON-RSC-1.2**.

End of Life Costs To stay in line with sustainability goals, the drones must be recyclable. The entire drone is built out of aluminium, which can be recycled. All internal components can be repurposed in less critical environments, except for the batteries. As a first order estimate, the end of life costs are assumed to be only recycling / disassembling costs. The labour for recycling is assumed to be half the manufacturing labour.

Total Swarm Costs From all estimated costs, the total cost of the swarm can be deduced. It comprises of the cost of the UAVs, the ground station and specific payload. The cost is shown in Table 43. The total cost of at most US\$ 755,146 complies with requirement **REQ-SYS-CON-RSC-1.1**.

Table 38: Development Costs of the Wildfire Drone Swarm. All upper limits accounted for 5 year average US\$ inflation

Description	Amount/Hours	Lower limit cost	Upper limit cost	Source
Development Costs				
Design team	5 [years]	\$ 7,534,800	\$ 8,675,696	[44]
Software Development	1	\$ 205,849.60	\$ 237,018.71	[44]
Ground Station Development	1	\$ 1,316,480.00	\$ 1,515,817.32	[44]
Testing	40 [hours]	\$ 57,828.00	\$ 66,584.14	[44]
Total Cost	-	\$ 9,114,957	\$ 10,495,116	

Table 39: UAV costs excluding the UAV specific payload. All upper limits accounted for 5 year average US\$ inflation

Description	Amount/Hours	Lower limit cost	Upper limit cost	Source
UAV Costs Excluding specific Payload				
Inertial Measurement Unit (IMMU)	1	\$ 41.00	\$ 47.21	website ¹
GPS	1	\$ 50.00	\$ 57.57	website ²
AoA Sensor	1	\$ 30.00	\$ 34.54	website ³
Battery	2	\$ 430.20	\$ 495.34	Estimation in Table 11.1.1
Fire suppression	1	\$ 70.00	\$ 80.60	website ⁴
Propeller	1	\$ 10.26	\$ 11.81	website ⁵
Electric Motor	1	\$ 108.00	\$ 124.35	website ⁶
ESC	1	\$ 95.00	\$ 109.38	website ⁷
CPU	1	\$ 105.54	\$ 121.52	website ⁸
Data Storage	1	\$ 30.00	\$ 34.54	website ⁹
Pitot Tube	1	\$ 56.00	\$ 64.48	website ¹⁰
Humidity, Pressure, Altitude sensor	1	\$ 17.95	\$ 20.67	website ¹¹
Actuators	6	\$ 1442.01	\$ 1660.35	website ¹²
Aluminium Structure + Skin	7.57 [kg]	\$ 102.91	\$ 118.49	website ¹³
Radio interface device	1	\$ 3,126.51	\$ 3,599.92	website ¹⁴
Patch antenna	16	\$ 57.92	\$ 90.82	website ¹⁵
Manufacturing	24 [hours]	\$ 2,017.12	\$ 2,322.54	[44]
End of Life	12 [hours]	\$ 1,008.56	\$ 1,161.27	[44]
Total Costs	-	\$ 8,798.97	\$ 10,115.42	

Table 40: Drone Specific Payload Costs. All upper limits accounted for 5 year average US\$ inflation

Description	Amount/Hours	Lower limit cost	Upper limit cost	Source
Observer Drone Specific Payload Cost				
Blade antenna	1	\$ 3,438.00	\$ 3,958.57	²⁰
IR Camera: Teledyne Flir Boson 640 (95deg FOV)	1	\$ 4,104.00	\$ 4,725.41	website ¹⁶
NIR Camera: Sentera Single Sensor	1	\$ 1,400.00	\$ 1,842.27	website ¹⁷
Visual Camera: Caddx Loris 4k	1	\$ 90.00	\$ 103.63	website ¹⁸
LiDAR RIEGL™VUX-160 (1 per swarm)	1	\$ 140,000.00	\$ 161,198.37	Quotation ¹⁹
Total Cost (Excluding LiDAR)	-	\$ 9,032.00	\$ 10,629.88	-
Relay Drone Specific Payload Cost				
Phased Array System	1	\$ 319	\$500	website ¹⁵

Table 41: Ground Station Costs. All upper limits accounted for 5 year average US\$ inflation

Description	Amount/Hours	Lower limit cost	Upper limit cost	Source
Ground Station Costs				
TOL Truss structure	1	\$ 1,026.00	\$ 1,181.35	website ²¹
Launching rail motor	1	\$ 3,832.79	\$ 4,413.13	website ²²
Antenna	1	\$ 10,000.00	\$ 17,271.25	website ²³
Truck	2	\$ 50,000.00	\$ 69,085.01	website ²⁴
Container	2	\$ 4,000.00	\$ 4,605.67	website ²⁵
Container interior	2	\$ 4,800.00	\$ 5,526.80	website ²¹
Total Costs	-	\$ 74,010.95	\$ 102,488.72	

¹IMMU. URL: <https://eu.robotshop.com/products/bno055-9-dof-absolute-orientation-imu-fusion-breakout-board>²GPS. URL: <https://www.droneshop.nl/gnss-compass-mateksys-m10q-5883>³AoA Sensor. URL: https://eu.mouser.com/ProductDetail/ams-OSRAM/AS5048A-TS_EK_AB⁴Fire suppression. URL: <https://brimstonefireprotection.com/>⁵Propeller. URL: <https://www.apcprop.com/product/13-5x13-5/>⁶Electric Motor. URL: <https://www.mad-motor.com/products/mad-components-5015-ipe-v3.html?VariantsId=10470>⁷ESC. URL: <https://www.mad-motor.com/products/ampx-60a-5-14s.html>⁸CPU. URL: <https://www.raspberrystore.nl/PrestaShop/nl/raspberry-pi-v5>⁹Data Storage. URL: <https://www.westerndigital.com/products/memory-cards/sandisk-extreme-pro-sd-uhs-ii-v60?sku=SDSDXEP-064G-GN4IN>¹⁰Pitot Tube. URL: <https://www.3dxr.co.uk/product/matek-systems-digital-air-speed-sensor-aspd-4525/>¹¹Humidity, Pressure, Altitude sensor. URL: <https://www.kiwi-electronics.com/nl/bme280-breakout-temperature-pressure-humidity-sensor-9901>¹²Actuators. URL: <https://www.horizonhobby.com/product/a6350-ultra-torque-high-speed-brushless-hv-servo/SPMSA6350.html>¹³Aluminium cost. URL: <https://www.gemmel-metalle.de/>¹⁴RID, Quotation email can be found in meeting minutes¹⁵Patch antenna. URL: <https://www.kyocera-avx.com/product/wi-fi-bt-zigbee-ceramic-patch-2-4-ghz-antenna-1003468/>¹⁶IR camera. URL: <https://www.oemcameras.com/thermal-imaging-cameras/thermal-imaging-cores/flir-boson-series>¹⁷NIR camera. URL: <https://senterasensors.com/hardware/sensors/single/>¹⁸Visual camera. URL: <https://oscarliang.com/>¹⁹LiDAR, Quotation email can be found in meeting minutes²⁰Blade antenna, Quotation email can be found in meeting minutes²²Launch rail motor. URL: <https://nl.rs-online.com/web/p/servo-motors/2561952>²³GS Antenna. URL: <https://www.extendingbroadband.com/bts-90/>²⁴Truck cost. URL: <https://insurancehub.com/how-much-does-a-semi-truck-cost/>²⁵Container Cost. URL: <https://www.brinkbox.nl/assortiment/20ft/20ft-zeecontainer-nieuw>²²Container Interior. URL: <https://www.alumeco.com/aluminium/profiles/square-tube/>²⁶Website. URL: <https://example.com>²⁷Engineer salary. URL: <https://www.bls.gov/ooh/architecture-and-engineering/aerospace-engineers.htm>²⁸US gas prices. URL: <https://gasprices.aaa.com/>²⁹Drone Certification. URL: <https://thedroneguide.com/drone-license-cost/>

Table 42: Operational Costs for a 2 Week Operation. All upper limits accounted for 5 year average US\$ inflation

Description	Amount/Hours	Lower limit cost	Upper limit cost	Source
2 Week Operational Costs				
Battery Charging	1686 [kWh]	\$ 281	\$ 324	website ¹
Inspection	14 [hours]	\$ 1,147	\$ 1,320	Engineer cost ²
Maintenance	1.12 [hours]	\$ 92	\$ 106	Engineer cost ²
Transport	2-18 [hours]	\$ 80	\$ 829	Fuel costs ³
Operator Costs	112-140 [hours]	\$ 18,346	\$ 26,404	Engineer cost ²
Total Cost	-	\$ 19,764	\$ 28,775	-

Table 43: Total Costs of the Swarm. All upper limits accounted for 5 year average US\$ inflation

Description	Amount/Hours	Lower limit cost	Upper limit cost
Drone Specific Payload Cost			
Empty UAV	30	\$ 263,969	\$ 304,662
Observer Drone Payload	24	\$ 216,768	\$ 255,000
Relay Drone Payload	6	\$ 1,911	\$ 2,997
1 LiDAR per Swarm	1	\$ 140,000.00	\$ 161,198.37
Ground Station	1	\$ 74,010.95	\$ 102,488.72
Drone Certification ²⁹	25	\$ 4,000.00	\$ 4,605.67
Total Cost	-	\$ 696,659	\$ 826,463

11.2 MARKET ANALYSIS

This section analyses the comprehensive landscape of UAV-based wildfire management. It will discuss the wildfire management market as well as the drone market. After which stakeholders, and buyers are addressed.

11.2.1 Risks & Requirements

The relevant risks from section 3.6 are: **R-T-23**: Model doesn't/stops improving and **R-T-24**: system is replaceable. The relevant requirements from Table 50 are:

- **REQ-SYS-CON-STB-2.1**: The system shall be modifiable to reflect the changing needs of the stakeholders.
- **REQ-SYS-CON-STB-2.2**: The system shall be modifiable to reflect the needs of different markets.
- **REQ-SYS-CON-STB-2.3**: The unit shall be inspectable.
- **REQ-SYS-CON-STB-2.4**: The unit shall be maintainable.

11.2.2 Market Definition

To fully assess the market for UAVs in wildfire management, The market for both the wildfire management, and drones looked at. The markets are fundamentally different: the drone market is competitive, while the wildfire management market is collaborative. Both come with their own stakeholders and dynamics. Figure 78 provides an overview of both markets.

Market Segments Firstly, the wildfire management market is categorised into three segments shown in Figure 78. Urban firefighting primarily presents humanitarian challenges, including evacuation efforts, whereas the non-urban segment encounters difficulties related to resource availability and accessibility [150]. Firefighting focuses on extinguishing the fire, whereas fire monitoring involves continuously observing and

Wildfire Management Market

Forecast period: (2023-2028)



Major Parties Involved

- Government Agencies
- Firefighting Departments
- Forestry Services
- Firefighting Plane Manufacturers
- Equipment Manufacturers
- Environmental Organisations
- Research Institutes
- Investors

Market Segmentations

- By End Use**
 - Urban
 - Non-Urban
- By Functionality**
 - Firefighting
 - Fire Monitoring
- By Technology**
 - Ground Based
 - Air Based
 - Satellite Based



Drone / UAV Market

Forecast period: (2024-2031)



Major Players

- DJI
- Parrot SA
- 3D Robotics, Inc
- Autel Robotics
- Kespry Inc.
- PrecisionHawk Inc.
- AeroVironment, Inc.
- Aeryon Labs Inc.
- FLIR Systems, Inc.
- Ehang
- Draganfly Innovations Inc.
- CyPhy Works, Inc.
- Airware, Inc.
- Skydio, Inc
- Walkera Technology
- MMC UAV
- Airbus

Market Segmentations

- By Drone Type**
 - Rotary Wing
 - Fixed Wing
 - Hybrid Wing
- By Application**
 - Hobbyist
 - Agricultural
 - Inspection
 - Delivery
 - Surveying
 - Cinematography
 - Reconnaissance
 - Combat

Figure 78: Wildfire Management Market & Stakeholder Overview. Data obtained from [3, 148, 4, 149]

assessing fire behaviour, environmental conditions, and potential risks to anticipate and prevent fire-related hazards. Lastly, the technology can be divided into ground-based, air-based, and satellite-based systems. The previously mentioned distinction between pre-, during and post-wildfire management can be made in all segments. Considering the system proposed, it is segmented as Non-Urban, Fire Monitoring and Air Based. Secondly, the drone/UAV market is segmented by drone type into rotary-wing, fixed-wing, and hybrid-wing categories. Additionally, it is divided by application, with various applications listed in Figure 78. The relevant segment for the system is the fixed-wing reconnaissance/surveying drone.

Market Dynamics The market dynamics of wildfire management are influenced by various growth drivers and restraints. The rising number of wildfires heightened awareness [148], and government initiatives in forest conservation [3], alongside stringent climate goals, are propelling the market growth. However, the market faces challenges such as the lengthy certification process for new aerial technologies and the extreme operating environments [150]. The drone market is mainly driven by the rising demand for photographic surveillance and the increased adaption of drones across various industries [149]. The market is held back by strict regulations and safety concerns.

Market Size As outlined in chapter 2, wildfires represent a serious issue projected to worsen in the coming years. In response to these statistics, governments worldwide increased the budget allocated to direct wildfire

response (firefighting) by around 50% [3]. However, the wildfire management budget is increasingly allocated towards prevention, prediction and recovery of wildfires, which claim two-thirds of the total budget [3]. In the United States, the Department of the Interior has requested US\$1.6 billion as their wildfire management budget for 2025 [151]. Out of this total, US\$1.26 is planned to be spent on wildfire preparedness and recovery.

The Institute for Defence and Government Advancements has conducted global wildfire management research, which concluded the following overview presented in Table 44. The columns show the budget allocated for each sector over a time span between 2023 and 2028.

Table 44: Global Wildfire Management Market, 2023-2028, US\$ Millions [3]

Types	2023	2024	2025	2026	2027	2028
Aerial Firefighting Capabilities	\$1,419.3	\$2,040.7	\$2,089.1	\$2,261.3	\$2,351.3	\$2,760.9
Fuel Management and Controlled burns	\$237.0	\$313.2	\$296.1	\$302.2	\$170.0	\$182.4
Mobile Communications	\$76.5	\$80.4	\$49.2	\$44.5	\$44.0	\$48.3
Remote Sensing Technologies	\$92.4	\$86.2	\$45.8	\$56.2	\$61.5	\$66.3
UAS (Unmanned Aerial Systems)	\$52.1	\$56.4	\$21.6	\$25.2	\$27.0	\$31.0
Other	\$692.9	\$637.5	\$746.6	\$713.9	\$474.4	\$506.9
Total	\$2,570.3	\$3,214.4	\$3,248.3	\$3,403.2	\$3,128.3	\$3,595.9

As shown in Table 44 and Figure 78, the market for wildfire management is expected to grow by 40% from 2023 to 2028, with a compound annual growth rate (hereafter: CAGR) of 6.9% [3]. Within the overall market, aerial firefighting capabilities are expected to increase in value rapidly in the coming years. This is mainly due to the United States being expected to spend around US\$10 billion dollars on leasing aerial equipment for firefighting [3]. It should also be noted, that at the start of 2024, the US Congress banned Chinese drones from the US market [152]. This has an effect on the Unmanned Aerial Systems (UAS) market size in the US, which is projected to decrease heavily in 2025, which can be seen in Table 44. Aside from this irregularity, the UAS market continues to grow.

The drone market is experiencing growth even more, as can be seen in Figure 78. With a CAGR of 25% it is expected to grow from US\$22.4 Billion to US\$166.7 Billion in 9 years [149]. This is mainly because of the aforementioned market drivers, being increased demand and adoption of drone technologies. Additionally, the FAA is expected to lift strict regulations on the number of drones per operator, which is a big opportunity for the drone market.

Stakeholders Lastly, the stakeholders are explored. To relate this to the proposed drone swarm both markets again need to be analysed. Because of the competitive nature of the drone / UAV market, the only major players (also shown in Figure 78) are drone manufacturers [149]. A share of these companies have an interest in the project as they are potential manufacturers of the proposed system. They can have an interest in collaboration, or in buying the developed concept. However, they can also be seen as competitors trying to produce a similar product. The wildfire management market has more parties involved, all with different functions. Governments, forestry services and environmental organisations drive the actions taken to preserve forests, whilst firefighting departments execute the fire control. The proposed system can provide better wildfire management by the fire departments, thereby satisfying the desires of these organisations. Plane and equipment manufacturers provide the means that fire departments need to work. They are crucial in the manufacturing of the system. Research institutes aim to improve the general methodology of fire management, who have, considering the novelty of the swarm a great interest in the technology. Lastly, investors are crucial as a catalyst of innovation. Figure 79 shows funding for startup types and locations for 10 highlighted startups by The Institute for Defence and Government Advancements' Wildfire Management Market Report. It indicates that the majority of funding

is directed towards software and satellite innovation, while drone startups remain an area with potential. Additionally, most of the funding is located in the United States. The expected development costs of the drone swarm are US\$ 10.5 Million, which is in the same order of magnitude as the funding received by the startups.

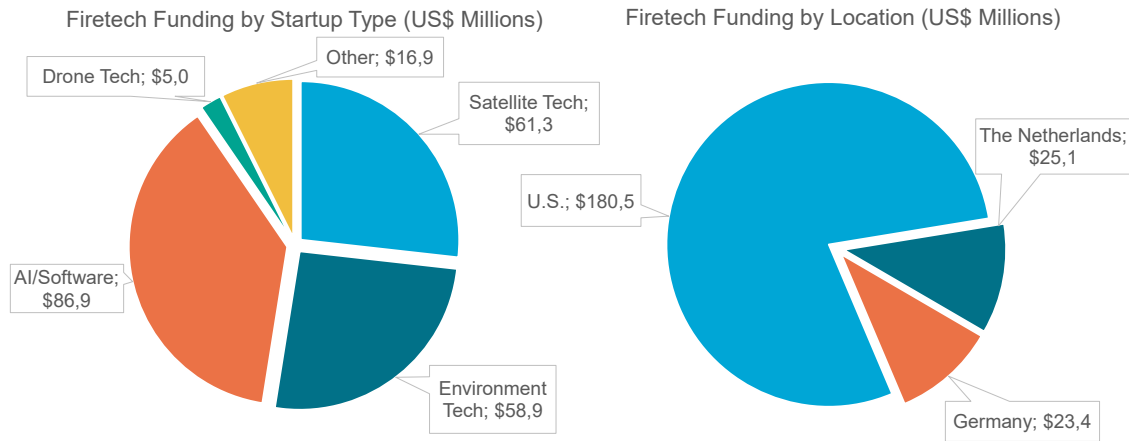


Figure 79: Firetech funding by type and location [3]

11.2.3 Market Positioning

After having explored the market in subsection 11.2.2, this subsection will position the system in the market, thereby defining its strengths, weaknesses, opportunities and threats (SWOT) and give a final list of project stakeholders along with their influence and interest. Both are summarised in Figure 80.

Wildfire Surveillance Drone Swarm Market Positioning

SWOT Analysis



Key Stakeholders

	Influence	Interest
Primary		
• Government Agencies	<div style="width: 75%;"></div>	<div style="width: 75%;"></div>
• Firefighting Departments	<div style="width: 75%;"></div>	<div style="width: 75%;"></div>
• Forestry Services	<div style="width: 75%;"></div>	<div style="width: 75%;"></div>
• Investors and Funders	<div style="width: 75%;"></div>	<div style="width: 75%;"></div>
• Drone Manufacturers	<div style="width: 75%;"></div>	<div style="width: 75%;"></div>
• Software Developers	<div style="width: 75%;"></div>	<div style="width: 75%;"></div>
Secondary		
• Environmental Organisations	<div style="width: 50%;"></div>	<div style="width: 75%;"></div>
• Insurance Companies	<div style="width: 50%;"></div>	<div style="width: 75%;"></div>
• Research Institutes	<div style="width: 50%;"></div>	<div style="width: 75%;"></div>

*In our case TU/eDelft has big influence, this is however not generally the case

Figure 80: Positioning in the Market of the Proposed Wildfire Drone Swarm [3, 148, 4, 149]

With the opportunities presented in Figure 80, the budget for wildfire management increasing and the fact that the product provided is not yet implemented, there is a perfect window to penetrate the market. Additionally, the growing drone market will allow for better scaling and lower manufacturing costs in the future. Generally, all stakeholders show a moderate to high level of interest in the system. However, drone and software developers exhibit the lowest interest, as their involvement is primarily tied to the production of the system. They have the flexibility to shift their focus to manufacturing alternative products if desired.

11.2.4 Return on Investment

This subsection proposes a selling price for the drone system and analyses the viability in the Californian wildfire management environment. The system has a proposed selling value of US\$900,000. From REQ-STK-LG-2 the cost of the system should be a tenth of the total wildfire prevention cost. California is spending US\$

600 Million on wildfire prevention in 2025⁶, therefore the budget for the system is US\$ 60 million annually. Given that the forested area of California amounts to around 133,546 km squared ⁷, approximately 133 swarms are required to effectively monitor the forests. This adds up to US\$ 119.7 Million for the swarm. Additionally, assuming the system is operating during the 20 hottest weeks of the year, the maximum cost for operations is:

$$10 \text{ operations} \cdot 28,775 \cdot 133 = \text{US}\$38,270,000 \quad (125)$$

Considering the assumed 10 year lifetime of the system, the annual cost percentage of the system is:

$$\text{Annual Cost Percentage} = \left(\frac{117,900,000 + 10 \cdot 38,270,000}{10 \times 600,000,000} \right) \times 100 \approx 8.34\% \quad (126)$$

Therefore the system meets **REQ-STK-LG-2** as the Californian government only has to allocate 8.34% of their wildfire budget to the systems. The return on investment of the system is:

$$\text{ROI} = \left(\frac{\text{Total Profit}}{\text{Initial Investment}} \right) \times 100 = \left(\frac{900,000.00 - 826,000.00}{826,000.00} \right) \times 100 \approx 8.9\% \quad (127)$$

In summary, the project offers a sustainable and financially viable solution for wildfire prevention in California, providing a significant return on investment while contributing to the safety and preservation of forested areas. Table 45 shows the final results for both the upper and lower limits.

Table 45: Financial Case Study Values

<i>Description</i>	<i>Values with Lower Limit Cost</i>	<i>Values with Upper Limit Cost</i>
Total Operations Cost	\$ 265,270,000	\$ 385,470,000
Total Swarm Cost	\$ 119,700,000	\$ 119,700,000
Annual Cost Percentage for Californian Government	6.42%	8.42%
Return on Investment	29.19%	8.90%

⁶Californian wildfire budget. URL: <https://lao.ca.gov/Publications/Report/4495>

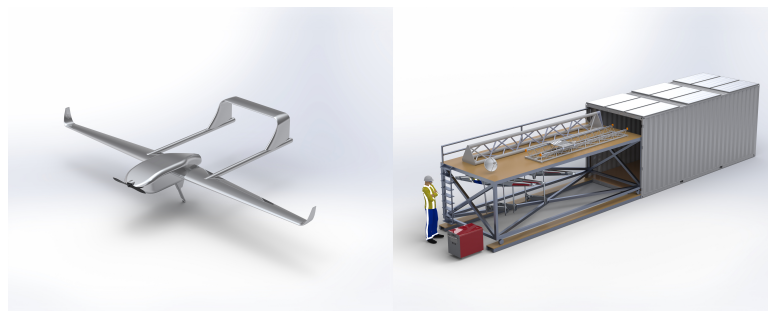
⁷Forest acres California. URL: <https://www.calforestfoundation.org/resource/california-forests>

CONCLUSION AND RECOMMENDATIONS

In 2022, Europe experienced severe wildfires, marking one of the most devastating years since 2006 regarding wildfire impact [1]. The increasing frequency and intensity of wildfires globally, exacerbated by human actions and climate change, underscore the urgent need for advanced wildfire management solutions (UN Wildfire Report). The Netherlands Aerospace Centre (NLR) has proposed a pioneering solution: a UAV swarm designed to monitor high-risk forests and gather critical environmental data [3]. This innovative approach aims to significantly enhance wildfire detection capabilities and provide early warnings through predictive modelling, thereby revolutionising current wildfire management strategies. By preemptively predicting and detecting wildfires, the system promises substantial reductions in forest loss, CO₂ emissions, and societal disruptions.

Integrating cutting-edge technologies such as autonomous UAVs ensures rapid response times and continuous, high-resolution monitoring, which are crucial for effective wildfire containment and mitigation. This approach enhances operational efficiency and minimises risks to firefighting personnel, particularly under challenging conditions such as nighttime operations or dense smoke environments. The financial analysis highlights the system's potential cost-effectiveness and market viability, projecting a significant increase in global demand for wildfire management technologies in the coming years [3]. This aligns the system with current market trends and positions it to address critical environmental and economic needs. In conclusion, introducing the wildfire drone swarm represents a transformative leap in wildfire management, promising enhanced safety, efficiency, and environmental stewardship. As wildfires continue to pose escalating threats worldwide, innovative solutions like the UAV swarm offer a proactive and sustainable approach to protecting communities and ecosystems [3].

The project aims to enhance drone capabilities through targeted improvements: increasing the coverage area of drones with laterally gimballed cameras within 3 months; integrating rectangular sector generation algorithms within 2 months for improved mission planning flexibility; integrating near Hamiltonian and spiral path generation algorithms within 3 months to enhance navigation adaptability; updating the swarm algorithm within 6 months to handle imperfect sensor data; conducting 6 months of research on fire and smoke attenuation mechanisms; and developing a flight profile for wildfire scenarios within 2 months. These initiatives aim to advance operational efficiency, expand technological capabilities, and improve response effectiveness in critical scenarios. Looking past recommendations into the capabilities of the wildfire drone swarm, it becomes evident that the system is versatile and capable of various applications involving any surveillance or communication relay functions, natural disaster rescue or defence applications. Moreover, since the payload module is exchangeable, the system offers a multi-use swarm of adjustable aerial platforms capable of carrying anything required by the user (within the mass limit). With all this in mind, the Wildfire Drone Swarm system is not only a new approach to wildfire management but also an adjustable framework upon which other, more complex projects with endless objectives can be built.



(a) Rendition of the UAV

(b) Ground Station Graphical

Figure 81: Renders

BIBLIOGRAPHY

- [1] San-Miguel-Ayanz, J., Durrant, T., Boca, R., Maiani, P., Libertà, G., Oom, D., Branco, A., Suarez-Moreno, M., Ferrari, D., Roglia, E., Scionti, N., De Rigo, D., and Broglia, M., *Forest fires in Europe, Middle East and North Africa 2022*, Publications Office of the European Union, 2023.
- [2] United Nations Environment Program (UNEP), "Spreading like Wildfire – The Rising Threat of Extraordinary Landscape Fires," feb 2022, <https://www.unep.org/news-and-stories/press-release/number-wildfires-rise-50-2100-and-governments-are-not-prepared>, Accessed: 2024-05-21.
- [3] Institute for Defence and Government Advancements, *Wildfire Management Market Report 2023-2028*, New York, NY, 2023, Accessed: 2024-05-01.
- [4] Boroujeni, S. P. H., Razi, A., Khoshdel, S., Afghah, F., Coen, J. L., O'Neill, L., Fule, P., Watts, A., Kokolakis, N.-M. T., and Vamvoudakis, K. G., "A comprehensive survey of research towards AI-enabled unmanned aerial systems in pre-, active-, and post-wildfire management," *Information Fusion*, Vol. 108, 2024, pp. 102369.
- [5] Sikkink, P. G. and Keane, R. E., "A comparison of five sampling techniques to estimate surface fuel loading in montane forests," *International Journal of Wildland Fire*, Vol. 17, No. 3, 2008, pp. 363 – 379, Cited by: 70.
- [6] Chamberlain, C. P., Sánchez Meador, A. J., and Thode, A. E., "Airborne lidar provides reliable estimates of canopy base height and canopy bulk density in southwestern ponderosa pine forests," *Forest Ecology and Management*, Vol. 481, 2021, pp. 118695.
- [7] Power, L., *Global wildfires, carbon emissions and the changing climate*, Future Directions International, 2013.
- [8] Service, C. A. M., "2023: A year of intense global wildfire activity," *Copernicus Atmosphere Monitoring Service*, 2023, Accessed: 2024-05-21.
- [9] Ritchie, H., "What share of global CO2 emissions come from aviation?" *Our World in Data*, 2024, <https://ourworldindata.org/global-aviation-emissions>.
- [10] Hurteau, M. D., Westerling, A. L., Wiedinmyer, C., and Bryant, B. P., "Projected effects of climate and development on California wildfire emissions through 2100," *Environmental science & technology*, Vol. 48, No. 4, 2014, pp. 2298–2304.
- [11] Burke, M., Driscoll, A., Heft-Neal, S., Xue, J., Burney, J., and Wara, M., "The changing risk and burden of wildfire in the United States," *Proceedings of the National Academy of Sciences*, Vol. 118, No. 2, 2021, pp. e2011048118.
- [12] Brito, T., Pereira, A., Lima, J., Castro, J., and Valente, A., "Optimal Sensors Positioning to Detect Forest Fire Ignitions," 01 2020, pp. 411–418.
- [13] AEM, "Weather Station Sensors: Types, Use Cases, & Selection Criteria," <https://blog.aem.eco/weather-station-sensors>, Blog post.
- [14] Nakata, M., Sano, I., Mukai, S., and Kokhanovsky, A., "Characterization of Wildfire Smoke over Complex Terrain Using Satellite Observations, Ground-Based Observations, and Meteorological Models," *Remote Sensing*, Vol. 14, No. 10, 2022.
- [15] Carta, F., Zidda, C., Putzu, M., Loru, D., Anedda, M., and Giusto, D., "Advancements in Forest Fire Prevention: A Comprehensive Survey," *Sensors*, Vol. 23, No. 14, 2023.
- [16] Payra, S., Sharma, A., and Verma, S., "Chapter 14 - Application of remote sensing to study forest fires," *Atmospheric Remote Sensing*, edited by A. Kumar Singh and S. Tiwari, Earth Observation, Elsevier, 2023, pp. 239–260.
- [17] NASA Earthdata, "Geographic Information Systems (GIS)," <https://www.earthdata.nasa.gov/learn/backgrounders/gis>, Accessed: 2024-06-05.
- [18] Abbenhuis, E., Agterdenbos, J., Bonanno, V., Camporeale, M., Do Cao, K., Kleipool, B., Lubbers, V., Mielczarek, A., Nakagawa, T., and Petrache, A., "Wildfire Drone Swarm Project Plan," Tech. rep., Technische Universiteit Delft, April 2024.
- [19] Li, F., Zhang, X., and Kondragunta, S., "Biomass Burning in Africa: An Investigation of Fire Radiative Power Missed by MODIS Using the 375 m VIIRS Active Fire Product," *Remote*

- Sensing*, Vol. 12, No. 10, 2020.
- [20] Federal Aviation Administration, “Unmanned Aircraft Systems (UAS),” <https://www.faa.gov/uas>, Accessed: 2024-05-01.
- [21] Nitoslawski, S., Wong-Stevens, K., Steenberg, J., Witherspoon, K., Nesbitt, L., and Konijnendijk van den Bosch, C., “The Digital Forest: Mapping a Decade of Knowledge on Technological Applications for Forest Ecosystems,” *Earth’s Future*, Vol. 9, No. 8, 2021, Cited by: 34; All Open Access, Gold Open Access.
- [22] Hartley, R. J. L., Davidson, S. J., Watt, M. S., Massam, P. D., Aguilar-Arguello, S., Melnik, K. O., Pearce, H. G., and Clifford, V. R., “A Mixed Methods Approach for Fuel Characterisation in Gorse (*Ulex europaeus* L.) Scrub from High-Density UAV Laser Scanning Point Clouds and Semantic Segmentation of UAV Imagery,” *Remote Sensing*, Vol. 14, No. 19, 2022.
- [23] Krisanski, S., Taskhiri, M. S., Gonzalez Aracil, S., Herries, D., Muneri, A., Gurung, M. B., Montgomery, J., and Turner, P., “Forest Structural Complexity Tool—An Open Source, Fully-Automated Tool for Measuring Forest Point Clouds,” *Remote Sensing*, Vol. 13, No. 22, 2021.
- [24] Krisanski, S., Taskhiri, M. S., Gonzalez Aracil, S., Herries, D., and Turner, P., “Sensor Agnostic Semantic Segmentation of Structurally Diverse and Complex Forest Point Clouds Using Deep Learning,” *Remote Sensing*, Vol. 13, No. 8, 2021.
- [25] “FAA BEYOND Program,” https://www.faa.gov/uas/programs_partnerships/beyond, Accessed: April 30, 2024.
- [26] Larrinaga, A. R. and Brotons, L., “Greenness Indices from a Low-Cost UAV Imagery as Tools for Monitoring Post-Fire Forest Recovery,” *Drones*, Vol. 3, No. 1, 2019.
- [27] Copernicus Atmosphere Monitoring Service, *2023: A year of intense global wildfire activity*, European Centre for Medium-Range Weather Forecasts, January 2024.
- [28] Ritchie, H. and Roser, M., “CO₂ emissions,” *Our World in Data*, 2020, <https://ourworldindata.org/co2-emissions>.
- [29] Urbanski, S., “Wildland fire emissions, carbon, and climate: Emission factors,” *Forest Ecology and Management*, Vol. 317, April 2014, pp. 51–60.
- [30] Burke, M., Heft-Neal, S., and Wara, M., “Managing the growing cost of wildfire,” Tech. rep., Stanford Institute for Economic Policy Research, oct 2020.
- [31] Smith, J. K., *Wildland fire in ecosystems: effects of fire on fauna*, 2000.
- [32] San-Miguel-Ayanz, J., Durrant, T., Boca, R., Maianti, P., Liberta’, G., Oom, D., Branco, A., De Rigo, D., Ferrari, D., Roglia, E., and Scionti, N., “Advance Report on Forest Fires in Europe, Middle East and North Africa 2022,” , No. KJ-NA-31-479-EN-N (online), 2023.
- [33] Center, N. I. F., “Federal Firefighting Suppression Costs,” =<https://www.nifc.gov/fire-information/statistics/suppression-costs>, Accessed 2024-04-29.
- [34] Commission, E., for Environment, D.-G., Nuijten, D., Onida, M., and Lelouvier, R., *Land-based wildfire prevention – Principles and experiences on managing landscapes, forests and woodlands for safety and resilience in Europe*, Publications Office of the European Union, 2021.
- [35] Meier, S., Elliott, R. J., and Strobl, E., “The regional economic impact of wildfires: Evidence from Southern Europe,” *Journal of Environmental Economics and Management*, Vol. 118, 2023, pp. 102787.
- [36] N. Iversen, M. Birkved, D. C., “Value Sensitive Design and Environmental Impact Potential Assessment for Enhanced Sustainability in Unmanned Aerial Systems,” 2020.
- [37] Efrogmson, R. A., “Ecological Risk Assessment Framework for Low Altitude Overflights by Fixed-wing and Rotary-wing Military Aircraft,” Tech. rep., Oak Ridge National Laboratory, 2001.
- [38] Mulero-Pázmány, M., Jenni-Eiermann, S., Strebel, N., Sattler, T., Negro, J. J., and Tablado, Z., “Unmanned aircraft systems as a new source of disturbance for wildlife: A systematic review,” *PLOS ONE*, Vol. 12, No. 6, 06 2017, pp. 1–14.
- [39] European Commission Joint Research Centre, Schulte, E., Maianti, P., Boca, R., De Rigo, D., Ferrari, D., Durrant, T., Loffler, P., San-Miguel-Ayanz, J., Branco, A., Vivancos, T., and Liberta’, G., *Forest fires in Europe, Middle East and North Africa 2016*, Publications Office, 2017.
- [40] San-Miguel-Ayanz, J., Durrant, T., Boca, R., Maianti, P., Liberta’, G., Artes Vivancos, T., Jacome Felix Oom, D., Branco, A., De Rigo, D., Ferrari, D., Pfeiffer, H., Grecchi, R., Nuijten, D.,

- Onida, M., and Loffler, P., "Forest Fires in Europe, Middle East and North Africa 2020," No. KJ-NA-30862-EN-N (online), KJ-NA-30862-EN-C (print), 2021.
- [41] National Interagency Coordination Center, "Wildland Fire Summary and Statistics Annual Report 2022," Tech. rep., 2023.
- [42] Nagaraju, S. B., Priya, H., Girijappa, Y. G. T., and Puttegowda, M., "9 - Lightweight and sustainable materials for aerospace applications," *Lightweight and Sustainable Composite Materials*, edited by S. M. Rangappa, S. M. Doddamani, S. Siengchin, and M. Doddamani, Woodhead Publishing, 2023, pp. 157–178.
- [43] Horvath, B. L. and Wells, D. P., "Comparison of Aircraft Conceptual Design Weight Estimation Methods to the Flight Optimization System," Technical report, NASA Langley Research Center, 2019, NASA Technical Reports Server.
- [44] Gundlach, J., *Designing Unmanned Aircraft Systems*, AIAA, 2012.
- [45] International Aluminium Institute, "Aluminium industry reports decline in greenhouse gas emissions," Februari 2024, <https://international-aluminium.org/aluminium-industry-reports-decline-in-greenhouse-gas-emissions/>; Accessed: 2024-05-21.
- [46] International Aluminium Institute, "Recycling," April 2024, https://international-aluminium.org/work_areas/recycling/, Accessed: 2024-05-21.
- [47] Mo, K., "Tackling emissions from logging," July 2019, <https://forestsnews.cifor.org/61492/reducing-emissions-with-logging?fnl=en>, Accessed: 2024-05-21.
- [48] ETM, "The Ultimate Guide to Wood Recycling," December 2001, <https://www.recyclingbristol.com/the-ultimate-guide-to-wood-recycling/>, Accessed: 2024-05-21.
- [49] Total Energies Corbion, "Reducing our carbon footprint," 2024, <https://www.totalenergies-corbion.com/about-pla/biobased/>, Accessed: 2024-05-21.
- [50] Pallet2Ship, "Sea Freight vs Air Freight," 2023, Accessed: 2024-06-19.
- [51] Freightos, "CO2 Emissions Sea & Air Freight Calculator," <https://www.freightos.com/freight-resources/air-sea-freight-co2-emissions-calculator/>, 2024, Accessed: 2024-06-19.
- [52] Abbenhuis, E., Agterdenbos, J., Bonanno, V., Camporeale, M., Do Cao, K., Kleipool, B., Lubbers, V., Mielczarek, A., Nakagawa, T., and Petrache, A., "Wildfire Drone Swarm Baseline Report," Tech. rep., Technische Universiteit Delft, May 2024.
- [53] Abbenhuis, E., Agterdenbos, J., Bonanno, V., Camporeale, M., Do Cao, K., Kleipool, B., Lubbers, V., Mielczarek, A., Nakagawa, T., and Petrache, A., "Wildfire Drone Swarm Midterm Report," Tech. rep., Technische Universiteit Delft, May 2024.
- [54] Abbenhuis, E., Agterdenbos, J., Bonanno, V., Camporeale, M., Do Cao, K., Kleipool, B., Lubbers, V., Mielczarek, A., Nakagawa, T., and Petrache, A., "Wildfire Drone Swarm Final Report Draft," Tech. rep., Technische Universiteit Delft, 2024.
- [55] Sullivan, B., "How aerial firefighters attack wildfires with air tankers, Broncos, and Super Hueys," Midwest ATC, Nov 2019, <https://atctower.com/how-aerial-firefighters-attack-wildfires-with->
- [56] "Wildfire climate connection," July 2023, <https://www.noaa.gov/noaa-wildfire/wildfire-climate-connection>.
- [57] Coen, J., "Modeling Wildland Fires: A Description of the Coupled Atmosphere-Wildland Fire Environment Model (CAWFE)," NCAR Technical Note NCAR/TN-500+STR, National Center for Atmospheric Research, 2013.
- [58] Rothermel, R. C., "A mathematical model for predicting fire spread in wildland fuels," Tech. Rep. INT-115, U.S. Department of Agriculture, Intermountain Forest and Range Experiment Station, Ogden, UT, 1972.
- [59] Bailon-Ruiz, R., *Design of a wildfire monitoring system using fleets of Unmanned Aerial Vehicles*, phdthesis, INSA de Toulouse, 2020, NNT: 2020ISAT0011, tel-02995471v3.
- [60] Reeves, M. C., Ryan, K. C., Rollins, M. G., and Thompson, T. G., "Spatial fuel data products of the LANDFIRE Project," *International Journal of Wildland Fire*, Vol. 18, 2009, pp. 250–267.
- [61] Büttner, G., "CORINE Land Cover and Land

- Cover Change Products,” *Land Use and Land Cover Mapping in Europe: Practices & Trends*, edited by I. Manakos and M. Braun, Remote Sensing and Digital Image Processing, Springer Netherlands, Dordrecht, 2014, pp. 55–74, Cited on page 44.
- [62] de Dios, J. R. M., Merino, L., and Ollero, A., “Fire Detection Using Autonomous Aerial Vehicles With Infrared And Visual Cameras,” *16th IFAC World Congress*, Vol. 38, IFAC Proceedings Volumes, January 2005, pp. 660–665.
- [63] Kogan, F. and Kogan, F., “Vegetation health method,” *Remote Sensing for Food Security*, 2019, pp. 51–73.
- [64] U.S. Government, “Landsat Enhanced Vegetation Index,” n.d., [https://www.usgs.gov/landsat-missions/landsat-enhanced-vegetation-index#:~:text=Landsat%20Enhanced%20Vegetation%20Index%20\(EVI,in%20areas%20with%20dense%20vegetation,](https://www.usgs.gov/landsat-missions/landsat-enhanced-vegetation-index#:~:text=Landsat%20Enhanced%20Vegetation%20Index%20(EVI,in%20areas%20with%20dense%20vegetation,) Accessed: 2024-05-14.
- [65] U.S. Government, “Normalized Difference Vegetation Index (NDVI),” n.d., <https://ipad.fas.usda.gov/cropexplorer/Definitions/spotveg.htm#:~:text=The%20Normalized%20Difference%20Vegetation%20Index,green%20vegetation%20from%20bare%20soils,> Accessed: 2024-05-14.
- [66] Bari, E., Nipa, N. J., and Roy, B., “Association of vegetation indices with atmospheric & biological factors using MODIS time series products,” *Environmental Challenges*, Vol. 5, 2021, pp. 100376.
- [67] Fan, X., Li, H., Chen, Y., and Dong, D., “A Path-Planning Method for UAV Swarm under Multiple Environmental Threats,” *Drones*, Vol. 8, No. 5, 2024, pp. 171.
- [68] Pachung, P., Pandya, K., Nagar, A., and Bansal, J. C., “Efficient 3D path planning for drone swarm using improved Sine Cosine Algorithm,” *SN Computer Science*, Vol. 5, No. 3, 2024, pp. 286.
- [69] National Park Service, “Understanding Fire Danger,” <https://www.nps.gov/articles/understanding-fire-danger.htm>.
- [70] Lozano-Parra, J., Pulido, M., Lozano-Fondón, C., and Schnabel, S., “How do Soil Moisture and Vegetation Covers Influence Soil Temperature in Drylands of Mediterranean Regions?” *Water*, Vol. 10, No. 12, 2018.
- [71] Baker, D., “Relative Humidity: To Average, or Not to Average?” 2020, <https://www.campbellsci.com/blog/averaging-relative-humidity>.
- [72] Coen, J., “Advanced Wildfire Mapping and Modelling Tools,” https://appliedsciences.nasa.gov/sites/default/files/2022-05/Schroeder_NASA_FactSheet.pdf.
- [73] Julian, K. D. and Kochenderfer, M. J., “Distributed wildfire surveillance with autonomous aircraft using deep reinforcement learning,” *Journal of Guidance, Control, and Dynamics*, Vol. 42, No. 8, 2019, pp. 1768–1778.
- [74] Bushnaq, O. M., Chaaban, A., and Al-Naffouri, T. Y., “The role of UAV-IoT networks in future wildfire detection,” *IEEE Internet of Things Journal*, Vol. 8, No. 23, 2021, pp. 16984–16999.
- [75] Ahmadzadeh, A., Jadbabaie, A., Kumar, V., and Pappas, G. J., “Multi-UAV cooperative surveillance with spatio-temporal specifications,” *Proceedings of the 45th IEEE Conference on Decision and Control*, IEEE, 2006, pp. 5293–5298.
- [76] “Meeting with NLR about drone swarm architecture.” Personal communication, Ricardo van der Pluijm, R&D Engineer Modelling and Simulation at NLR.
- [77] Dedrone, “DeDrone Worldwide drone incidents,” November 2020, <https://www.dedrone.com/resources/incidents-new/all>, Accessed: 3-6-2024.
- [78] Nigam, N., Bieniawski, S., Kroo, I., and Vian, J., “Control of multiple UAVs for persistent surveillance: Algorithm and flight test results,” *IEEE Transactions on Control Systems Technology*, Vol. 20, No. 5, 2011, pp. 1236–1251.
- [79] Chen, Y. and Tricaud, C., “Optimal interlaced mobile sensor motion planning and parameter estimation for distributed parameter systems,” *Proceedings of 2008 Engineering Research and Innovation Conference, Knoxville, Tennessee, USA*, Citeseer, 2008.
- [80] Burrough, P. A., McDonnell, R., and Lloyd, C., “8.11 nearest neighbours: Thiessen (dirichlet/voronoi) polygons,” *Principles of Geographical Information Systems*, 2015.
- [81] Torpelund-Bruin, C. and Lee, I., “A Voronoi-based model for emergency planning using

- sequential-scan algorithms,” *2009 IEEE International Conference on Intelligence and Security Informatics*, IEEE, 2009, pp. 83–88.
- [82] Hayajneh, A. M., Zaidi, S. A. R., McLernon, D. C., and Ghogho, M., “Drone empowered small cellular disaster recovery networks for resilient smart cities,” *2016 IEEE international conference on sensing, communication and networking (SECON Workshops)*, IEEE, 2016, pp. 1–6.
- [83] Derflinger, G., Hörmann, W., and Leydold, J., “Random variate generation by numerical inversion when only the density is known,” *ACM Transactions on Modeling and Computer Simulation (TOMACS)*, Vol. 20, No. 4, 2010, pp. 1–25.
- [84] Encyclopedia of Mathematics, “Dichotomy method,” 2020, https://encyclopediaofmath.org/wiki/Dichotomy_method, Accessed: 2024-05-18.
- [85] ScienceDirect, Computers & Operations Research, “Path Planning Problem,” 2018, <https://www.sciencedirect.com/topics/computer-science/path-planning-problem>, Accessed: 2024-06-17.
- [86] Huang, J., Fu, W., Luo, S., Wang, C., Zhang, B., and Bai, Y., “A Practical Interlacing-Based Coverage Path Planning Method for Fixed-Wing UAV Photogrammetry in Convex Polygon Regions,” *Aerospace*, Vol. 9, No. 9, 2022, pp. 521.
- [87] Torres, M., Pelta, D. A., Verdegay, J. L., and Torres, J. C., “Coverage path planning with unmanned aerial vehicles for 3D terrain reconstruction,” *Expert Systems with Applications*, Vol. 55, 2016, pp. 441–451.
- [88] Gotti, F., “MIT 18.211 Combinatorial Analysis Lecture 22: Hamiltonian Cycles and Paths,” Lecture notes, 2024, <https://math.mit.edu/~fgotti/docs/Courses/Combinatorial%20Analysis/22.%20Hamiltonian%20Graphs/Hamiltonian%20Graphs.pdf>.
- [89] Aircraft Cost Calculator, “Beechcraft King Air 350 Price and Operating Costs,” 2024, <https://www.aircraftcostcalculator.com/AircraftOperatingCosts/24/Beechcraft+King+Air+350>, Accessed: 2024-06-16.
- [90] Liberty Jet, “King Air 350 Operating Costs,” 2024, <https://www.libertyjet.com/jet-ownership-costs.aspx?jetType=King%20Air%20350>, Accessed: 2024-06-16.
- [91] Hensoldt, “ARGOS-II HD / HDT: Airborne ISR and ISTAR system,” 2020, <https://www.hensoldt.net/products/optronics/argos-ii/>, Accessed: 2024-06-17.
- [92] European Telecommunications Standards Institute, “ETSI TS 100 392-15 V1.4.1 (2004-06),” Tech. rep., June 2004.
- [93] Boan, J., *Radio Propagation in Fire Environments*, Ph.D. thesis, University of Adelaide, 2009.
- [94] Hong, S. G., Lee, H., Yang, H., Jin, J., Lee, H., and Lee, K., “Experimental Study of Microwave Attenuation in a Compartment Fire,” *Journal of Electromagnetic Engineering and Science*, Vol. 21, No. 3, July 2021, pp. 249–251.
- [95] Kim Tae-Dong, Y. I.-S., “Attenuation of Microwaves Received From a Drone Owing to Smoke Obscuration,” *Fire Sci. Eng.*, Vol. 35, No. 1, 2021, pp. 128–131.
- [96] Kaur, R. and Singh, G., “Modulation Techniques in ISM Band,” *International Journal of Engineering Research & Technology (IJERT)*, Vol. 5, No. 1, 2017, pp. 123–126.
- [97] Kyocera, “Wi-Fi/ BT/ Zigbee Ceramic Patch 2.4 GHz Antenna,” September 2023, https://datasheets.kyocera-avx.com/ethertronics/AVX-E_1003468.pdf.
- [98] Engineering, J., “UVW 0430 Blade Antenna,” <https://jemengineering.com/wp-content/uploads/2021/05/UVW-0430-Datasheet-Rev3.pdf>.
- [99] Benson, K., “Phased Array Beamforming ICs Simplify Antenna Design,” January 2019, <https://www.analog.com/en/resources/analog-dialogue/articles/phased-array-beamforming-ics-simplify-antenna.html>.
- [100] Horvath, B. L. and Wells, D. P., “Comparison of aircraft conceptual design weight estimation methods to the flight optimization system,” *2018 AIAA Aerospace Sciences Meeting*, 2018, p. 2032.
- [101] Ruijgrok, G., *Elements of Airplane Performance*, VSSD, 3rd ed., 1990.
- [102] Anderson, J., *Introduction to Flight 8th Edition*, McGraw-Hill Education, 2016.
- [103] Roskam, J., *Airplane Design, Part 2: Preliminary*

- Configuration Design and Integration of the Propulsion System*, DARcorporation, 1985.
- [104] Roskam, J., *Airplane Design, Part 5: Component Weight Estimation*, Roskam Aviation and Engineering Corporation, 1985.
- [105] Administration, F. A., “Code of Federal Regulations, Title 14, Part 23 – Airworthiness Standards: Normal Category Airplanes,” *Code of Federal Regulations*, 2024, Available at <https://www.ecfr.gov/current/title-14/chapter-I/subchapter-C/part-23>.
- [106] Administration, F. A., “Code of Federal Regulations, Title 14, Part 23 – Airworthiness Standards: Transport Category Airplanes,” *Code of Federal Regulations*, 2024, Available at <https://www.ecfr.gov/current/title-14/chapter-I/subchapter-C/part-25>.
- [107] Rokhsaz, K., Kliment, L. K., Ali, S. J., and Nelson, J. A., *Exploratory Study of C-130 Flight Loads in Forest Service Operation*, <https://arc.aiaa.org/doi/abs/10.2514/6.2021-0301>.
- [108] Anderson, J. D., *Introduction to Flight*, McGraw-Hill Education, 8th ed., 2015.
- [109] Mulder, J., van Staveren, W., van der Vaart, J., de Weerdt, E., de Visser, C., in 't Veld, A., and Mooij, E., “Flight Dynamics Lecture Notes,” March 2013.
- [110] Roskam, J., *Preliminary Calculation of Aerodynamic, Thrust and Power Characteristics*, Roskam Aviation and Engineering Corporation, 1987.
- [111] Gudmundsson, S., “Chapter 9 - The Anatomy of the Wing,” *General Aviation Aircraft Design (Second Edition)*, edited by S. Gudmundsson, Butterworth-Heinemann, second edition ed., 2022, pp. 321–413.
- [112] Deperrois, A., “About XFLR5 calculations and experimental measurements,” October 2011, https://www.xflr5.tech/docs/Results_vs_Prediction.pdf.
- [113] Kundu, A. K., *Aircraft Design*, Cambridge University Press, 2010.
- [114] Oliviero, F., Gill, E.K.A., J., “AE3211-I Systems Engineering & Aerospace Design,” 2024, TU Delft.
- [115] Scholz, “Chapter 9 empennage general design,” https://www.fzt.haw-hamburg.de/pers/Scholz/H00U/AircraftDesign_9_EmpennageGeneralDesign.pdf, accessed on: 12/06/2024.
- [116] Torenbeek, E., *Synthesis of Subsonic Airplane Design*, Delft University Press, 1982.
- [117] Mulder, J., van Staveren, W., van der Vaart, J., de Weerdt, E., de Visser, C., in 't Veld, A., and Mooij, E., “Flight Dynamics Lecture Notes AE3202,” March 2013.
- [118] Shen, J., Su, Y., Liang, Q., and Zhu, X., “Calculation and identification of the aerodynamic parameters for small-scaled fixed-wing UAVs,” *Sensors*, Vol. 18, No. 1, 2018, pp. 206.
- [119] Wang, Y., Zhu, H., Zhao, Z., Zhang, C., and Lan, Y., “Modeling, System Measurements and Controller Investigation of a Small Battery-Powered Fixed-Wing UAV,” *Machines*, Vol. 9, No. 12, 2021.
- [120] Abbenhuis, E., FitzGerald, O., De Laere, T., Ibrahim, M., Szeibert, B., and Wijgerse, T., “Simulation, Verification & Validation Report,” Tech. rep., Technische Universiteit Delft, 2024.
- [121] “Amprius Technology — Products,” 2024, <https://amprius.com/products/>, accessed on: 18/06/2024.
- [122] Poff, S., “Executive Summary,” 2023, <https://amprius.com/500whenergydensityreport/>, accessed on: 18/06/2024.
- [123] Dupiech, A., “Airbus partners with Amprius, leader in high energy density battery technology,” 2019, <https://www.airbus.com/en/newsroom/press-releases/2019-10-airbus-partners-with-amprius-leader-in>, accessed on: 18/06/2024.
- [124] Nigel, “Battery Design from chemistry to pack,” 2023, <https://www.batterydesign.net/bmw-i3-2/>, accessed on: 18/06/2024.
- [125] Staples, G., “Propeller Static & Dynamic Thrust Calculation,” 2014, <https://www.electricrcaircraftguy.com/2014/04/propeller-static-dynamic-thrust-equation-backg.html>, accessed on: 18/06/2024.
- [126] Kundu, A. K., *Aircraft Design*, Cambridge University Press, 2010.
- [127] “5015 IPE V3.0 VTOL Drone Motor,” .
- [128] Protection, B. F., “Heavy Duty Lithium-Ion Battery Fire Containment Blanket- 5' X 6',” Tech. rep., Deep Three Inc., 2024.
- [129] van Horssen, L., de Visser, C., and Pool, D.,

- “Aerodynamic Stall and Buffet Modeling for the Cessna Citation II Based on Flight Test Data,” Technical report, Delft University of Technology, Delft, Netherlands, 2020.
- [130] Mulder, M., Lubbers, B., Zaal, P., van Paassen, M., and Mulder, J., *Aerodynamic Hinge Moment Coefficient Estimation Using Automatic Fly-by-Wire Control Inputs*.
- [131] Nurohman, C., Arifianto, O., and Barecasco, A., “Hinge Moment Coefficient Prediction Tool and Control Force Analysis of Extra-300 Aerobatic Aircraft,” *Journal of Physics: Conference Series*, Vol. 1005, No. 1, apr 2018, pp. 012020.
- [132] Purser, P. E. and Cook, C. B., “Collection and Analysis of Hinge-Moment Data on Control-Surface Tabs,” Technical Report 1113, National Advisory Committee for Aeronautics, Langley Aeronautical Laboratory Langley Field, Va., 1947.
- [133] Mangurian, G. N., “The Aircraft Structural Factor of Safety,” Tech. Rep. 154, North Atlantic Treaty Organization Advisory Group for Aeronautical Research and Development, 1957.
- [134] “Structural factors of safety for spaceflight hardware,” Standard, European Coordination for Space Standardization, Noordwijk, NL, August 2019.
- [135] Martin, D. M., “Technical Note 4197,” Technical Note 4197, National Advisory Committee for Aeronautics, Langley Aeronautical Laboratory Langley Field, Va, February 1958.
- [136] Anderson, J. D., *Fundamentals of Aerodynamics*, McGraw-Hill Education, New York, NY, 6th ed., 2016.
- [137] MatWeb, LLC, “Aluminum 6082-T6,” 2024, Accessed: 2024-06-18.
- [138] Hibbeler R. C. , *Mechanics of Materials*, Pearson, Harlow, 10th ed., 2018.
- [139] Budynas, R. G. and Nisbett, J. K., *Shigley’s Mechanical Engineering Design*, McGraw-Hill, New York, 9th ed., 2011.
- [140] “Astronautic Structures Manual, Volume 2,” Technical Memorandum NASA-TM-X-73306, National Aeronautics and Space Administration, Marshall Space Flight Center, Alabama, 1975.
- [141] Megson, T., *Aircraft Structures for Engineering Students*, Butterworth-Heinemann, Oxford, UK, 6th ed., 2017.
- [142] Knacke, T. W., “Parachute Recovery Systems Design Manual,” Tech. Rep. NWC-TP-6575, Naval Weapons Center, China Lake, CA, 1991.
- [143] UKRSpecSystems, “Pneumatic UAV launching system GLS-1A,” 2021, <https://ukrspecsystems.com/uascomponents/pneumatic-uav-launching-system-gls-1a>, Accessed: 2024-05-17.
- [144] ElevonX, “ElevonX Scorpion,” 2020, <https://www.elevonx.com/solutions/elevonx-scorpion/>, Accessed: 2024-05-17.
- [145] Ashby, M., Shercliff, H., and Cebon, D., *Materials: Engineering, Science, Processing and Design*, University of Cambridge, Cambridge, UK, 4th ed., 2019.
- [146] Smith, D. J., *Reliability, Maintainability, and Risk: Practical Methods for Engineers*, Butterworth-Heinemann, Oxford, 2005.
- [147] Kinnison, H. and Siddiqui, T., *Aviation Maintenance Management*, McGraw-Hill, 2nd ed., 2011.
- [148] “Aerial Firefighting Market Share Growth Analysis by 2030: Aerial Firefighting Market Size and Forecast (2020 - 2030), Global and Regional Share, Trend, and Growth Opportunity Analysis,” Market analysis report, The Insight Partners, jan 2020, By End Use (Forest Firefighting, Urban Firefighting, and Others), Aircraft Type (Fixed Wing and Rotary Wing), and Geography.
- [149] SkyQuest, “Global Drone Market,” Tech. rep., SkyQuest, 2023, Market Forecast, Competitive Analysis, Market Segmentation, Pricing Analysis & Market Dynamics.
- [150] U.S. Fire Administration, “Wildland Urban Interface: A Look at Issues and Resolutions,” 2022.
- [151] USDA Press, “Biden-Harris Administration Announces \$500 Million to Confront the Wildfire Crisis as Part of Investing in America Agenda,” 2024, <https://www.usda.gov/media/press-releases/2024/02/20/biden-harris-administration-announces-500-million>, Accessed: 3-6-2024.
- [152] 118th Congress (2023-2024), H., “National Defense Authorization Act for Fiscal Year 2024,” dec 2023, <https://www.congress.gov/bill/118th-congress/house-bill/2670/text>.
- [153] Hambridge, N., *Conducting a Risk Assessment*, Harvard Financial Administration, 2024.

APPENDIX

Table 46: Work Distribution Table

Chapter	Section	People (hrs)
Executive Overview	-	Kevin (1), Takayoshi (2), Vittorio (1), Aleks(5), Vince(1), Jack(2)
Introduction		Aleks(3)
Project Overview	Background Information	Marco(5)
	Mission Statement	Jack(2)
	Mission Concept Description	Jack(2), Vince(4)
	Top-level Functional Flow	Vince(8), Jack(2)
	Sustainability Strategy	Aleks(10)
	Top -level Risk Analysis	Takayoshi (40)
	Requirement Strategy	Ebbe (5), Vittorio (8), Jack (4), Vince(2)
Mission Logistics & Operations Design	Operational Modes Definition	Björn (6), Marco (15)
	Swarm Sizing	Vince(24), Marco(15)
	Ground System Sizing	Vince(24), Jack (6), Marco(30)
	Human Resources	Ebbe (1)
	Location Definition	Aleks(2)
	Wildfire Models	Ebbe (20), Vince(4)
	Sensors Selection	Ebbe (15), Vince(16)
	Environmental Analysis	
	Communication Infrastructure	Kevin (85), Aleks (50)
Swarm Design	Definition of Swarm Framework	Björn (16), Marco(5)
	Sector Generation	Björn (32), Marco(2)
	Pathfinding Methods	Björn (24), Ebbe (10)
	Drone Contingent Behaviour	Björn (4)
	Swarm Performance & Comparison	Björn (16)
UAV Design	Design Methodology	Björn (24), Jack(10), Marco(60)
	Weight Estimation	Aleks (6), Vince(16)
	Flight Performance	Jack(12)
	Aerodynamics	Takayoshi (60), Jack (20)
	Stability & Control	Jack (25), Vince(16)
	Propulsion & Power	Vittorio (58), Jack(15)
	Avionics & Electrical System	Kevin (22), Andrei(8)
	Structures	Aleks(40), Vince(24), Andrei(64)
	Ballistic Recovery System & Fire Suppression System	Takayoshi (16), Andrei(14), Vince(8)
	Design Results	Björn (10), Vittorio (32), Vince(40), Jack(10), Andrei(4), Marco (10)
Manufacturing & Integration Plan	-	Aleks(16), Vince(4)
Financial Valuation	Cost Analysis	Ebbe (25), Kevin (5)
	Market Analysis	Ebbe (25)
Design Assessment	Verification & Validation Plan	Kevin (5), Jack(5), Vince(5)
	Assumptions	Kevin (3), Vittorio (2), Aleks (2), Takayoshi (6), Jack (2), Andrei(16)
	V&V	Takayoshi (6), Jack(8), Andrei(24), Marco(10)
	Dynamic Analysis	Ebbe (40), Jack (5)
	Requirement Compliance Verification	Vittorio (10)
Conclusion, Discussion& Recommendations	-	Jack (4)
Bibliography	-	Kevin (3)
Appendix	Task distribution	Kevin (2)
	Requirements	Vittorio (25)
	Diagrams	Vince(24)
Latex formatting	-	Björn (8), Ebbe (5), Kevin (3), Takayoshi (4)
Logbook	-	Ebbe (5), Kevin (5)

Table 46 – continued from previous page

Chapter	Section	People (hrs)
PM&SE Lectures, Update Meetings	-	All (10)

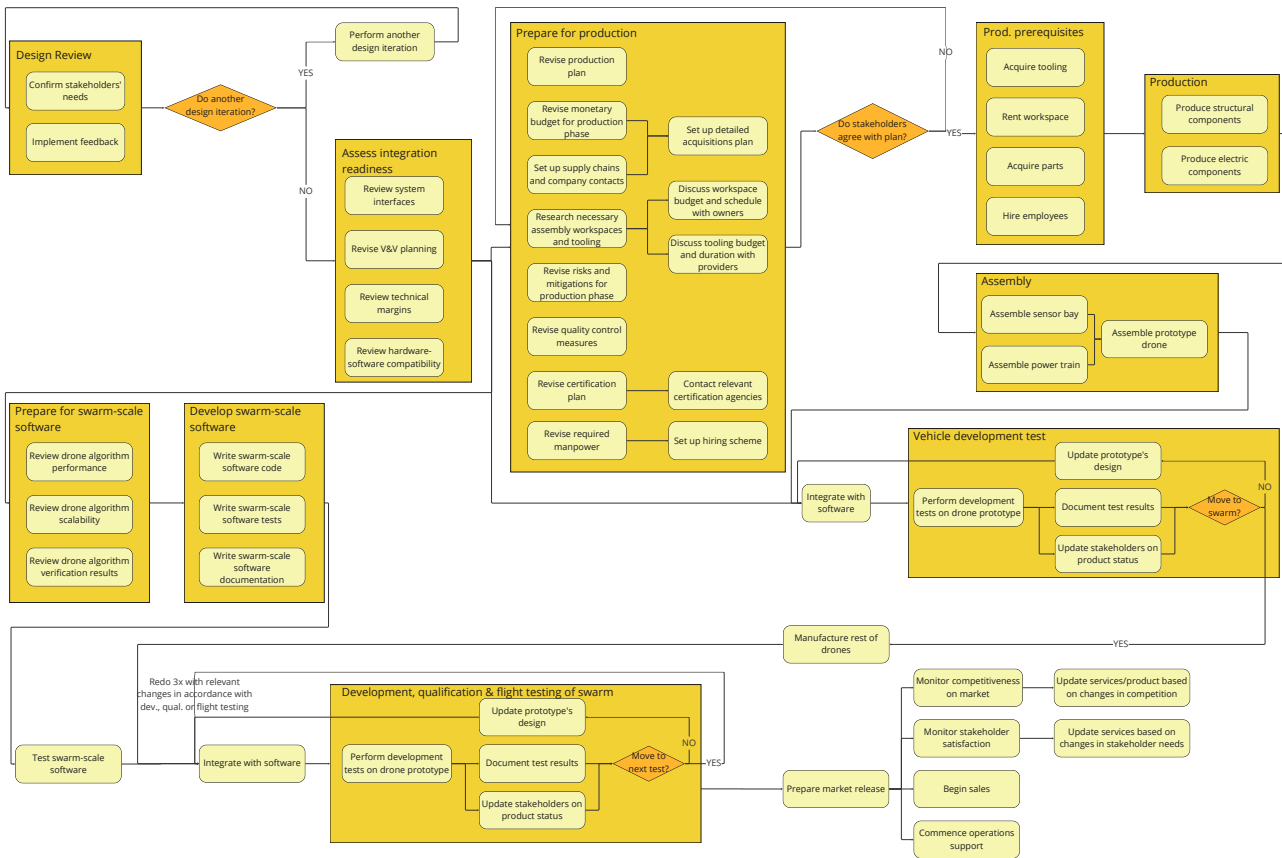


Figure 82: Design and development logic diagram

Table 47: Technical Risk Matrix [153]

Impact on Project				Likelihood				
	Performance (40%)	Cost (20%)	Schedule (40%)	<0.1% Very Low (1)	0.1% - 10% Low (2)	10% - 50% Medium (3)	50% - 90% High (4)	> 90% Very High (5)
Very High (5)	Catastrophic effect on performance. Cannot perform the mission	Cannot finance project	Must stop operation	5	10	15	20	25
High (4)	Major effect on performance. Requires significant redesign/production to perform the mission	Major/recurring expenses	Major delay. Must temporarily stop operation. recurring delay.	4	8	12	16	20
Medium (3)	Moderate effect on performance. Requires some redesigning/production to perform the mission.	Moderate/stand-alone expenses	Moderate delay. cannot continue operation for the day. stand-alone delay	3	6	9	12	15
Low (2)	Minimal adverse effect on performance.	Minimal expenses	Minimal delay. Will restart operation during the day	2	4	6	8	10
Very Low (1)	No effect on performance	No expenses	No delay	1	2	3	4	5

Table 50: **System and Subsystem Requirements.**

The verification IDs include: A - Analysis; T - Testing; D - Demonstration; I - Inspection

ID [REQ-SYS-...]	Requirement	Rational	Verification	Traceability
Subsystem Requirements				
Mission Technicality				
Unit Performance				
TEC-UNI-1	The propulsion system of the unit shall be able to sustain all flight operations.	Ensure mission execution	A, D, T	O-F4.1.4
TEC-UNI-1.1	The propulsion system of the units shall be able to achieve a ground speed of no less than 30 m/s.	Required cruise velocity for an optimal swarm coverage of the area of interest	A, T	REQ-SYS-TEC-SWM-1.1
TEC-UNI-1.2	The propulsion system of the unit shall achieve an endurance of no less than 6 hrs.	To minimise the downtime of each UAV	A, T	REQ-STK-FB-1.2
TEC-UNI-1.3	The propulsion system of the units shall be able to operate nominally at temperatures between 0 and 45 °C.	Expected operating conditions from consultation with DSE Group 13	T	REQ-SYS-TEC-UNI-1
TEC-UNI-1.4	The battery shall provide a maximum power of 1 kW.	Power requirements of the payload and propulsion system	T	REQ-SYS-TEC-UNI-1
TEC-UNI-1.5	The unit shall be able to cruise at 850 m above sea level.	Required altitude for optimal FOV	A, D	REQ-SYS-OPS-PLD-1.1; REQ-SYS-OPS-PLD-1.2
TEC-UNI-1.6	The unit shall have a stall speed of 20 m/s or less.	Maximum stall speed for launching operations, from analysis of comparable designs	A, D	Midterm Report, Section 5.2.1
TEC-UNI-2	The flight control & stability performance of the unit shall be able to sustain all flight operations.	Ensure mission execution	A, D	O-F4.1.4
TEC-UNI-2.1	The unit shall demonstrate longitudinal static stability.	For a safer and more reliable platform	D	REQ-SYS-TEC-UNI-2
TEC-UNI-2.2	The unit shall demonstrate longitudinal dynamic stability.	For a safer and more reliable platform	D	REQ-SYS-TEC-UNI-2
TEC-UNI-2.3	The unit shall have a longitudinal stability margin of 5%.	Safety margins	A	REQ-SYS-TEC-UNI-2.1, REQ-SYS-TEC-UNI-2.2
TEC-UNI-2.4	The unit shall demonstrate lateral static stability.	For a safer and more reliable platform	D	REQ-SYS-TEC-UNI-2
TEC-UNI-2.5	The unit shall demonstrate lateral dynamic stability.	For a safer and more reliable platform	D	REQ-SYS-TEC-UNI-2
TEC-UNI-3	The unit emergency recovery system shall be able to recover the unit during any mission phase.	For reusability and safe retrieval	A, D, T	REQ-SYS-CON-SFT-2-3.1
TEC-UNI-3.1	The BRS deployment shall minimise damage to the unit.	For reusability and safe retrieval	D	REQ-STK-LG-2
TEC-UNI-3.2	The BRS landing shall minimise damage to the environment surrounding the unit.	For environmental reasons and safe retrieval	D	REQ-SYS-CON-SFT-3
TEC-UNI-3.3	The BRS shall ensure a landing velocity of 5 m/s.	Generated from Risk Analysis	A, T	REQ-SYS-TEC-UNI-3.1
TEC-UNI-3.4	The BRS shall withstand shock loads of 6.5 G upon deployment.	Generated from Risk Analysis. Compliance with launch and recovery loads.	A, T	REQ-SYS-TEC-UNI-3.1, REQ-SYS-TEC-UNI-5.5
TEC-UNI-3.5	The BRS shall be fireproof.	Generated from Risk Analysis	D	REQ-SYS-TEC-UNI-3.1, REQ-SYS-TEC-UNI-3.2
TEC-UNI-4	The communication system shall ensure communication between the ground station and active units at all times.	Operational control and coordination	A, D, I, T	REQ-STK-FB-2.1; REQ-STK-FB-2.2
TEC-UNI-4.1	The communication system shall operate in the frequencies included in the range of 380 MHz to 2.4 GHz.	Full range of telecommunications including emergency services and ground station	A, T	REQ-SYS-TEC-UNI-4; REQ-STK-FB-2.1
TEC-UNI-4.2	The communication system shall require no more than 30 W of power.	Based on preliminary equipment sizing	A, D	REQ-SYS-TEC-UNI-4
TEC-UNI-4.3	The communication system shall have a mass of no more than 5 kgs.	Mass budget	I	REQ-SYS-TEC-UNI-4

Table 50 – continued from previous page

ID [REQ-SYS-...]	Requirement	Rational	Verification	Traceability
TEC-UNI-4.4	The communication network should be able to relay a data rate of 40 Mbps to the ground station at all times.	From preliminary sensor analysis	A, D	REQ-SYS-TEC-UNI-4; REQ-SYS-OPS-PLD-1.2
TEC-UNI-4.5	The link margin for the system shall be greater than 5 dB	To ensure communication reliability [44]	A, D	REQ-SYS-TEC-UNI-4;
TEC-UNI-5	The unit's structure shall ensure structural integrity in all operating conditions.	Ensure mission execution	A, I, T	O-F4.1.4
TEC-UNI-5.1	The unit's structure shall provide an interface infrastructure for all other unit subsystems.	Ensure a casing structure for all subsystems.	I	REQ-SYS-OPS-PLD-1; REQ-SYS-OPS-AVI-1
TEC-UNI-5.2	The structure shall provide the main load-carrying capability of the unit.	Ensure structural integrity	A, T	REQ-SYS-TEC-UNI-5
TEC-UNI-5.3	The structure shall withstand a maximum static load factor of 3.	Ensure mission execution	T	REQ-SYS-TEC-UNI-5.2
TEC-UNI-5.4	The structure shall be able to withstand thermal loads due to temperatures between 0 and 45 °C.	Expected operating conditions from consultation with DSE Group 13	T	REQ-SYS-TEC-UNI-1.3
TEC-UNI-5.5	The structure shall withstand shock loads of 6.5 G.	Compliance with launch and recovery loads.	T	REQ-SYS-TEC-UNI-3.4; REQ-SYS-TEC-GRD-1.3
Swarm Performance				
TEC-SWM-1	The swarm system shall be able to coordinate the movement of every airborne unit.	Ensure precise navigation	A, D, T	REQ-STK-FB-1.1
TEC-SWM-1.1	The swarm system shall calculate the optimal flight path to ensure that 50% of wildfires are detected within 15 minutes.	Ensure quick detection time to allow for fast response by the Fire Brigade.	A, T	REQ-STK-FB-1.2
TEC-SWM-1.2	The swarm system shall create a sectorial division of the area of interest based on the area's risk.	Ensure effective swarm coverage	D	REQ-STK-FB-1
Ground System Performance				
TEC-GRD-1	The ground system shall be able to support the continuous operation of the swarm.	Ensure effective and continuous operations	A, D, I, T	REQ-STK-FB-1; REQ-STK-LG-1
TEC-GRD-1.1	The system shall ensure that 25 units are airborne at all times during operations.	Ensure optimal swarm strategy	A, T	REQ-SYS-TEC-SWM-1.1
TEC-GRD-1.2	The launcher system shall be able to accelerate the UAV units up to 20 m/s.	Ensure that the unit is launched at a higher speed than the stall speed	A, T	REQ-SYS-TEC-UNI-1.6
TEC-GRD-1.3	The launcher and recovery system shall not exact load of more than 6.5 G to the units during launch and recovery.	Maximum load previously estimated from comparable designs	D	Midterm Report, Section 5.2.1
TEC-GRD-1.4	The recovery system shall guarantee that the unit is fully stopped in the recovery area.	Ensure recovery of the units	D	REQ-SYS-TEC-GRD-1
TEC-GRD-1.5	The recovery system shall guarantee that the unit is recovered with minimal/no damage.	Reduce maintenance time, downtime and costs	D	REQ-STK-LG-2
TEC-GRD-1.6	The entire ground system shall be transportable by semi-truck.	Improve adaptability and versatility of system	D	REQ-STK-LG-3
TEC-GRD-1.7	The units shall be stored such that they are not damaged.	Lifetime purposes	I	REQ-SYS-CON-RSC-1.2
Operational Goals				
Payload Sensors				
OPS-PLD-1	The monitoring units shall be able to collect sufficient data for the mission's success.	Ensure effective monitoring	A, D, T	REQ-STK-FB-1
OPS-PLD-1.1	The monitoring units shall detect wildfires with a 3 m resolution.	Ensure effective monitoring	D	Consistency with REQ-SYS-OPS-PLD-1.1
OPS-PLD-1.2	The monitoring units shall collect all data required by the CAWFE™ model with 3 m resolution.	Ensure effective monitoring	D	CAWFE Model Requirements
OPS-PLD-1.3	The monitoring units shall be able to receive radio transmissions from the firefighter units on the ground at any frequency within the 380-400 MHz range.	Ensure effective reception of firefighter radio transmissions	T	Standardised Firefighter Radio Transmitters
OPS-PLD-1.4	The monitoring units shall take sufficient data measurements to ensure continuous coverage of the ground track.	Ensure effective monitoring	T	REQ-SYS-OPS-PLD-1; REQ-SYS-TEC-UNI-1.1

Table 50 – continued from previous page

ID [REQ-SYS-...]	Requirement	Rational	Verification	Traceability
OPS-PLD-1.5	The monitoring units shall be able to store 40 GB of on-board data.	Ensure sufficient data handling	A	REQ-SYS-OPS-PLD-1.2
Avionics Sensors				
OPS-AVI-1	Each unit shall be able to measure all the state data required to allow for automatic flight.	Ensure flight-worthiness	T	REQ-SYS-TEC-UNI-1
Constraints				
Safety				
CON-SFT-1	The individual system units shall perform the mission safely.	Safety reasons	D, T	REQ-STK-WE-2, REQ-STK-LP-2;
CON-SFT-1.1	The individual system units shall automatically avoid collision with stationary and dynamic obstacles.	Damage, safety, lifetime	D	REQ-STK-AT-1; REQ-STK-WE-2, REQ-STK-LP-2;
CON-SFT-1.2	The system shall be able to operate in adverse weather conditions.	Ensure mission execution	D	REQ-STK-FB-2;
CON-SFT-1.3	The unit shall be able to relay its GCS position following an emergency landing.	Vehicle recovery reasons	T	REQ-STK-LG-2;
CON-SFT-2	The system shall ensure the safety of its operators.	Safety reasons	D, I	REQ-STK-FB-2;
CON-SFT-2.1	Personnel shall be trained per EASA's regulations on medium-risk drone operations.	Certification, Safety	I	REQ-SYS-CON-SFT-3;
CON-SFT-2.2	The system units shall be lighter than 25 kg.	Max mass to be carried by 1 person	T	REQ-SYS-CON-SFT-3;
CON-SFT-3	The system shall not harm the environment.	Environmental health	I, T	REQ-STK-WE-2;
CON-SFT-3.1	All flammable substances within the units shall be encased in protective casings.	Fire safety	I	REQ-SYS-CON-SFT-4;
CON-SFT-3.2	The protective casings of flammable substances shall withstand loads during all landing cases.	Fire safety	T	REQ-SYS-CON-SFT-4;
CON-SFT-3.3	The protective casings of flammable substances shall contain the substance in case of ignition.	Fire safety	T	REQ-SYS-CON-SFT-4;
CON-SFT-3.4	All toxic substances within the units shall be encased in protective casings.	Environmental safety	I	REQ-SYS-CON-SFT-4;
CON-SFT-3.5	The protective casing of damaging substances shall withstand loads during all operational cases.	Environmental Safety	T	REQ-SYS-CON-SFT-4;
Resources				
CON-RSC-1	The project shall stay within the allocated budget.	Profitability	I	REQ-STK-LG-2;
CON-RSC-1.1	The marginal cost of one system shall not cost more than \$ 1.8 million.	From Swarm Performance section, half the cost of a surveillance aircraft (Competitor Comparison)	I	REQ-SYS-CON-RSC-1
CON-RSC-1.2	One system's total operating cost shall not exceed \$ 650 per hour.	From Swarm Performance section, half the cost of operating a surveillance aircraft (Competitor Comparison)	I	REQ-SYS-CON-RSC-1;
CON-RSC-1.3	The units shall promote ease of development with a modular design.	Risk Generated	I	REQ-SYS-CON-RSC-1;
CON-RSC-2	The project shall be completed within the set time.	Unwanted costs	D, I, T	REQ-SYS-CON-RSC-1;
CON-RSC-2.1	The manufacturing of one system shall not take longer than 8 weeks.	From Manufacturing Plan	T	REQ-SYS-CON-RSC-1;
CON-RSC-2.2	One system's operational lifetime shall be at least 4 years.	Maximise utility and ROI, following the market analysis	D	REQ-SYS-CON-RSC-1; REQ-SYS-RSC-1.1
CON-RSC-2.3	The system shall be designed with existing technology.	Certified for safety, faster to market	I	REQ-SYS-CON-RSC-1;
Legality				
CON-LGL-1	The system shall comply to all certification requirements.	Certification purposes	I	REQ-STK-AA-1;
CON-LGL-1.1	A special class type certificate shall be requested from the FAA under 14 CFR 21.17(b).	Certification purposes	I	REQ-SYS-CON-LGL-1;

Table 50 – continued from previous page

ID [REQ-SYS-...]	Requirement	Rational	Verification	Traceability
CON-LGL-1.2	The system shall comply with the special airworthiness criteria received from the FAA.	Certification purposes	I	REQ-SYS-CON-LGL-1;
CON-LGL-2	The system's production shall comply with local and international legislation.	Ensure compliance with all laws	I	Local and International Law
CON-LGL-2.1	The manufacturing processes used for the system shall comply with local and international legislation.	Ensure compliance with all laws	I	REQ-SYS-CON-LGL-2
CON-LGL-2.2	The materials used for the system shall comply with local and international legislation.	Ensure compliance with all laws	I	REQ-SYS-CON-LGL-2
CON-LGL-2.3	The materials used for the system shall not be listed in the sanctioned materials list of the local government.	Ensure compliance with all laws	I	REQ-SYS-CON-LGL-2
CON-LGL-3	The system's operations shall adhere to local and international legislation.	Ensure compliance with all laws	I	Local and International Law
Sustainability				
CON-STB-1	The system shall meet the predetermined environmental sustainability requirements.	Environmental purposes	I, T	REQ-STK-WE-2; REQ-STK-GP-1
CON-STB-1.1	The system's manufacturing process shall not include any toxic materials.	Environmental purposes	I	REQ-SYS-CON-STB-1
CON-STB-1.2	The system's structure shall not include any components composed of toxic materials.	Environmental purposes	I	REQ-SYS-CON-STB-1
CON-STB-1.3	The system operations shall not produce more than 93.8 kg of CO ₂ per year per system.	Necessary emission limit to positively offset the effect of wildfires	T	Midterm Report, Section 7.3
CON-STB-1.4	The delivery of the system to its operational location shall not produce more than 0.5 kg of CO ₂ per km.	Estimated CO ₂ emissions of a shipment of 5 standardised containers.	T	REQ-SYS-CON-STB-1
CON-STB-1.5a	For a unit MTOW < 25kg, the system units shall not fly any closer than 600m to any known nesting spot of protected bird species.	Wildlife Regulations	T	REQ-SYS-CON-STB-1
CON-STB-1.5b	For a unit MTOW ≥ 25kg, the system units shall not fly any closer than 2000m to any known protected bird species nesting spot.	Wildlife Regulations	T	REQ-SYS-CON-STB-1
CON-STB-1.6	The end-of-life disposal procedure shall be able to recycle at least 90% of the materials.	Environmental purposes	T	REQ-SYS-CON-STB-1
CON-STB-2	The system shall be designed for economic sustainability.	Profitability	D	REQ-STK-LG-2
CON-STB-2.1	The system shall be modifiable to reflect the changing needs of the stakeholders.	Stakeholder satisfaction	D	REQ-SYS-CON-STB-2
CON-STB-2.2	The system shall be modifiable to reflect the needs of different markets.	Easy implementation in future	D	REQ-SYS-CON-STB-2
CON-STB-2.3	The unit shall be inspectable.	Mission Sustainability	D	REQ-SYS-CON-STB-2
CON-STB-2.4	The unit shall be maintainable.	Mission Sustainability	D	REQ-SYS-CON-STB-2
CON-STB-3	The system shall meet the predetermined societal sustainability requirements.	Social impact	D, T	REQ-STK-LP-2
CON-STB-3.1	The system shall not fly above residential areas below an altitude of 30 m.	Social impact	T	REQ-SYS-CON-STB-3; EASA Regulations
CON-STB-3.2	The system's adoption shall be announced to the local public before operation.	Social impact	D	REQ-SYS-CON-STB-3

Table 48: Link Budget between Observational Drones

Crosslink (Tx Drone, Rx Drone)				
	Symbol		Units	Value
Transmitter	P_T	Tx Power	dBm	30.0
	L_T,Line	Tx Component Line Loss	dB	-1.0
	G_T	Tx Antenna Gain	dB	7.2
	L_T,Point	Tx Pointing Loss	dB	-1.0
	L_T,Radome	Tx Radome Loss	dB	0.0
		EIRP		dBm
Propagation	L_FS	Free Space Loss	dB	-109.6
	L_P,Atm	Atmospheric Absorbtion	dB	0.0
	L_P,Precip	Fire Attenuation Losses	dB	-26.8
		Total Propagation Loss	dB	-136.4
Receiver	G_R	Rx Peak Antenna Gain	dB	7.2
	L_R,Polar	Rx Polarization Loss	dB	-3.0
	L_R,Point	Rx Pointing Loss	dB	-0.5
	L_R,Radome	Rx Radome Loss	dB	0.0
	L_R,Line	Rx Component Line Loss	dB	-1.0
		Effective Carrier Power		dBm
Noise	kT	Thermal Noise Density	dBm/Hz	-174.0
	BW	Rx Noise Bandwidth	dBHz	42.9
	P_TN	Thermal Noise Power	dBm	-131.1
	NF	Rx Noise Figure	dB	8.0
		Effective Noise Power		dBm
Summary		Available SNR	dB	24.5
		Required SNR	dB	15.0
		Net Signal Margin	dB	9.5
Crosslink (Tx Relay, Rx Relay)				
	Symbol		Units	Value
Transmitter	P_T	Tx Power	dBm	40.0
	L_T,Line	Tx Component Line Loss	dB	-1.0
	G_T	Tx Antenna Gain	dB	21.9
	L_T,Point	Tx Pointing Loss	dB	-3.0
	L_T,Radome	Tx Radome Loss	dB	-0.5
		EIRP		dBm
Propagation	L_FS	Free Space Loss	dB	-123.6
	L_P,Atm	Atmospheric Absorbtion	dB	0.0
	L_P,Precip	Fire Attenuation Losses	dB	-27.7
		Total Propagation Loss	dB	-151.3
Receiver	G_R	Rx Peak Antenna Gain	dB	21.9
	L_R,Polar	Rx Polarization Loss	dB	-3.0
	L_R,Point	Rx Pointing Loss	dB	-3.0
	L_R,Radome	Rx Radome Loss	dB	-0.5
	L_R,Line	Rx Component Line Loss	dB	-1.0
		Effective Carrier Power		dBm
Noise	kT	Thermal Noise Density	dBm/Hz	-174.0
	BW	Rx Noise Bandwidth	dBHz	68.5
	P_TN	Thermal Noise Power	dBm	-105.4
	NF	Rx Noise Figure	dB	8.0
		Effective Noise Power		dBm
Summary		Available SNR	dB	17.9
		Required SNR	dB	12.0
		Net Signal Margin	dB	5.9

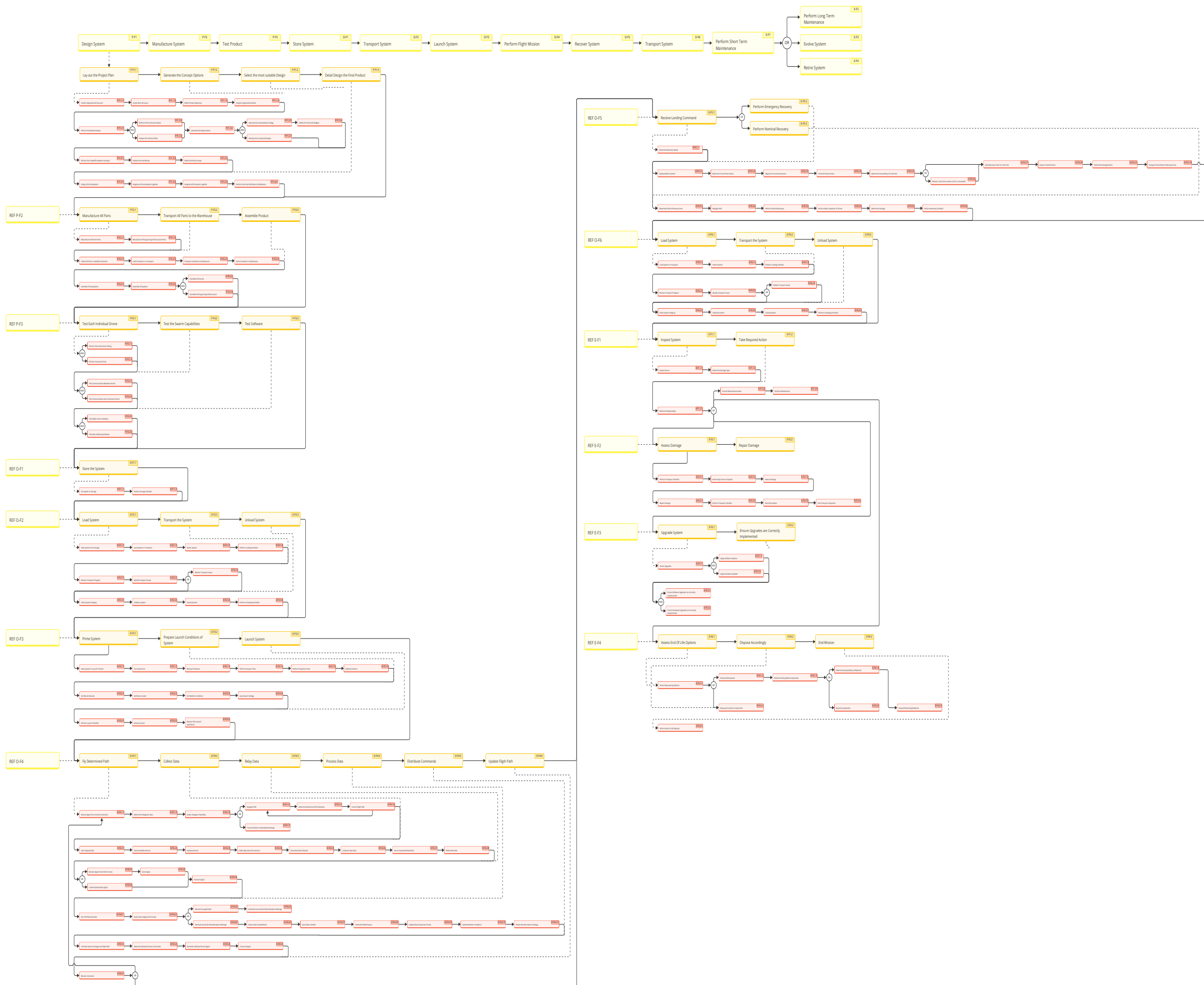
Uplink (Tx Drone, Rx Relay)				
	Symbol		Units	Value
Transmitter	P_T	Tx Power	dBm	27.0
	L_T,Line	Tx Component Line Loss	dB	-1.0
	G_T	Tx Antenna Gain	dB	20.3
	L_T,Point	Tx Pointing Loss	dB	-3.0
	L_T,Radome	Tx Radome Loss	dB	-0.5
		EIRP		dBm
Propagation	L_FS	Free Space Loss	dB	-112.1
	L_P,Atm	Atmospheric Absorbtion	dB	0.0
	L_P,Precip	Fire Attenuation Losses	dB	-22.6
		Total Propagation Loss	dB	-134.6
Receiver	G_R	Rx Peak Antenna Gain	dB	20.3
	L_R,Polar	Rx Polarization Loss	dB	-3.0
	L_R,Point	Rx Pointing Loss	dB	-3.0
	L_R,Radome	Rx Radome Loss	dB	-0.5
	L_R,Line	Rx Component Line Loss	dB	-1.0
		Effective Carrier Power		dBm
Noise	kT	Thermal Noise Density	dBm/Hz	-174.0
	BW	Rx Noise Bandwidth	dBHz	61.5
	P_TN	Thermal Noise Power	dBm	-112.4
	NF	Rx Noise Figure	dB	8.0
		Effective Noise Power		dBm
Summary		Available SNR	dB	25.4
		Required SNR	dB	15.0
		Net Signal Margin	dB	10.4

Downlink (Tx Relay, Rx Drone)				
	Symbol		Units	Value
Transmitter	P_T	Tx Power	dBm	27.0
	L_T,Line	Tx Component Line Loss	dB	-1.0
	G_T	Tx Antenna Gain	dBi	20.3
	L_T,Point	Tx Pointing Loss	dB	-3.0
	L_T,Radome	Tx Radome Loss	dB	-0.5
		EIRP		dBm
Propagation	L_FS	Free Space Loss	dB	-112.1
	L_P,Atm	Atmospheric Absorbtion	dB	0.0
	L_P,Precip	Fire Attenuation Losses	dB	-22.6
		Total Propagation Loss	dB	-134.6
Receiver	G_R	Rx Peak Antenna Gain	dBi	15.9
	L_R,Polar	Rx Polarization Loss	dB	-3.0
	L_R,Point	Rx Pointing Loss	dB	-3.0
	L_R,Radome	Rx Radome Loss	dB	-0.5
	L_R,Line	Rx Component Line Loss	dB	-1.0
		Effective Carrier Power		dBm
Noise	kT	Thermal Noise Density	dBm/Hz	-174.0
	BW	Rx Noise Bandwidth	dBHz	41.1
	P_TN	Thermal Noise Power	dBm	-132.8
	NF	Rx Noise Figure	dB	8.0
		Effective Noise Power		dBm
Summary		Available SNR	dB	41.4
		Required SNR	dB	15.0
		Net Signal Margin	dB	26.4

Table 49: Link Budget between Relay Drone and Ground Control Unit

Uplink (Tx Ground, Rx Relay)				
	Symbol		Units	Value
Transmitter	P_T	Tx Power	dBm	30
	L_T,Line	Tx Component Line Loss	dB	-3
	G_T	Tx Antenna Gain	dBi	26.2
	L_T,Point	Tx Pointing Loss	dB	-4
	L_T,Radome	Tx Radome Loss	dB	0
		EIRP		dBm
Propagation	L_FS	Free Space Loss	dB	-120
	L_P,Atm	Atmospheric Absorbtion	dB	0
	L_P,Precip	Fire Attenuation Losses	dB	-31
		Total Propagation Loss	dB	-151
Receiver	G_R	Rx Peak Antenna Gain	dBi	21.9
	L_R,Polar	Rx Polarization Loss	dB	-3
	L_R,Point	Rx Pointing Loss	dB	-3
	L_R,Radome	Rx Radome Loss	dB	-0.5
	L_R,Line	Rx Component Line Loss	dB	-1
	L_R,Spread	Spreading Implementation Loss	dB	0
		Effective Carrier Power	dBm	-87
Noise	kT	Thermal Noise Density	dBm/Hz	-173
	BW	Rx Noise Bandwidth	dBHz	37
	P_TN	Thermal Noise Power	dBm	-135.9
	NF	Rx Noise Figure	dB	15
		Effective Noise Power	dBm	-121
Summary		Available SNR	dB	34
		Required SNR	dB	12
		Net Signal Margin	dB	22

Downlink (Tx Drone, Rx Relay)				
	Symbol		Units	Value
Transmitter	P_T	Tx Power	dBm	30
	L_T,Line	Tx Component Line Loss	dB	-1
	G_T	Tx Antenna Gain	dBi	21.9
	L_T,Point	Tx Pointing Loss	dB	-0.5
	L_T,Radome	Tx Radome Loss	dB	-0.5
		EIRP		dBm
Propagation	L_FS	Free Space Loss	dB	-120
	L_P,Atm	Atmospheric Absorbtion	dB	0
	L_P,Precip	Fire Attenuation Losses	dB	-31
		Total Propagation Loss	dB	-151
Receiver	G_R	Rx Peak Antenna Gain	dBi	26.2
	L_R,Polar	Rx Polarization Loss	dB	-3
	L_R,Point	Rx Pointing Loss	dB	-1
	L_R,Radome	Rx Radome Loss	dB	-0.5
	L_R,Line	Rx Component Line Loss	dB	-1
	L_R,Spread	Spreading Implementation Loss	dB	0
		Effective Carrier Power	dBm	-80
Noise	kT	Thermal Noise Density	dBm/Hz	-173
	BW	Rx Noise Bandwidth	dBHz	63
	NF	Rx Noise Figure	dB	8
		Effective Noise Power	dBm	-102
Summary		Available SNR	dB	22
		Required SNR	dB	15
		Net Signal Margin	dB	7



Functional Breakdown Diagram

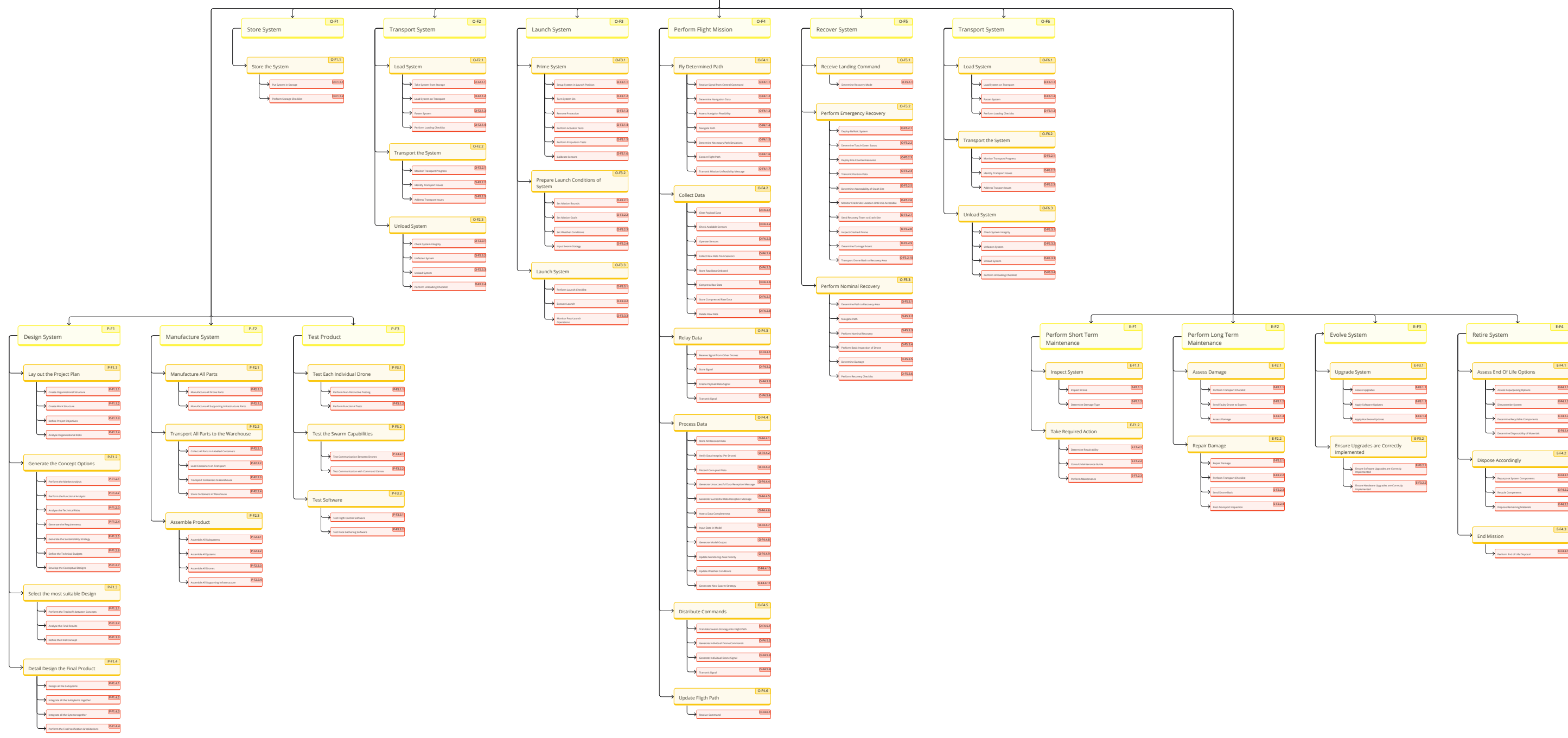


Figure 85: Functional Breakdown Diagram